A STUDY OF PHOTONS FROM DECAYS OF THE K_L^o

A DISSERTATION

SUBMITTED TO THE DEPARTMENT OF PHYSICS

AND THE COMMITTEE ON GRADUATE STUDIES

OF STANFORD UNIVERSITY

IN PARTIAL FULFILLMENT OF THE REQUIREMENTS

FOR THE DEGREE OF

DOCTOR OF PHILOSOPHY

By

John Field Greenhalgh

January 1981

I certify that I have read this thesis and that in my opinion it is fully adequate, in scope and quality, as a dissertation for the degree of Doctor of Philosophy.

(Principal Advisor)

I certify that I have read this thesis and that in my opinion it is fully adequate, in scope and quality, as a dissertation for the degree of Doctor of Philosophy.

I certify that I have read this thesis and that in my opinion it is fully adequate, in scope and quality, as a dissertation for the degree of Doctor of Philosophy.

Sidney D. Drell

Approved for the University Committee on Graduate Studies:

Dean of Graduate Studies

PREFACE

I would like to acknowledge first my advisor, Mel Schwartz, whose enthusiasm and imagination have given me inspiration as well as new perspectives on physics. My association with him has been extremely rewarding. I am particularly indebted also to Bob Cousins, with whom I enjoyed a close working relationship over the last four years, a fitting sequel to a spectacular collaboration at Princeton. I look forward to putting our heads together at some time in the future.

The efforts and ideas of our collaborators (and co-authors) from the Universities of Chicago and Wisconsin, Sam Aronson, Bob Bernstein, Greg Bock, Dave Hedin, Gordon Thomson, and Bruce Winstein, are inadequately reflected in this thesis. I learned a great deal from them. Among other responsibilities, Dave Hedin shared with Bob and me the bulk of the data analysis.

We were ably assisted during set-up and data taking by Bindu Bambah, David Berg, Chris Gardner, and Hamish Norton.

Superb technical and engineering support was provided by Adrian Alexander, Dale Ouimette, Dan Porat, and Thomas Shea. Bob and I are grateful to Dan and Dale for teaching

us the rudiments of digital electronics. The Physical Sciences Laboratory of the University of Wisconsin built our beam line and vacuum window with great skill.

The operators and crews of the Meson Lab (as well as Accelerator Operations) made it possible for us to take data under much less trying circumstances than might have otherwise prevailed.

The staff of the Computing Department gave us much assistance. In particular, Dave Ritchie deserves special thanks for his unselfish and considerable labors in introducing us to the PDP 11 computer, assembly language, and on-line programming. Much of our expertise is directly attributable to his pedagogy.

I thank my good friends Peter Brooks, Jay Dworkin, Alan Katz, and Greg Snow for their logistical support.

Bob Cousins forgot to thank Petros Rapidis for carefully reading his thesis. I thank Petros for many valuable discussions.

Finally, I am grateful to my parents and sister Anne for their continual good will. For having accelerated the pace of my efforts to complete this experiment, and for her patience and good sense, I thank Thalia Wilber.

TABLE OF CONTENTS

Signature Page	ii
Preface	iii
Table of Contents	v
List of Tables	viii
List of Figures	ix
Chapter 1. Introduction	1
1.1 Spectroscopy and Rare Decays	1
1.2 Motivation for Present Experiment	4
1.3 Outline of the Remainder of this Thesis	8
Chapter 2. Theoretical Considerations: Part I	9
2.1 Pi-Mu Atoms	9
2.2 Pi-Mu Atom Branching Ratio	11
Chapter 3. Theoretical Considerations: Part II	22
3.1 $K_L^0 \to \pi^0 \pi^0$	22
3.2 $K_L^0 \to \gamma\gamma$	27
Chapter 4. Experimental Technique	30
4.1 Using a Neutral Kaon Beam	30
4.2 Detecting Pi-Mu Atoms	33
4.3 Detecting Photons	39
Chapter 5. Apparatus	46
5.1 Coordinate System	46
5.2 Beam and Decay Region	46
5.3 Vacuum Window	48
5.4 Break-up Foils	49
5.5 Magnets	50

5.6 Multi-wire Proportional Chambers 51
5.7 Scintillation Counters 53
5.8 Shower Counters 54

Chapter 6. Data Acquistion 56
6.1 Trigger Logic 56
6.2 Data Acquisition Hardware and Software 59
6.3 Data Runs 62

Chapter 7. The Monte Carlo Computer Program 64
7.1 General Description 64
7.2 Tracking Through Magnets 68
7.3 Kinematics of Particle Decays 69
7.4 Electromagnetic Processes 72
7.4.1 Radiative Energy Loss 77
7.4.2 Pair Production by Photons 77
7.4.3 Pair Production by Electrons 80
7.4.4 Multiple Scattering 82

Chapter 8. Electromagnetic Shower Simulation Using EGS 87

Chapter 9. Event Selection 93
9.1 Event Reconstruction and Normalization Schemes 94
9.2 Two-Track Event Reconstruction 99
9.3 Momentum Measurement 101
9.4 Particle Identification 102
9.5 Event Selection 106
9.5.1 Foil Events (Pi-Mu Atoms and e^+e^- Pairs) 107
9.5.2 Non-foil Events 136

Chapter 10. Calibrations 155
10.1 Determining the Geometry of the Apparatus 155
10.2 Magnetic Field Calibrations 157
10.3 Determining the Geometry of the Beam 159
10.4 The Input K_L^o Momentum Spectrum 160
10.5 Multi-wire Proportional Chamber Efficiencies 163
10.6 Scintillation Counter Efficiencies 164
10.7 Extra Hits in the W and H Counters 165
10.8 Extra Hits in the A,B and G Counters 168

Chapter 11. The Probability of Formation of Pi-Mu Atoms 169
11.1 Pi-Mu Atom and $K_{\mu 3}$ Backgrounds 169

11.2 The Pi-Mu Atom Branching Ratio 171
11.3 The Pi-Mu Atom Lifetime 175

Chapter 12. The Single Photon Transverse Momentum Spectrum 180
12.1 The Components of the Spectrum, Including Backgrounds 181
12.2 The Loss of Events Due to Electromagnetic Showers 194
12.3 The Fitting Procedure 202
12.4 The $2\pi^0$ and $\gamma\gamma$ Branching Ratios 205

Chapter 13. Conclusions 212

References 215

LIST OF TABLES

1. Results of Brookhaven Experiment 6
2. Characteristics of Pi-Mu and Hydrogen Atoms 10
3. Photon-producing Decays of the K_L^o 43
4. Sources of Systematic Errors 174
5. Sources of Systematic Errors 209

LIST OF FIGURES

1. Comparison of momentum spectra for pi-mu atom data and Monte Carlo generated pi-mu atom events (normalized to 10^{12} protons/pulse), from the Brookhaven experiment. 7

2. The ratio R defined in the text, as a function of $\xi(0)$. Experimentally, $\xi(0) = -0.14 \pm 0.11$, while $\lambda_+ = 0.034 \pm 0.005$. From top to bottom, the three curves are for $\lambda_+ = 0.039$, 0.034, and 0.029, respectively. 20

3. Elevation view of the M3 beam line at Fermilab. 32

4. Elevation view of the pi-mu atom spectrometer. Distances from the Meson target are given at the bottom. 34

5. Plan view of the pi-mu atom spectrometer. 35

6. Plan view of a pi-mu atom event. 40

7. Plan view of a $K_{\mu 3}$ event. 41

8. Vertical displacement of muons (from $K_{\mu 3}$ decay) due to scattering in the steel filter. 86

9. Fraction of events remaining after electromagnetic shower simulation. From top to bottom, decay modes are $K_L^o \to \pi^+\pi^-\pi^o$, $K_L^o \to \gamma\gamma$, $K_L^o \to \pi^o\pi^o$, and $K_L^o \to \pi^o\pi^o\pi^o$. 92

10. Fraction of a particle's energy observed in the shower counters, for a sample of events containing muons, pions, and electrons. 105

11. Relative change in the separation of tracks in the rear of the spectrometer, for data containing both foil and non-foil events, before cuts. 108

12. Relative change in the separation of tracks in the rear of the spectrometer, for the final sample of e^+e^- pairs, compared to Monte Carlo generated e^+e^- events. 109

13. The quantity $(4 \cdot \Delta_1 - \Delta_3)$, described in the text, before cuts. 111

14. The quantity $(4 \cdot \Delta_1 - \Delta_3)$, described in the text, for the final sample of e^+e^- pairs, compared to Monte Carlo generated e^+e^- events. 112

15. Separation of the two tracks at their closest approach, before the cut. 113

16. Separation of the two tracks at their closest approach, for the final sample of e^+e^- pairs, compared to Monte Carlo generated e^+e^- events. 114

17. Z of the vertex of the "V" formed by two tracks, before cuts. 115

18. Z of the vertex of the "V" formed by two tracks, for the final sample of e^+e^- pairs, compared to Monte Carlo generated e^+e^- events. 116

19. Largest side view separation of tracks, before the cut. The spikes are at multiples of wire spacings. 118

20. Largest side view separation of tracks, for the final sample of e^+e^- pairs, compared to Monte Carlo generated e^+e^- events. 119

21. Smallest side view separation of tracks, before the cut. 120

22. Smallest side view separation of tracks, for the final sample of e^+e^- pairs, compared to Monte Carlo generated e^+e^- events. 121

23. Fraction of a particle's energy observed in the shower counters, for tracks of pi-mu atom candidates. 123

24. The variable $\alpha=(p_\pi-p_\mu)/(p_\pi+p_\mu)$, for pi-mu atom candidates, before shower counter cuts. 124

25. The variable $\alpha=(p_\pi-p_\mu)/(p_\pi+p_\mu)$, for pi-mu atom candidates, after shower counter cuts. 125

26. Transverse momentum spectrum of pi-mu atom candidates, before cuts. 127

27. Invariant mass of e^+e^- pairs, compared to Monte Carlo generated e^+e^- events, before the cut. 129

28. Z position of the K_L^o decay, for pi-mu atom candidates, before cuts. 131

29. Z position of the K_L^o decay, for e^+e^- pairs with p_t > 160 MeV/c, before cuts. 132

30. Z position of the K_L^o decay, for the final sample of e^+e^- pairs, compared to Monte Carlo generated e^+e^- events. 133

31. Y position of photons at the foil, before the cut. 135

32. The variable $\alpha=(p_\pi-p_\mu)/(p_\pi+p_\mu)$, for the final sample of pi-mu atoms, compared to Monte Carlo generated pi-mu atoms. 137

33. Transverse momentum of photons in the final sample. 138

34. Transverse momentum of pi-mu atoms in the final sample, compared to Monte Carlo generated pi-mu atoms. 139

35. Z position of the K_L^o decay, for the final sample of pi-mu atoms, compared to Monte Carlo generated pi-mu atoms. 140

36. Momentum spectrum of pi-mu atoms in the final sample, compared to Monte Carlo generated pi-mu atoms. 141

37. Momentum spectrum of photons in the final sample, compared to Monte Carlo generated e^+e^- events. 142

38. Largest side view track separation, for non-foil event candidates, before the cut. 144

39. Separation of the two tracks at their closest approach (the K_L^o decay point), for non-foil event candidates, before the cut. 146

40. Separation of the pion and muon at their closest approach (the K_L^o decay point), for the final sample of $K_{\mu 3}$ events, compared to Monte Carlo generated $K_{\mu 3}$ events. 147

41. Z position of the K_L^o decay, for the final sample of $K_{\mu 3}$ events, compared to Monte Carlo generated $K_{\mu 3}$ events. 148

42. Transverse momentum of the pion-muon pair, for the final sample of $K_{\mu 3}$ events, compared to Monte Carlo generated $K_{\mu 3}$ events. 149

43. The kinematic variable P_o^2 defined in the text, for $K_{\mu 3}$ candidates, before cuts. 151

44. The variable ARG defined in the text, for the final sample of $K_{\mu 3}$ events, compared to Monte Carlo generated $K_{\mu 3}$ events. 153

45. K_L^o momentum spectrum, for the final sample of $K_{\mu 3}$ events, compared to Monte Carlo generated $K_{\mu 3}$ events. 154

46. Momentum spectrum of forward neutral kaons emerging from the Meson target. 161

47. K_L^o momentum spectrum cut on the variable ARG, for the final sample of $K_{\mu 3}$ events, compared to Monte Carlo generated $K_{\mu 3}$ events. 162

48. Lifetime of pi-mu atoms, compared to Monte Carlo pi-mu atoms generated with the lifetime of the pion (normalized to equal areas). 177

49. Lifetime of pi-mu atoms, compared to Monte Carlo pi-mu atoms generated with one third the lifetime of the pion (normalized to equal areas). 178

50. Monte Carlo simulation of the portion of the photon transverse momentum spectrum due to $K_L^o \to \pi^o \pi^o \pi^o$. 182

51. Monte Carlo simulation of the portion of the photon transverse momentum spectrum due to $K_L^o \to \pi^+ \pi^- \pi^o$. 183

52. Monte Carlo simulation of the portion of the photon transverse momentum spectrum due to $K_L^o \to \pi e \nu \gamma$. 184

53. Monte Carlo simulation of the portion of the photon transverse momentum spectrum due to $K_L^o \to \pi^o \pi^o$. 185

54. Monte Carlo simulation of the portion of the photon transverse momentum spectrum due to $K_L^o \to \gamma\gamma$. 186

55. Transverse momentum of photons, from data taken with the vacuum spoiled. 187

56. Transverse momentum of photons attributed to beam-gas interactions. 189

57. The ratio of the energies of the positron and photon, for the final sample of e^+e^- pairs, compared to Monte Carlo generated e^+e^- events, <u>not</u> including tridents. 192

58. The ratio of the energies of the positron and photon, for the final sample of e^+e^- pairs, compared to Monte Carlo generated e^+e^- events, including tridents. 193

59. Transverse momentum spectrum of e^-e^- pairs passing all cuts for foil events, compared to Monte Carlo generated e^-e^- events from trident production. 195

60. Monte Carlo simulation of the portion of the photon transverse momentum spectrum due to e^+e^- pairs from trident production. 196

61. Complete Monte Carlo simulation of the transverse momentum spectrum of reconstructed photons, after the fit to the data described in the text. 203

62. Transverse momentum of photons in the final sample, compared to the complete Monte Carlo simulation. 204

63. Transverse momentum of photons compared to the complete Monte Carlo simulation, for the largest number of events available. 211

CHAPTER 1

INTRODUCTION

1.1 SPECTROSCOPY AND RARE DECAYS

Spectroscopy and the study of rare decay modes have been fruitful ways of achieving deeper insights into the forces and symmetries of nature, and the characteristics of the fundamental constituents of matter. A cursory glance at a textbook treatment of the hydrogen atom, for instance, demonstrates that the nature of the electromagnetic interaction at short distances and certain characteristics of the electron and proton were revealed through a detailed study of the atom's energy levels.

To account for the observed "fine structure", a relativistic correction to the kinetic energy and an interaction between the moving electron's spin angular momentum with the proton's electric field had to be included in the Hamiltonian describing the bound states of

the atom. The fact that the proton, too, has spin one-half is manifest in the spectrum of the hydrogen atom, as a "hyperfine" splitting of each level as characterized by principal quantum number n, orbital angular momentum ℓ, and total angular momentum j. The splitting of states with the same n and j (degenerate according to the Dirac theory), in particular the $2S_{\frac{1}{2}}$ and $2P_{\frac{1}{2}}$ separation discovered in 1947 by Lamb and Retherford, is mainly a consequence of the electron's interaction with the quantized radiation field, and may be calculated quite accurately using the machinery of quantum electrodynamics. Spectroscopy is not limited to atomic physics, however. For example, today's study of the psi and upsilon families of mesons may be regarded as the spectroscopy of quark-antiquark bound states.

Three rare decay processes immediately come to mind that have played or perhaps will play a significant role in the development of theories of the interactions of elementary particles. The smallness of the ratio of the electronic to the muonic decay rates of the pion, about 1.27×10^{-4} despite the larger Q-value available, demonstrated convincingly that the coupling is axial vector and not pseudoscalar, in conformity with the V-A form of the effective weak current. The detection of the decay $K_L^o \to \pi^+\pi^-$, which has a branching ratio about 2×10^{-3} compared to all K_L^o decays, signalled the discovery of the

violation of the combined symmetries of charge conjugation and parity (CP). Today experiments are being mounted to search for an extremely rare process, proton decay, which is predicted to occur by certain theories which attempt to unify the strong, electromagnetic, and weak interactions.

In this glorious context, the experiment described here is best appreciated. The experiment was about the pi-mu atom, a Coulomb bound state of a pion and a muon; it was also about the long-lived neutral kaon K_L^o, thought to be a gluon bound state of a d (down) and an $\bar{s}$ (anti-strange) quark. A pi-mu atom is born when a pion and a muon are brought together. Conveniently, the K_L^o often decays to a pion, muon, and muon-neutrino. Occasionally, the pion and muon come off close enough in phase space to bind, although the process may be regarded as a two-body decay. The experiment was designed primarily to measure the rate of K_L^o decay to pi-mu atoms, expected to occur with a branching ratio compared to all K_L^o decays of $(1.20 \pm 0.04) \times 10^{-7}$ (see Chapter 2). This is clearly a rare decay. Rare, too, are the decays $K_L^o \to \pi^o \pi^o$ and $K_L^o \to \gamma\gamma$ which were detected simultaneously. Unfortunately, the spectroscopy of the pi-mu atom system could not be performed in this experiment. (The conquering of that mountain remains for another generation of hardy, idealistic graduate students.) This thesis, then, is really only about certain rare K_L^o

decays. However, the atomic physics is not lost altogether, as the rate of production of pi-mu atoms depends directly upon the square of the atom's wave function evaluated at the origin.

1.2 MOTIVATION FOR PRESENT EXPERIMENT

One would expect the wave function of the pi-mu atom, upon which the rate of formation hinges, to be simply the solution to the non-relativistic Schrodinger equation with a Coulomb potential. Evaluated at the origin and squared, this is

$$|\psi_n(\vec{r}=0)|^2 = \frac{\alpha^3\mu^3}{\pi n^3}$$

where n is the principal quantum number, α the fine structure constant, and μ the reduced mass of the atom. A disagreement between the observed and predicted rates might be a manifestation of some new short-range interaction between the pion and the muon which would distort the wave function. (The Bohr radius of the pi-mu atom is 450 fm which is large on nuclear scales, but considerably smaller than in hydrogen (see Table 2, Chapter 2).) Such a discrepancy was found in the first pi-mu atom experiment.

Pi-mu atoms from K_L^0 decay were first detected at Brookhaven National Laboratory by Mel Schwartz and

collaborators (ref. 1,2). Monte Carlo calculations predicted a higher rate of production than was found, as shown in Table 1 (ref. 3).

The Brookhaven data raised several questions. Was the surprisingly low rate due to errors in the normalization? In fact the Monte Carlo predictions for the normalization data were about 20% low, making the disparity worse than indicated in Table 1 (ref. 4). Could there be some physical effect which suppresses K_L^o decay into pi-mu atoms, or put another way: is the pi-mu atom wave function not simply a Coulomb wave function? Fewer atoms would have been detected than anticipated if the pi-mu atom has a lifetime shorter than its shortest-lived constituent, the pion. Could, then, the rate of production have been as expected but the atom lifetime be anomalously short? It was suggested that the differences between the momentum spectra of detected pi-mu atoms and Monte Carlo generated ones, reproduced in Figure 1 (ref. 5), might be resolved if the atom lifetime were one third the pion lifetime (ref. 6).

To answer these questions a second pi-mu atom experiment was proposed and approved at the Fermi National Accelerator Laboratory (Experiment 533). The problem was also scrutinized from a theoretical point of view (ref. 7). Some results from that experiment, bearing on the decays

Table 1. Results of Brookhaven Experiment

Run Condition*	Atoms Observed	Atoms/10^{12} p on target
Cycle 5 250 mil	11	$(2.13 \pm 0.75) \times 10^{-4}$
Monte Carlo		$(1.13 \pm 0.18) \times 10^{-3}$
Cycle 6 250 mil	9	$(1.64 \pm 0.93) \times 10^{-4}$
Monte Carlo		$(1.13 \pm 0.18) \times 10^{-3}$
Cycle 6 30 mil	24	$(4.60 \pm 1.22) \times 10^{-4}$
Monte Carlo		$(1.67 \pm 0.27) \times 10^{-3}$

*Indicated is the thickness of the aluminum foil used to dissociate the atom into a π and μ, which were detected separately.

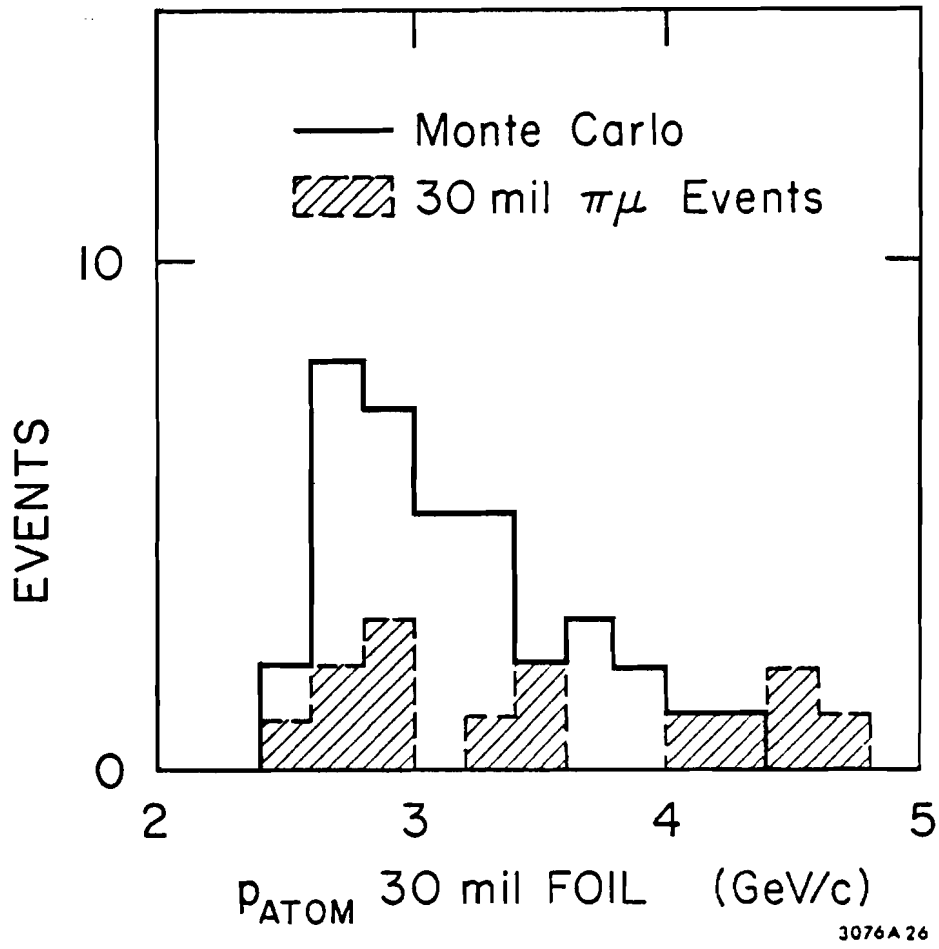

Figure 1. Comparison of momentum spectra for pi-mu atom data and Monte Carlo generated pi-mu atom events (normalized to 10^{12} protons/pulse), from the Brookhaven experiment.

$K_L^o \to \gamma\gamma$ and $K_L^o \to \pi^o\pi^o$ as well as $K_L^o \to (\pi\mu)_{atom}\nu$, are reported here.

1.3 OUTLINE OF THE REMAINDER OF THIS THESIS

Chapter 2 displays the principal characteristics of the pi-mu atom and a calculation of the rate of K_L^o decay into pi-mu atoms. As noted above, the rare processes $K_L^o \to \pi^o\pi^o$ and $K_L^o \to \gamma\gamma$ were also observed. Chapter 3 indicates why measurements of these decay rates have been of theoretical interest. Chapter 4 surveys the experimental layout, stressing the method of detecting pi-mu atoms and photons from K_L^o decays. It is therefore crucial to the rest of the thesis. The various components of the apparatus are described in greater detail in Chapter 5, the trigger and data acquisition in Chapter 6. The succeeding two chapters are devoted to the Monte Carlo simulation of the experiment. Data analysis and event selection procedures are discussed in Chapter 9. Calibrations are treated in Chapter 10. In Chapter 11 we obtain a measurement of the rate of formation of pi-mu atoms. Chapter 12 presents the derivation of branching ratios for K_L^o $\pi^o\pi^o$ and $K_L^o \to \gamma\gamma$. Results are summarized in Chapter 13.

CHAPTER 2

THEORETICAL CONSIDERATIONS: PART I

2.1 PI-MU ATOMS

The essential characteristics of the bound state of a pion and a muon are readily calculated using the non-relativistic Schrodinger equation with a Coulomb potential. At this level, the pi-mu atom is identical to hydrogen except that its reduced mass is about 120 times larger, so that the Bohr radius is about 120 times smaller, and the binding energy about 120 times greater (see Table 2). Whereas hydrogen is stable, the pi-mu atom presumably has the lifetime of the pion, since the muon lives about 100 times longer than the pion, and the effect of the binding energy on the phase space of the atom decay is negligible.

A more detailed study of the energy levels of the pi-mu atom reveals interesting differences in comparison with

Table 2. Characteristics of Pi-Mu and Hydrogen Atoms

	π-μ atom	p-e atom
reduced mass	60.13 MeV	0.511 MeV
Bohr radius	4.50×10^{-11} cm	5.29×10^{-9} cm
binding energy	1.6 keV/n^2	13.6 eV/n^2
lifetime	2.57×10^{-8} sec	stable

hydrogen. For example, the sign of the $2P_{\frac{1}{2}} - 2S_{\frac{1}{2}}$ splitting (the Lamb shift) is opposite that in hydrogen. Due to the smallness of the pi-mu atom's Bohr radius, the pion and muon spend considerable time in the region in which the Coulomb potential is modified by the electron-positron vacuum polarization. This effect contributes 77.174×10^{-3} eV to a splitting of 79.45×10^{-3} eV in the pi-mu atom (neglecting pion size corrections), whereas in hydrogen it amounts to about 3% of 4.376×10^{-6} eV. An additional 0.5 to 1.0×10^{-3} eV is due to the finite size of the pion, which means that a measurement of the $2S_{\frac{1}{2}} - 2P_{\frac{1}{2}}$ splitting accurate to a part in a thousand could provide an independent measurement of the pion charge radius (ref. 8). These and other properties of the pi-mu atom have been discussed by several authors and will be pursued no further here (ref. 9).

2.2 PI-MU ATOM BRANCHING RATIO

The rate of formation of pi-mu atoms in K_L^0 decay has been calculated by many people (ref. 1,7,10,11), all of whom obtained a number for the ratio

$$R \equiv \frac{\Gamma(K_L^o \to (\pi\mu)_{atom}\nu)}{\Gamma(K_L^o \to \pi\mu\nu)}$$

on the order of 10^{-7}. The purpose of this discussion is to sketch the calculation (ref. 12) and to display the final formula for R before substituting the numerical values of physical constants, masses, and parameters characterizing the decay $K_L^o \to \pi\mu\nu$ (referred to as $K_{\mu 3}$). The sensitivity of R to the $K_{\mu 3}$ decay parameters will be discussed. Then a number for R will be obtained and compared to the previously calculated values.

Since the electromagnetic and strong interactions conserve strangeness, and the K_L^o is the lightest strange particle, the decay $K_L^o \to \pi\mu\nu$ must be due to the weak interaction. We are therefore justified in carrying out a calculation of the S-matrix expansion to lowest non-trivial order. Consider, then, the Lorentz invariant matrix element

$$M_{fi} = \langle (\pi\mu)_n \nu | H_{wk} | K_L^o \rangle$$

where H_{wk} is the weak interaction Hamiltonian density. The initial state is a K_L^o at rest, the final state a pi-mu atom with principal quantum number n.

The complication of an atomic system in the final state may be handled in the following way. For an unbound system consisting of a pion and a muon, whose momenta sum to $\vec{Q}$, we may write

$$\vec{p}_\pi = \frac{m_\pi}{m_\pi+m_\mu}\vec{Q} + \vec{q}$$

$$\vec{p}_\mu = \frac{m_\mu}{m_\pi+m_\mu}\vec{Q} - \vec{q}$$

and trivially satisfy $\vec{p}_\pi + \vec{p}_\mu = \vec{Q}$. Then the bound state has an expansion in terms of a complete set of states for the observable $\vec{q}$ given by

$$<(\pi\mu)_n| = \int d^3\vec{q} <(\pi\mu)_n|\pi\mu_{unbound}(\vec{q})><\pi\mu_{unbound}(\vec{q})| \quad .$$

We may make the identification

$$<(\pi\mu)_n|\pi\mu_{unbound}(\vec{q})> = \psi_n^*(\vec{q}) \quad .$$

$\psi_n(\vec{q})$ is the probability amplitude that the pion and muon in the atom have relative momentum $\vec{q}$, in other words, $\psi_n(\vec{q})$ is the momentum space wave function of the pi-mu atom. Thus the matrix element becomes

$$M_{fi} = \int d^3\vec{q}\ \psi_n^*(\vec{q})\ <\pi\mu_{unbound}(\vec{q})\nu|H_{wk}|K_L^o> \quad .$$

The wave function contributes to the integral only over a small region of momentum space, since the relative momentum in the 1S state is about 0.4 MeV/c. The approximation $\vec{q}$ = 0 leads to

$$M_{fi} \cong <\pi\mu_{unbound}(\vec{q}=0)\nu|H_{wk}|K_L^o> \int d^3\vec{q}\ \psi_n^*(\vec{q}) \quad .$$

The integral may be rewritten as

$$\int d^3\vec{q}\ \psi_n^*(\vec{q}) = \int d^3\vec{q}\ \psi_n^*(\vec{q})\ e^{-i\vec{q}\cdot 0} \quad .$$

This Fourier transform may be recognized as the wave function of the pi-mu atom in coordinate space, evaluated at the origin.

The matrix element thus factors into two parts:

$$M_{fi} \sim \langle \pi\mu_{unbound}(\vec{q}=0)\nu | H_{wk} | K_L^o \rangle\ \psi_n^*(\vec{r}=0) \quad .$$

One part is the wave function of the pi-mu atom evaluated at the origin, the other is the matrix element for $K_{\mu 3}$ decay with constraints on the four-momenta of the pion and muon given by

$$p_\pi = \frac{m_\pi}{m_\pi + m_\mu}\ Q$$

$$p_\mu = \frac{m_\mu}{m_\pi + m_\mu}\ Q$$

where $p_K = Q + p_\nu$. (The four-momentum of the pi-mu atom is $p_A \equiv Q$.) We see explicitly now that the differential decay rate

$$dW_{atom} = \frac{(2\pi)^4}{2m_K}\ |M_{fi}|^2\ \delta^4(p_f - p_i)\ \frac{d^3p_A}{(2\pi)^3(2E_A)}\ \frac{d^3p_\nu}{(2\pi)^3(2E_\nu)}$$

depends directly upon the square of the atom's wave function at the origin. In the approximation made above, all atoms are therefore produced in S states. In the above formulae, p represents four-momentum and E energy, with subscripts f, i, A, and ν referring to the final state,

initial state, pi-mu atom, and neutrino, respectively. The mass of the K_L^o is m_K.

The serviceable phenomenological weak interaction Lagrangian provides an expression for the $K_{\mu 3}$ decay amplitude

$$M(\overline{K}_L^o \to \pi^+ \mu^- \bar{\nu}_\mu) = \frac{G_F}{\sqrt{2}} \langle \pi^+ | J^\lambda_{wk\ hdrn} | \overline{K}_L^o \rangle\ \bar{u}_\mu \gamma_\lambda (1-\gamma_5)$$

in terms of Dirac spinors and γ-matrices, and an as yet unspecified weak hadronic matrix element. G_F is the Fermi coupling constant. By the Lorentz covariance of the Lagrangian density, the hadronic current can consist of only vector and axial-vector parts. Since the π^+ and K_L^o have the same parity, the axial vector part must vanish. Now the weak hadronic matrix element must also be related to physically observable quantities. The only relevant ones available are the four-momenta of the K_L^o and the π, which can be combined to form only one independent scalar (aside from the two masses), and two independent vectors. Thus, using the conventional choice of basis vectors, we have

$$\langle \pi + | J^\lambda | \overline{K}_L^o \rangle = \sin\theta_c \left[f_+(t)(p_K+p_\pi)^\lambda + f_-(t)(p_K-p_\pi)^\lambda \right]$$

where the scalar t, the four-momentum transfer to the lepton pair, is $t = (p_K - p_\pi)^2$. The factor $\sin\theta_c$ is incorporated to account for the experimental observation that strangeness changing decays are suppressed relative to

strangeness conserving ones (Θ_c is the Cabibbo angle and $\sin\Theta_c \cong 0.21$). The magnitude and t dependence of the form factors f_+ and f_- must be determined experimentally from the $K_{\mu 3}$ pion and muon energy spectra. This has been done (ref. 13).

Having surveyed the essential steps in the transition rate calculation, we state the final result:

$$\Gamma(K_L^o \to (\pi\mu)_n \nu)$$

$$= \frac{1}{2m_K} \frac{G_F^2 \sin^2\Theta_c}{2} \left[(f_+ + f_-)(m_\pi + m_\mu) + (f_+ - f_-) m_\pi \right]^2$$

$$\cdot \frac{m_\mu (m_K^2 - (m_\pi + m_\mu)^2)^2}{2\pi m_K^2 (m_\pi + m_\mu)} \frac{1}{2m_r} \sum_n |\psi_n(\vec{r}=0)|^2 \quad .$$

The reduced mass of the pi-mu atom is m_r. Recalling from the Introduction that the square of the Coulomb wave function at the origin is

$$|\psi_n(\vec{r}=0)|^2 = \frac{\alpha^3 m_r^3}{\pi n^3} \quad ,$$

we see that the sum

$$\sum \frac{1}{n^3} \cong 1.2$$

enhances the decay rate by 20%. Making this substitution and defining $\xi(t) \equiv f_-(t)/f_+(t)$, the decay rate may be rewritten

$$\Gamma(K_L^o \to (\pi\mu)_n \nu)$$

$$= \frac{1}{2m_K} \frac{G_F^2 \sin^2\Theta_c}{2} f_+^2(t)$$

$$\cdot \left[(m_\mu + 2m_\pi)^2 + 2\xi(t)(m_\mu^2 + 2m_\pi m_\mu) + \xi^2(t) m_\mu^2 \right]$$

$$\cdot \frac{m_\mu (m_K^2 - (m_\pi + m_\mu)^2)^2}{2\pi m_K^2 (m_\pi + m_\mu)} \frac{1}{2m_r} \frac{\alpha^3 m_r^3}{\pi} \quad (1.2) \quad .$$

(The excellent approximation $m_{atom} = m_\pi + m_\mu$ may be made throughout the calculation.) The four-momentum transfer varies linearly with the pion energy ($t = m_K^2 + m_\pi^2 - 2m_K E_\pi$), which has a unique value in this case since the decay is two-body. Therefore t_{atom} is

$$t_{atom} = m_K^2 + m_\pi^2 - (m_K^2 + m_{atom}^2) \frac{m_\pi}{m_{atom}} = 0.092 \ (\mathrm{GeV}/c^2)^2 \ .$$

The formula above for the decay rate to pi-mu atoms is identical to the ones found by Nemenov and Staffin. Anne Hall's differed, it appears, only in that she did not sum over final states of different principal quantum number n.

It is convenient to compare the decay rate to pi-mu atoms to the familiar decay rate $\Gamma(K_L^o \to \pi\mu\nu)$. One finds that the Dalitz plot density is given by (ref. 14)

$$\frac{d^2N}{dE_\pi dE_\mu} = \frac{G_F^2 \sin^2\theta_c}{4\pi^3} \left[Af_+^2(t) + Bf_+(t)f_-(t) + Cf_-^2(t)\right]$$

where

$$A = m_K(2E_\mu E_\nu - m_K E_\pi') - m_\mu^2(E_\nu - E_\pi'/4)$$

$$B = m_\mu^2(E_\nu - E_\pi'/2)$$

$$C = m_\mu^2 E_\pi'/4$$

$$E_\pi' = E_\pi^{max} - E_\pi = \frac{m_K^2 + m_\pi^2 - m_\mu^2}{2m_K} - E_\pi$$

and E_π, E_μ, and E_ν are respectively the pion, muon, and neutrino energies in the K_L^o center of mass system. The decay rate is obtained after integrating over the Dalitz plot and yields (ref. 15)

$$\Gamma(K_L^o \to \pi\mu\nu) = \frac{G_F^2 \sin^2\theta_c \, m_K^5}{16\pi^3} f_+^2(0) \cdot 10^{-2}$$

$$\cdot \left[0.9255 + 0.4221\, \lambda_+(m_K^2/m_\pi^2) - 0.1900\, (1-\xi(0))\right.$$

$$- 0.0544\, (1-\xi(0))(m_K^2/m_\pi^2)\left(\lambda_+ + \left(\frac{\lambda_+ - \xi(0)\lambda_-}{1-\xi(0)}\right)\right)$$

$$\left. + 0.0219\, (1-\xi(0))^2\right.$$

$$+ 0.0141\ (1-\xi(0))(m_K^2/m_\pi^2)(\lambda_+-\xi(0)\lambda_-)\Big] \quad .$$

A linear dependence of the vector form factors has been assumed:

$$f_\pm(t) = f_\pm(0)\ (1 + \frac{\lambda_\pm t}{m_\pi^2}) \quad .$$

Experiments to date are adequately described in this way, with $\lambda_- = 0$. Now upon forming the branching ratio

$$R \equiv \frac{\Gamma(K_L^o \to (\pi\mu)_{atom}\nu)}{\Gamma(K_L^o \to \pi\mu\nu)}$$

we see that the factor

$$G_F^2 \sin^2\theta_c\ f_+^2(0)$$

cancels, so that R depends upon essentially three quantities: $|\psi_n(\vec{r}=0)|^2$, the pi-mu atom wave function; $\xi(0)$, the ratio of the $K_{\mu 3}$ form factors; and λ_+, the slope of the t dependence of the f_+ form factor. R is plotted in Figure 2 as a function of $\xi(0)$, for three values of λ_+: the top curve corresponds to $\lambda_+ = 0.039$, the middle to $\lambda_+ = 0.034$, and the bottom to $\lambda_+ = 0.029$. The expression used for the pi-mu atom wave function was the simple one that derives from the non-relativistic Schrodinger equation with a Coulomb potential. For the Particle Data Group world averages, $\xi(0) = -0.14 \pm 0.11$ and $\lambda_+ = 0.034 \pm 0.005$, we obtained

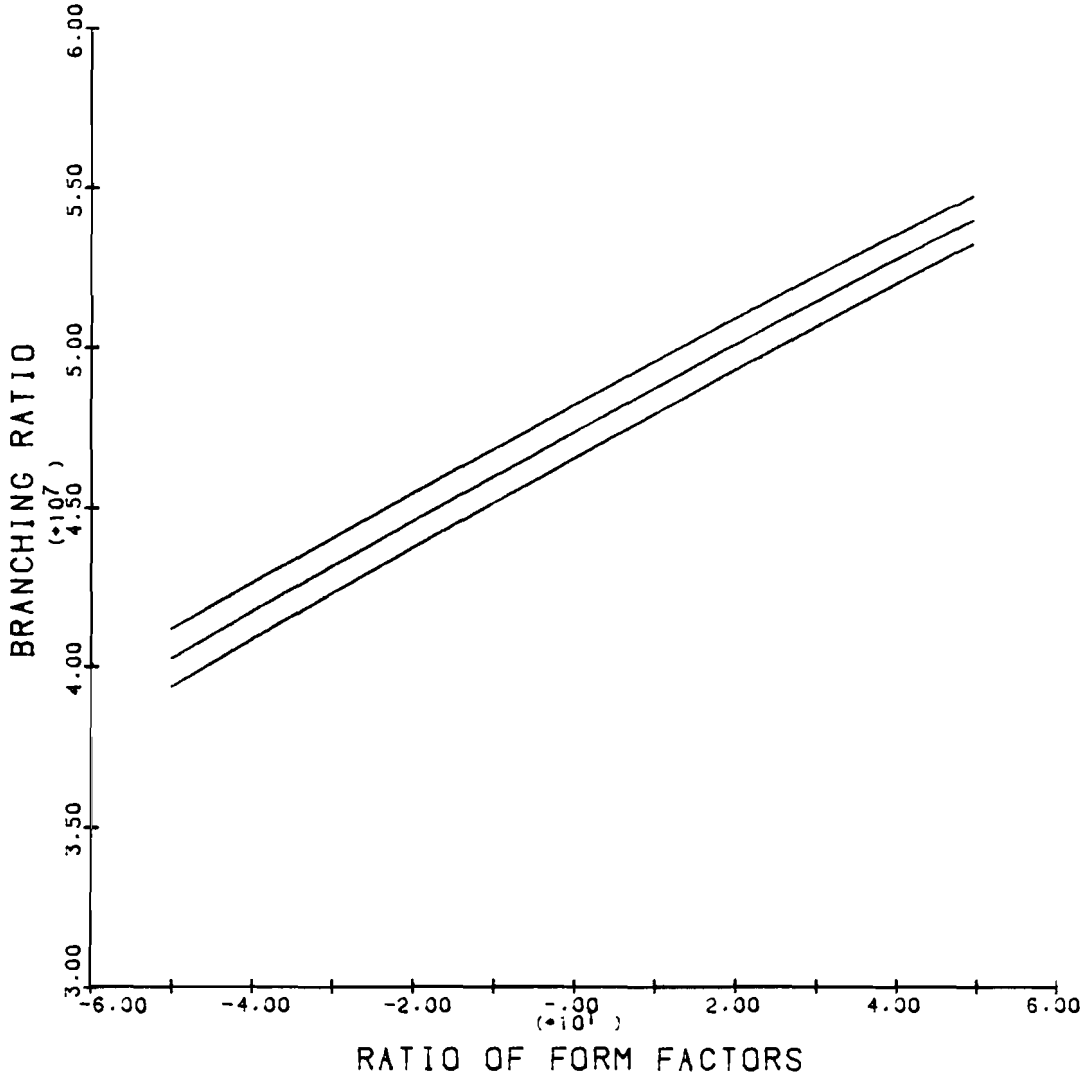

Figure 2. The ratio R defined in the text, as a function of $\xi(0)$. Experimentally, $\xi(0) = -0.14 \pm 0.11$, while $\lambda_+ = 0.034 \pm 0.005$. From top to bottom, the three curves are for $\lambda_+ = 0.039$, 0.034, and 0.029, respectively.

$$R = (4.55 \pm 0.12) \times 10^{-7} \quad .$$

The quoted error gives the minimum and maximum values that R assumed for variations of $\xi(0)$ and λ_+ within the limits given above, subject to the experimental correlation between the two parameters ($d\xi(0)/d\lambda_+ = -15$).

Three small corrections to this value of R have been calculated. Taking account of the finite size of the pion and the vacuum polarization reduces R by 0.37% and 0.19%, respectively (ref. 12). Radiative corrections increase the $K_{\mu 3}$ width by 2.1% (ref. 16). Relativistic corrections are negligible. The result which we compared with our experimental measurement was thus

$$R = (4.43 \pm 0.12) \times 10^{-7} \quad .$$

The family of curves for $R(\xi(0),\lambda_+)$ drawn by Nemenov agrees well with the numerical results presented here. It is not clear whether Hall compared the decay rate $\Gamma(K_L^o \to (\pi\mu)_{atom}\nu)$ to the theoretical $K_{\mu 3}$ decay rate or to its measured value. Staffin used the measured rate (ref. 17).

CHAPTER 3

THEORETICAL CONSIDERATIONS: PART II

3.1 $K_L^o \to \pi^o \pi^o$

The decay to two neutral pions $K_L^o \to \pi^o \pi^o$ is an interesting one because the K_L^o also decays to three neutral pions $K_L^o \to \pi^o \pi^o \pi^o$. Both final states have charge conjugation (C) eigenvalue +1, since the neutral pion has C = +1. The two neutral pion final state, consisting of two spinless and indistinguishable particles, can exist only in even orbital angular momentum states. Hence, it has even parity (P). The intrinsic parity of the neutral pion is odd, making the three neutral pion final state odd under parity. Thus, the K_L^o decays to final states with CP eigenvalues +1 and -1.

The violation of CP invariance has been known since the discovery in 1964 of the rare decay $K_L^o \to \pi^+ \pi^-$ (ref. 18). No experimental evidence for the breaking of CP symmetry has

been found outside of the neutral K meson system.

The subject of CP violation has been discussed extensively in the literature (ref. 19). This brief outline of the phenomenology of the neutral K meson system is intended simply to state the main results that are relevant to measurements of CP noninvariance in $K_L^o \to 2\pi$ decays.

The degree of CP violation is usually characterized by the amplitude ratios

$$\eta_{+-} = |\eta_{+-}|\, e^{i\Phi_{+-}} \equiv \frac{\langle \pi^+\pi^- | H_{wk} | K_L^o \rangle}{\langle \pi^+\pi^- | H_{wk} | K_S^o \rangle}$$

and

$$\eta_{oo} = |\eta_{oo}|\, e^{i\Phi_{oo}} \equiv \frac{\langle \pi^o\pi^o | H_{wk} | K_L^o \rangle}{\langle \pi^o\pi^o | H_{wk} | K_S^o \rangle}$$

where H_{wk} is the weak interaction Hamiltonian. The most recent Particle Data Group constrained fits for these parameters give

$$\eta_{+-} = (2.274 \pm 0.022) \times 10^{-3}$$

$$\eta_{oo} = (2.33 \pm 0.08) \times 10^{-3}$$

$$\Phi_{+-} = (44.6 \pm 1.2)^o$$

$$\Phi_{oo} = (54 \pm 5)^{o} \quad .$$

Two observations can be made immediately: CP violation occurs at a very small level, and the magnitudes of η_{+-} and η_{oo} are nearly equal. Whether or not $|\eta_{+-}|$ and $|\eta_{oo}|$ are in fact identical is a question that has received considerable attention.

Before discussing η_{+-} and η_{oo} further, other important parameters must be introduced. By carrying out a conventional perturbation calculation to second order in the weak interaction Hamiltonian, one can relate the states of definite lifetime K_L^o and K_S^o to the eigenstates of the strong and electromagnetic interactions with definite strangeness: K^o (S = +1) and $\overline{K}^o$ (S = -1). The expressions are given in terms of a single complex number ε (under the assumption of CPT invariance):

$$|K_L^o\rangle = \frac{1}{\left(2(1+|\varepsilon|^2)\right)^{\frac{1}{2}}} \left((1+\varepsilon)|K^o\rangle + (1-\varepsilon)|\overline{K}^o\rangle\right)$$

$$|K_S^o\rangle = \frac{1}{\left(2(1+|\varepsilon|^2)\right)^{\frac{1}{2}}} \left((1+\varepsilon)|K^o\rangle - (1-\varepsilon)|\overline{K}^o\rangle\right) \quad .$$

The parameter ε measures the admixture of the CP odd eigenstate K_2^o in the K_S^o and, simultaneously, the admixture of the CP even eigenstate K_1^o in the K_L^o. That is,

$$|K_L^o\rangle = \frac{1}{(1+|\varepsilon|^2)^{\frac{1}{2}}}\left(|K_2^o\rangle + \varepsilon|K_1^o\rangle\right)$$

$$|K_S^o\rangle = \frac{1}{(1+|\varepsilon|^2)^{\frac{1}{2}}}\left(|K_1^o\rangle + \varepsilon|K_2^o\rangle\right)$$

where

$$|K_1^o\rangle = \frac{1}{\sqrt{2}}\left(|K^o\rangle - |\overline{K}^o\rangle\right)$$

$$|K_2^o\rangle = \frac{1}{\sqrt{2}}\left(|K^o\rangle + |\overline{K}^o\rangle\right) \quad .$$

(We define $|\overline{K}^o\rangle \equiv -CP|K^o\rangle$.)

Now if one supposes that there is no "direct" CP violation, i.e. the CP = -1 eigenstate K_2^o does not decay to two pions, then clearly $\eta_{+-} = \eta_{oo} = \varepsilon$. This is the prediction of the "super-weak" model of CP noninvariance (ref. 20), which confines the violation entirely to an impurity in the decay eigenstates. The alternative case, which allows $K_2^o \to 2\pi$, is called "direct" CP violation, and necessitates the decomposition of the 2π final states into isospin I = 0 and I = 2 components. A straightforward analysis (ref. 21) results in the relations $\eta_{+-} \cong \varepsilon + \varepsilon'$ and $\eta_{oo} \cong \varepsilon - 2\varepsilon'$ where

$$\varepsilon' \equiv \frac{1}{\sqrt{2}} \left(\frac{\mathrm{Im}\ A_2}{A_0}\right) e^{i(\pi/2 + \delta_2 - \delta_0)}$$

$$A_0 \equiv \langle (2\pi)_{I=0} | H_{wk} | K^o \rangle$$

$$A_2 \equiv \langle (2\pi)_{I=2} | H_{wk} | K^o \rangle$$

and δ_2 and δ_0 are, respectively, the I = 2 and I = 0 strong interaction π-π phase shifts due to the final state interactions. Recently, some theoretical models incorporating CP violation have predicted that $|\varepsilon'|/|\varepsilon|$ may be sizable, i.e. on the order of a few percent (ref. 22).

In principle, $|\eta_{+-}|$ and $|\eta_{oo}|$ can be calculated from measurements of branching ratios for K_L^o and K_S^o decay into two pions, and measurements of the lifetimes of the K_L^o and K_S^o. For example, we have

$$|\eta_{oo}|^2 = \frac{\Gamma(K_L^o \to \pi^o\pi^o)}{\Gamma(K_S^o \to \pi^o\pi^o)}$$

$$= \frac{\Gamma(K_L^o \to \pi^o\pi^o)}{\Gamma(K_L^o \to \mathrm{all})} \cdot \frac{\Gamma(K_S^o \to \mathrm{all})}{\Gamma(K_S^o \to \pi^o\pi^o)} \cdot \frac{\Gamma(K_L^o \to \mathrm{all})}{\Gamma(K_S^o \to \mathrm{all})}$$

where

$$\frac{\Gamma(K_L^o \to \mathrm{all})}{\Gamma(K_S^o \to \mathrm{all})} = \frac{\tau_{K_S^o}}{\tau_{K_L^o}} = \frac{0.8923 \times 10^{-10}\ \mathrm{s}}{5.183 \times 10^{-8}\ \mathrm{s}} \quad .$$

As in this experiment, one often measures

$$\frac{\Gamma(K_L^o \to \pi^o \pi^o)}{\Gamma(K_L^o \to \pi^o \pi^o \pi^o)}$$

which yields a number for $|\eta_{oo}|$ when combined with the measured branching ratio

$$\frac{\Gamma(K_L^o \to \pi^o \pi^o \pi^o)}{\Gamma(K_L^o \to \text{all})} \quad .$$

This approach is quite indirect, and clearly compounds several experimental uncertainties. As of this writing, a new experiment is in preparation at Fermilab to measure $|\eta_{oo}/\eta_{+-}|$ directly, to high precision, by simultaneously detecting $K_L^o \to 2\pi$ and $K_S^o \to 2\pi$ decays (ref. 23).

3.2 $K_L^o \to \gamma\gamma$

In the early 1970's, attention was attracted to the decay $K_L^o \to \gamma\gamma$ in connection with experimental searches for the extremely rare decay $K_L^o \to \mu^+\mu^-$ (ref. 24). Early measurements yielded only upper limits, most notably (ref. 25)

$$R_{\mu\mu} = \frac{\Gamma(K_L^o \to \mu^+\mu^-)}{\Gamma(K_L^o \to \text{all})} \leq 1.8 \times 10^{-9} \text{ (90\% confidence level)}.$$

However, quantum electrodynamics and the requirement of unitarity placed a lower limit on the decay rate into two muons in terms of the two photon decay rate (ref. 26)

$$\frac{\Gamma(K_L^o \to \mu^+\mu^-)}{\Gamma(K_L^o \to \gamma\gamma)} \geq 1.2 \times 10^{-5} \quad .$$

Using the Particle Data Group world average

$$\frac{\Gamma(K_L^o \to \gamma\gamma)}{\Gamma(K_L^o \to \text{all})} = (4.9 \pm 0.5) \times 10^{-4}$$

one expected $R_{\mu\mu} \geq (5.9 \pm 0.6) \times 10^{-9}$. Subsequent experiments detected the two muon decay and obtained consistent branching ratio measurements, above the unitarity bound. The Particle Data Group weighted average of these experiments is $R_{\mu\mu} = (9.1 \pm 1.9) \times 10^{-9}$.

It should be noted that $K_L^o \to \mu^+\mu^-$ was studied as a test of the existence of strangeness-changing weak neutral currents. Since the observed rate was not far above the lower bound predicted by quantum electrodynamics and the measured $K_L^o \to \gamma\gamma$ branching ratio, there was no evidence for such an interaction (ref. 25). However, contributions to the $\mu^+\mu^-$ decay rate from second order weak charged current interactions (involving the exchange of two charged intermediate vector bosons) as well as first order weak, fourth order electromagnetic diagrams (with one charged boson and two photons) boosted the theoretical prediction well above the experimentally determined branching ratio (ref. 27). The suppression of these "induced" neutral currents was eventually accounted for by the introduction of the charmed quark, according to the

Glashow-Iliopoulos-Maiani scheme (ref. 28).

CHAPTER 4

EXPERIMENTAL TECHNIQUE

As a prelude to a detailed description of the components of the apparatus in the next chapter, this chapter provides an overview of the rationale behind the organization of what might otherwise appear to be a disjointed collection of pieces of hardware. Emphasis is placed on the principles behind detecting pi-mu atoms and distinguishing them from $K_{\mu 3}$ decays. Also stressed are the methods of detecting photons and distinguishing various K_L^o decays with photons in the final state.

4.1 USING A NEUTRAL KAON BEAM

The design of the experiment was dictated largely by two considerations. The first was that the experiment was to be performed at Fermilab, in the M3 beam line of the Meson Laboratory, where 400 GeV protons striking a fixed target manufactured the most intense and energetic neutral

kaon beam available. Such a beam is desirable because the data-taking rate usually depends linearly upon the intensity, and a higher energy beam throws a larger fraction of a parent particle's decay products into a detector of given aperture situated in the forward direction.

Another consequence of the high energy of the incident proton beam was that particles, such as the K_L^o and charged pion, were typically produced with Lorentz gamma (γ) factors of 100 to 1000. Since their lifetimes are roughly 10^{-8} seconds, they traveled hundreds or thousands of meters in the laboratory before decaying. Thus even if the detector were as far from the kaon source (target) as could be accommodated in order to see as many K_L^o decays as possible, in principle pi-mu atoms would live long enough to be observed. The detector, essentially a multi-wire proportional chamber (MWPC) spectrometer, was therefore assembled at the downstream end of a long evacuated pipe and viewed this pipe or decay volume through a thin, D-shaped window from above the beam. An elevation view of the beam line is shown in Figure 3. (Notice the difference between the horizontal and vertical scales.) A sampling of those K_L^o decays which occurred within the decay region and sent particles up out of the beam and into the spectrometer was recorded.

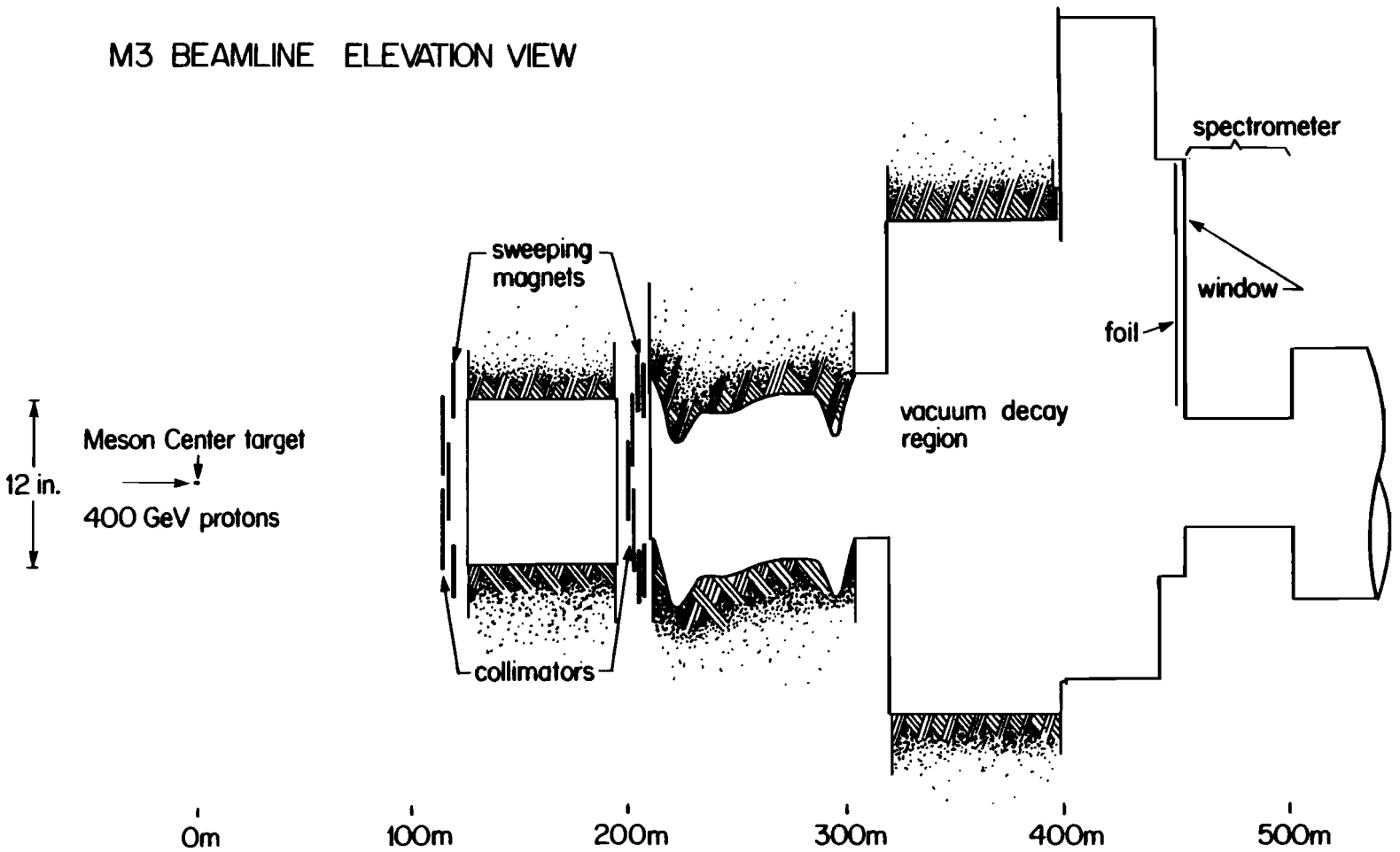

Figure 3. Elevation view of the M3 beam line at Fermilab.

4.2 DETECTING PI-MU ATOMS

The second consideration guiding the design of the experiment was that the rare pi-mu atom decays be distinguished unambiguously from the flood of other K_L^o decays. To achieve this, the atoms first were broken apart to identify the pion and the muon, and, though it may seem paradoxical, to establish that they originated in a bound state. Placed in the path of atoms hurling at nearly the speed of light toward the thin window to the detector was an aluminum foil to gently separate the two charged particles. The foil thickness was chosen to be sufficient to break up all the atoms passing through it (ref. 29); otherwise, a measurement of the branching ratio would have depended upon an uncertain theoretical calculation of the break-up probability. Indeed, data were taken at two foil thicknesses (0.020 and 0.035 in.) with the expectation that the measured branching ratio would be the same for both. The foils were thin enough, though, to keep the direction and velocity of the emerging pion and muon the same as the direction and velocity of the incident atom.

Three magnets and ten MWPC planes (five chambers) were arranged judiciously to facilitate the clear separation of pi-mu atoms from ordinary $K_{\mu 3}$ decays. (Schematic illustrations of the spectrometer in elevation and plan

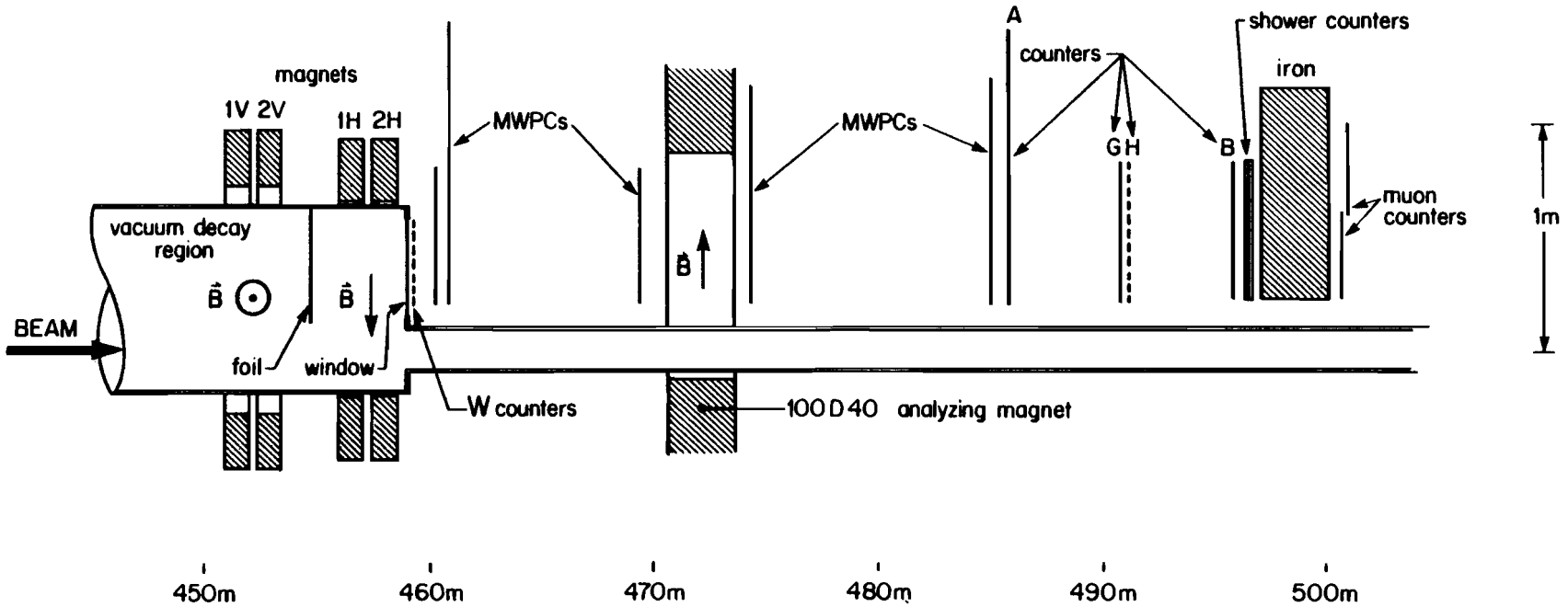

PI-MU ATOM SPECTROMETER ELEVATION VIEW

Figure 4. Elevation view of the pi-mu atom spectrometer. Distances from the Meson target are given at the bottom.

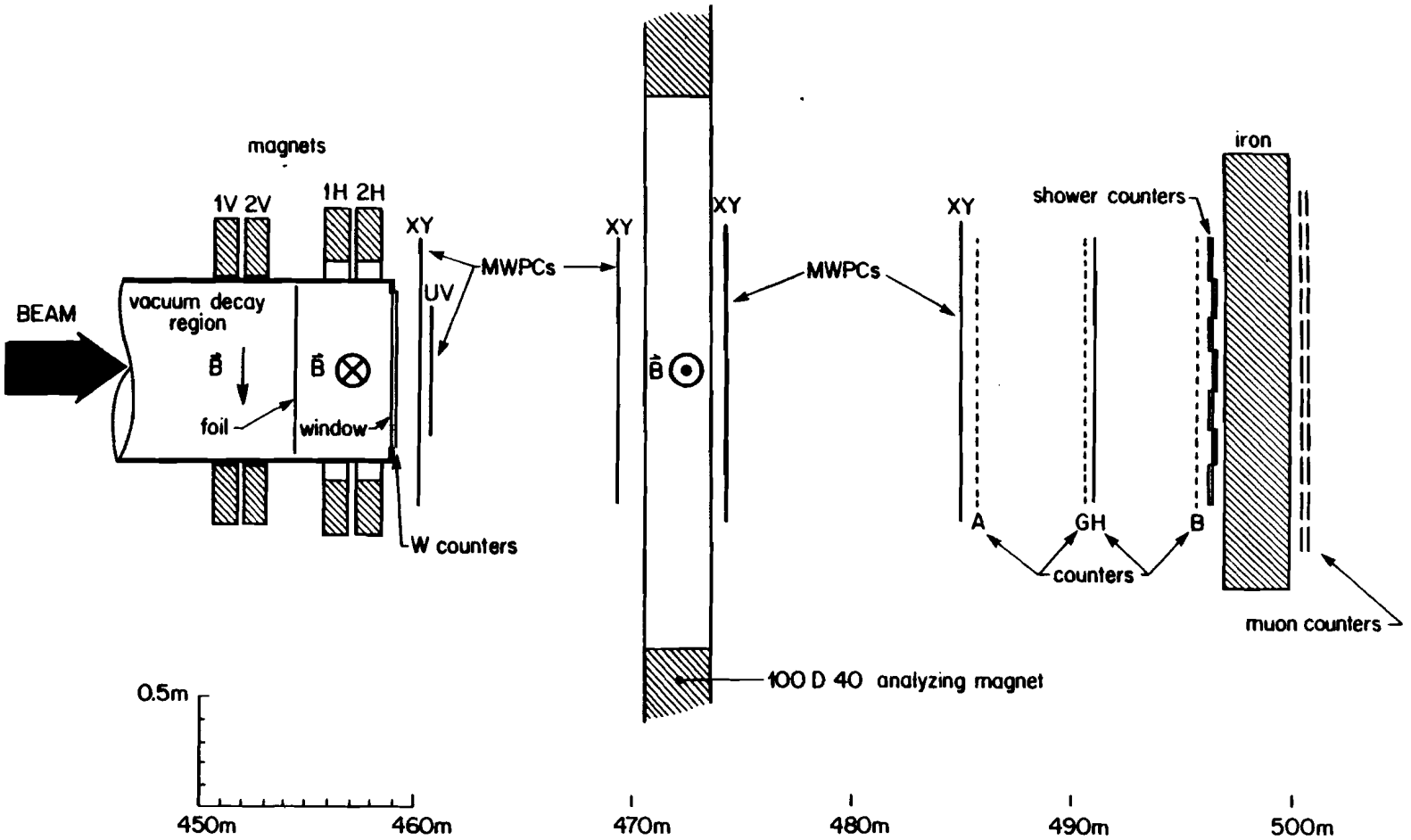

PI-MU ATOM SPECTROMETER PLAN VIEW

Figure 5. Plan view of the pi-mu atom spectrometer.

views are shown in Figures 4 and 5.) Downstream of the foil, a pion and muon from the dissociation of an atom would have traveled with the same velocity, in the same direction, and along nearly spatially coincident trajectories. A horizontally bending magnet stood just after the foil to force such charged particles to diverge, forming an apparent "V" with vertex in the vertical plane at the center of the magnet (2.6 m from the foil). (This was actually a closely spaced pair of magnets, 1H and 2H, which shall be referred to as a unit labelled H.) Six planes of proportional chamber wires downstream of this magnet allowed charged particle trajectories to be reconstructed by the data analysis program. Thus, two charged particles which came from the break-up of an atom at a point on the foil would necessarily have had reconstructed tracks which met somewhere near that magnet's center.

The existence of such a "vertex" would not have ensured that the particles also originated at a common point on the foil, that is, that they followed parallel paths downstream of the foil. To test for "parallelism", a second, large-aperture horizontally bending magnet (the 100D40) was planted just beyond the first six MWPC planes (17.2 m from the foil), and operated at a current such that its magnetic field integral was equal in magnitude but opposite in sign

to that of the first magnet (H). Thus, a charged particle deflected through an angle θ by the first magnet was deflected through an angle $-\theta$ by the second. In particular, two particles that entered the first with parallel trajectories emerged from the second with parallel trajectories, regardless of their charges.

The combination of these two magnets insured that a pion and a muon had passed through a single point on the break-up foil, and had been going in the same direction, if they left two parallel tracks in the MWPC's downstream of the 100D40, and tracks between the two magnets which converged at a point (vertex) in or near the vertical mid-plane of the first (H). Of course such a pair might not have come from the dissociation of a pi-mu atom, even if the pion and muon had been of opposite charge. Had it not been for the third magnet alluded to above, a $K_{\mu 3}$ decay in which the pion and muon traveled nearly identical paths, but were not bound, would have satisfied the two criteria above and thereby mimicked the break-up of an atom at the foil. The third magnet (again actually a pair, 1V and 2V) was positioned just upstream of the foil (2.6 m) and deflected charged particles in the vertical plane. The crucial point is that the pi-mu atom, a neutral object, would not have deviated in its course through this magnet. Thus, in an elevation (side) view the hit proportional

chamber wires would have revealed one or two very closely spaced tracks if the pion and muon had come from an atom, and widely separated tracks (diverging or crossing) otherwise.

In fact, events were found in this experiment which had an oppositely charged pion and muon that satisfied the vertex, parallelism, and side view requirements. However, the positive identification of a pi-mu atom rested finally upon a demonstration that the pion and muon had the same velocity. The ratio of the momenta of two particles with the same velocity equals the ratio of their rest masses. Thus once having measured the pion and muon momenta with the 100D40 magnet, the candidate events were histogrammed in a variable named alpha (α), defined as the difference of the momenta divided by the sum:

$$\alpha = \frac{p_\pi - p_\mu}{p_\pi + p_\mu} \quad .$$

A narrow peak at the value $\alpha = 0.138$, which is the difference of the pion and muon masses divided by their sum, attested to the detection of pi-mu atoms.

The preceeding discussion was intended to demonstrate how the experiment was designed to exploit the neutrality of the pi-mu atom and the non-zero charges of the pion and muon from ordinary $K_{\mu 3}$ decay. To summarize the scheme, the vertically bending magnet upstream of the foil prohibited

the unbound pion and muon from $K_{\mu 3}$ decay from leaving the foil along parallel and spatially coincident paths and thereby imitating a pi-mu atom event. Downstream, horizontally bending magnets with equal and opposite momentum impulse provided, in conjunction with MWPC's, a simple means of telling the charge of the object or objects that entered the foil and the spatial relationship of the charged particles that emerged. Figures 6 and 7, depicting typical signatures for a pi-mu atom and a $K_{\mu 3}$ decay, illustrate the differences between the two topologies.

4.3 DETECTING PHOTONS

Let us now consider how an experimental layout so well adapted to differentiating "bound" and "unbound" $K_{\mu 3}$ decays served as a tool for measuring other K_L^o decays.

Neutrons, neutrinos, and photons were the only neutral particles aside from long-lived kaons expected in appreciable numbers in the beam, far from the target. Photons that rose out of the beam and struck the aluminum break-up foil had a small and calculable probability of producing an electron-positron pair. Due to the high energy of the photons and the thinness of the foil, the opening angle between the electron and positron was usually extremely small. This situation is analogous to that of a

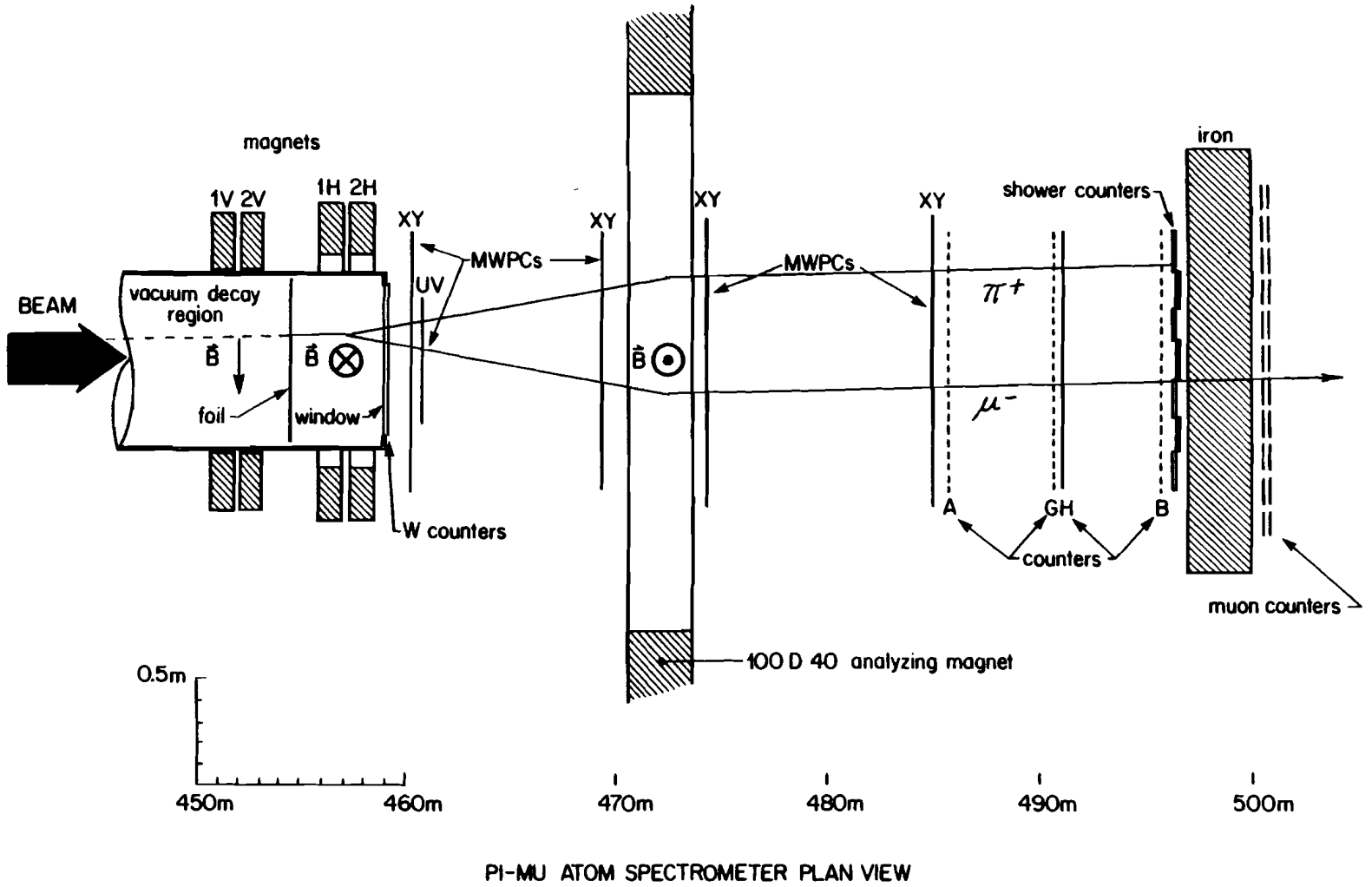

Figure 6. Plan view of a pi-mu atom event.

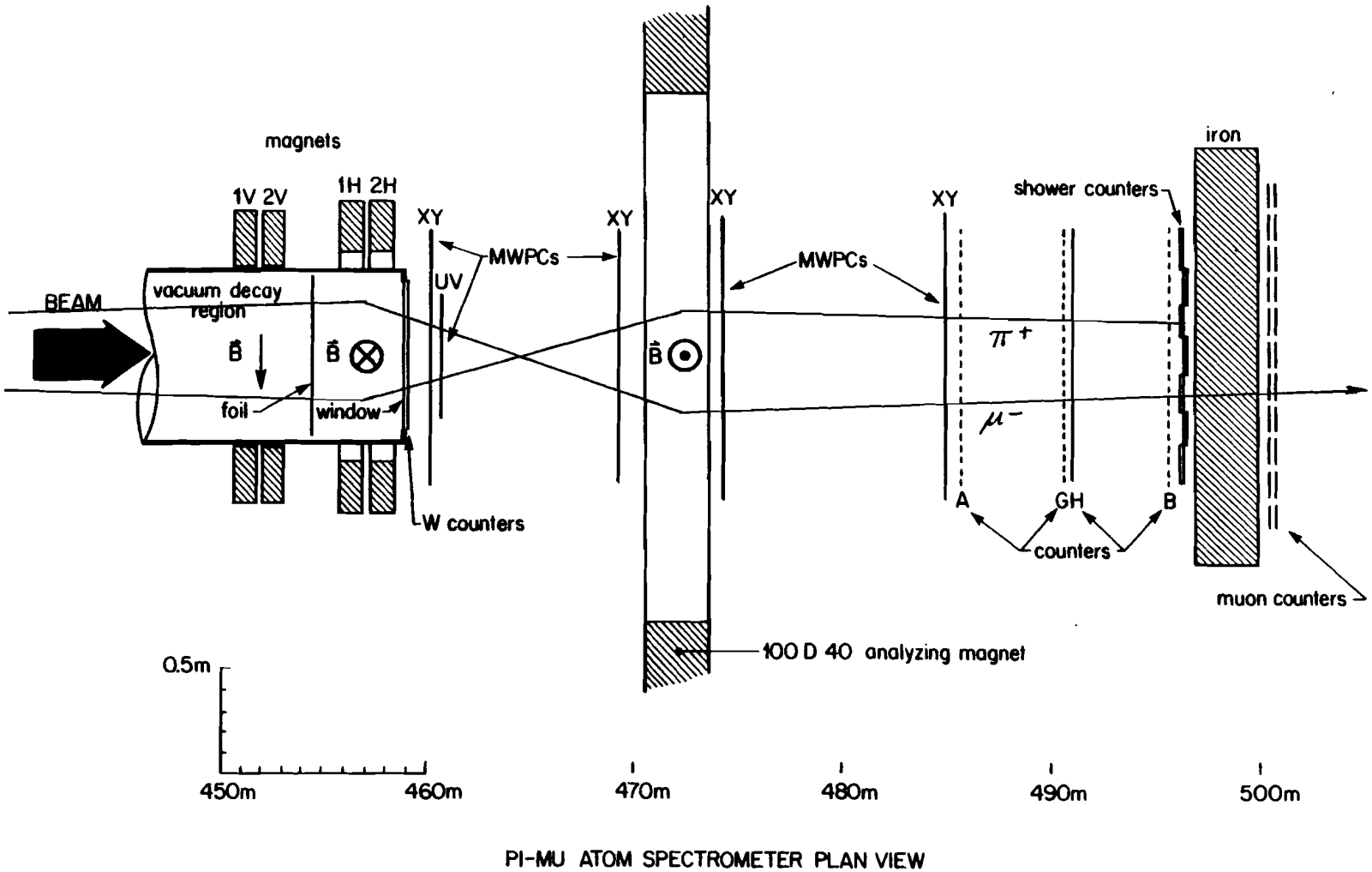

Figure 7. Plan view of a $K_{\mu 3}$ event.

neutral pi-mu atom "producing" a pion-muon pair at the foil. Thus, apart from differences in particle identification and the fact that the electron and positron did not necessarily have a fixed ratio of momenta, photon detection with this apparatus was nearly identical to pi-mu atom detection.

The sources of photons were many. Neutron collisions with the residual gas in the decay pipe, or with the beam pipe walls, yielded neutral pions with a lifetime of 0.8×10^{-16} seconds for decay to two photons. This was a small contribution compared to K_L^o decays. A list of observed decay modes with a photon in the final state, with branching fractions noted, appears in Table 3.

If one were to design an experiment to examine these decays, one might surround the beam pipe with a large array of lead glass blocks equipped with photomultiplier tubes to detect and measure the energy of some or all of the photons. The detector employed in the experiment reported here furnished a good measurement of the photon energy by measuring the momentum of the e^+e^- pair, yet it was suited in practice to the detection of only one of the final state photons.

Despite this apparent deficiency, the decay modes could still be distinguished by the different maximum photon momenta kinematically allowed a K_L^o decaying at rest (see

Table 3. Photon-producing Decays of the K_L^o

Mode	Max p of π^o (Mev/c)	Max p of γ (Mev/c)	Branching Ratio
$\pi^o\pi^o\pi^o$	139.3	166.6	0.215 ± 0.007
$\pi^+\pi^-\pi^o$	132.1	160.5	0.1239 ± 0.0018
$\pi e \nu \gamma$		229.1	0.013 ± 0.008
$\pi^o\pi^o$	209.1	228.9	$(9.4 \pm 1.8) \times 10^{-4}$
$\gamma\gamma$		248.8	$(4.9 \pm 0.5) \times 10^{-4}$
$\pi^+\pi^-\gamma$		170.6	$(6.0 \pm 2.0) \times 10^{-5}$
$e^+e^-\gamma$		248.	$(1.74 \pm 0.87) \times 10^{-5}$

Table 3). Since the component of a four-vector perpendicular to the direction of boost is unaffected by a Lorentz transformation, the laboratory photon momenta transverse to the K_L^o (or beam) direction have the same distribution as the transverse momenta (p_t) in the rest frame. In particular, the p_t distribution has the same kinematic maximum.

A histogram of the transverse momenta of photons in the data displayed a rich structure on a logarithmic scale, including a relatively small number of events with high p_t corresponding to the rare modes $K_L^o \to \pi^o \pi^o$ and $K_L^o \to \gamma\gamma$. Prominent features of the spectrum were a peak and a sharp fall-off at about one half the K_L^o mass, ascribed to the decay $K_L^o \to \gamma\gamma$. (Since the transverse momentum was measured with a finite resolution and calculated with respect to the center line of a beam with an appreciable angular divergence, the cut-off was actually above half the K_L^o mass.) Let us see how such a shape arises.

The p_t distribution can be derived from an expression for the probability $P_1(\theta)$ that a decay product makes an angle θ with respect to an arbitrarily chosen axis in the rest frame of the parent particle. Letting p^* be the rest frame momentum, the transverse momentum is $p^* \sin\theta$ and the probability density $P_2(p_t)$ as a function of p_t is

$$P_2(p_t) \sim P_1(\theta)\left|\frac{dp_t}{d\theta}\right|^{-1} .$$

If the decay product is distributed isotropically in the rest frame, $P_1(\theta)$ is proportional to $\sin\theta$ (from the unit element of solid angle) and the probability density $P_2(p_t)$ becomes

$$P_2(p_t) \sim p_t/(p^{*2} - p_t^2)^{\frac{1}{2}} .$$

$P_2(p_t)$ is infinite at the "Jacobian peak" where $p_t = p^*$, but is integrable. Of course for two-body decays, p^* is fixed. In the case of $K_L^o \to \gamma\gamma$, most of the shape below the peak was obscured by other K_L^o decays yielding photons, in particular, $K_L^o \to \pi^o\pi^o$. Pi-mu atoms, however, afforded a striking illustration of this p_t distribution (see Figure 34).

The unravelling of branching ratios for $K_L^o \to \pi^o\pi^o$ and $K_L^o \to \gamma\gamma$ hinged upon a complete understanding of the shape of the single photon transverse momentum spectrum.

CHAPTER 5

APPARATUS

5.1 COORDINATE SYSTEM

In order to describe the location of the components of the apparatus, a right handed coordinate system was adopted with the positive Z axis pointing along the nominal beam direction and the positive Y axis in the vertical. Thus, the positive X direction was to the left of the beam. The origin was close to the target. The procedures employed in precisely determining the geometry of the experiment are discussed in Chapter 10.

5.2 BEAM AND DECAY REGION

The neutral beam was produced by 400 GeV/c protons striking a 30.5 cm long beryllium target at targeting angles varying from 0.75 to 1.25 milliradians. Its

dimensions were restricted by holes bored in a series of three steel collimators (totaling about 14 m in length) placed immediately downstream of the target, and by two pairs of variable horizontal and vertical steel collimators at 113 m and 200 m (see Figure 3). During data taking, the beam was typically trimmed to a height of 1 in. and a width of 3 to 5 in. at the second set of collimators. Magnets following the primary collimators and the downstream collimating stations swept aside charged particles.

The beam traveled through air until it reached the beginning of the decay volume at 212 m, except for a section of pipe (not shown in Figure 3) between 126 m and 195 m that was evacuated to reduce interactions of beam particles with air. The neutral beam passed through vacuum from 212 m until it reached a leaded concrete dump at 595 m, well beyond the detector. The portion of the pipe between 212 m and 459 m constituted the decay region, downstream parts of which were of considerable radius (e.g. 16 in.) to permit the detector to view the beam as far upstream as possible. A conspicuous settling of the pipe near 300 m reduced somewhat the length of the decay region visible from the D-shaped window at 459 m. A pressure of approximately 12 microns of mercury was maintained in the decay volume throughout the data gathering.

The pipes which threaded the spectrometer magnets were made of stainless steel so as to minimize distortion of the magnetic fields.

Normally, 5×10^{12} protons delivered per accelerator pulse (1 second) resulted in a flux of about 8×10^{6} K_L^o per pulse with a useful momentum range of about 10 to 220 GeV/c. Pulses were spaced 7 to 17 seconds apart. The neutron to kaon ratio varied roughly between 50:1 and 125:1 depending upon the targeting angle. In order to diminish the direct photon flux from the target, 1 to 3 in. of lead could be inserted in the beam just upstream of the first pair of variable collimators. (Beam stops were located at about 100 m and 111 m.)

5.3 VACUUM WINDOW

The D-shaped window was designed to hold a vacuum in the 125 m^3 decay volume while keeping to a minimum the scattering of particles passing through to the detector.

The window had three components: a main window, a backup window, and a metering membrane (ref. 30). The main window, of 5.6 oz/yd^2 biaxially woven Kevlar fabric (Reeves Bros., Inc. no. 15726), had a urethane coating on both sides, for a total weight of 20.0 oz/yd^2. The backup window was an uncoated triaxially woven 440 denier

polyester fabric (N. F. Doweave, Inc. no. BP44P) weighing 7.0 oz/yd^2. The metering membrane was of a 2.25 oz/yd^2 nylon material (Reeves no. 3906) coated with urethane on one side giving a total weight of 5.0 oz/yd^2. It featured a 1.25 in. diameter hole to allow a 200 cu. ft per minute flow (at a pressure difference of one atmosphere) in case the others broke. The entire assembly covered 445 sq. in. and was 0.00254 radiation lengths thick.

5.4 BREAK-UP FOILS

Three D-shaped aluminum foils nominally of thicknesses 0.005, 0.010, and 0.020 in. were mounted in aluminum frames that could be rotated separately and manually (like pages in a book) through 90° to a vertical position from outside the 32 in. pipe. In the upright position they covered approximately the top 5/8ths of the pipe, allowing the neutral beam to pass below.

Since the photon conversion probability was calculated from the thickness of the foil expressed as a fraction of a radiation length of aluminum (24.011 gm/cm^2), the density of the foils was carefully measured. This probability had to be known for a quantitative comparison of the number of observed $K_{\mu 3}$ or pi-mu atom decays with the number of events in the single photon transverse momentum spectrum. The

densities of the 5 and 20 mil (1 mil ≡ 0.001 in.) foils were found to be 0.03374 ± 0.00005 gm/cm^2 and 0.1399 ± 0.0001 gm/cm^2 respectively, giving a photon conversion probability of (4.49 ± 0.02) × 10^{-3} for the 20 mil data and (7.74 ± 0.03) × 10^{-3} for the 35 mil data. (The 10 mil foil was made of two 5 mil foils.)

5.5 MAGNETS

The four dipole magnets on either side of the foil were of identical dimensions (1.12 m deep, 0.83 m between pole faces, and 1.03 m across the return yoke). The upstream pair ran at a combined integrated magnetic field of 2.80 kG-m, thereby delivering an 83.9 MeV/c downward impulse to positively charged particles. The downstream pair (horizontally bending) had an integrated field of 5.697 kG-m (170.9 MeV/c impulse). The magnetic field of each magnet had been mapped previously in a 2 in. × 1 in. × 1 in. grid at an integrated field of 3.36 kG-m (ref. 31).

The 100D40 dipole magnet aperture measured 100 in. across, 40 in. deep, and 40 in. high. After the field strength of the horizontally bending pair had been chosen at the beginning of the experiment, the 100D40 momentum impulse was set to 165.2 MeV/c (corresponding to 5.507 kG-m) by varying the current until the copious electrons

and positrons from photon conversions in the foil assumed parallel trajectories downstream. Positively charged particles were deflected to the right of the beam (-X). The magnetic field had been measured previously (ref. 32) at 36,000 points in a 10 cm × 2.5 cm × 2.5 cm grid, at a magnetic field integral of 12.6 kG-m. Line integrals through the magnet $\int B_y dz$ had also been taken at each (X,Y) point, and gave results consistent with the point by point figures.

Calibration data demonstrated that the field maps were adequate, up to overall scale factors, at the currents chosen for the experiment (see Chapter 10).

5.6 MULTI-WIRE PROPORTIONAL CHAMBERS

Each of the five MWPC's contained two orthogonal planes of parallel signal wires. Chambers 1, 3, and 4 had vertical and horizontal wires which determined charged particle positions in the top and side views, respectively. (Chamber 1 was furthest upstream.) Chamber 2 had wires inclined at 45° to the horizontal; chamber 5 was rotated counterclockwise (with respect to the beam direction) by 42 milliradians. The latter two modules furnished the information necessary to correlate tracks found in the top view with those in the side. The horizontal wires in the

third chamber were separated in two, so that particles traversing the right and left halves of the chamber could be distinguished in the side view alone.

A mixture of argon, CO_2, and Freon in the ratios 0.8 : 0.2 : 0.0025 provided the gaseous medium ionized by the passage of charged particles. The 20 micron thick, gold coated tungsten anode (signal) wires were strung 16 to the inch. (The number of anode wires per plane varied from 384 to 896.) On both sides of the anode wires, 4.8 mm away, were planes of cathode wires typically held at a potential 3900 volts lower.

The encoding of the numbers of the hit wires was performed by electronics mounted on the chambers. After amplification, the pulse on an anode wire initiated an 800 nano-second long delay signal, at the termination of which a short logical signal was generated. If the latter coincided with a 50 ns pulse sent to the chambers on the basis of the fast, scintillation counter trigger (see Chapter 6), the number of the struck wire and the number of the plane were stored ("latched") in the form of a 16 bit binary word. Up to eight hit wires were latched in each plane.

The momentum resolution of the detector was limited by the wire spacing coupled with the 100D40 field strength, and by multiple scattering of particles. To reduce the

latter contribution, three helium filled bags (not shown in Figures 4 or 5) displaced the air between the last four MWPC's. The chambers were each 0.00244 radiation lengths, neglecting the wires, which added another 0.00422 radiation lengths (ref. 33).

The measurement of MWPC efficiencies is discussed in Chapter 10.

5.7 SCINTILLATION COUNTERS

Six scintillation counter banks (see Figures 4 and 5), provided the fast signals from the passage of charged particles that were combined in a logical way to determine if the particular event was of interest.

The W bank was almost flush with the D-shaped vacuum window. Its seven horizontal counters, each 1/16 in. thick (0.0067 radiation lengths) and 2.12 in. wide, were of different lengths so that the active area approximated that of the window. (Photomultiplier tubes were mounted on the beam-right ends.)

The other banks, all downstream of the last MWPC, consisted of vertical staves, except the H bank, which had eleven horizontal scintillators 1/4 in. thick, 2.2 in. wide, and 4 ft long. (Phototubes viewed these counters alternately from the left and right ends.) The A and B

banks, 9.9 m apart, were each fitted with 22, 1/4 in. thick, 2.2 in. wide scintillators. The A counters were 4 ft in length, the B two ft. The 24 G counters, 1/8 in. thick, 2 in. wide, and 24 in. long, overlapped one another slightly.

The 22 muon counters were situated behind about 3 m (169 radiation lengths) of steel. They were arranged in two rows of eleven overlapped 1.125 inches. Each counter was 1/4 in. thick, 6 in. wide, and 14 in. high. The rather coarse position measurement for penetrating particles suited the multiple scattering expected in the steel. Adjacent counters were also overlapped 1/4 inch. The active area of the bank was thus 0.68 m by 1.61 m.

The measurement of the efficiencies of the counters is outlined in Chapter 10.

5.8 SHOWER COUNTERS

A bank of seven lead-lucite shower counters, in conjunction with the muon counters and steel absorber, was used to identify particles (see Chapter 9). Each module was composed of 15 layers of 1/4 in. lead interspersed with 1/4 in. lucite sheets (17.3 radiation lengths total). A 5 in. phototube sat atop a bundle of light guides which collected the Cerenkov light from the lucite layers. The

counters were each 8 in. wide and 24 in. high. Adjacent modules were overlapped one inch.

The output pulse from each tube was passively split into two signals. One was integrated and digitized in an analog-to-digital converter (ADC) and stored in the record of the event written on magnetic tape (see Chapter 6). The other was added to the signals from the other six shower counters. The operating high voltage for each phototube was adjusted so that at a discrimination level of 40 millivolts, the summed pulse heights corresponded to an electromagnetic energy deposit in the bank of about 4 GeV.

CHAPTER 6

DATA ACQUISITION

6.1 TRIGGER LOGIC

The analog output signals (some of them amplified) from the scintillation counters were discriminated so that minimum ionizing particles would register hits in the counters. The resulting logic ("yes"/"no") pulses passed through coincidence (and anti-coincidence) circuits to form three signals ("triggers"), any of which could initiate the retrieval of hit wire information from the MWPC's and the writing of an event record to tape.

The three triggers were called atom, e^+e^-, and $K_{\mu 3}$ and were defined as follows:

$$\text{atom} = 2A \cdot 234B \cdot TC \cdot \geq 2G \cdot 1H \cdot 1W \cdot \geq 1\mu$$

$$e^+e^- = 2A \cdot 234B \cdot TC \cdot \geq 2G \cdot 1H \cdot 1W \cdot \geq 4 \text{ GeV}$$

$$K_{\mu 3} = (2A \cdot 234B \cdot TC \cdot \geq 2G \cdot \geq 1H \cdot \geq 1W \cdot \geq 1\mu)/32 \quad .$$

(The dot indicates logical "and".) The interpretation of the symbols is given below.

All three triggers required two tracks in the top view, i.e. 2 hit counters in the A bank, 2, 3, or 4 hit counters in the B bank, and at least 2 hit counters in the G bank. Up to four hit counters were allowed in the B bank so as not to reject good two-track events accompanied by delta rays produced upstream, or by stray particles from electromagnetic showers not entirely contained within the shower counters immediately behind the B bank. Because the G counters were overlapped, two or more struck counters in this bank satisfied each trigger.

All three triggers also demanded that the pattern of hit A and B counters pass the Track Correlator (TC) test. This electronic module compared the 22 A and 22 B input logic signals with allowable configurations stored in its memory (and set using the on-line computer), to see if the hit counters corresponded to particle trajectories of roughly equal separation at the two banks. Thus, at least one pair of hit A counters and one pair of hit B counters were required in order to satisfy the Track Correlator. The number of counters between the pair of hit A counters

could differ from the number between the pair of hit B counters by at most one. Furthermore, there had to be at least one counter between each pair. Since pi-mu atoms and photons sent two charged particles along parallel trajectories through the downstream portion of the detector, the Track Correlator decided, in effect, whether or not there were two roughly parallel tracks through the A and B banks. This took 190 ns. In general, $K_{\mu 3}$ events did not have two parallel tracks downstream of the analyzing magnet, although many still passed the test. (Tracks could also cross in such a way as to satisfy the Track Correlator logic.) A detailed description of the module has been published (ref. 34).

Because of the vertically bending magnets upstream of the foil, $K_{\mu 3}$ decays sent two particles along distinctly different paths as seen in the side view. Thus, $K_{\mu 3}$ triggers could have one or more hit counters in each of the horizontal counter hodoscopes (W and H), whereas atom and e^+e^- triggers were asked to have exactly one hit counter in each. (This resulted in a small loss of pi-mu atoms and e^+e^- pairs, as explained in Chapter 10.)

Finally, both atom and $K_{\mu 3}$ triggers had to have at least one hit muon counter. (Because they overlapped, a single muon could fire as many as four counters.) The on-line particle identification requirement for e^+e^- pairs

was met if more than 4 GeV was deposited in the shower counters.

If any of the three triggers defined above was satisfied, the event was recorded on magnetic tape for off-line analysis. Only one in 32 $K_{\mu 3}$ triggers was retained, since they were plentiful in comparison with atom triggers.

6.2 DATA ACQUISITION HARDWARE AND SOFTWARE

The acquisition of data was supervised by a program which resided within the 32K 16-bit words of memory in a Digital Equipment Corp. PDP 11/45 computer. The program was written expressly for this experiment in PDP 11 MACRO assembly language, and was therefore extremely compact and efficient. All of the electronics which connected the conventional NIM-standard fast trigger electronics to the computer was designed to communicate directly with the computer's central processor on the PDP 11 data and address lines (the "unibus"). Also on the unibus was an auxiliary memory of 64K 16-bit words, built for the rapid storage of data accumulated during an accelerator pulse. The combination of electronics (hardware) and a computer program (software) tailored to the PDP 11 computer permitted the acquisition of data at a very high rate.

The sequence of events leading to the recording of an event record on tape was as follows. Once one of the three triggers occurred, a signal (load pulse) was sent to each of the proportional wire chamber planes, causing them to return up to 64 16-bit words containing the numbers of the hit wires and the planes to which they belonged. This information was deposited directly in the 64K memory through 16 external inputs, beginning in a location that had been predetermined by the computer program. After the transfer of the last MWPC word, whatever data analysis chores were being performed by the program were temporarily suspended, and the readout of the scintillation counters and ADC's was begun.

The scintillation counter information was stored temporarily in 16-channel coincidence latches. When a trigger was satisfied, bits corresponding to the hit counters were set in the latches. These modules could be addressed and read as though they were 16-bit words in the PDP 11 memory. They were cleared automatically when read by the computer. The shower counter pulse heights were digitized in LeCroy 2249 10-bit ADC's which had been modified so that they, too, could be read directly by the computer.

The interruption of the computer, following the transfer of the MWPC data to the 64K memory, caused the

data acquisition program to read the counter latch units and ADC's, and write this information next to the MWPC data in the 64K memory. (An address register and a data register allowed the program to read or write into the 64K memory.) Also stored in an event record was a binary word indicating which of the triggers had been satisfied for that event. (For bookkeeping purposes, the data acquisition program kept count of and stored the numbers of words of various kinds of data contained in an event record.) Event records varied in length, depending upon the number of proportional chamber wires struck. Typically, they were 50 words.

No new event could initiate the data acquisition sequence until the current event either failed to fulfill one of the triggers, or was successfully stored in the 64K memory. In the latter case, regardless of which trigger had occurred for that event, the fast logic was disabled for a total of 250 microseconds.

All the data from one accelerator pulse was stored temporarily in the 64K memory. Between pulses, the accumulated contents were transferred to magnetic tape. In addition, the contents of scalers, the magnet current settings, and the collimator settings were written to tape once per pulse.

Between pulses, the data acquisition program incremented a number of histograms and performed a crude event reconstruction using the MWPC information, so that the wire chamber planes and counters, taken individually and in concert, could be readily monitored during data taking. Graphical representations of events, selected according to various criteria, could be displayed on a storage scope.

6.3 DATA RUNS

Data were collected in two periods. The first was from July 23 to September 6, 1978. The second was from August 4 to December 1, 1979. Approximately two dozen pi-mu atoms were detected during the first period. Modifications to the beam line, detector, trigger, and data acquisition system were made in the succeeding months. Hence, none of that data is reported here.

As the data were gathered, they were naturally separated into "runs", which contained no more than the maximum number of events (about 190,000) that could be written on a 2400 foot tape at 800 bpi (bytes per inch). Roughly 300 tapes were written during the experiment.

Most of the data was taken with the trigger previously described, typically at 250 triggers per pulse. (In

practice, the data taking rate was limited by radiation monitor "trip" levels in the beam line and experimental areas.) At this rate a run usually lasted one or two hours, during which time beam intensity, singles counting rates, coincidence rates, magnet currents, high voltages, the vacuum decay region pressure, MWPC dark currents, collimator settings, targeting angle, and other experimental parameters were monitored to keep data taking conditions constant.

A variety of runs for calibration purposes were interspersed with normal data taking. These runs are described in the context of the calibrations, in Chapter 10.

CHAPTER 7

THE MONTE CARLO COMPUTER PROGRAM

A simple comparison of the number of events belonging to different kaon decay modes does not constitute a measurement of the relative branching ratios unless the detection efficiencies for each mode are identical. A computer program relying on the Monte Carlo method of simulating probability distributions using random numbers calculated the relative detection efficiencies or "acceptances" for the decay modes observed. In addition, the Monte Carlo program was a valuable tool in understanding background events and estimating systematic errors.

7.1 GENERAL DESCRIPTION

The fact that pi-mu atoms, $K_{\mu 3}$ decays, and the entire single photon spectrum were studied in this experiment necessitated the creation of a Monte Carlo code

sufficiently general and flexible to incorporate K_L^o decays with various numbers of particles in intermediate and final states, as well as production processes like pair creation by photons and electrons. A brief outline of the structure of the program follows.

The Monte Carlo program simulated the physical apparatus by a series of "apertures" representing elements such as magnets, MWPC's, scintillation counters, pipes, helium bags, etc., through which were moved individual particles. Each of these apertures was assumed to be perpendicular to the Z axis of the internal coordinate system, just as they were in the analysis program. They had specified boundaries in the X and Y directions, radiation lengths, and thicknesses (in the Z direction). For example, the 20 mil foil, at Z = 454.6 m and positioned in X and Y according to the measured location of the 32 in. pipe in which it was housed, was approximately semi-circular, and 0.00583 radiation lengths thick.

At any time in a particle's course through the apparatus it was described by the following: type (e.g. muon), charge, laboratory four-vector momentum, position, direction cosines, and the Z coordinates of its points of creation and eventual decay. As a particle was transported through the apertures, it underwent multiple scattering and bent through magnets according to its

charge, and suffered radiative energy losses if it was an electron. Each deflection and energy loss resulted in a correction to the appropriate parameters. X and Y coordinates were recorded at MWPC's and scintillation counters.

Each particle was advanced through the apertures from its point of creation to the Z coordinate of its decay. For unstable particles, the latter was computed from the initial position, direction, and momentum, assuming straight line motion, with a rest-frame lifetime chosen according to an exponential decay curve with the appropiate half-life. However, only muons penetrated the shower counters and the steel absorber to register hits in the muon counters. Furthermore, only particles that moved downstream (increasing Z) were considered. A particle was disregarded if it passed outside one of the apertures that defined the evacuated beam pipe. These included flanges between pipe sections, bends in the pipe, and the D-shaped window. For convenience, particles that journeyed outside the active areas of certain apertures within the detector were also discarded. Pi-mu atoms that decayed before reaching the foil were considered lost.

A list of the particles generated by the particular K_L^0 decay that was unfolding was always maintained. A particle's position in the list corresponded to an array of

numbers characterizing the particle, as specified above. In addition, each particle "pointed" to another particle which was to be tracked through the apparatus after it had completed its own course. By reassigning these pointers as new particles were added to the list, various numbers of particles could be handled for a given K_L^o decay. This technique lent the Monte Carlo program its versatility.

Each Monte Carlo K_L^o decay began by choosing at random a point on the target and a point within the (adjustable) jaws of the steel collimator at 200 m which fixed the trajectory of the kaon. A momentum was selected from an input spectrum of K_L^o momenta at the target (see Chapter 10). Once a lifetime had been picked, the kaon's decay point was calculated. If this point fell outside the decay region (210 m to 454 m), a new momentum and a new lifetime were generated using the Monte Carlo method, from which a new decay point was derived. Finally, the K_L^o was decayed in its rest frame, its decay products were Lorentz transformed to the laboratory frame, and one by one particles were sent through the detector as sketched above.

After all particles had been traced for the current K_L^o decay, the list of particles was consulted to see if at least two charged ones reached the shower counters. If so, then whatever information was deemed essential or useful to the subsequent examination of the event was written to

magnetic tape (e.g. the coordinates of hits in the MWPC'S and the disposition of photons that failed to convert in the foil). For convenience, the coordinates of hits in the MWPC's and counters were digitized as each event was read by the event reconstruction and analysis program, taking into account chamber and counter geometry, inefficiencies, and extra-hit probabilities. The Monte Carlo generated events were then subjected to the same trigger requirements and analysis cuts as the data (see Chapter 9).

A separate Monte Carlo program, which was not used to obtain any of the results presented here, was written primarily for the analysis of $K_{\mu 3}$ events and pi-mu atoms (ref. 35).

7.2 TRACKING THROUGH MAGNETS

A charged particle followed a helical path through magnets. The radius of curvature in the plane normal to the field direction was calculated from the particle's component of momentum in that plane, the width of the magnet (in Z), and the magnetic field integral, which was derived from the field maps. Particles that curled up in the field were discarded.

7.3 KINEMATICS OF PARTICLE DECAYS

The kinematics of two-body decays is trivial since the decay products have unique momenta in the parent particle's rest frame. After picking a random direction for one of the decay products in that frame, a Lorentz transformation using the parent's momentum fixed the laboratory four-momenta for both. Then, as described above, the Z coordinates of the daughter particles' decay points could be computed, completing the specifications for those particles and inaugurating the transport of one of them through the apparatus.

Two-body decays incorporated in the program were $K_L^o \to (\pi\mu)_{atom}\nu$, $K_L^o \to \pi^o\pi^o$, $K_L^o \to \gamma\gamma$, $\pi \to \mu\nu$, and $\pi^o \to \gamma\gamma$. Other charged pion and neutral pion decay modes (all of which have branching ratios about 1% or less) were neglected. (The binding energy of the pi-mu atom was ignored.)

Three-body decays were also easily encoded. However, the forms of the square of the matrix element had to be known in order to simulate, with a large number of decays, the correct Dalitz plot distributions. The decays generated included $K_L^o \to \pi\mu\nu$, $K_L^o \to \pi e\nu$, $K_L^o \to \pi^+\pi^-\pi^o$, $K_L^o \to \pi^o\pi^o\pi^o$ and $\mu \to e\nu\nu$. The Particle Data Group conventions and parameters for these decays were used in most cases. The only other relevant three-body K_L^o decays that had been

measured were $K_L^o \to \pi^+\pi^-\gamma$ and $K_L^o \to e^+e^-\gamma$ (ref. 36). The former could not contribute to the photon p_t spectrum beyond the three-pion fall-off, and was negligible compared to the those decays. The latter was estimated to account for less than 0.5% of the $\gamma\gamma$ events. Hence neither was integrated into the program.

The calculation of the pi-mu atom branching ratio with respect to the decays $K_L^o \to \pi\mu\nu$ depended upon a careful simulation of the Dalitz plot density. The form factors for $K_{\mu 3}$ decay have been discussed (see Chapter 2). First order radiative corrections were included, according to the formulae of Ginsberg (ref. 16). The K_{e3} semi-leptonic decay proved relevant not to a search for pi-e atoms but to a background in the single photon spectrum due to electrons that produced e^+e^- pairs in the foil. (This "trident" process is treated below.) Since the form factor f_- entered the matrix element with the lepton mass it was neglected, as is customary, for K_{e3} decay.

With regard to the three-pion decays, the matrix element is, of course, a constant for the $3\pi^o$ mode. For the other, a series expansion was used which depended linearly and quadratically on the kinetic energy of the π^o, and quadratically on the difference between the kinetic energies of the charged pions. CP invariance was assumed to hold, so there was no linear term in that difference.

Since the muon lifetime is so long (2.197×10^{-6} s), few muons decayed in the course of a typical running of the Monte Carlo program. Hence a simple expression for the electron energy spectrum was installed, taking the momentum parameter ρ to be 0.75, and neglecting terms proportional to the electron mass (ref. 37).

Once energies for two of the three final state particles had been picked according to the previously measured and parameterized distributions, the opening angles between pairs of particles were kinematically determined. Thus in the parent particle's rest frame an arbitrary direction was chosen for one of the decay products, after which the decay plane was rotated through a random angle about that direction. Finally, the momenta in the laboratory were obtained by a Lorentz transformation.

Only one four-body decay was considered, $K_L^o \rightarrow \pi e \nu \gamma$, which has a branching fraction $(1.3 \pm 0.8) \times 10^{-2}$ ($E_\gamma > 15$ MeV) compared to all K_L^o decays, and so could not be ignored in the study of the photon spectrum. Only the photon was followed, since the upstream vertically bending magnet reduced the probability that both the primary electron and the e^+e^- pair from photon conversion would traverse the spectrometer. In any case, the contribution of this radiative decay was determined empirically from Monte Carlo fits to the data, as discussed in Chapter 12. Photon

energies were selected from 40 MeV to 210 MeV using the theoretical spectrum of Fearing, Fischbach, and Smith (ref. 38).

7.4 ELECTROMAGNETIC PROCESSES

Photons required special handling in the Monte Carlo program because of the relatively large cross-sections for electromagnetic processes. We were led, therefore, to consider generally the interactions of photons and electrons with matter, that is, with the Coulomb fields of nuclei and atomic electrons treated classically or as quantized radiation fields (photons). Three examples are bremsstrahlung radiation, pair creation by photons, and Coulomb scattering, all of which can take place in the vicinity of nuclei or atomic electrons. (Although charged particles more massive than the electron also participate in electromagnetic interactions, many of the cross-sections are reduced by some power of the ratio of the particle's mass with the electron mass. Hence with the exception of the discussion of multiple Coulomb scattering in 7.4.4, in this section we confine ourselves to electrons and photons.)

For the purposes of a Monte Carlo simulation, the myriad electromagnetic processes may be considered from the

point of view of the energy lost by a particle incident upon some material. A distinction is usually made between discrete and continuous energy losses. In the discrete case, secondary particles with energies above some cut-off are created. This cut-off is sometimes a matter of choice, for the continuous losses may be the result of identical processes which, however, yield new particles with energies below the cut-off (e.g. the radiation of soft photons). Let us look briefly at the principal energy loss mechanisms.

Electrons lose energy in matter through collisions and by radiation (bremsstrahlung). In the former case, the atoms are left in excited states or they are ionized. If the atom is ionized and the ejected electron has considerable energy, it may be treated as a secondary particle (a "delta ray"). Delta rays were not integrated directly into the computer program as discrete particles occasionally "created" by others to be then transported through the apertures. Rather, they were accounted for after the complete evolution of an event, in the course of digitizing the scintillation counters that were hit by the primary charged particles, using experimental measurements as a guide. Delta rays are discussed more fully in Chapter 10. Strictly speaking, then, the primary charged particle's energy loss due to collisions was neglected.

More important at high energies than energy loss by collision is the bremsstrahlung process. Bremsstrahlung photons are distributed in energy from zero up to the energy of the primary particle. For a reason that will become apparent shortly, the Monte Carlo program treated this as a continuous energy loss for electrons in the sense that discrete photons were not themselves transported through the apparatus. The relevant formula is discussed below in Section 7.4.1.

At high energies, photons lose energy in traversing matter almost entirely through pair creation with a cross-section essentially independent of energy, whereas at low energies Compton scattering and the photoelectric effect dominate (the crossover depending on the medium) (ref. 39).

The combination of pair creation and bremsstrahlung gives rise to the well known electromagnetic cascade shower phenomenon. Multiple Coulomb scattering dominates the spread of the shower. The Compton effect, the photoelectric effect, and positron annihilation perturb the development of the shower to some degree. The shower is finally dissipated in low energy inelastic collisions.

Returning now to the Monte Carlo program, we may now see why it was convenient to consider separately the photon detected by virtue of its having produced an e^+e^- pair in

the foil and the other photon (or photons) from the decay. With regard to the electron and positron, there was no need to follow bremsstrahlung photons for the sake of an occasional e^+e^- pair that might have been produced somewhere in the detector and vetoed the event by firing an extra counter, since the amount of material in the spectrometer from the D-shaped window to the back of the B bank of counters amounted to a small fraction of a radiation length (0.142). In any case, the negligibly small fraction by which the acceptance would have been reduced had the photon been properly "showered" downstream of the foil would have been essentially the same for the various K_L^o decays to photons. Thus in the Monte Carlo, pair production took place only at the foil (see Section 7.4.2). Except for the possibility that one or more of the other photons might convert in the foil, they were otherwise treated as non-interacting particles in the computer code being described.

The sketch of the electromagnetic shower above was not in vain, for photons other than the one detected were often headed for the walls of the beam pipe at a grazing angle: they therefore saw many radiation lengths of steel. A separate computer program, the EGS Code System, was used to explore the fate of these photons from K_L^o decay. Chapter 8 is devoted to it. (The somewhat pedantic point can be made

here that those photons which did not convert in the foil yet entered the detector were also showered, that is, the EGS Code System incorporated the detector as well as the entire beam pipe in its electromagnetic cascade simulation.)

Before concluding this overview of the electromagnetic interactions of electrons and photons with matter that were relevant to the Monte Carlo simulation of the experiment, another word of introduction is in order. Because photons were detected by their having created an e^+e^- pair at the break-up foil, particular attention was paid to other electromagnetic interactions that could have given rise to a pair of oppositely charged particles. For example, an energetic delta ray knocked out of an atom by a positron (Bhabha scattering) might have mimicked a photon conversion in the foil. In fact this was not a source of background events, for reasons given in Chapter 12. As already noted, the higher order process of direct pair production by electrons did contribute a significant number of events to the photon p_t spectrum in the region of interest (above the three-pion fall-off). Trident production is treated in Section 7.4.3.

7.4.1 RADIATIVE ENERGY LOSS

The electron's loss of energy by radiation was simulated using Bethe and Heitler's expression for the probability $w(E_o,E,x)dE$ that an electron of initial energy E_o has energy between E and E + dE after traversing a thickness of x radiation lengths (ref. 40). Although on average an electron loses 1% of its energy by passing through 1% of a radiation length, the average is much higher than the most probable energy loss (none, i.e. $E = E_o$), owing to a long tail in the distribution. The effect of this energy loss was apparent in the departure of the electron and positron tracks from parallelism, after the 100D40 (see Figure 12, Chapter 9).

7.4.2 PAIR PRODUCTION BY PHOTONS

Since the discovery of the positron, considerable effort has been invested in calculating the pair production total and differential cross-sections. Motz, Olsen, and Koch (ref. 41) have written a critical review of these calculations.

For a Monte Carlo simulation, one needs an expression for the differential cross-section as a function of the energies and angles of emission of the electron and positron, and as a function of the energy of the incident

photon. A formula of Davies, Bethe, and Maximon (ref. 42), applicable to extreme relativistic energies and screening of the electric field of a point nucleus by the atomic electrons, was chosen for the differential cross-section $d\sigma/dE_+$, where E_+ is the positron energy. (Although the importance of screening depends upon the fraction of the incident photon energy carried by the positron, complete screening is a good approximation for high photon energies, so it was assumed.)

In this work, the angle between the positron (or electron) and the incident photon was found to be unimportant. However, conspicuous differences between the data and Monte Carlo events were resolved only after handling properly the angle between the two leptons. We used the formula for the distribution of the angle of divergence obtained by Borsellino (ref. 43), which depends upon the photon energy and the ratio in which that energy is divided between the electron and positron. Given the high energies of the particles involved, the recoiling nucleus could be completely neglected, so that the incident photon and outgoing pair were assumed to be coplanar. The orientation of the plane of the pair about the axis of the photon's direction was chosen randomly.

Since the K_L^o decays were generated in a random way, there was no bias introduced by converting the first photon

to strike the foil 100% of the time. The second photon from a given decay that struck the foil was assigned a small conversion probability P_{2nd}, taken to be the ratio of the probability that exactly two converted to the probability that any converted at all. If P_{cnv} is the conversion probability, then P_{2nd} is

$$P_{2nd} = P_{cnv}/(2 - P_{cnv}) \quad .$$

(The probability that three photons would convert in the 35 mil foil was 4.64×10^{-7}, so it was ignored.)

The conversion probabilities for 20 and 35 mil thick aluminum foils were computed in two different (but related) ways, with consistent results (given in Chapter 5). The first used the well known formula from Rossi (ref. 44)

$$P_{cnv} = 1 - \exp\left(- \frac{x}{X_o} \left(\frac{7}{9} - \frac{B}{3}\right)\right)$$

$$B = \left(18 \ln(183 \, Z^{-1/3})\right)^{-1}$$

where x is the density of the foil in gm/cm^2, X_o the radiation length of aluminum in the same units, and Z the atomic number. In the second, a number for the total electron pair production cross-section $\sigma(\infty)$ (for infinite photon energy), with a small energy-dependence correction (ref. 45), was used in the expression

$$P_{cnv} = 1 - \exp\left(- x \frac{N}{A} \sigma\right) \quad .$$

(N and A are Avogadro's number and the atomic weight, respectively.)

7.4.3 PAIR PRODUCTION BY ELECTRONS

The nature of the background from tridents produced in the foil is described in Chapter 12. Briefly, if the electron in the created pair went undetected (because it had very low energy), yet the positron and the incident electron were observed, then such an event could not be distinguished from a photon converting in the foil.

Many theoretical and experimental papers on the trident process have been published since the early work of Carlson and Furry (ref. 46), stimulated, in later years, by tests of quantum electrodynamics and studies of cosmic ray muon interactions (ref. 47). Though there has long been a consensus on the form of the differential cross-section when the energy of the created pair is small compared to the energy of the incident charged particle, successive authors have endeavored to improve on prior formulae in the regime of large pair energy. In 1967, Kel'ner (ref. 48) obtained an expression valid for both small and large energy transfers, which was subsequently improved by

Kel'ner and Kotov (ref. 49) with a more satisfactory treatment of screening. We have relied on the work of Kokoulin and Petrukhin (ref. 50,51), who have made the formulae of Kel'ner and Kotov more tractable. (In the second paper, nuclear form factor corrections were taken into account.) All the expressions in the later papers are derived subject to the condition that the energies of all the particles are large compared to their rest masses.

For the Monte Carlo simulation of tridents, three probability distributions were required:

1. The probability for creation of a pair of total energy ε with a fraction $v = \varepsilon/E$ of the incident charged particle energy E.
2. The probability distribution for division of the energy of the pair between the two created particles, characterized by $\rho = (\varepsilon_+ - \varepsilon_-)/\varepsilon$ where ε_+ and ε_- are the positron and electron energies, respectively.
3. The probability distributions for the opening angles involved.

For the first two, Kokoulin and Petrukhin wrote the differential cross-section as

$$\sigma(E,v,\rho)dvd\rho = \frac{2}{3\pi}(Z\alpha r_e)^2 \frac{1-v}{v}\left(\Phi_e + \frac{m^2}{m_\mu^2}\Phi_\mu\right)dvd\rho$$

where $\Phi_{e,\mu}$ depend in a complicated way upon E, v, and ρ. The mass of the primary particle is m_μ (an electron, in our case), m is the electron mass, r_e is the classical electron radius, and α is the fine structure constant. The third

distribution is not discussed in detail in the literature, so the Borsellino formulae, derived for pair production by real photons, were applied in the manner described above (Section 7.4.2).

7.4.4 MULTIPLE SCATTERING

On traversing a medium a charged particle suffers numerous independent small-angle Coulomb scatterings. The interactions result in essentially no energy loss for the incident particle, as the bulk of the deflection is due to scatterings from nuclei which are much more massive. In this respect, as well as the fact that multiple scattering is important not just for electrons but all charged particles, the process differs from the others discussed in this section. Nevertheless, it falls naturally under the heading of electromagnetic processes.

Multiple scattering may be described by the probability $P(\theta)d\theta$ of scattering into the angular interval between θ and $\theta+d\theta$. The distribution is approximately Gaussian, although single large-angle scatters give the true distribution a long non-Gaussian tail below the 5% level. Highland (ref. 52) has given a simple formula, based partly on the Moliere theory, for the angle at which which $P(\theta)$ has fallen by 1/e

$$\theta_{1/e} = \frac{E_s}{p\beta c} x^{\frac{1}{2}} \left[1 + 0.125 \log_{10}(10x)\right] \quad .$$

The thickness of the material in radiation lengths is x, p the momentum and βc the velocity of the incident particle in the laboratory. E_s is a parameter that ranges from about 16 to 18, depending on the atomic number Z of the scatterer, when p is expressed in MeV/c. (In the Gaussian approximation, $\theta_{rms} = \theta_{1/e}$.)

In the Monte Carlo, multiple scattering was simulated in one of two ways, depending upon the thickness of the detector element. For the thin ones (everything except the shower counters and the steel muon filter), the scattering angle was chosen from a distribution of normalized scattering angles θ/θ_{rms} corresponding to 10^{-3} radiation lengths of aluminum, and then scaled by $\theta_{1/e}$ for the element in question. The tables of Marion and Zimmerman (ref. 53), derived from the theory of Nigam, Sundaresan, and Wu, furnished this distribution. The displacement of the incident particle after scattering was found using the expression for the average displacement projected in a plane

$$y = D\theta/\sqrt{6}$$

where D is the thickness of the element. This was an adequate approximation since D was small.

For the thicker elements, the Gaussian angular distribution sufficed. However, the displacement transverse to the direction of motion was better described, using Rossi's formula (ref. 54) for the probability $P(x,y,\theta_y)dyd\theta_y$ that at a thickness x, the scattered particle would have a lateral displacement in dy at y and be traveling in $d\theta_y$ at an angle θ_y with respect to the direction of incidence. (Also, in the calculation, the particle's momentum was diminished by the equivalent of one half the average energy lost in the element.)

Care was taken to include in the Monte Carlo all the matter in the spectrometer, including the foil, helium, the helium bag windows, air, MWPC's, scintillation counters, et cetera. The probability that a particle struck a proportional chamber wire was 21.8%. The simulation of multiple scattering was studied by comparing the deviations of reconstructed tracks from straight lines, as a function of momentum, for both data and Monte Carlo events. Single-track data taken with the magnets off, as well as normal data (using only the side view track projections), served this purpose. Good agreement was found, with the largest deviations at low momentum, as expected. Multiple scattering through the thick elements was checked using events with a single muon that fired two overlapping muon counters, one from the upper row, and the other from the

lower row. The Y location of this region was compared to the Y coordinate that the particle would have intersected had it traveled in a straight course, as defined by the MWPC's. The displacements for data and Monte Carlo events agreed nicely, as shown in Figure 8.

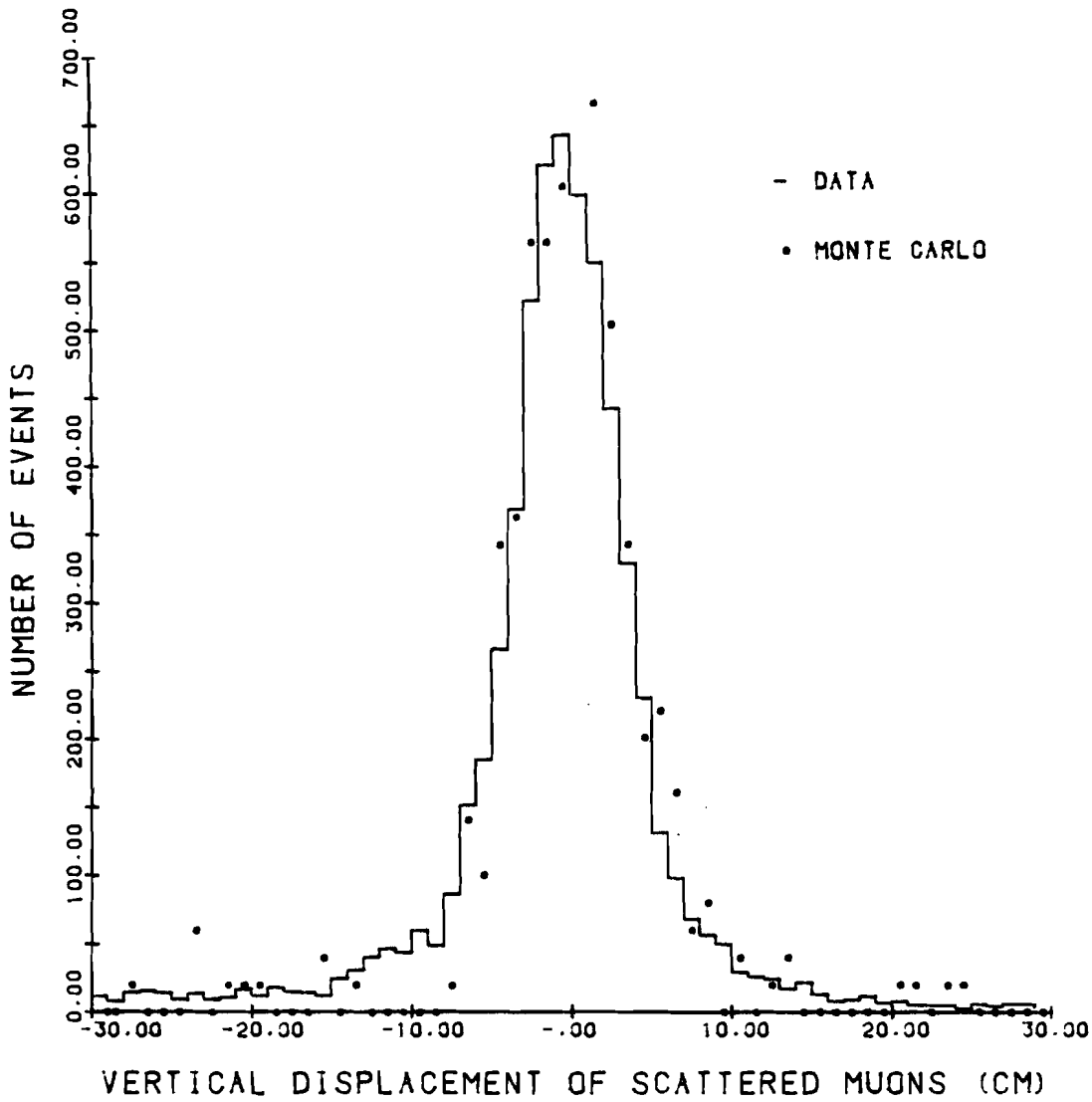

Figure 8. Vertical displacement of muons (from $K_{\mu 3}$ decay) due to scattering in the steel filter.

CHAPTER 8

ELECTROMAGNETIC SHOWER SIMULATION USING EGS

The Monte Carlo simulation described in the previous chapter treated photons which did not convert in the break-up foil as non-interacting particles. Under this assumption, the expected number of e^+e^- pairs in the data attributed to $K_L^o \to \pi^o\pi^o\pi^o \to 6\gamma$ (and $K_L^o \to \pi^+\pi^-\pi^o \to 2\gamma$) was about four times larger than observed, based on the number of detected $K_{\mu 3}$ decays and the $K_{\mu 3}$ acceptance calculation. Obviously, photons which did not convert in the foil often struck the walls of the beam pipes, flanges, and other matter in and around the apparatus, resulting in electromagnetic cascade showers which sent many charged and neutral particles into the detector. Some of these fired scintillation counters, causing the event to fail the trigger requirements, or they hit MWPC's, causing the event to fail the event reconstruction requirements.

The sophisticated and well documented EGS (Electron-Gamma Shower) Code System developed at the

Stanford Linear Accelerator Center by Ford and Nelson (ref. 55) was adapted to the task of determining what fraction of the otherwise detectable decays were lost in the manner described. EGS performed a simulation of an electromagnetic cascade shower using the Monte Carlo method. Photons, electrons, and positrons were individually transported through matter, and interacted in various ways with appropriately calculated probabilities. The basic strategy of the program was as follows. Having been given the charge, energy, position, and direction cosines of a particular particle, as well as the nature of the surrounding medium, EGS determined that it would like to transport that particle a certain distance along a straight line. The user of EGS was then asked if the particle would thereby cross an interface between two regions or two media. If so, the transport took place only as far as that interface, and the cycle began anew. The most formidable chore for the user of EGS was to specify, as completely as possible, the geometry and composition of the materials (i.e. the apparatus) through which the showers were to propagate. EGS transported each particle in the shower until an interaction occurred, or until the particle energy fell below a predetermined value (1.5 MeV for charged particles, and 1 keV for photons), or until the particle entered a region of space where the user requested

that it be discarded. (Showers could be initiated in the energy range 1.5 MeV to 100 GeV.)

In the present application, the cylindrical beam pipes and flanges which surrounded the decay volume, as well as the rectangular pipe which contained the neutral beam beneath the spectrometer, were specified in the user-written code. This code also included the polystyrene of the scintillation counters, the air in the spectrometer, and the iron in the 100D40 analyzing magnet. The helium, helium bags, and chambers were neglected, as were the D-shaped window, the foil, and all matter outside of the decay volume but upstream of the D-shaped window. Showers were followed from their points of origin (usually in the walls or flanges of the decay pipe) as far as the B bank of counters.

As the version of EGS used (version 3) was not equipped to transport charged particles through magnetic fields, subroutines were written for this purpose. The magnetic field regions had a significant effect on the shower development, since they trapped low energy electrons and positrons. In particular, the four magnets upstream of the spectrometer swept aside most of the charged particles generated in the showers, yet they did not prevent photons from flooding the detector.

The effect of these showers was quantified by registering a hit in a scintillation counter every time EGS indicated that a charged particle had struck. If a photon entered a counter, a hit was recorded only a fraction p of the time. In principle, p could be calculated on the basis of four things: the photon energy; cross-sections for pair production (if the enegy was above threshold), Compton scattering, and the photoelectric effect; some knowledge of the attenuation lengths of the counters; and the frequency response and quantum efficiency of the photomultiplier tubes. Instead, the parameter p became the principal adjustable parameter of the simulation (others were the low energy cut-offs for electrons and photons). To a certain extent, the parameter p also accounted for those losses which would have resulted had the apparatus been described more completely than it was; there was a practical limit to the accuracy with which the apparatus and the showers could be duplicated. The manner in which p was tuned is described in Sections 9.1 and 12.2.

The complexity of the apparatus and the physical processes, as well as the large numbers of particles involved, meant that a considerable amount of computer time was required to run one shower history (about 5 seconds on the Fermilab Control Data Corp. CYBER 175). Therefore, the EGS shower simulation was performed only for those Monte

Carlo events which survived all the data analysis cuts (see Chapter 9). All photons, except the one which gave rise to the detected e^+e^- pair, were run through the EGS program. The resulting counter and chamber hits were added to the original hits of the e^+e^- pair, with care taken to avoid double counting. The events that still satisfied the trigger and event reconstruction requirements (on the maximum number of hits per plane) were counted; the rest were discarded. In this way, multiplicative loss factors were determined for several K_L^o decays with photons in the final state. In Figure 9 the number of events remaining divided by the total number of events run through the shower simulation (i.e. the acceptance reduction factor) is plotted as a function of p, for four decay modes. From top to bottom, they are $K_L^o \to \pi^+\pi^-\pi^o$, $K_L^o \to \gamma\gamma$, $K_L^o \to \pi^o\pi^o$, and $K_L^o \to \pi^o\pi^o\pi^o$. (A linear interpolation was made between points, as is most apparent between p = 0.18 and p = 1.0.)

The large demands on computer time by the EGS program limited the statistical significance of the results. Nonetheless, we concluded that the shapes of the single photon transverse momentum spectra for the above decay modes were not appreciably affected by the shower losses. Hence, the EGS loss factors simply reduced the acceptances of the detector for the various decays in an overall way.

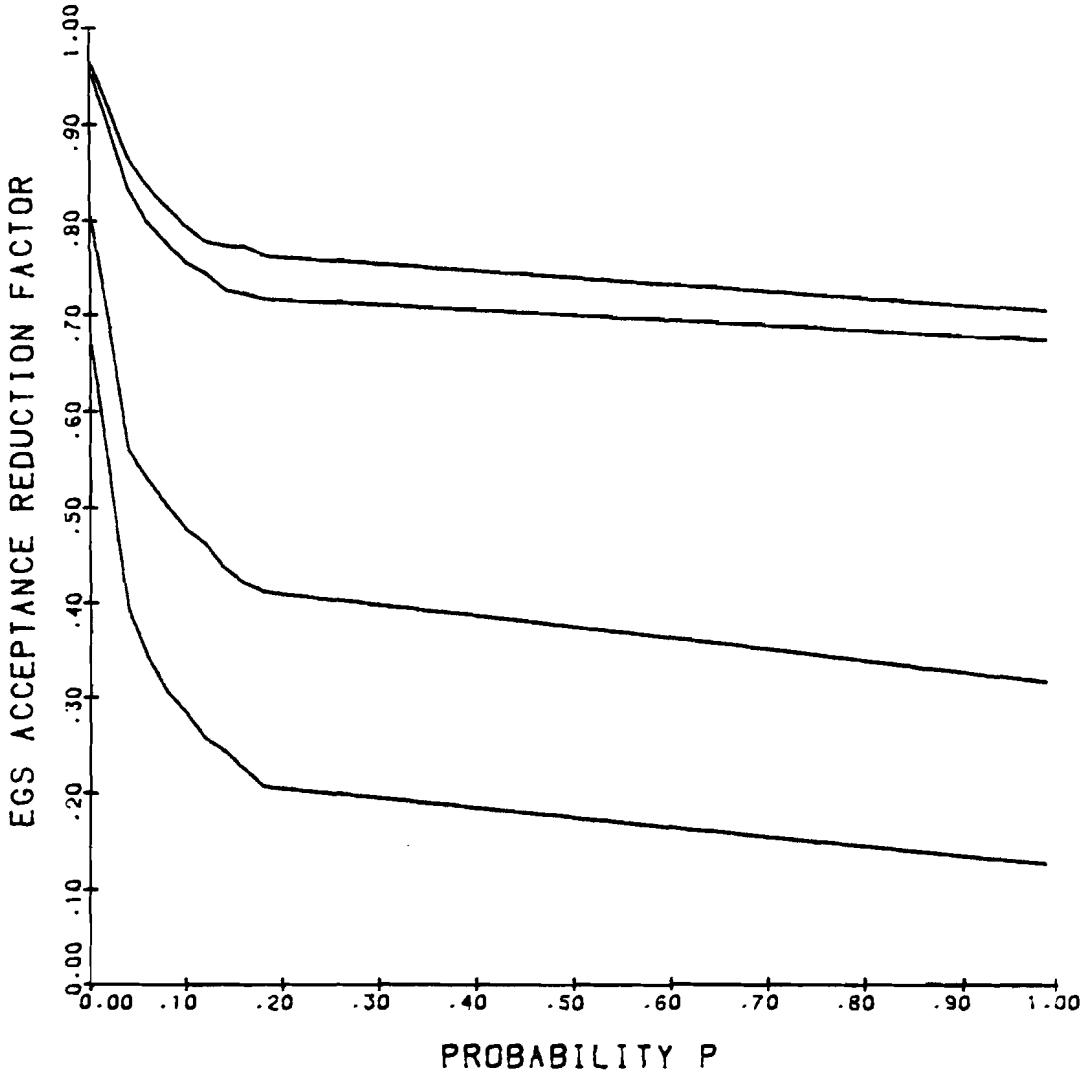

Figure 9. Fraction of events remaining after electromagnetic shower simulation. From top to bottom, decay modes are $K_L^o \to \pi^+\pi^-\pi^o$, $K_L^o \to \gamma\gamma$, $K_L^o \to \pi^o\pi^o$, and $K_L^o \to \pi^o\pi^o\pi^o$.

CHAPTER 9

EVENT SELECTION

This chapter describes the reduction of the raw data and Monte Carlo generated events to final samples of pi-mu atoms, e^+e^- pairs, and $K_{\mu 3}$ decays.

The event selection was accomplished by data analysis programs which performed three functions: the retrieval and decoding of events from the raw data and Monte Carlo tapes; the reconstruction of charged particle trajectories (tracks) using the MWPC information; and the analysis of events. Event analysis included the determination of the momenta of particles, the identification of particle types, and the calculation of various quantities for the selection and study of particular kinds of events.

Two event reconstruction routines evolved along independent lines during the course of the experiment—hence the reference above to more than one analysis program. The routines differed not only in the method by which events were reconstructed, but in the kinds of events

that were sought. They were best suited, therefore, to different branching ratio measurements, as discussed in the next section.

9.1 EVENT RECONSTRUCTION AND NORMALIZATION SCHEMES

One of the event reconstruction (or pattern recognition) programs was written to maximize the number of pi-mu atoms and e^+e^- pairs culled from the data, with the intention of normalizing the pi-mu atom signal to the distinctive $K_L^o \to \gamma\gamma$ Jacobian peak (at least that portion of the transverse momentum spectrum above $K_L^o \to \pi^o\pi^o$).

The $\gamma\gamma$ decay attracted attention because $K_L^o \to \gamma\gamma$ differs kinematically from $K_L^o \to (\pi\mu)_{atom}\nu$ only in that the atom is massive and the photon is not. Hence the ratio of the acceptances for the two decays was relatively insensitive to the input K_L^o momentum spectrum as well as to the decay kinematics. Furthermore, since the topology of e^+e^- pairs in the spectrometer was very similar to that of pi-mu atoms, the efficiency of the pattern recognition computer code was the same for both decay modes. A third advantage to this approach was that the vertically bending magnet could be ignored (provided that it was at least turned on during data taking).

However, this normalization scheme suffered from several defects. First, the $K_L^0 \to \gamma\gamma$ branching fraction had been measured previously only to 10%. Second, the $\gamma\gamma$ signal had a significant background from trident production in the foil, and interactions of neutrons in the beam. Third, the expected cancellation of acceptance corrections from having had identical atom and e^+e^- scintillation counter trigger requirements (neglecting the shower and muon counters) was not realized in actuality. Between 5 and 16% of the time, depending on the photon momentum, particles "splashed" back from the shower counters and contributed to a total of more than four hits in the nearby B counters, thereby vetoeing the event (see Chapter 10). Fourth, the $\gamma\gamma$ normalization demanded that the particle identification techniques be especially well understood, including efficiencies and multiple scattering in the steel muon filter. The fifth difficulty also arose from the characteristically different electromagnetic interactions of the final state particles, yet could not be circumvented reliably using only the event reconstruction routine optimized for recovering pi-mu atoms and e^+e^- pairs.

The problem lay in answering the question: what fraction of $\gamma\gamma$ decays were lost because the undetected photon showered somewhere upstream of the spectrometer, sending many charged and neutral particles into the

detector? The answer furnished by the EGS Code System (Chapter 8) had to be checked. The solution was to measure the relative branching ratios of two copious K_L^o decays, namely $K_{\mu 3}$ and $K_{\pi 3}$, and compare the result with their well known rates. If they agreed after the EGS acceptance correction for the $K_{\pi 3}$ decays had been included, then the EGS adjustment for $K_L^o \to \gamma\gamma$ could be trusted. (The reader may have inferred that $K_L^o \to 3\pi$ was not put forth as a possible normalization to begin with because of the anticipated size of the correction for these decays; on the other hand, $K_L^o \to \gamma\gamma$ was originally thought to be quite clean.)

The other event reconstruction routine (ref. 35) was thus called into play, for it sifted $K_{\mu 3}$ events as well as pi-mu atoms and e^+e^- pairs from the data. It had been written with a second pi-mu atom normalization scheme in mind, which used $K_{\mu 3}$ decays rather than $K_L^o \to \gamma\gamma$ events. This program sought to pick out pi-mu atom and $K_{\mu 3}$ decays with the same efficiency, independent of the performance of the various MWPC's, despite the dissimilarity between the two with regard to the pion and muon trajectories through the apparatus. Consequently, a more general algorithm had developed, with stricter prerequisites, resulting in a loss of pi-mu atoms and photon conversions (roughly 25%).

The loss in statistics from using the second event reconstruction program, as well as the sacrifice of the

desirable aspects of the $\gamma\gamma$ normalization for pi-mu atoms, was partially compensated by the elimination of most of the sources of error mentioned above. The $K_{\mu 3}$ decay mode promised to be a good normalization for pi-mu atoms not only because its rate was well known, but because the particles in the final state were the same for both decays. Although $K_{\mu 3}$ decays were not without background events, the background was small. The source of error pertaining to trigger biases was still present, but in relation to different triggers than before: care had to be taken to account for the loss of pi-mu atoms stemming from the tighter atom trigger requirement on the horizontal counter hodoscopes (W and H) (see Chapter 10).

By providing a means of testing the validity of the EGS Code System shower simulation, the second event reconstruction routine also facilitated a measurement of branching ratios for the rare decays $K_L^o \rightarrow \gamma\gamma$ and $K_L^o \rightarrow \pi^o \pi^o$. To reiterate, $K_{\pi 3}$ decays could now be compared with $K_{\mu 3}$ events, in order to judge the success of the EGS Code System in reducing the $K_{\pi 3}$ signal generated by the original Monte Carlo (which neglected the photons that did not convert in the foil) to the size of the signal in the data. Actually, the object of the comparison was not only to check that the EGS Code System gave reasonable results, but to tune the one adjustable parameter (p) of the simulation.

Provided, then, that the $K_{\pi 3}$ decays were well understood, they furnished an appropriate normalization for $K_L^o \to \gamma\gamma$ and $K_L^o \to \pi^o\pi^o$. As in the case of pi-mu atoms versus $K_{\mu 3}$ decays, the normalization events ($K_L^o \to \pi^+\pi^-\pi^o$ and $K_L^o \to \pi^o\pi^o\pi^o$) had well known branching ratios, and the detected particles were the same as those in the rare decays of interest.

In the course of dismissing the $\gamma\gamma$ normalization for pi-mu atoms and undertaking a measurement of the branching ratios of rare K_L^o decays to photons, the burden of measuring a decay to photons relative to a semi-leptonic decay simply shifted from the rare decay modes (K_L^o $\gamma\gamma$ and $K_L^o \to (\pi\mu)_{atom}\nu$) to the common ones ($K_{\pi 3}$ and $K_{\mu 3}$). However, the comparison of the photon decays to one another was less sensitive to the accuracy of the shower simulation than was the direct comparison to the semi-leptonic K_L^o decays. The former depended only upon the ratios of EGS acceptance corrections, while the latter depended upon their absolute magnitudes.

The measurements that have been discussed in this section, including the several adjustments performed in extracting results, are described explicitly in subsequent chapters. It should be pointed out that both event reconstruction routines were employed in the data analysis. The first one furnished the largest sample of pi-mu atoms and e^+e^- pairs that could be extracted from the raw data.

This was especially important for studies of subsamples of the data which were limited by statistics. The second reconstruction program was used for normalization purposes.

9.2 TWO-TRACK EVENT RECONSTRUCTION

The data reduction began by discarding events which (because of inefficiencies) had too few wires registering hits to permit reconstruction of two trajectories. The numbers of the hit wires belonging to the vertical and horizontal planes were then simply translated into cartesian coordinates, using the measured locations of the planes. The intersections of orthogonal hit wires in the rotated chambers (2 and 5), unlike the others, furnished coordinates in pairs (X and Y). In any plane, when two or more adjacent wires were struck, the average was taken to represent the hit. Following these preliminaries, the programs searched for tracks joining the coordinates of hits.

Although the pattern recognition algorithms became quite sophisticated, the results may be stated simply, and in the same terms for both event reconstruction routines. The side view (Y) coordinates were fit with straight lines using the least-squares technique. In the top view, line segments drawn through hit locations in planes upstream and

downstream of the 100D40 were projected to the center of the magnet. If they converged within a certain distance, consistent with the position resolution as determined by the Monte Carlo, then the side view lines were assigned to one or the other completed track in the top view, according to the mapping provided by the rotated chambers. A correlation between both top view tracks and only one side view track was not uncommon for atom-like events.

The first event reconstruction routine narrowed its search in the top view to events with two roughly parallel tracks downstream of the 100D40, and two tracks upstream of the 100D40 which formed a "V" with vertex approximately midway between the two horizontally bending magnets. The simplicity of this topology was exploited in writing an unbiased and efficient pattern recognition program for pi-mu atoms and e^+e^- pairs, referred to collectively as "foil" events.

The second event reconstruction routine had to contend with a variety of two-track configurations from $K_{\mu 3}$ decays ("non-foil" events). To insure, in principle, that the efficiencies for finding pi-mu atoms and $K_{\mu 3}$ events would be the same, all of the X-Y chambers would have been rotated with respect to the symmetry axes defined by the magnets' field directions. Then both kinds of events would have hit at least two different wires in each of the

orthogonal wire planes. This was not done, except in chamber 5. Therefore at least two hits were required in each plane of that chamber, regardless of event type. The alternative for the remaining chambers was to stiffen the criteria defining a good side view track, but only for those events in which just one track could be reconstructed. Thus, if but one track could be found in the side view, then it had to have at least three of the four coordinates. If two side view tracks could be found, they were permitted to have as few as two (one hit from chambers 1 or 2, and one from 3 or 4). An explicit calculation, corroborated by Monte Carlo studies, showed that the relative $K_{\mu 3}$ and pi-mu atom pattern recognition efficiency was 97.7% and insensitive to reasonable fluctuations in chamber efficiencies (ref. 35). (Since chamber efficiencies were included in the Monte Carlo calculation of acceptances, there was no pattern recognition correction to the final results.)

9.3 MOMENTUM MEASUREMENT

After having met the pattern recognition criteria for a two-track event, the momentum p of each particle was computed using the 100D40 field map and the change in the particle's X direction cosines (Δu):

$$p = (\Delta u)^{-1} \int B_y(X,Y)\,dz \quad .$$

The location (X,Y) of the particle trajectory at the midplane of the 100D40 (Z_m) was found by simulating a parabolic orbit through the magnet which connected smoothly on both sides with straight trajectories fit to the coordinates of the MWPC hits. The sign of p determined the particle's charge. For the rest of the analysis, each track was defined by its momentum, its direction cosines before and after the 100D40, and a single point (X',Y',Z_m) where the upstream and downstream straight line tracks converged.

9.4 PARTICLE IDENTIFICATION

Electrons and muons were identified by the pulse height information in the shower counters and the muon counter hits. Particles that satisfied neither the electron nor muon criteria were called pions. Before specifying those criteria, the calibration of the shower counters will be described.

The pulse height was proportional to the energy deposited. Since electrons typically deposited all of their energy in the shower counters, and their momenta were measured in the spectrometer, the calibration was performed using good e^+e^- pair candidates, i.e. foil events with a

large pulse height in each of two non-adjacent counters. The pulse height (a number from 0 to 1024) for each event was plotted versus the momentum of the particle that struck the counter, provided that the track projected to the central region of the shower counter. A straight line was fit to the data points and the slope, i.e. channels per GeV/c, determined. The intercept of the line with the pulse height axis was a second calibration constant for each shower counter. This offset, or "pedestal", corresponded to no energy deposit. Thus the energy (momentum) deposited in a counter was

$$\text{energy deposited} = \frac{(\text{pulse height} - \text{pedestal})}{\text{slope}} .$$

The attenuation of the signal with distance from the phototube was also measured for each module, using particles of a given momentum and fitting to an exponential decay curve.

In the course of data analysis, the ratio of the energy deposited to the particle's momentum was computed using the expression above, corrected for attenuation. This variable, called $FRAC_n$, for the fraction of the nth particle's momentum appearing as energy in the shower counter, was defined as

$$FRAC_n = \frac{\text{energy deposited}}{\text{momentum} \times \text{attenuation}} .$$

Thus, $FRAC_n$ was peaked about 1.0 for electrons, and peaked near 0.0 for considerably heavier charged leptons (e.g. muons), which do not shower, but leave only an ionization track. If a particle struck the overlap of two counters, $FRAC_n$ was obtained simply by summing $FRAC_n$ for adjacent counters. Occasionally, two tracks projected to the same counter, in which case it was not possible to determine $FRAC_n$ for each particle. For such events, the quantity $FRAC_{total}$ was computed, which was the ratio of the total energy deposited in the bank to the sum of the momenta of the charged tracks (each adjusted for attenuation).

The FRAC distribution for pions was studied using the decays $K_L^o \rightarrow \pi e \nu$. The particle with $FRAC_n > 0.85$ was identified as an electron, and the other particle was called a pion. It was determined that 96% of the pions and 2.7% of the electrons had $FRAC_n$ below 0.7 (0.9% of the electrons were below 0.6). Figure 10 shows a histogram of $FRAC_n$ from a sample of two-track events containing muons, pions, and electrons.

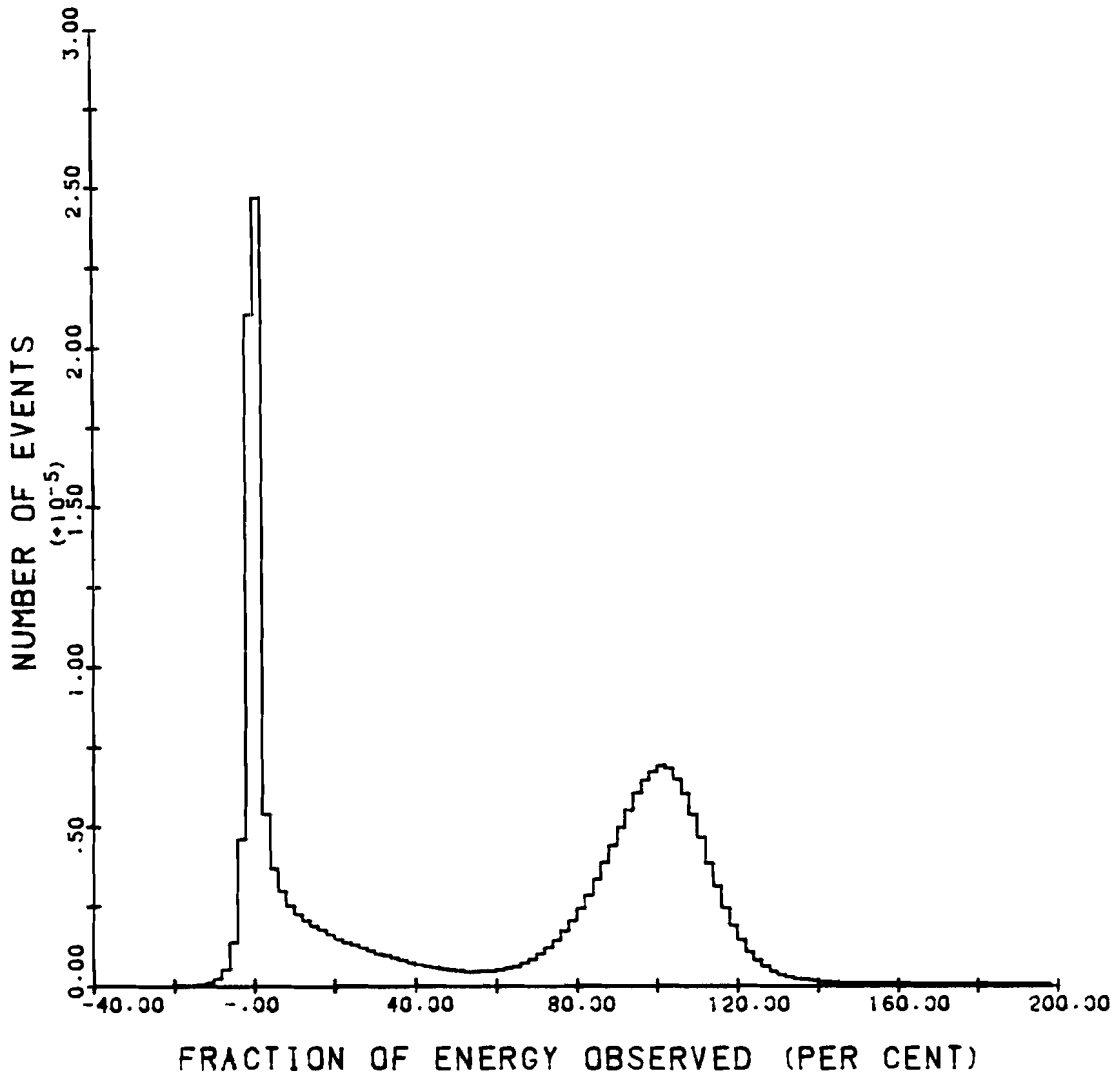

Figure 10. Fraction of a particle's energy observed in the shower counters, for a sample of events containing muons, pions, and electrons.

9.5 EVENT SELECTION

We now catalog the cuts that were applied to the reconstructed events to obtain samples of pi-mu atoms, e^+e^- pairs, and $K_{\mu 3}$ decays with as little background as possible. Since the reduction of the data proceeded along parallel lines for pi-mu atoms and e^+e^- pairs (foil events), they are considered together in the first subsection; $K_{\mu 3}$ (non-foil) events are treated separately in the second. The justification for the cuts pertaining to event topology can be inferred from the survey of the experiment found in Chapter 4.

The figures which illustrate how the data were cut are generally of two types. One shows a histogram of data just before the cut in question was applied. The other displays the same quantity, but histogrammed for the final samples of data and Monte Carlo events, i.e. after all cuts. In most cases, the Monte Carlo histograms were normalized so that they contained the same number of events as the data. (In the case of Monte Carlo distributions for e^+e^- pairs, the histograms have contributions from many sources of photons, weighted in a manner described in Chapter 12.)

Certain cuts were made regardless of event type. Events were discarded which did not have two oppositely charged tracks; which did not have two tracks whose

projections to the shower counters were within the active area of the bank; or which had individual tracks with momenta less than 5 GeV/c or greater than 400 GeV/c. The 5 GeV/c lower bound was chosen to be comfortably above the shower counter total energy requirement for e^+e^- pairs. (The upper bound was the energy of the primary proton beam.)

9.5.1 FOIL EVENTS (PI-MU ATOMS AND e+e- PAIRS)

The deviation of the tracks from parallelism downstream of the analyzing magnet is shown in Figure 11, where the difference of the track separations (in X) at chambers 4 and 5, normalized to the separation at chamber 4, is histogrammed. In an obvious notation, the quantity plotted is

$$(\Delta_4 - \Delta_5)/\Delta_4 \quad .$$

For both pi-mu atoms and e^+e^- pairs, the tracks were required to be parallel to 6%. The same quantity is shown after all cuts in Figure 12. Notice the tail in the distribution for e^+e^- pairs tending toward a smaller separation at chamber 5. This was due to the electron or positron's radiative loss of energy between the horizontally bending magnets and the 100D40.

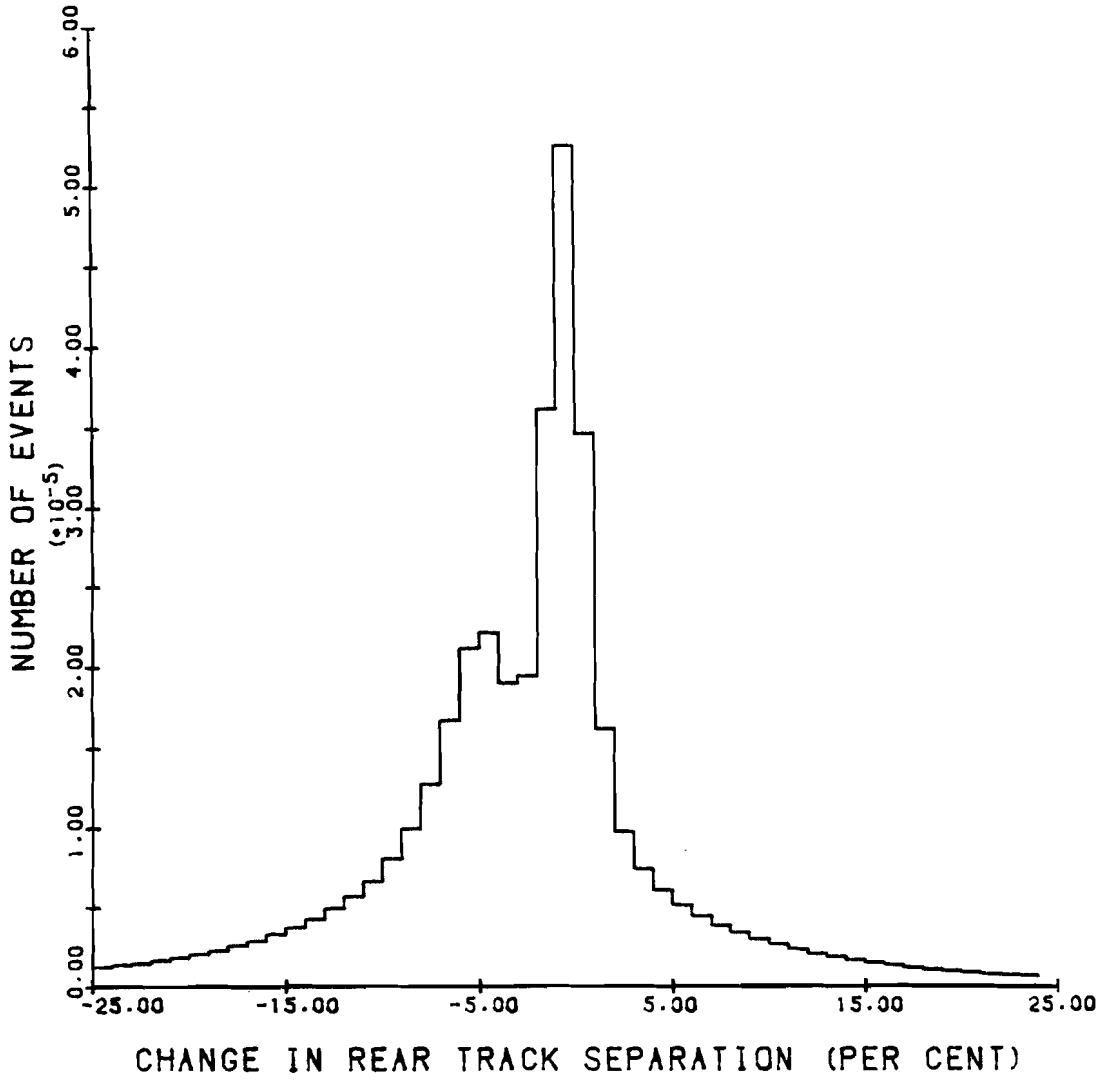

Figure 11. Relative change in the separation of tracks in the rear of the spectrometer, for data containing both foil and non-foil events, before cuts.

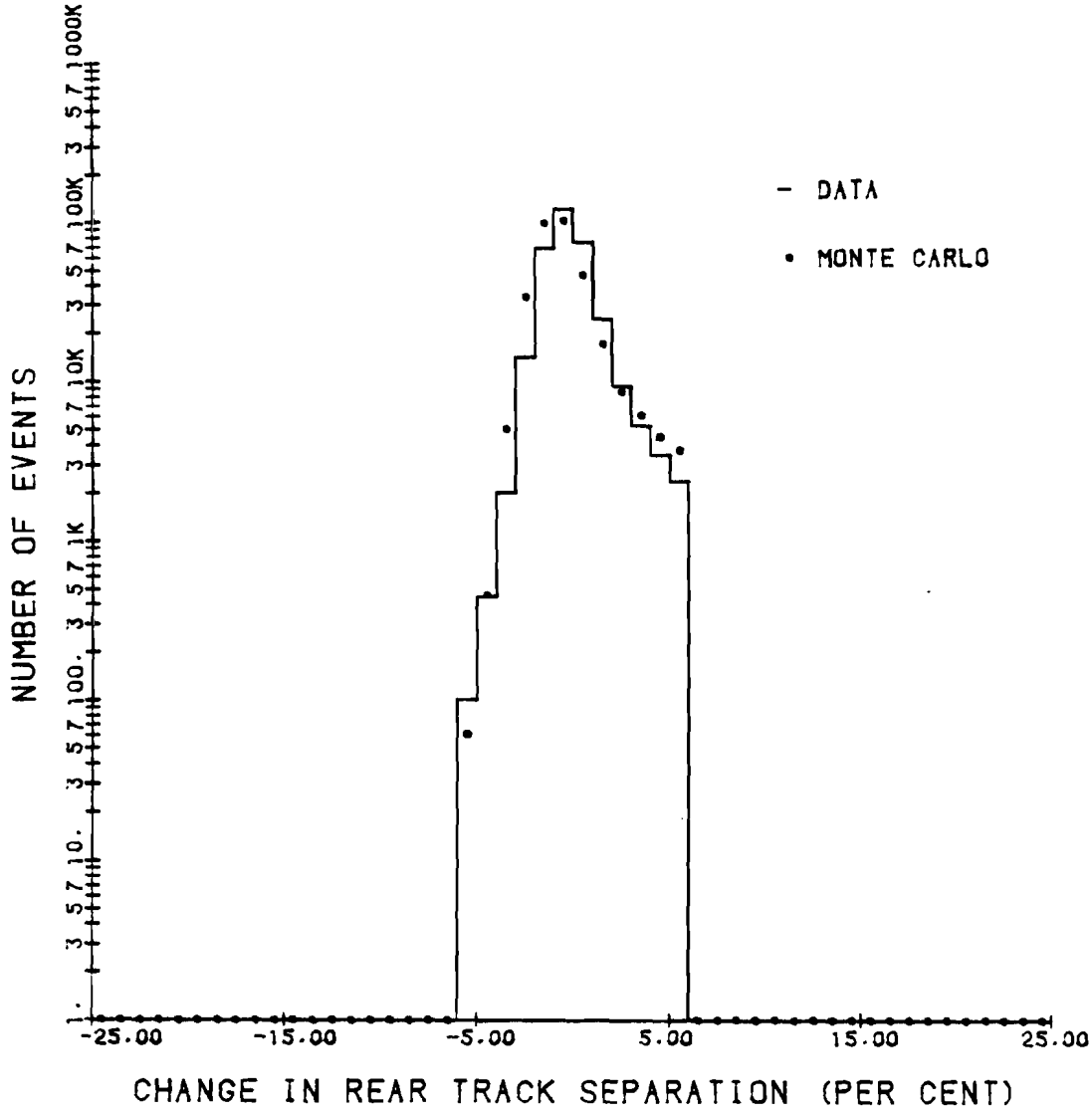

Figure 12. Relative change in the separation of tracks in the rear of the spectrometer, for the final sample of e^+e^- pairs, compared to Monte Carlo generated e^+e^- events.

The "vertex" cut was made in three ways. The first was straightforward, like the "parallelism" cut, since it involved only the number of wires (i.e. the separation) between hits in certain MWPC planes. By the simple properties of similar triangles with a common vertex and angle at the "bend-plane" of the pair of magnets 1H and 2H, the track separation (in X) at the third chamber was required to be in a fixed ratio to the separation (in X) at the first, namely, 4:1. (Chambers 3 and 1 were deliberately stationed at distances in a 4:1 ratio from the point midway between the magnets, 457.19 m.) Histograms of

$$4 \cdot \Delta_1 - \Delta_3$$

in Figures 13 and 14 indeed show a peak about zero. Cuts were placed at ±1.34 cm. The other two vertex cuts depended upon actually finding a vertex by projecting the two particles back upstream (along straight lines), and noting the point on each line at which the distance to the other line was a minimum. The midpoint of the line segment joining the two tracks at closest approach was declared to be the vertex. The second cut was placed on the length of that segment to insure that the two tracks did indeed converge somewhere, as indicated in Figures 15 and 16. A maximum separation of 5.5 mm was allowed. The Z of the vertex is histogrammed in Figures 17 and 18. The cut in Z (±16 cm about 457.19 m) was somewhat more delicate than the

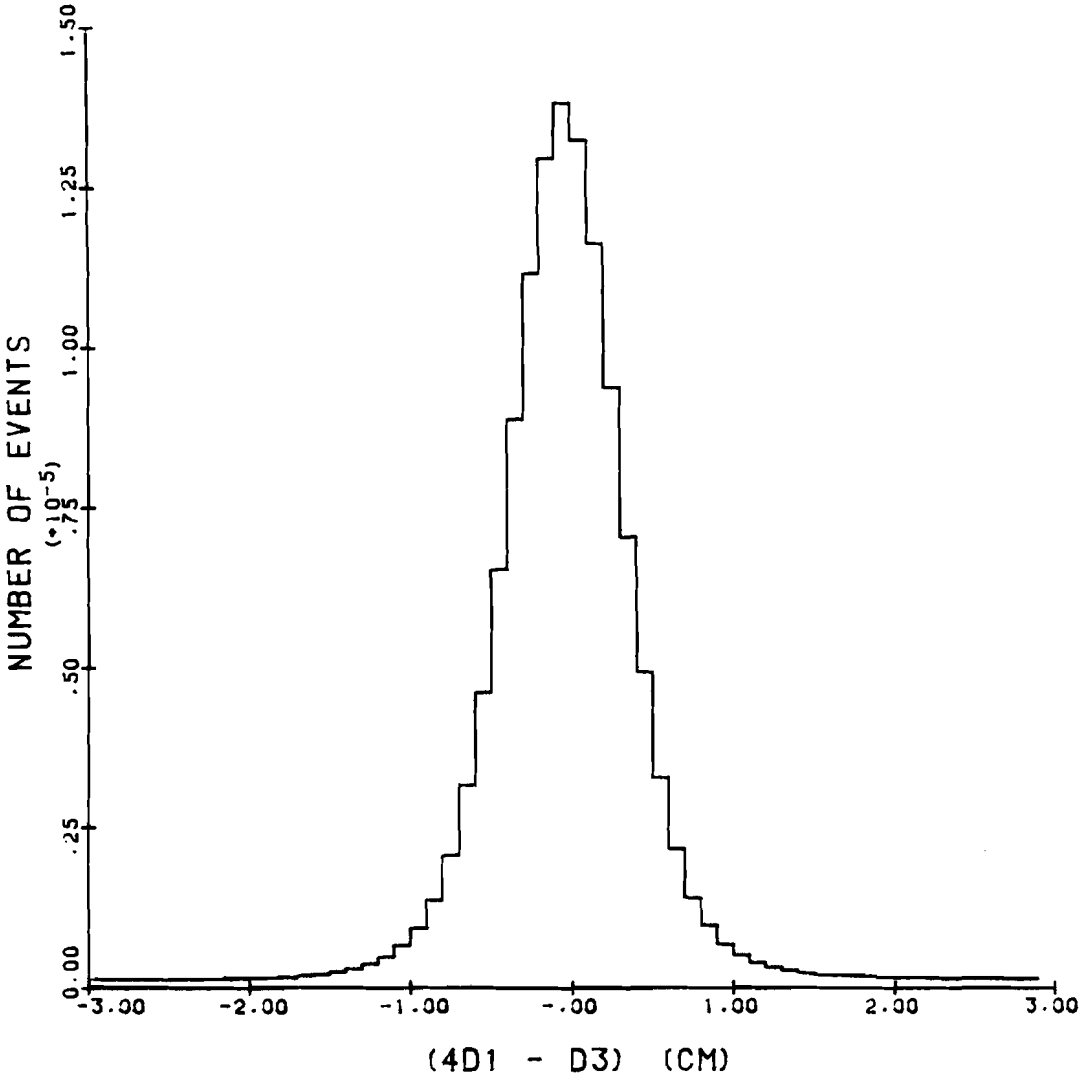

Figure 13. The quantity $(4 \cdot \Delta_1 - \Delta_3)$, described in the text, before cuts.

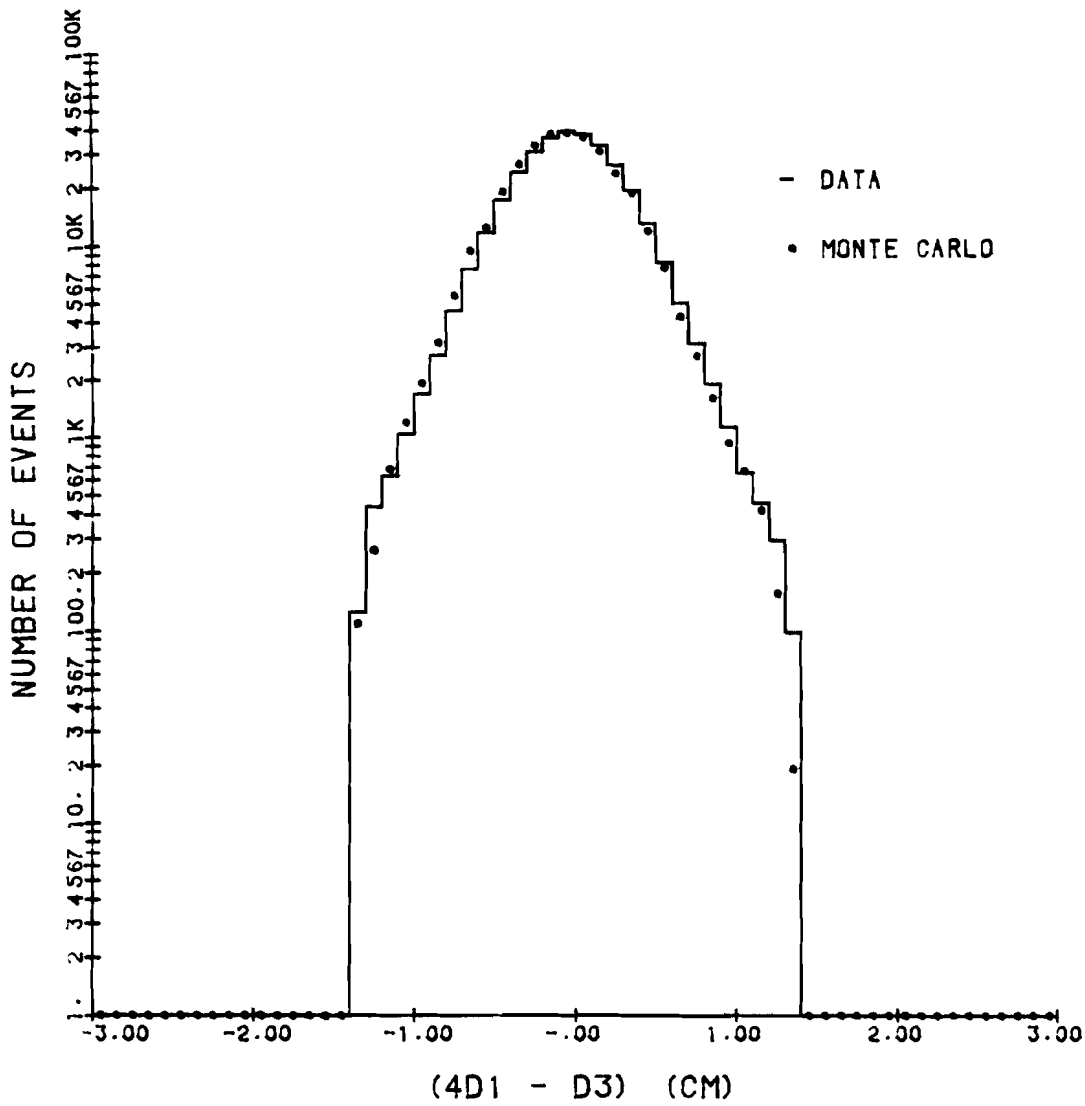

Figure 14. The quantity $(4 \cdot \Delta_1 - \Delta_3)$, described in the text, for the final sample of e^+e^- pairs, compared to Monte Carlo generated e^+e^- events.

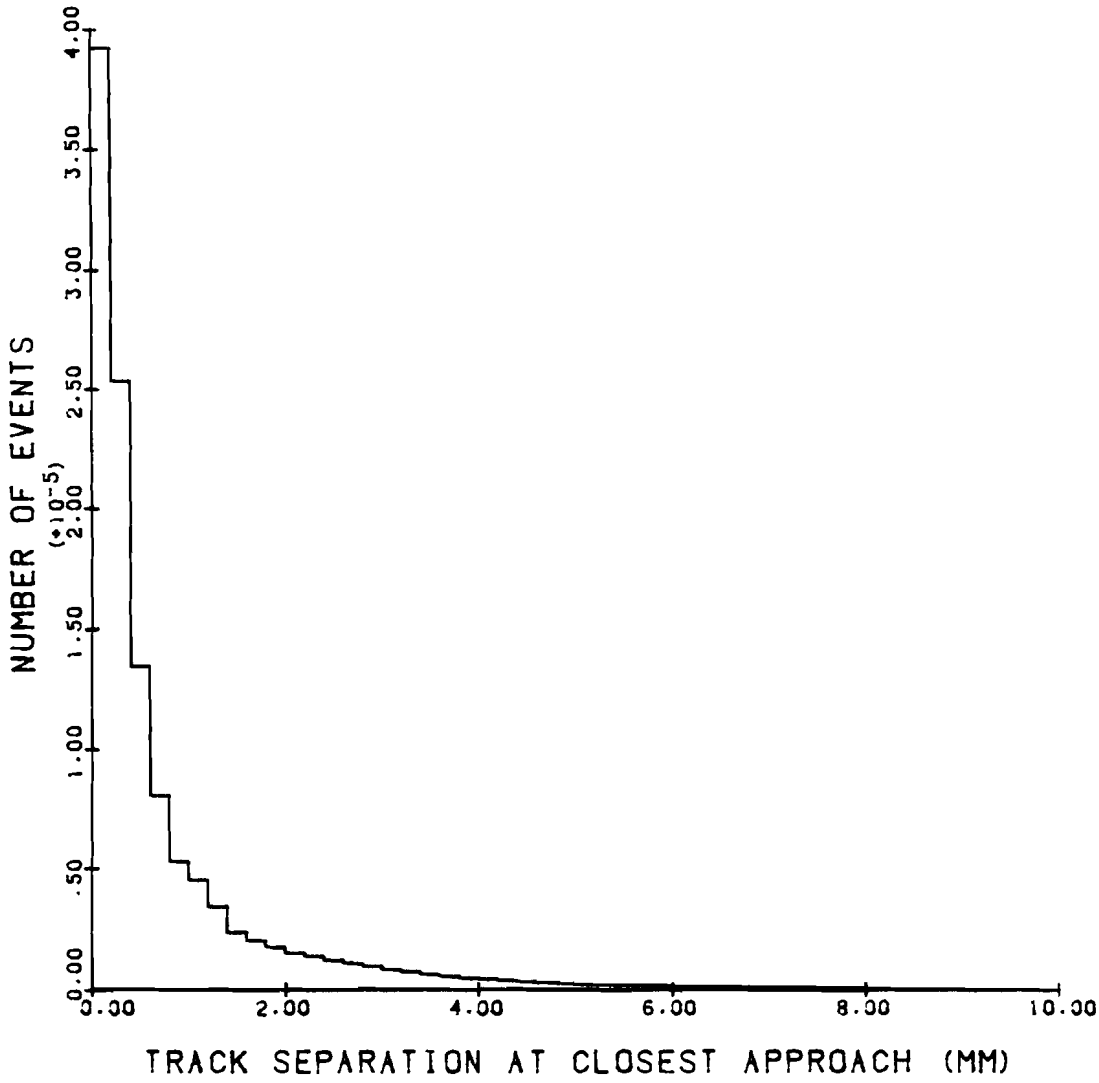

Figure 15. Separation of the two tracks at their closest approach, before the cut.

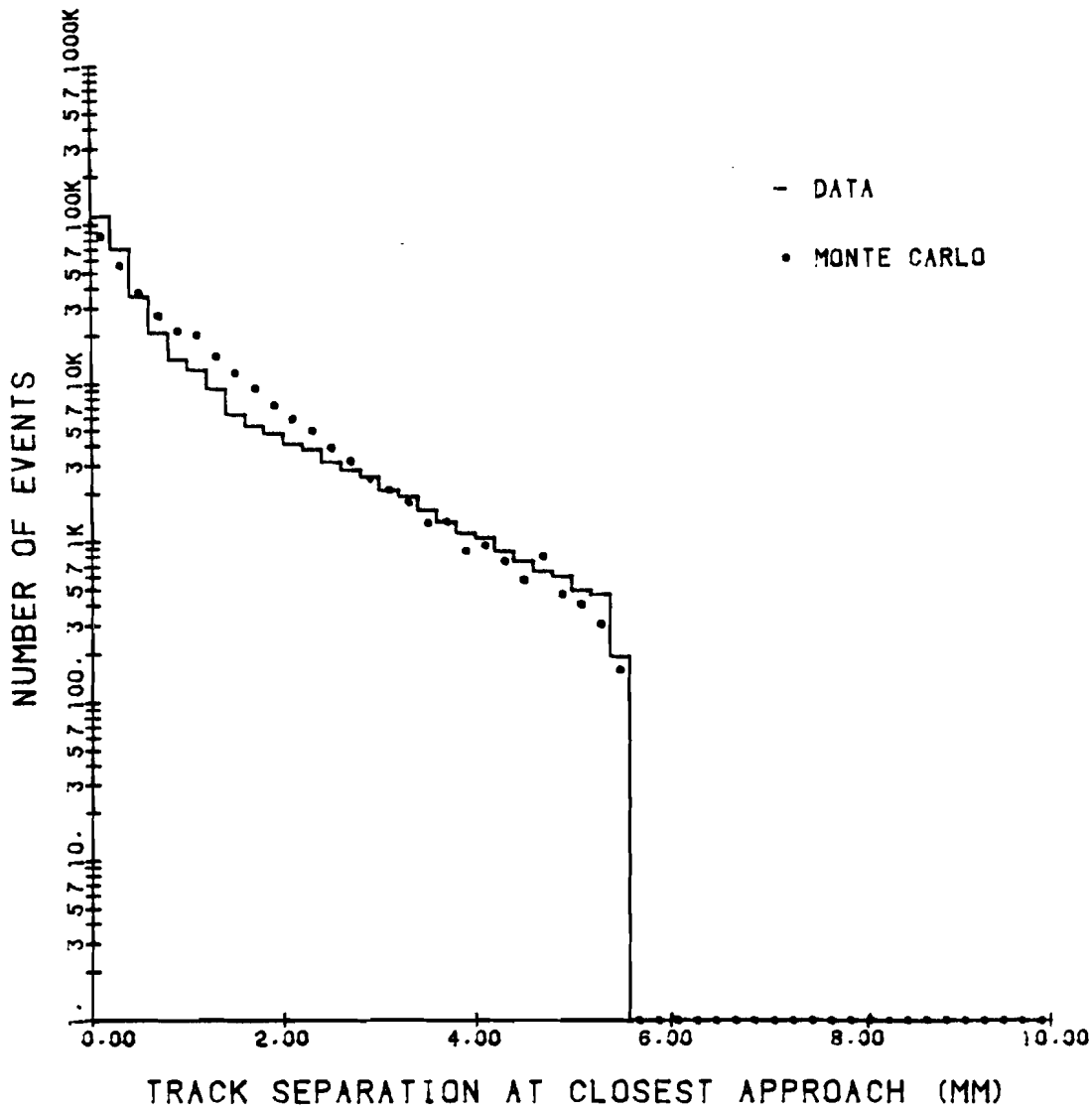

Figure 16. Separation of the two tracks at their closest approach, for the final sample of e^+e^- pairs, compared to Monte Carlo generated e^+e^- events.

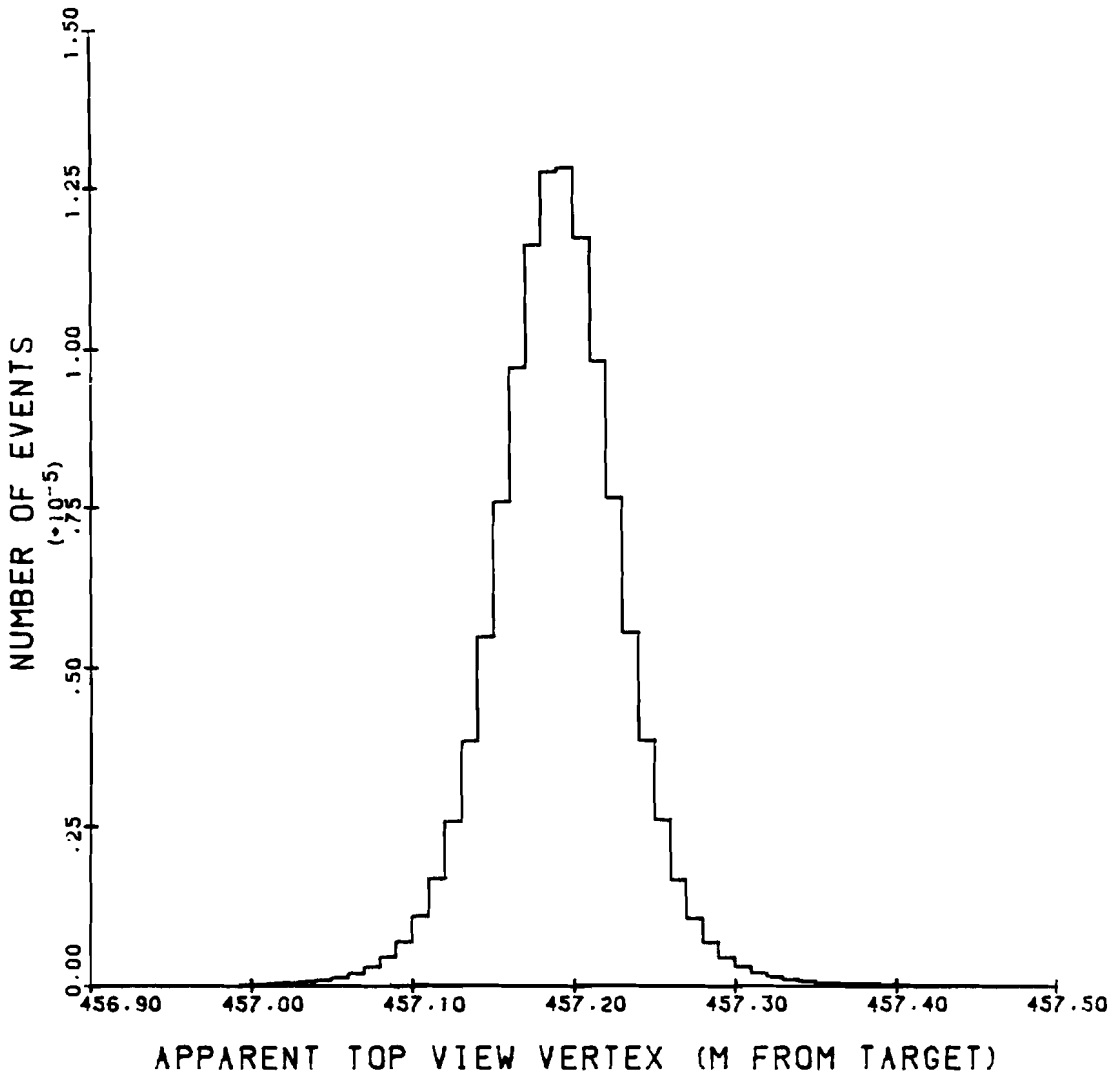

Figure 17. Z of the vertex of the "V" formed by two tracks, before cuts.

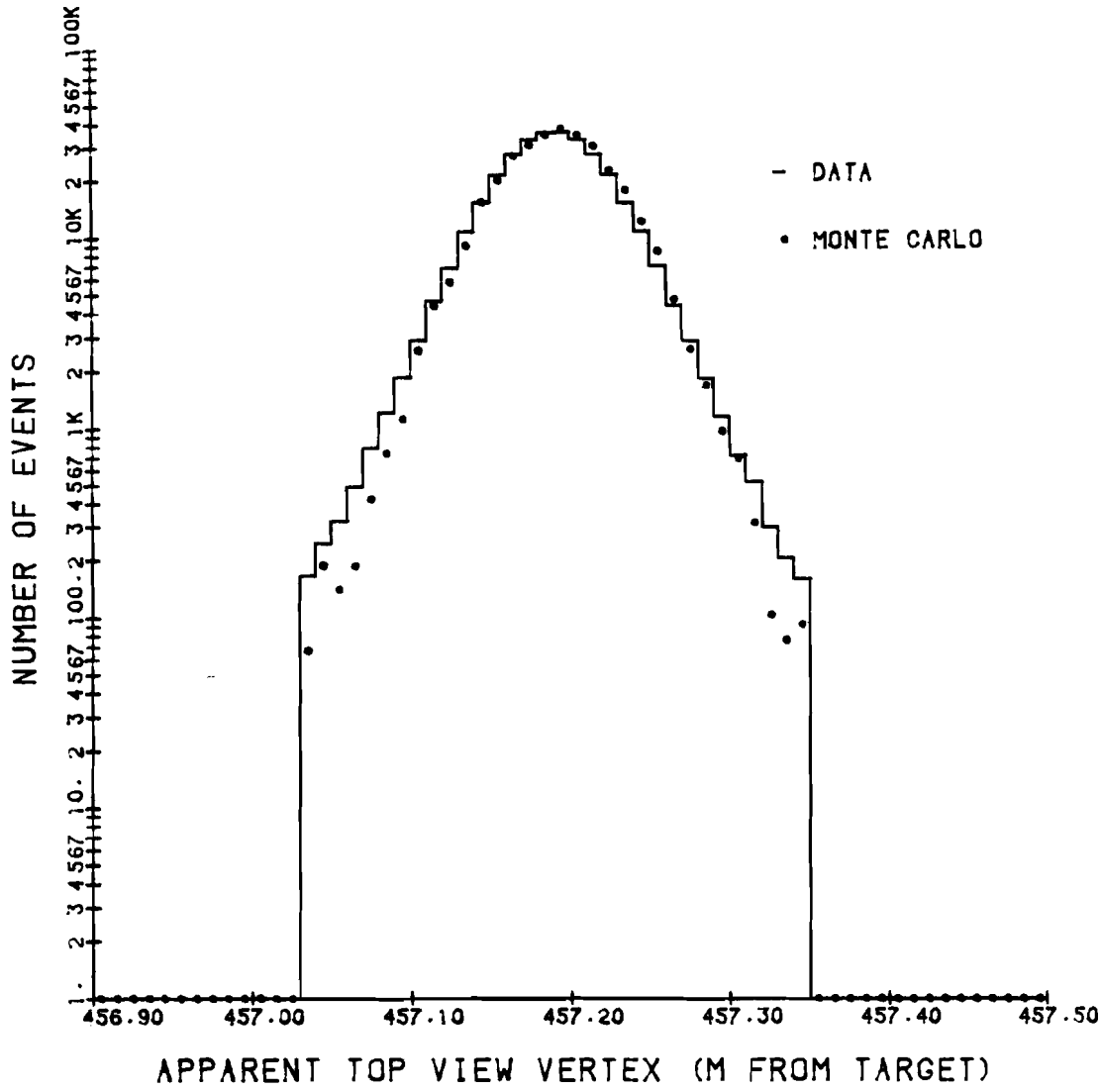

Figure 18. Z of the vertex of the "V" formed by two tracks, for the final sample of e^+e^- pairs, compared to Monte Carlo generated e^+e^- events.

4:1 cut owing to the "leverage" each track has in shifting this point. The agreement between data and Monte Carlo signified that the momenta of the two tracks were computed properly and that the relative positions of the chambers and magnets, as well as the field maps, were correctly entered in the Monte Carlo and analysis programs.

The closeness of the particle trajectories as seen from the side was judged on the basis of both the minimum and maximum track separations at the chambers. The side view maximum track separation is shown in Figures 19 and 20; the minimum separation in Figures 21 and 22. The two side view track projections were required to be within 3.33 cm of each other everywhere between chambers 1 and 5, and to be as close as 4.8 mm somewhere in the same region.

The three classes of cuts discussed so far selected events with two-track trajectories in the spectrometer characterizing foil events. All the events that remained at this stage were subjected to both pi-mu atom and e^+e^- pair cuts. Particle identification cuts separated pi-mu atoms from e^+e^- pairs. Subsequent cuts reduced backgrounds.

The separation of pi-mu atoms from e^+e^- pairs began with a loose requirement on the trigger. Recall that each event record on tape included a binary word reflecting which of the three two-track triggers had been satisfied.

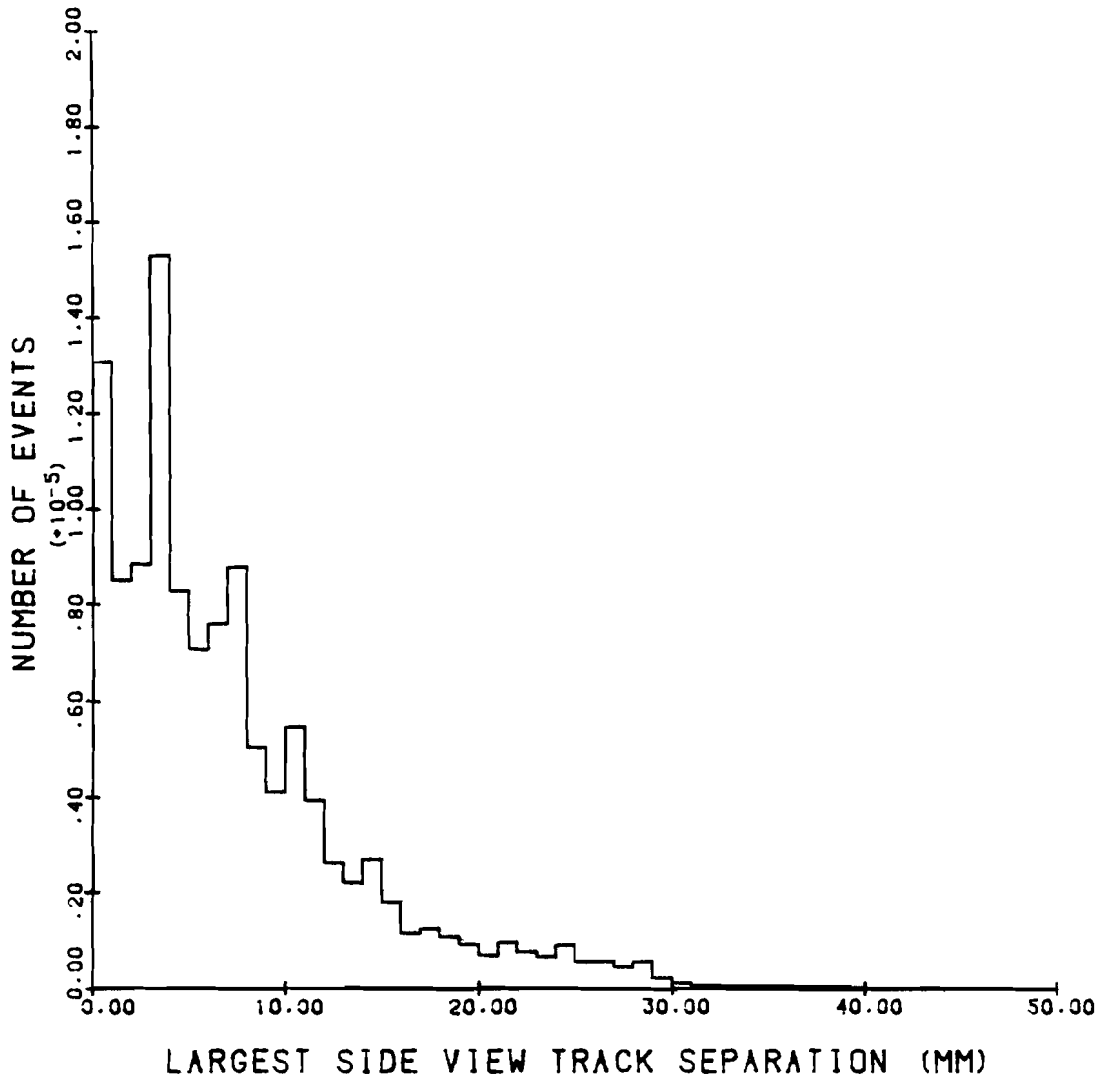

Figure 19. Largest side view separation of tracks, before the cut. The spikes are at multiples of wire spacings.

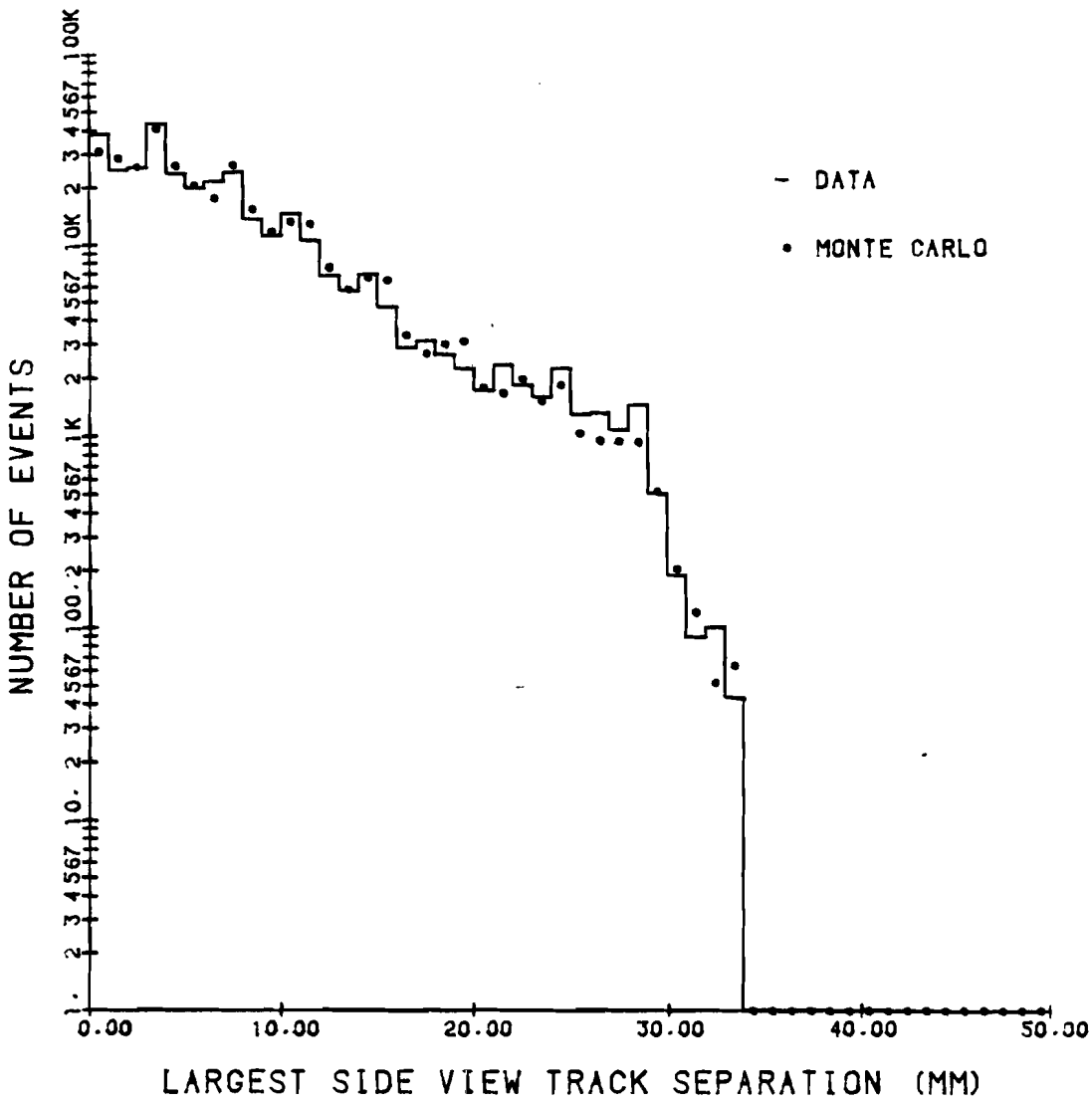

Figure 20. Largest side view separation of tracks, for the final sample of e^+e^- pairs, compared to Monte Carlo generated e^+e^- events.

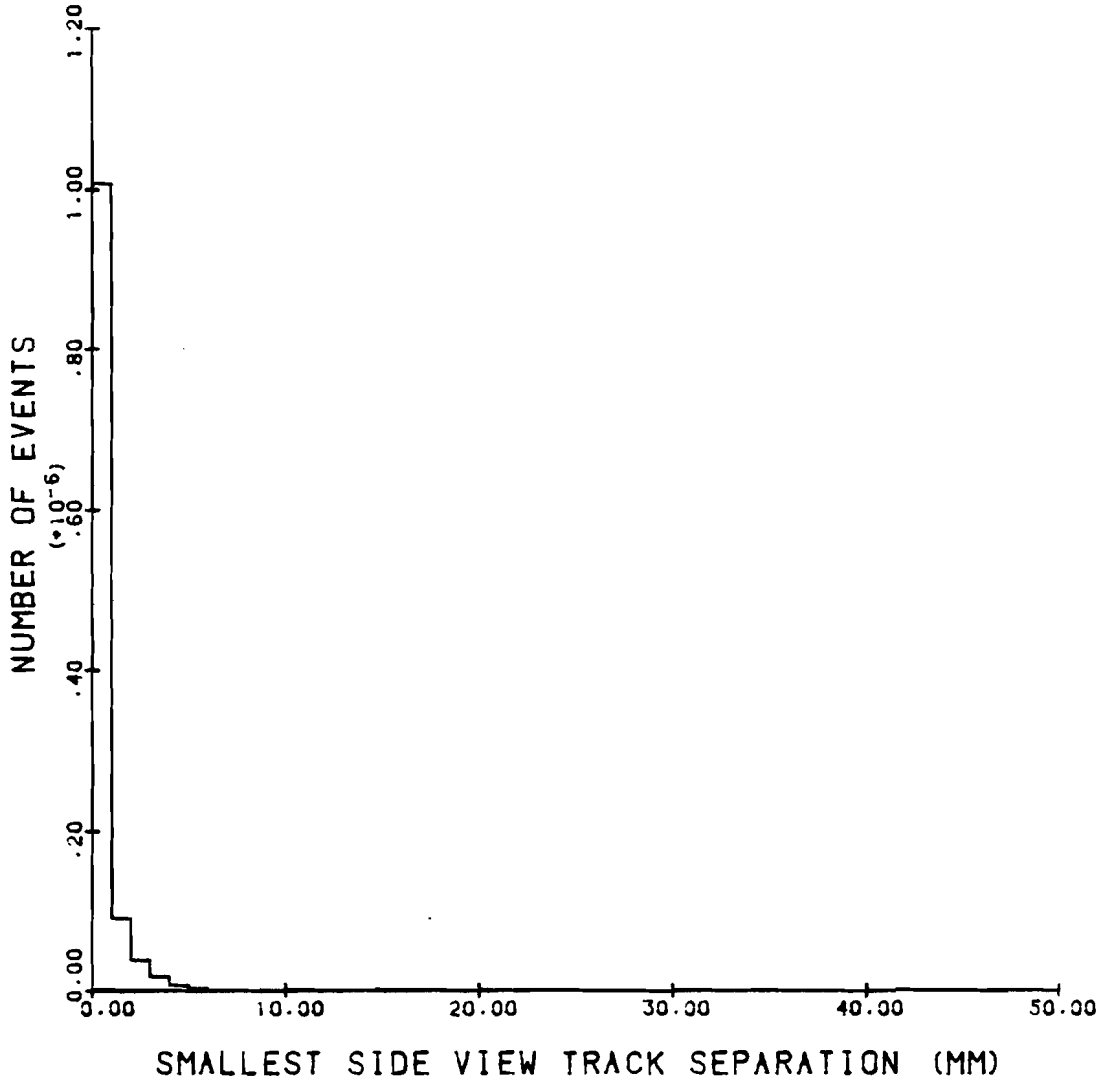

Figure 21. Smallest side view separation of tracks, before the cut.

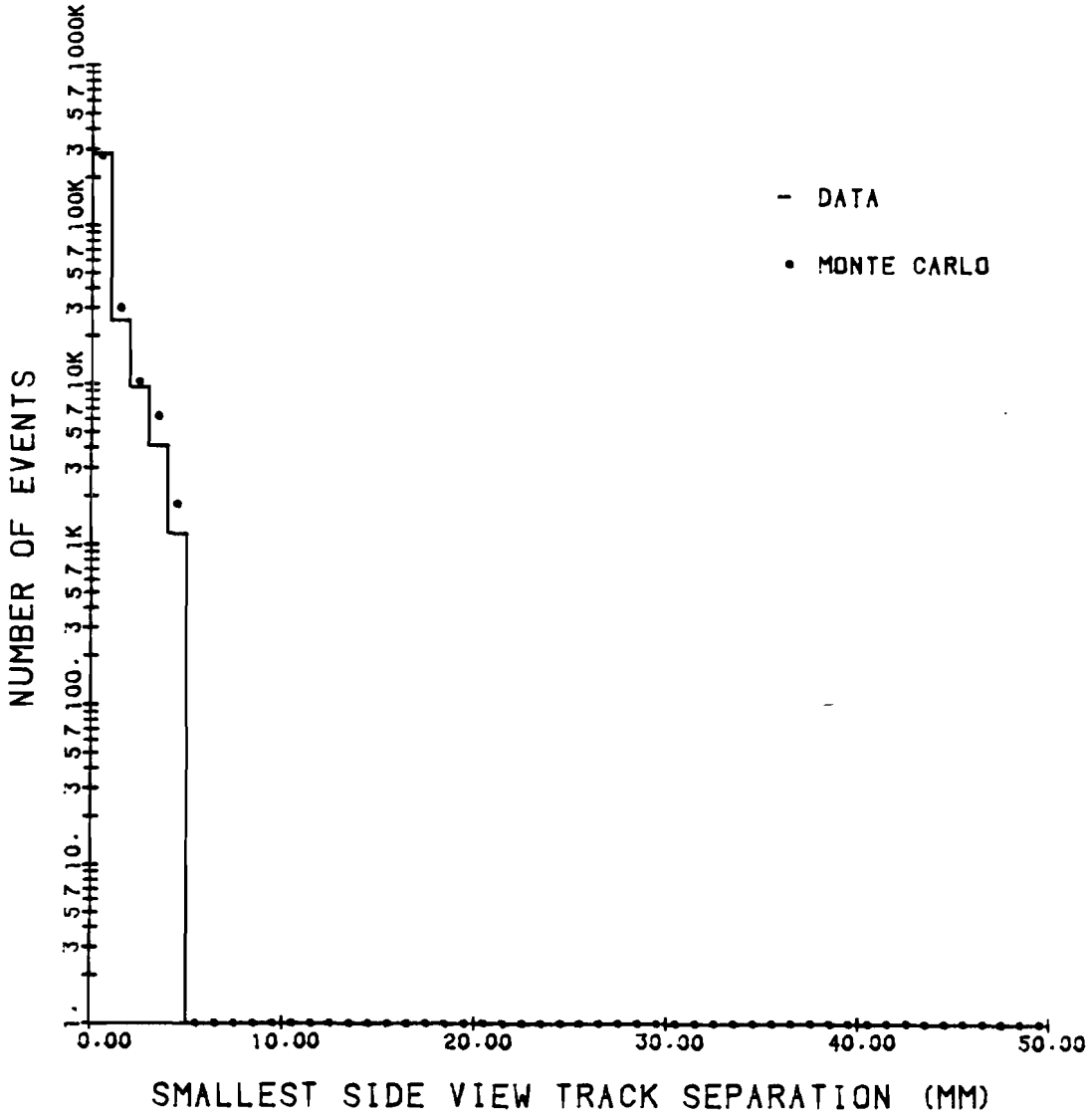

Figure 22. Smallest side view separation of tracks, for the final sample of e^+e^- pairs, compared to Monte Carlo generated e^+e^- events.

If only the e^+e^- trigger had been fulfilled, the event did not qualify as a pi-mu atom. Conversely, if the e^+e^- trigger had not registered but some other had, the event did not qualify as an e^+e^- pair.

The energy deposited in the shower counters divided by the momentum was calculated for each track, as shown above. Pi-mu atoms were required to have at least one particle fulfill the muon criterion, $FRAC_n \leq 0.2$. Also, if either satisfied the electron criterion, $FRAC_n \geq 0.6$, the event was discarded. The cuts were made in this fashion so as not to exclude events with a pion that deposited a substantial fraction of its energy in the shower counters. In cases where the two tracks pointed to the same counter, $FRAC_{total} \leq 0.3$ was required. A histogram of $FRAC_n$ before the pi-mu atom shower counter cuts is shown in Figure 23. The parameter α, defined in Chapter 4 as the difference of the pion and muon momenta divided by their sum, is shown in Figure 24 before the pi-mu atom shower counter cuts were made. The muon track was assumed to be the one which projected nearest a hit muon counter. The effect of the cut is apparent in Figure 25. The events removed were e^+e^- pairs with a hit muon counter in accidental coincidence. (These muons could have been cosmic ray muons or muons from K_L^o decays occurring in the beam beneath the spectrometer.) A clear signal at $\alpha = 0.138$ attests to the detection of

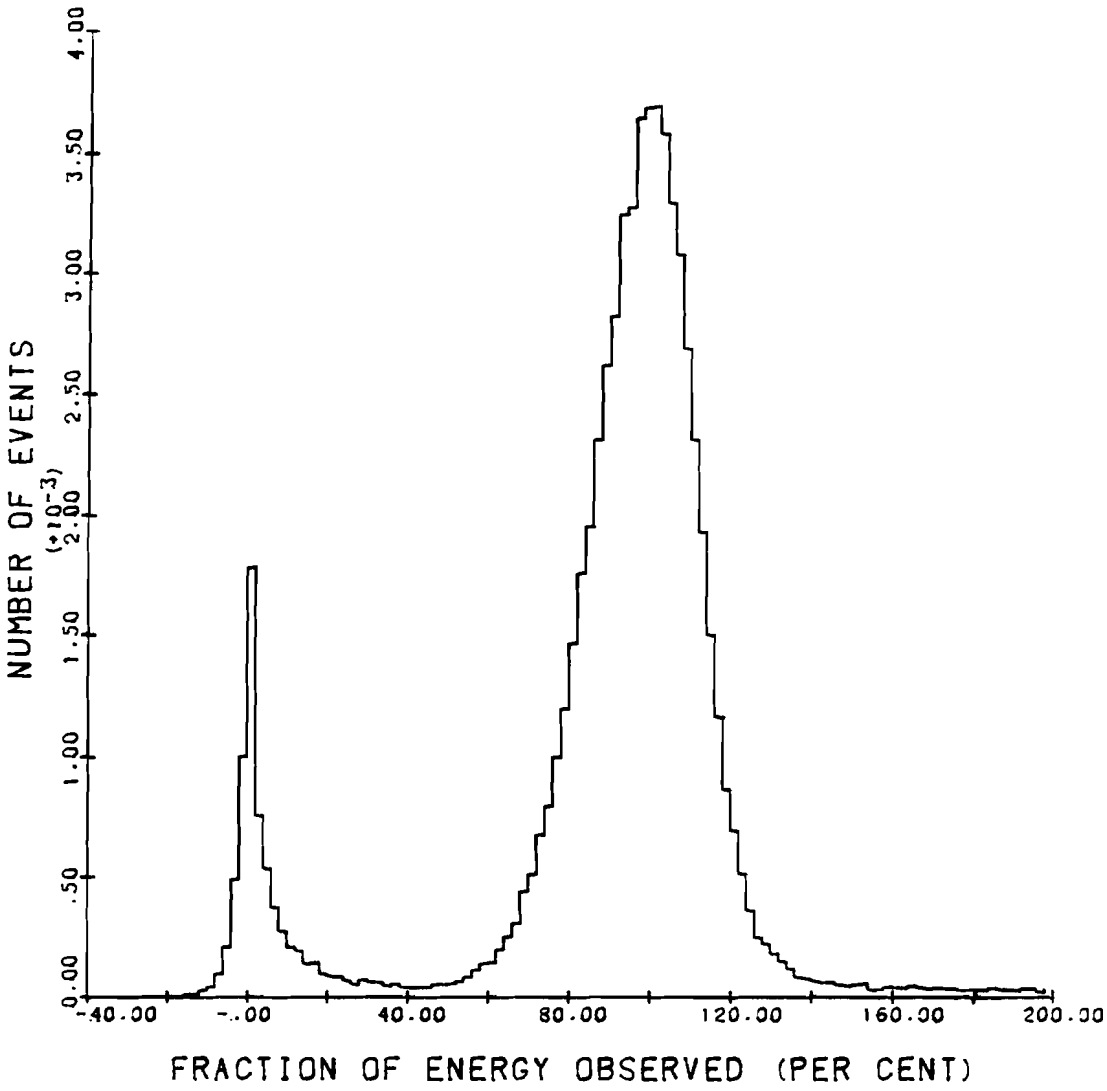

Figure 23. Fraction of a particle's energy observed in the shower counters, for tracks of pi-mu atom candidates.

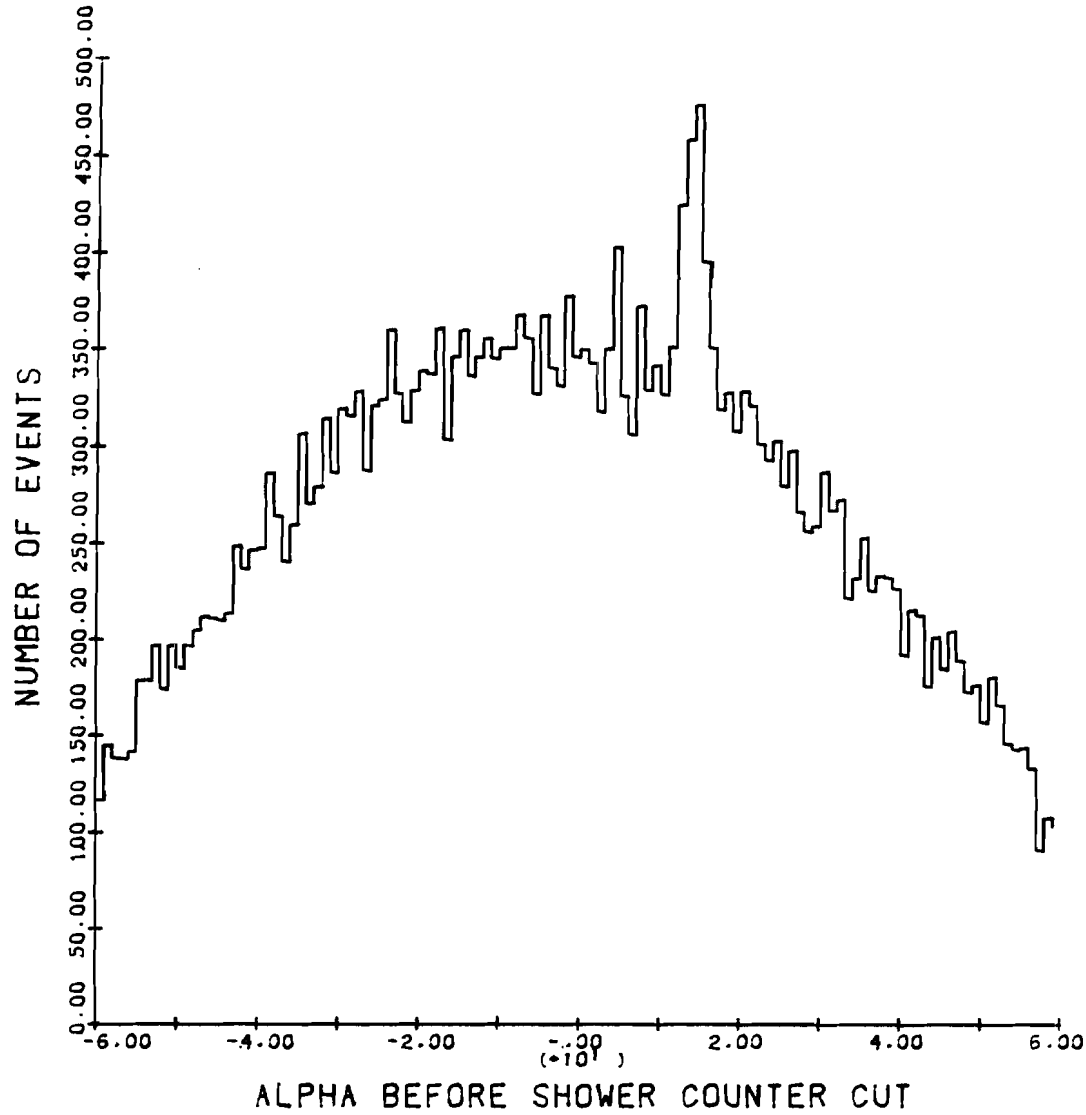

Figure 24. The variable $\alpha=(p_\pi-p_\mu)/(p_\pi+p_\mu)$, for pi-mu atom candidates, before shower counter cuts.

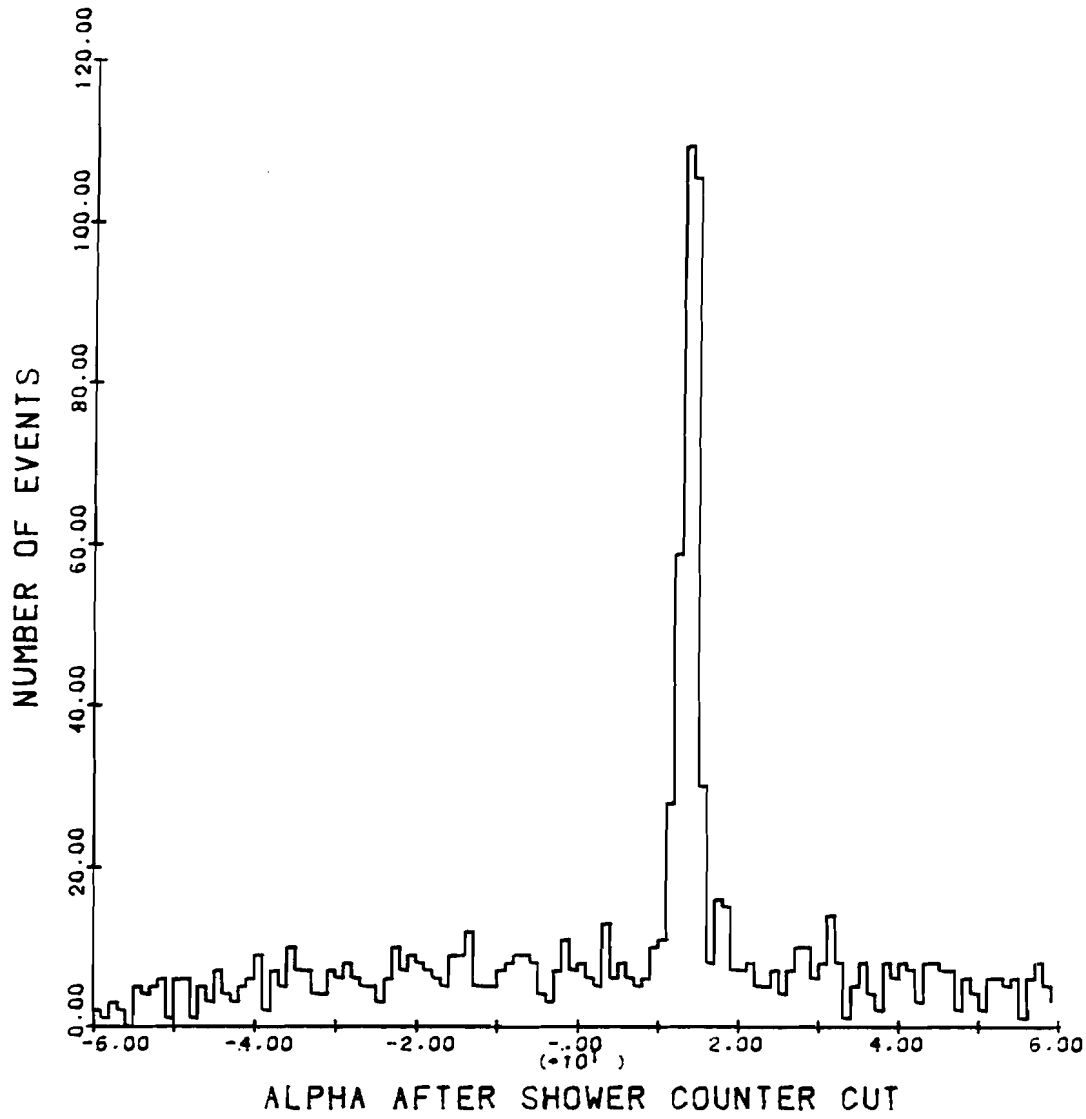

Figure 25. The variable $\alpha=(p_\pi-p_\mu)/(p_\pi+p_\mu)$, for pi-mu atom candidates, after shower counter cuts.

pi-mu atoms. A smaller peak at $\alpha = -0.138$ also contains pi-mu atoms in which the pion was mislabeled a muon and vice versa.

For e^+e^- pairs, the corresponding shower counter requirement was simply that the fraction of each particle's momentum appearing as energy equal or exceed 0.6, i.e. $FRAC_n \geq 0.6$ or $FRAC_{total} \geq 0.6$.

Most of the remaining cuts were relatively insignificant, yet they were necessary for an unambiguous comparison of pi-mu atoms and e^+e^- pairs with Monte Carlo and $K_{\mu 3}$ events.

For both pi-mu atoms and e^+e^- pairs, the next cut was a kinematic one. Pi-mu atoms had to have transverse momenta (with respect to the beam direction) between 2 MeV/c and 210 MeV/c, as shown in Figure 26. The lower limit was an acceptance cut-off from the fixed height of the spectrometer above the beam. (Recall from Chapter 4 that the p_t distribution also vanishes as $p_t \rightarrow 0$.) The upper cut was placed just above the kinematic maximum for pi-mu atoms. The background removed by this cut consisted primarily of $K_{\mu 3}$ events for which only one side view track was found, due to inefficiencies in the wire planes. For e^+e^- pairs, the invariant mass of the pair was computed. The calculation depended upon knowing the momenta of the two particles and their directions at the foil. Hence, it

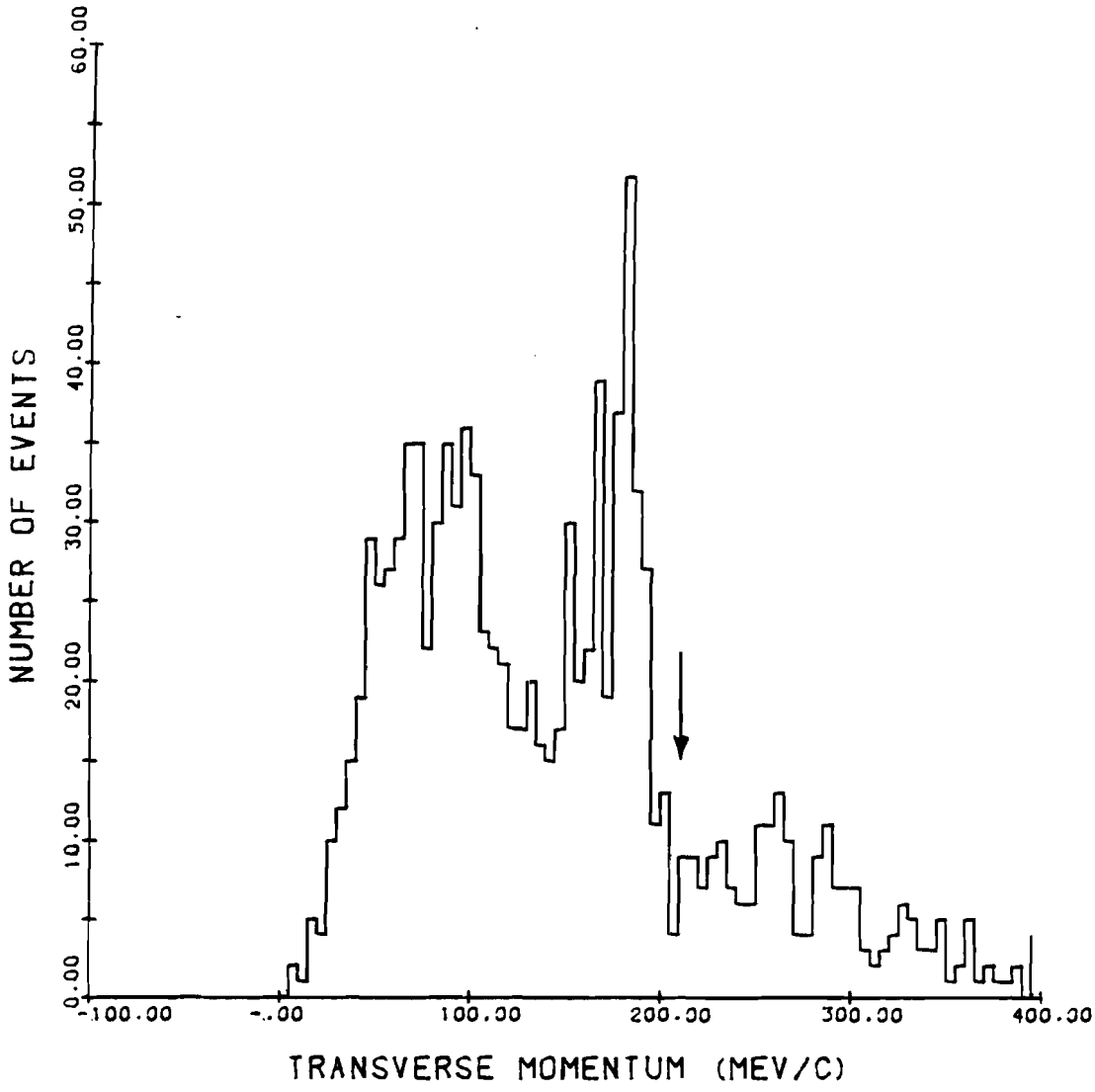

Figure 26. Transverse momentum spectrum of pi-mu atom candidates, before cuts.

was sensitive to tracking back through the horizontally bending pair of magnets just downstream of the foil. The distribution is shown in Figure 27. Events above 35 MeV/c^2 were thrown out.

Pi-mu atoms and the photons that gave rise to the observed e^+e^- pairs were then required to have originated in the beam. The vector sum of the momenta of the two tracks (at the entrance to the horizontally bending magnets) defined the momentum of the atom or the photon. The K_L^o decay point was then assumed to be the midpoint of the segment joining the points of intersection of the atom or photon trajectory with the pyramid describing the beam. The pyramid had its apex at the target and base at the beam dump. Its rectangular cross section at any Z was determined by the collimator settings for the data run being analyzed. Any event for which the K_L^o decay point could be computed in this way thereby satisfied the beam requirement. In case the reconstructed atom or photon trajectory did not intercept this pyramid, owing to the finite position resolution of the spectrometer, the decay point was taken to be the point on the trajectory which was closest to the beam center line. Cuts were then placed separately on the X and Y components of that distance, according to collimator size and distance from the target. (Only a few percent of the events fell in the latter

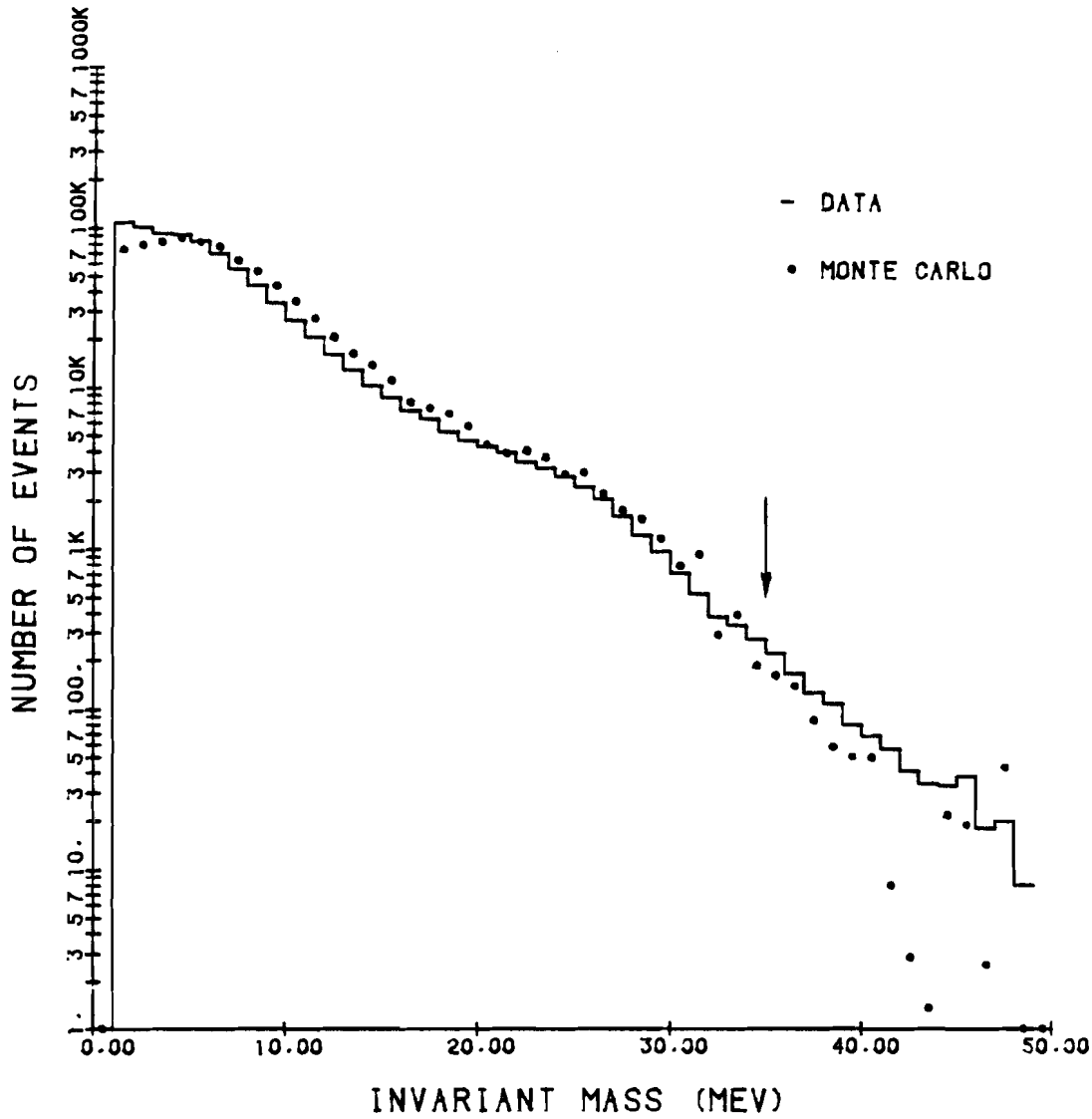

Figure 27. Invariant mass of e^+e^- pairs, compared to Monte Carlo generated e^+e^- events, before the cut.

category.)

Events were then discarded which appeared to originate too far upstream or downstream to be valid decays. The acceptable region in Z for pi-mu atoms was chosen to be 150 m to 440 m. The cut at 150 m was made far upstream of the actual beginning of the decay region at 212 m because of the poor Z resolution for events coming from far upstream. A histogram of the Z distribution before these cuts were applied is shown in Figure 28. Identical upstream and downstream cuts were made for e^+e^- pairs. In addition, events coming from the region in Z between 285 m and 350 m were discarded. As Figure 29 shows, there was a large background of photons coming from the vicinity of 310 m. (The figure has only events with $p_t > 160$ MeV/c. The background was not as pronounced for the entire e^+e^- pair sample.) These events were associated with the right half of the beam, and were present only in data runs with the collimators opened wide in the horizontal direction. The background was therefore associated with the halo of the beam scraping the walls of the vacuum pipe near the sag at 300 m (see Figure 3). The Z distribution for photons after all cuts is displayed in Figure 30. One other special beam-related cut applied to photons eliminated e^+e^- pairs that came from conversions in the thick horizontal aluminum support rods for the foils. (These events peak at about

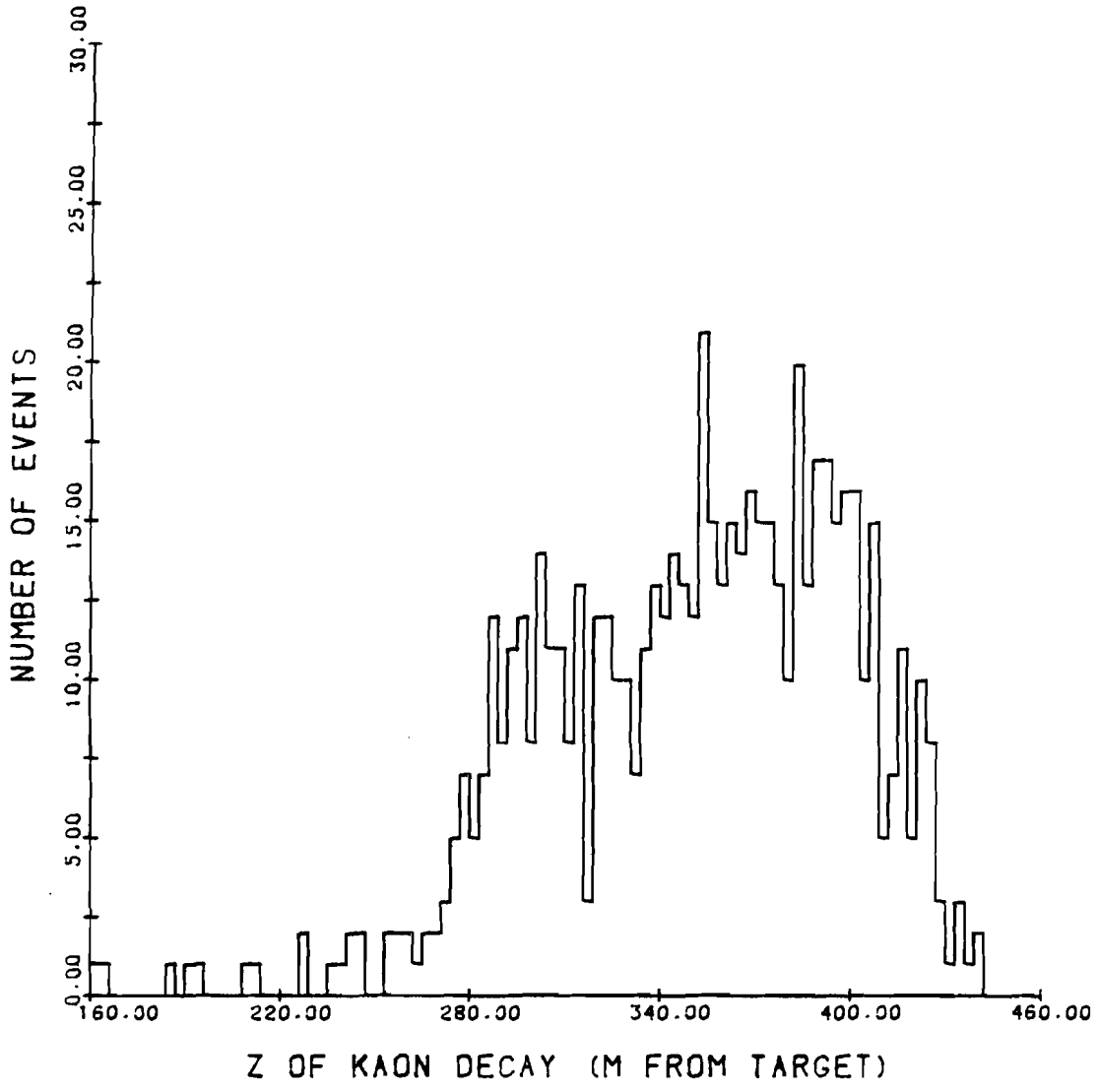

Figure 28. Z position of the K_L^o decay, for pi-mu atom candidates, before cuts.

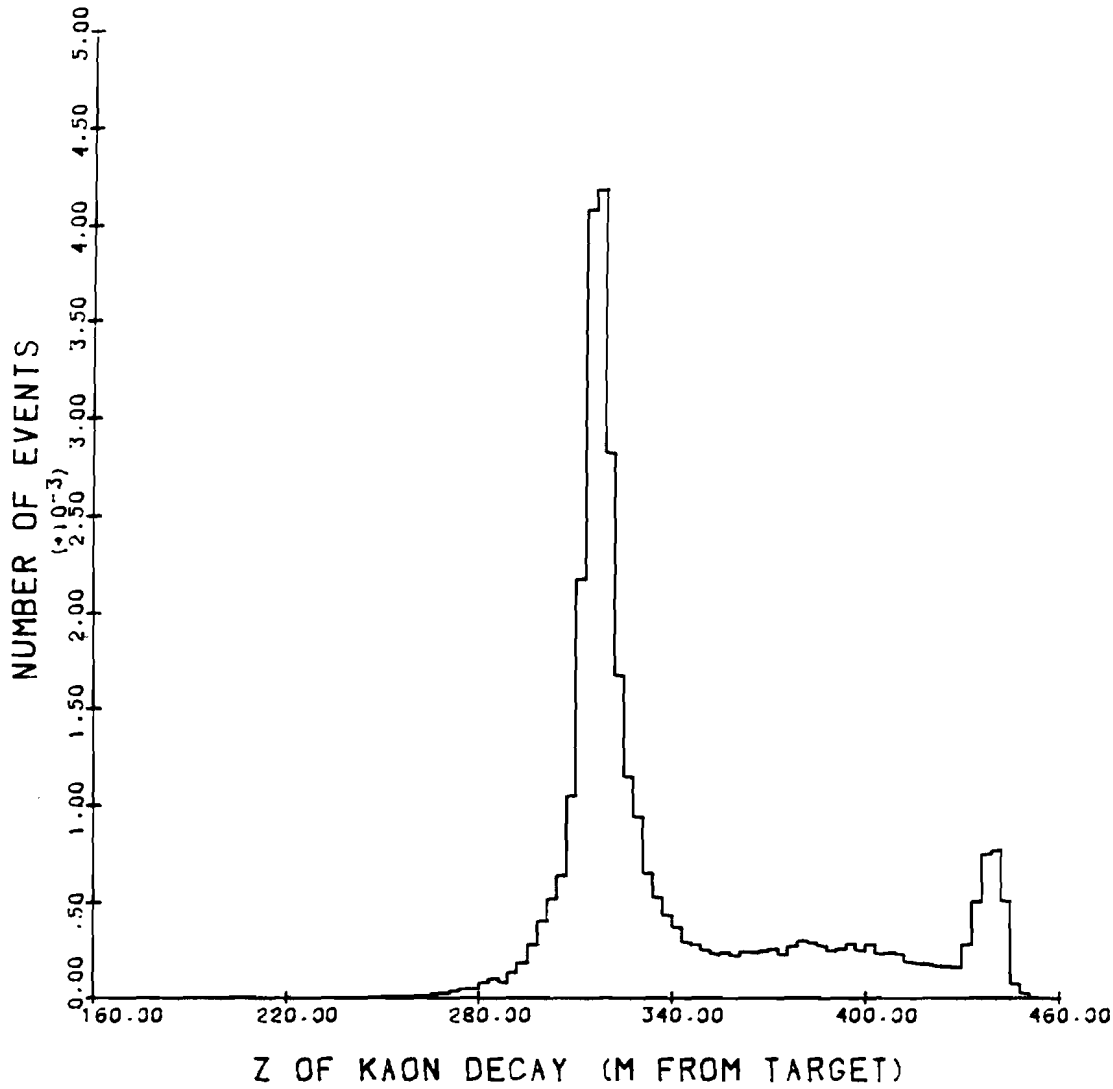

Figure 29. Z position of the K_L^0 decay, for e^+e^- pairs with p_t > 160 MeV/c, before cuts.

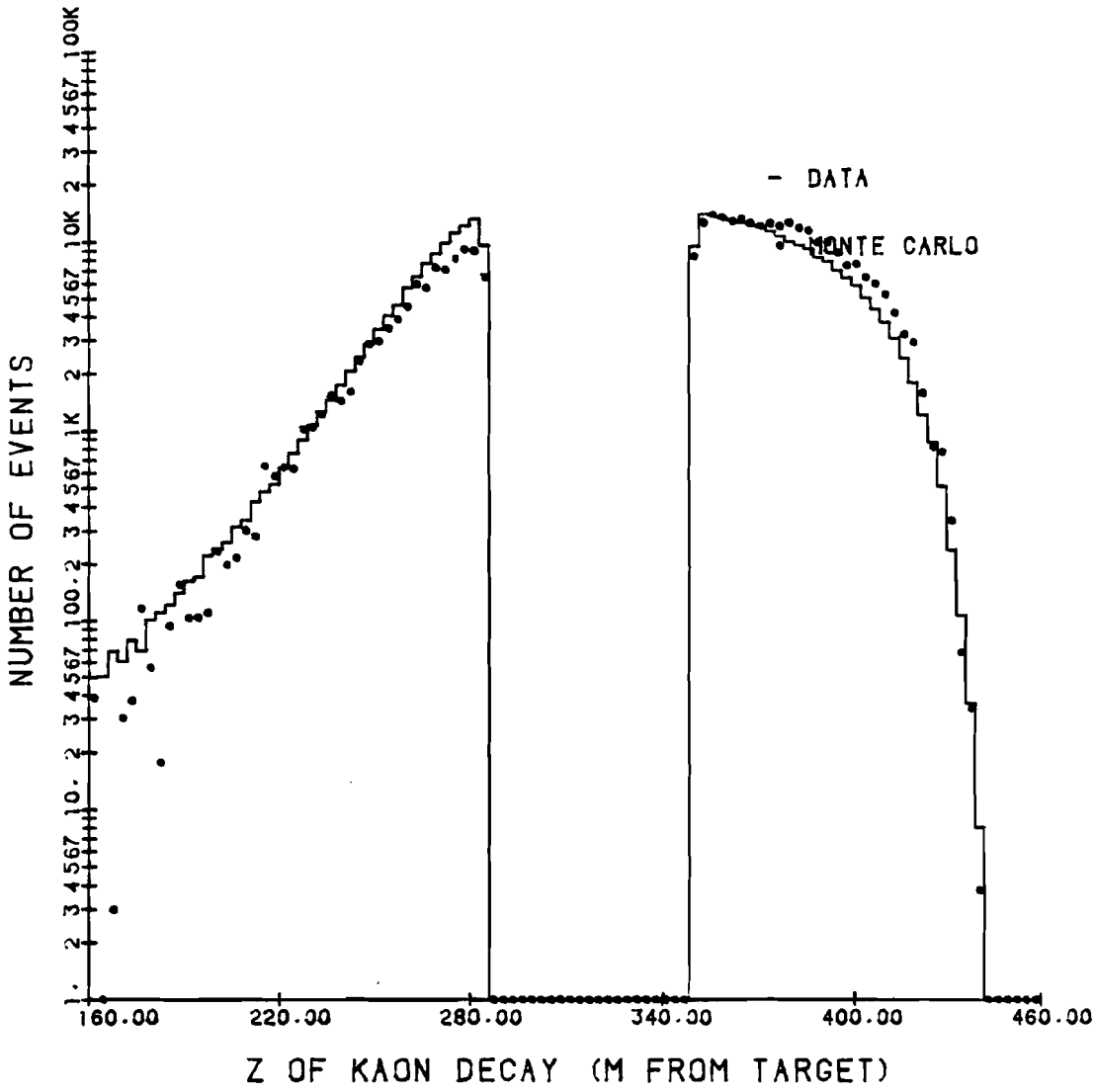

Figure 30. Z position of the K_L^o decay, for the final sample of e^+e^- pairs, compared to Monte Carlo generated e^+e^- events.

437 m in Figure 29.) Photons which intersected the foil below 0.21 m in the Y direction were cut, as illustrated in Figure 31.

The final two cuts applied to pi-mu atoms and e^+e^- pairs were a trigger cut and a fiducial volume cut.

Due to the uncertainty in the precise locations of edges of counters and MWPC's in the apparatus, only events were retained whose tracks came no closer than 4 mm to any edge. Unfortunately, this cut reduced the pi-mu atom and the e^+e^- pair samples by about 9%, yet it was deemed necessary for a trustworthy comparison of data to Monte Carlo. (The loss was primarily in chamber 2, which was considerably narrower, in the X direction, than chamber 1.)

Pi-mu atom candidates and e^+e^- pairs were discarded if they had more than one H counter hit or more than one W counter hit, in keeping with the fast trigger. For pi-mu atom candidates, each track had to point to the muon bank, and at least one of the counters had to have fired. Both pi-mu atoms and e^+e^- pairs were required to have satisfied their respective triggers as recorded in the trigger latch word: no events were lost on this cut. (Pi-mu atoms which might have been logged on the basis of the $K_{\mu 3}$ trigger would have had to be discarded, because those triggers had been prescaled by a factor of 32.) The recorded scintillation counter hits in the A and B banks were run

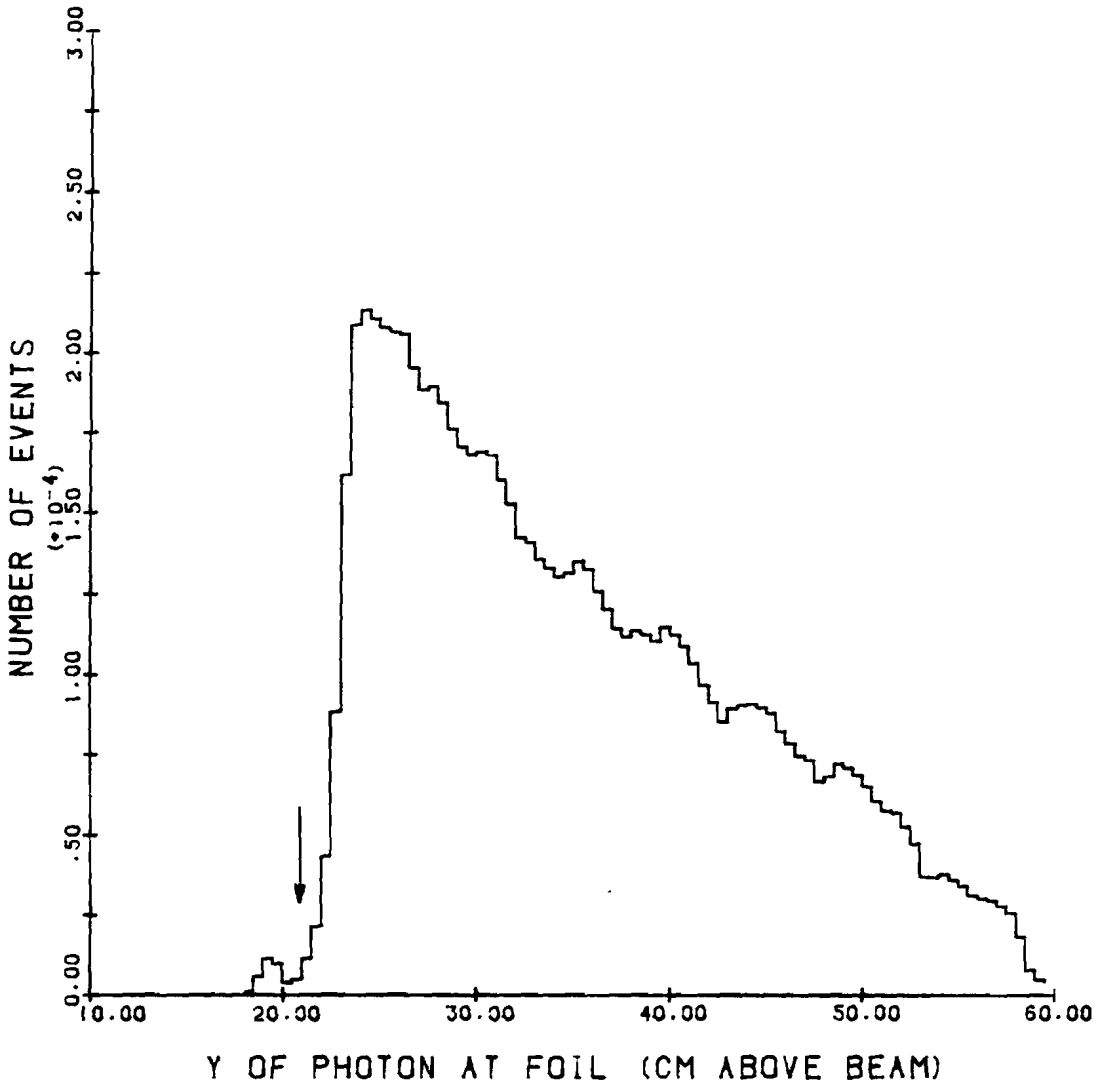

Figure 31. Y position of photons at the foil, before the cut.

through a simulation of the Track Correlator as well: no events were lost here either.

The events that remained after all cuts are shown in histograms of α for pi-mu atoms (Figure 32) and p_t for e^+e^- pairs (Figure 33). These events were obtained using the event reconstruction routine optimized for recovering pi-mu atoms and e^+e^- pairs. The signal at $\alpha = 0.138$ (defined by $0.09 \leq \alpha < 0.19$) has 314 pi-mu atoms with a background of 11. The p_t distribution, the Z position of the K_L^o decay point, and the momentum spectrum of pi-mu atoms are shown in Figures 34, 35, and 36. There are 309 events in these three figures, selected according to $|\alpha - 0.138| \leq 0.045$. (Of these, 165 are $\pi^+\mu^-$ atoms, and 144 are $\pi^-\mu^+$ atoms; the corresponding percentages for the Monte Carlo are 49.7% and 50.3%.) The momentum spectrum for photons is shown in Figure 37.

9.5.2 NON-FOIL EVENTS

The principal sources of non-foil events were $K_{\mu 3}$, K_{e3}, and $K_{\pi 3}$ decays. The selection of $K_{\mu 3}$ events and the study of $K_{\mu 3}$ backgrounds are described in greater detail elsewhere (ref. 35). The main points are reviewed here.

In order to select non-foil events, geometrical requirements complementary to those for foil events were

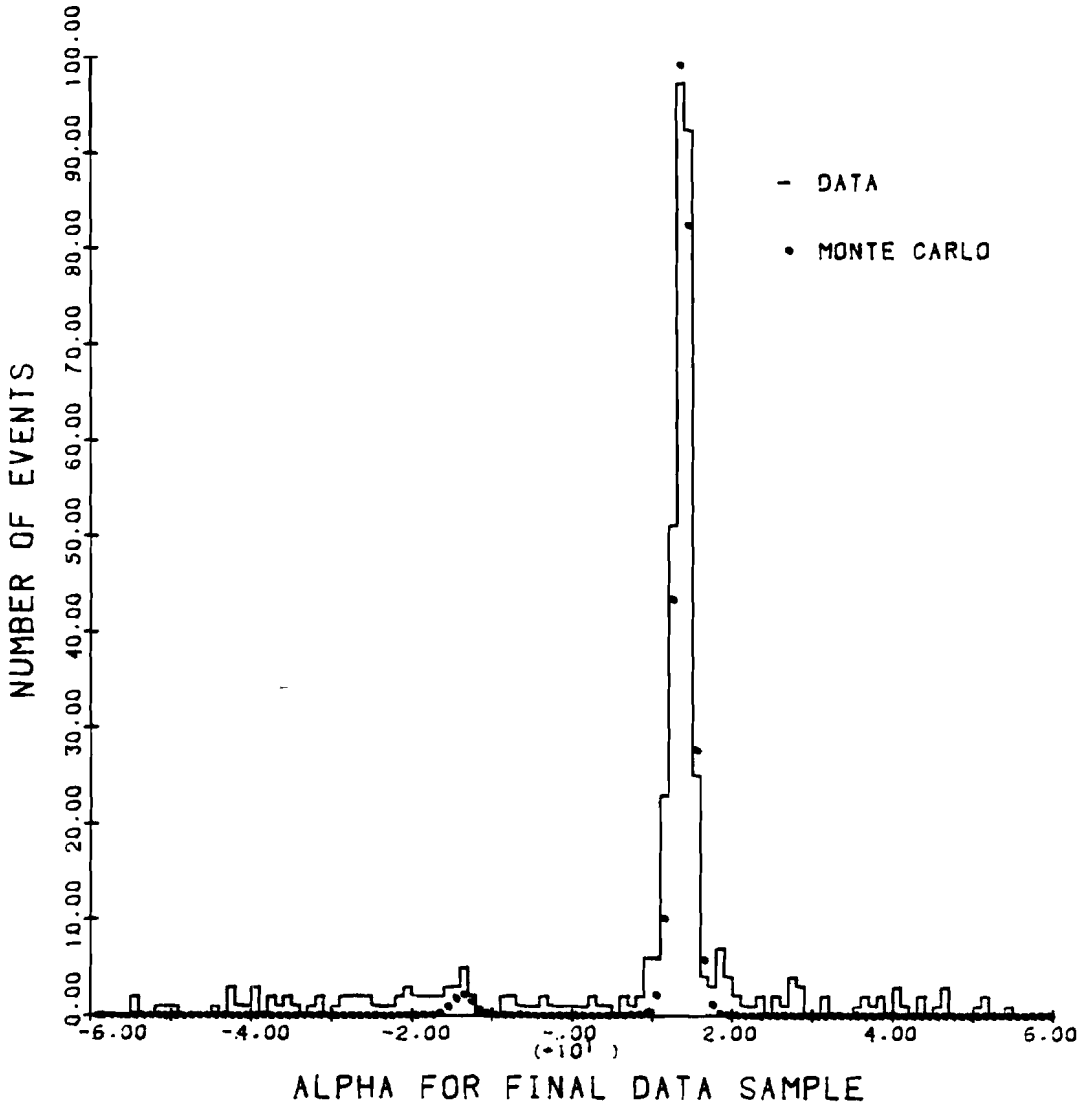

Figure 32. The variable $\alpha=(p_\pi-p_\mu)/(p_\pi+p_\mu)$, for the final sample of pi-mu atoms, compared to Monte Carlo generated pi-mu atoms.

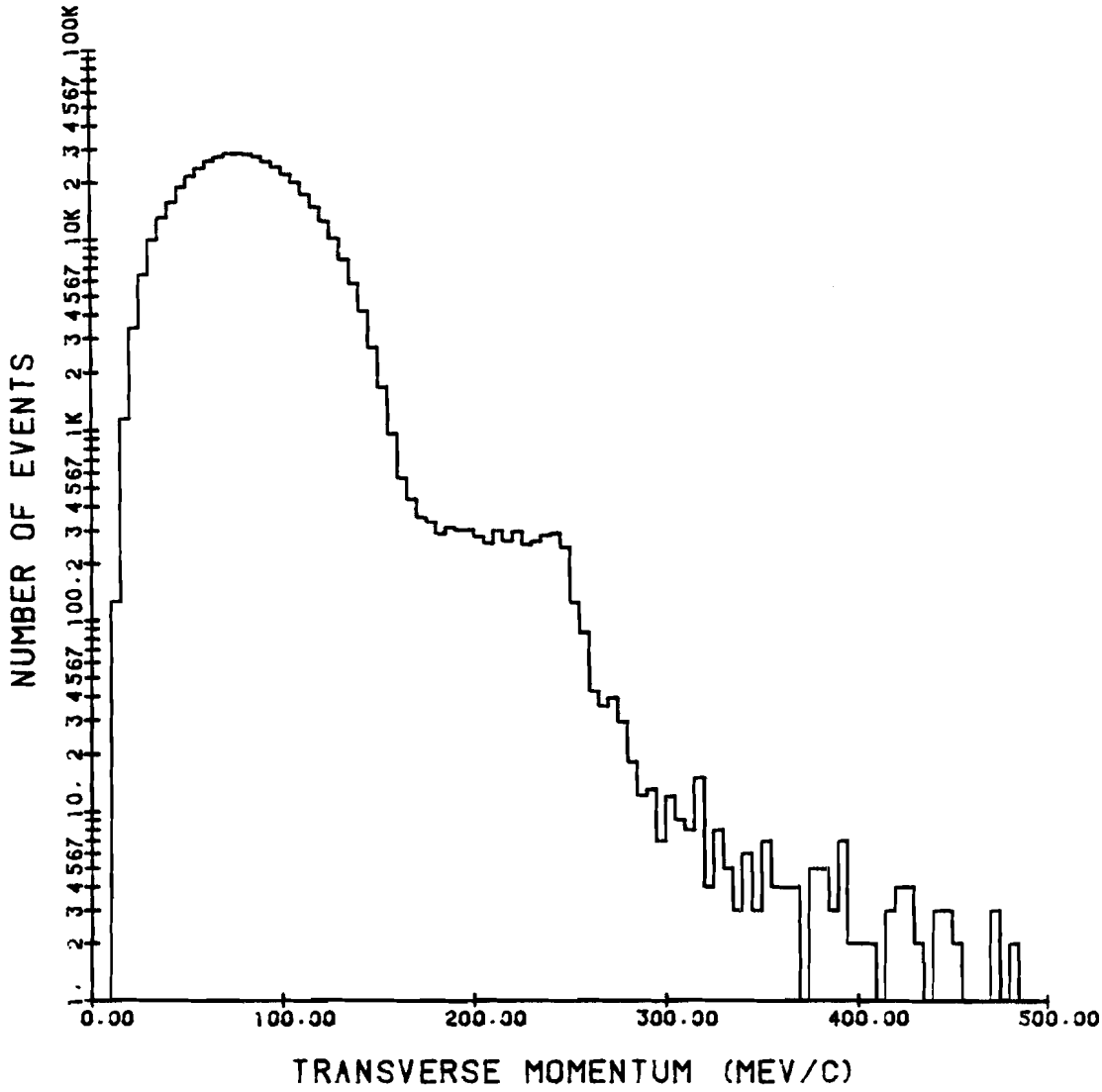

Figure 33. Transverse momentum of photons in the final sample.

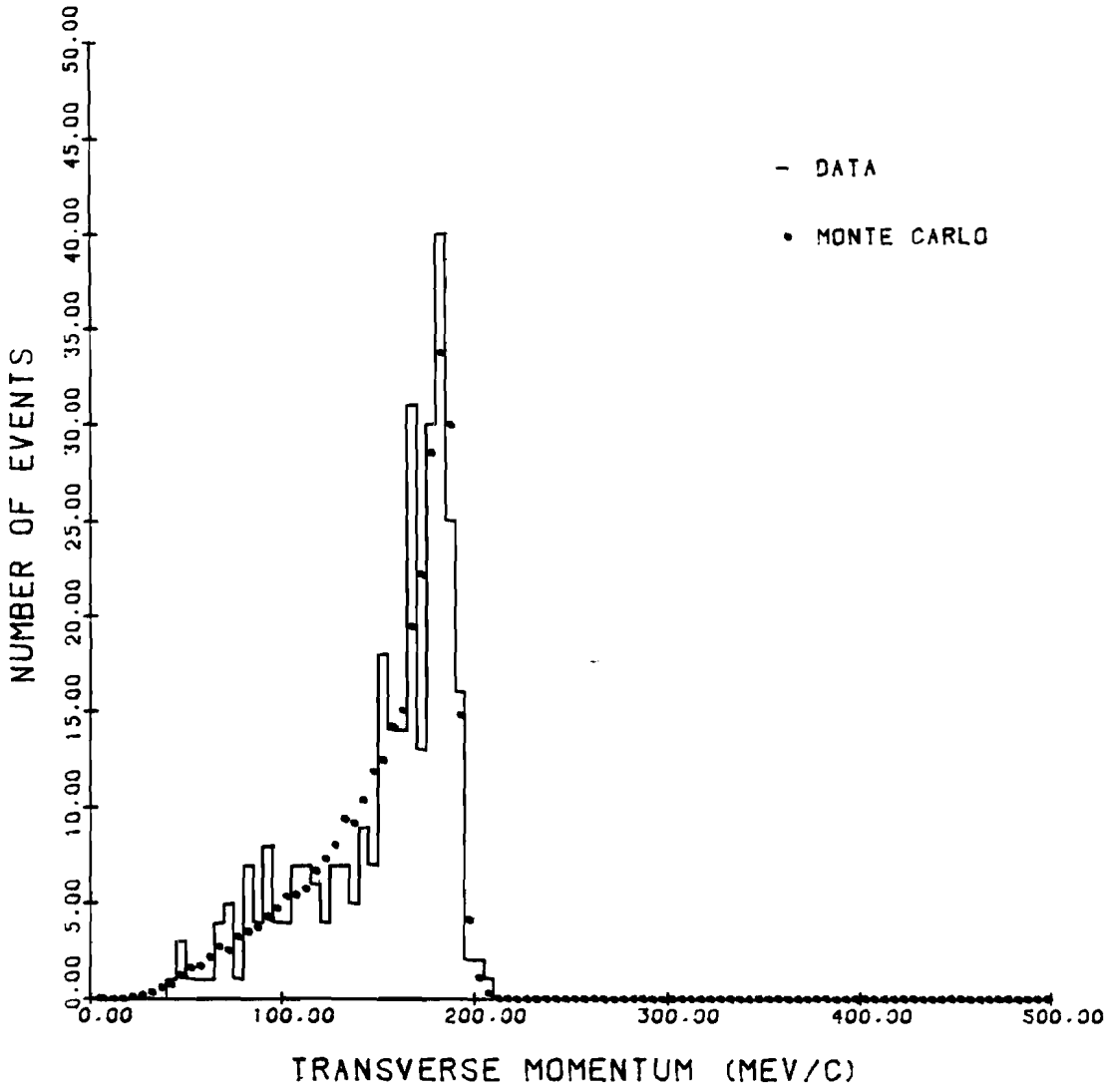

Figure 34. Transverse momentum of pi-mu atoms in the final sample, compared to Monte Carlo generated pi-mu atoms.

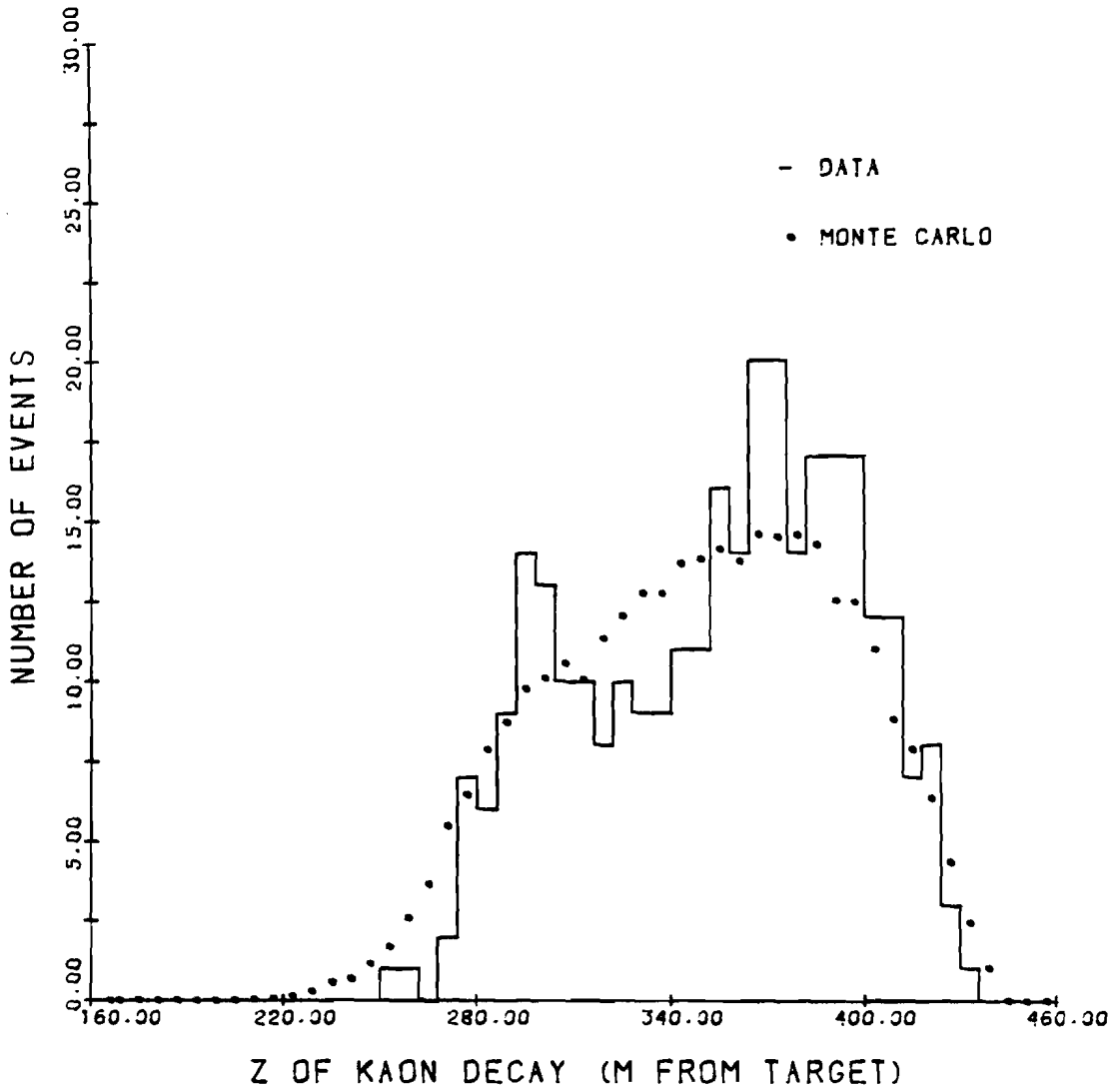

Figure 35. Z position of the K_L^o decay, for the final sample of pi-mu atoms, compared to Monte Carlo generated pi-mu atoms.

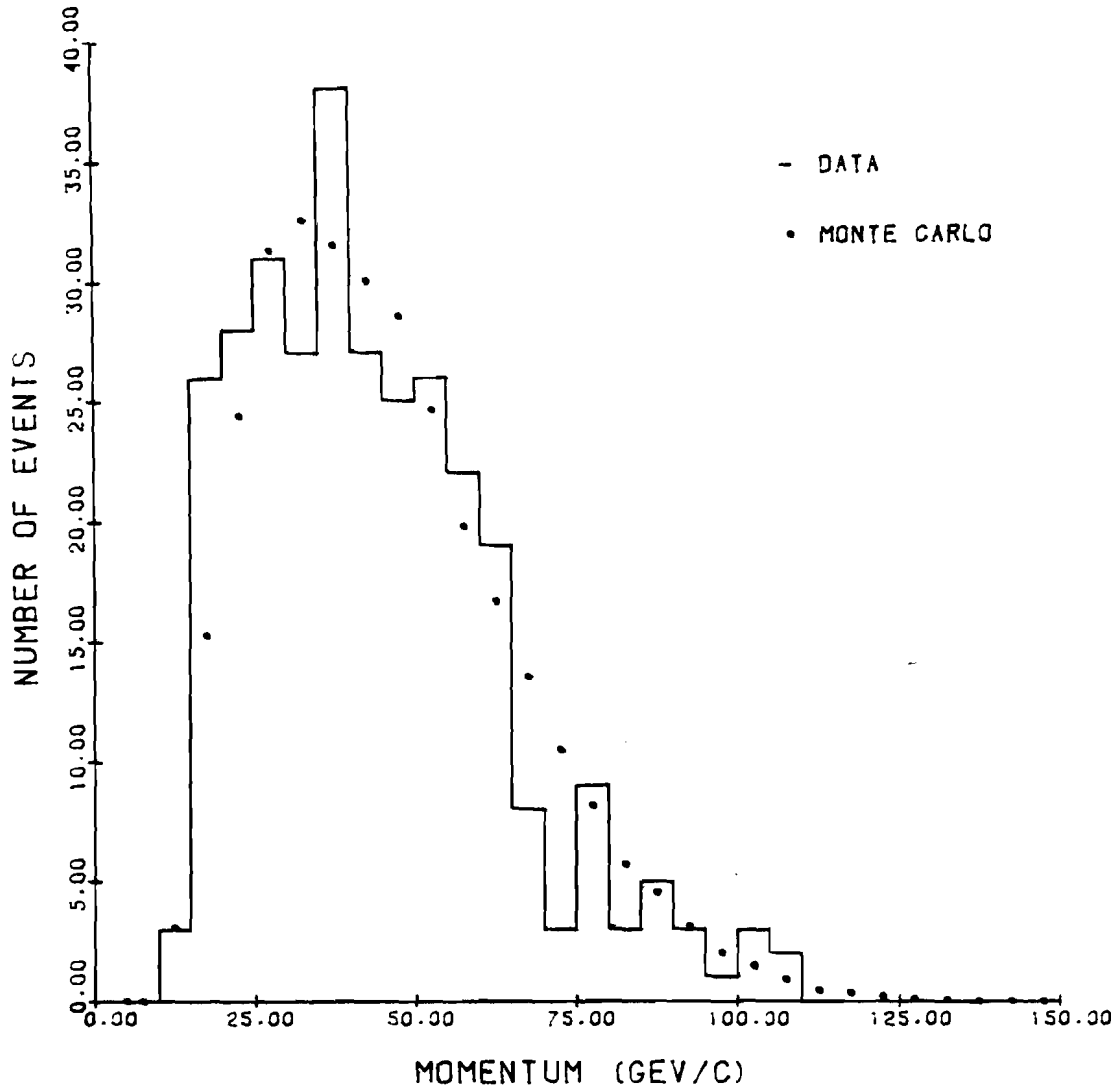

Figure 36. Momentum spectrum of pi-mu atoms in the final sample, compared to Monte Carlo generated pi-mu atoms.

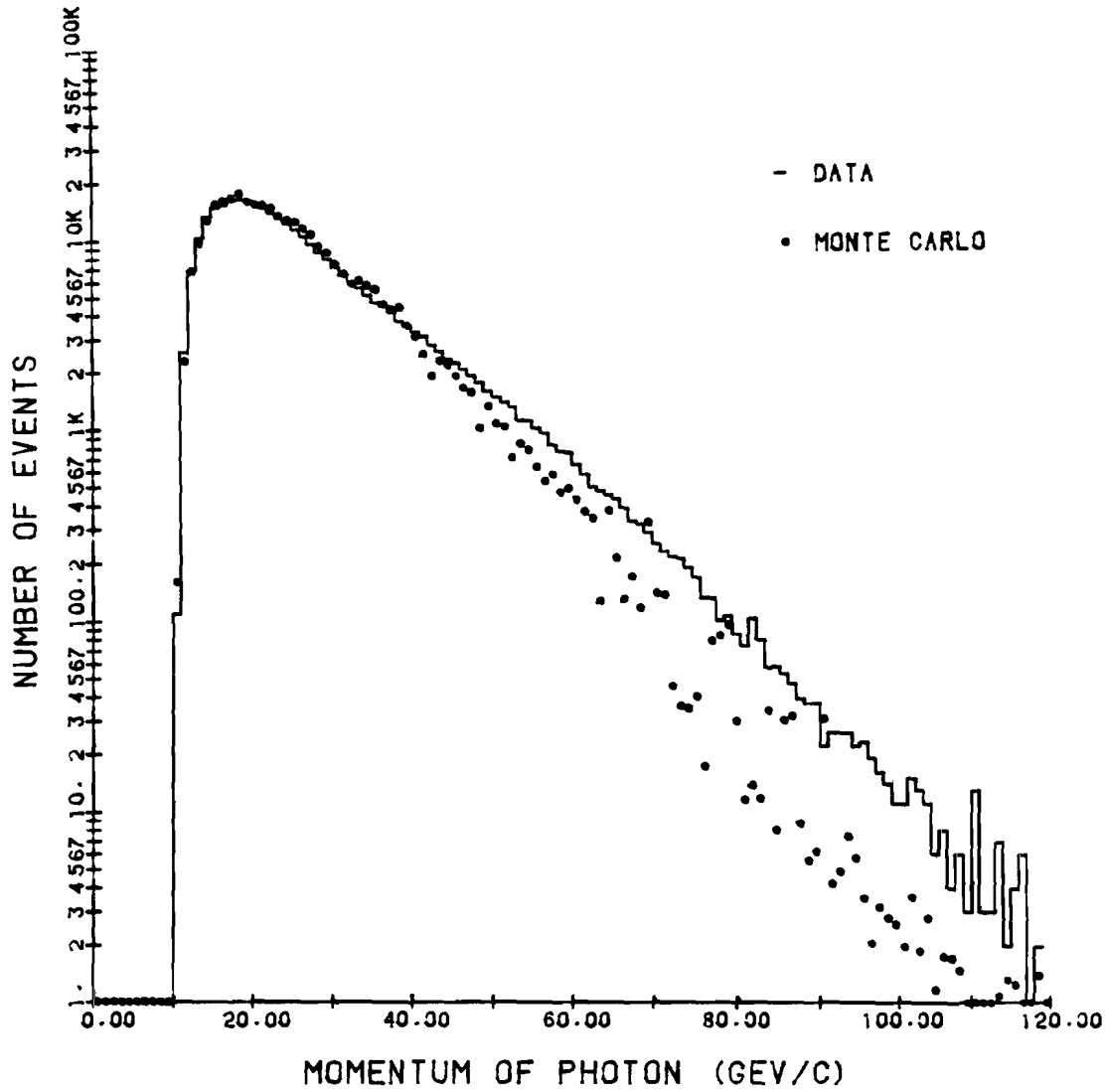

Figure 37. Momentum spectrum of photons in the final sample, compared to Monte Carlo generated e^+e^- events.

imposed on the reconstructed tracks. The most important were the requirements on the apparent vertex of the two tracks upstream of the 100D40, and on the separation of the tracks as seen from the side. Non-foil events, which would not likely have two tracks that converged near the midplane of the horizontally bending magnets, were required to have an apparent vertex 14 cm or more away from 457.19 m. Also, they had to have tracks which were separated by at least 1.27 cm in the side view, somewhere between chambers 1 and 5. The largest side view track separation for reconstructed $K_{\mu 3}$ triggers is shown in Figure 38.

The particle identification requirements for $K_{\mu 3}$ candidates were identical to those for pi-mu atoms. The scintillation counter hits were checked to see if they were in conformity with the $K_{\mu 3}$ trigger. Also, $K_{\mu 3}$ events were rejected if the pion or muon passed outside the bounds of the D-shaped window, the MWPC's, or the scintillation counter banks.

The K_L^o decay point for non-foil events was determined in a different way than for foil events. The two tracks were projected upstream and their deflections through all four magnets were simulated. The separation of the two tracks at their closest approach to one another was found, and the midpoint of the line segment defining that separation was called the decay point. The pion and muon

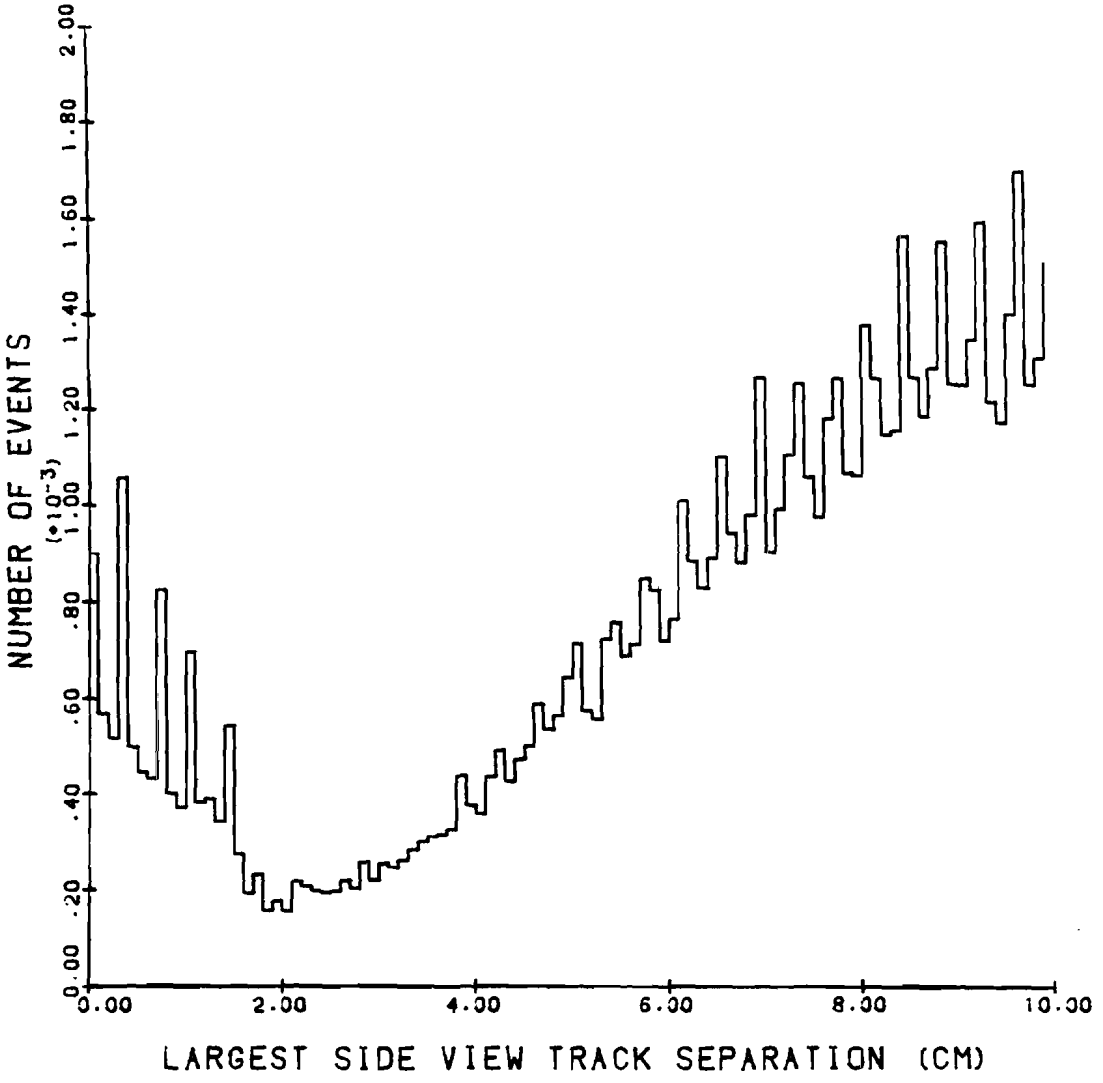

Figure 38. Largest side view track separation, for non-foil event candidates, before the cut.

were required to converge within a certain distance, scaled by the distance of the decay point from an arbitrary point in the detector (chosen to be chamber 1). This procedure accommodated the worsening of the position resolution as the decay point moved upstream. Specifically, the separation at closest approach divided by the distance (in Z) between chamber 1 and the decay point was required to be less than or equal to 0.0015. Figures 39 and 40 display this quantity before the cut was applied, and after all cuts. The location of the decay point was required to lie in the Z interval from 250 m to 430 m. In addition, the decay point had to fall within the beam. Figure 41 shows the Z distribution of the K_L^o decay point for the final $K_{\mu 3}$ sample, with the Monte Carlo distribution superposed.

Once the K_L^o decay point was established, various kinematical quantities could be calculated. First, the transverse momentum p_t of the π-μ pair was computed relative to the line from the target to the decay point. Events with p_t less than 90 MeV/c or greater than 195 MeV/c (the kinematic maximum) were eliminated. Figure 42 shows the p_t spectrum for the final sample of $K_{\mu 3}$ events, compared to Monte Carlo.

Background events from $K_{\pi 3}$ decays, in which one of the pions decayed to a muon, were reduced to a few percent by making a cut on another kinematic quantity, P_o^2, defined as

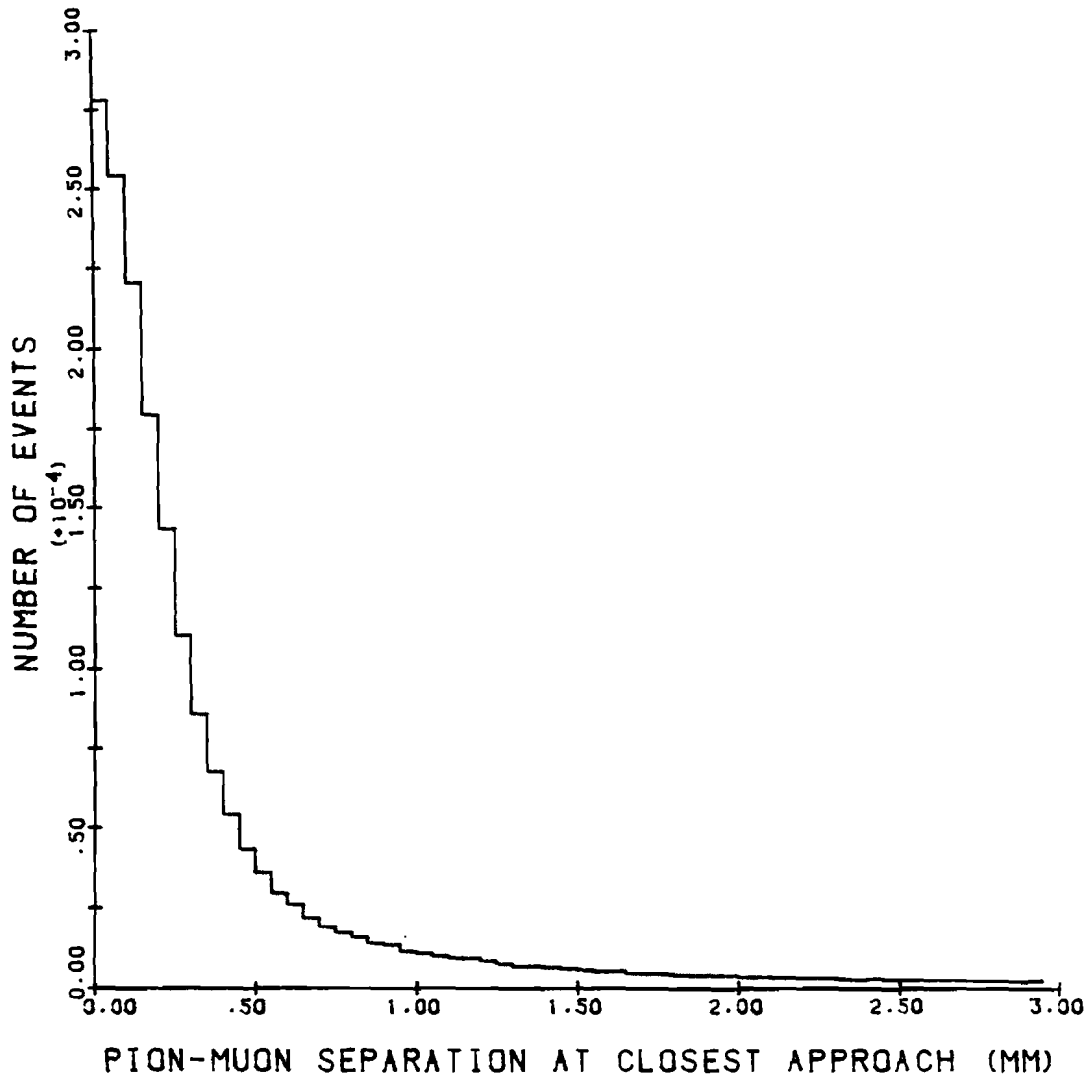

Figure 39. Separation of the two tracks at their closest approach (the K_L^0 decay point), for non-foil event candidates, before the cut.

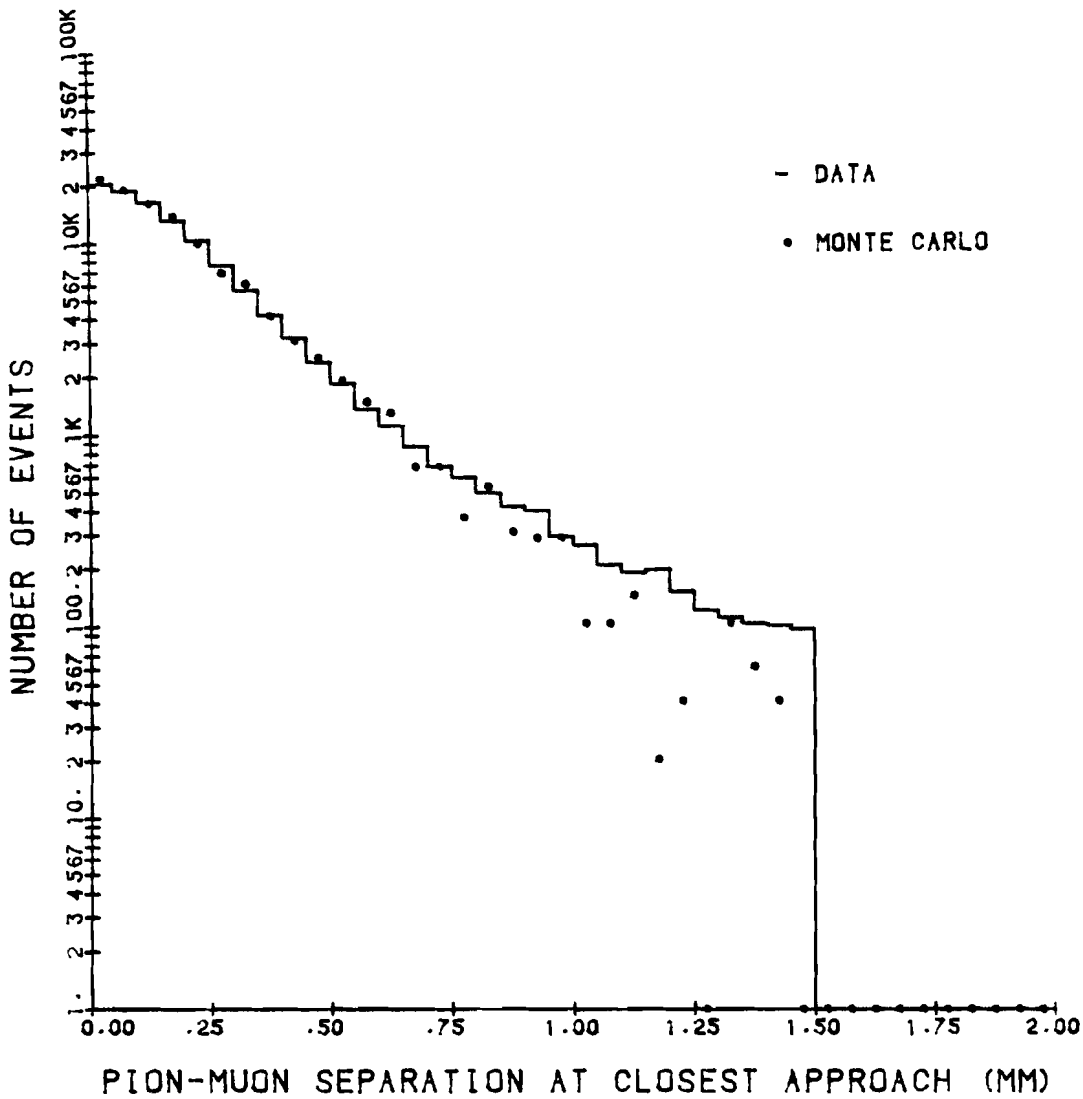

Figure 40. Separation of the pion and muon at their closest approach (the K_L^0 decay point), for the final sample of $K_{\mu 3}$ events, compared to Monte Carlo generated $K_{\mu 3}$ events.

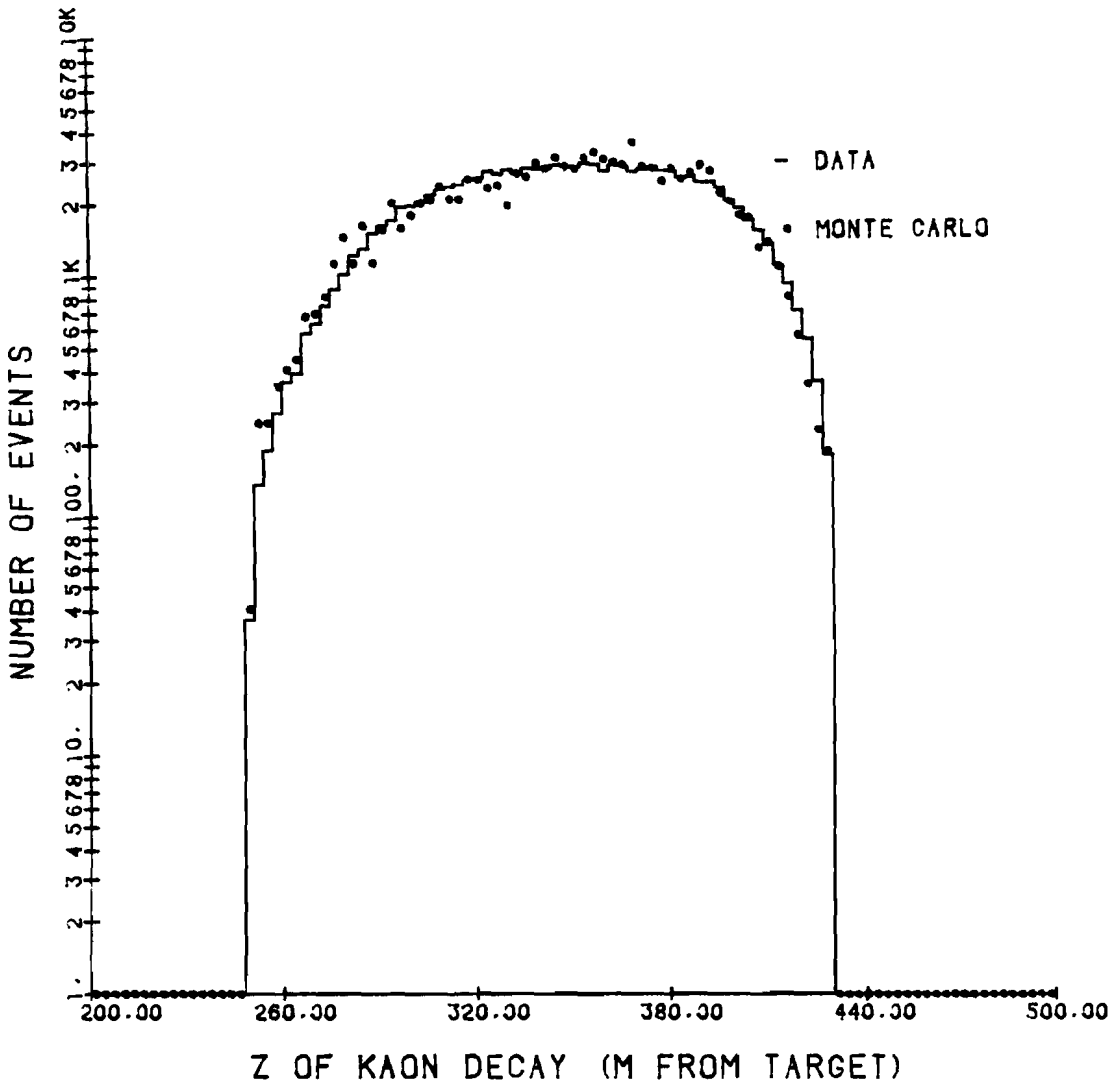

Figure 41. Z position of the K_L^o decay, for the final sample of $K_{\mu 3}$ events, compared to Monte Carlo generated $K_{\mu 3}$ events.

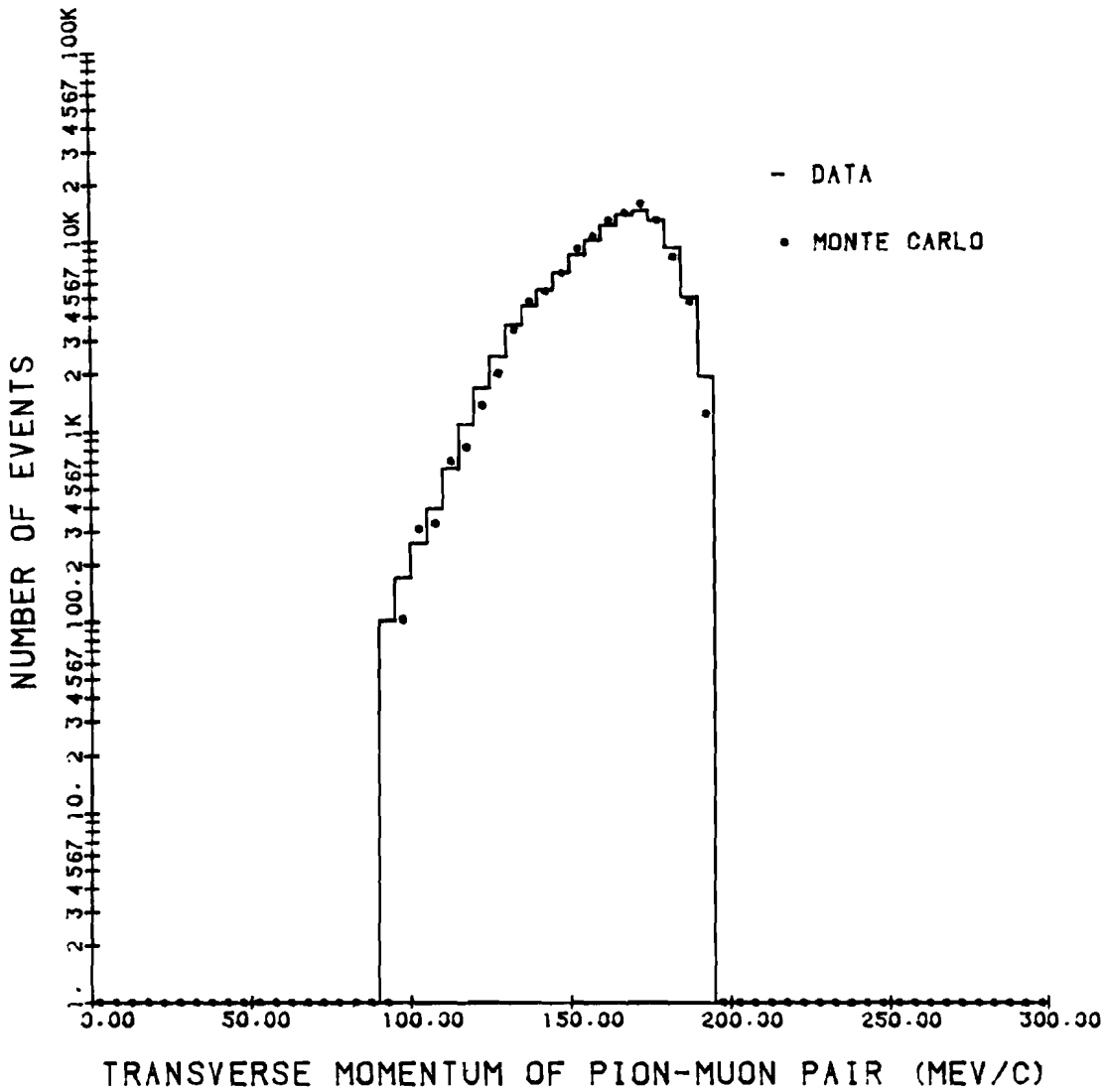

Figure 42. Transverse momentum of the pion-muon pair, for the final sample of $K_{\mu 3}$ events, compared to Monte Carlo generated $K_{\mu 3}$ events.

$$P_o^2 = \frac{(m_K^2 - m_{+-}^2 - m_o^2)^2 - 4(m_{+-}^2 m_o^2 + m_K^2 p_t^2)}{4(p_t^2 + m_{+-}^2)} ,$$

(ref. 14) where m_{+-} is the invariant mass of the two particles, under the assumption that each was a charged pion, rather than a pion and muon. The masses of the K_L^o and neutral pion are m_K and m_o, respectively. It can be shown that P_o^2 is positive if the two particles actually come from $K_{\pi 3}$ decay, and negative if they come from $K_{\mu 3}$ decay. P_o^2 can be even more negative if they arise from K_{e3} decay. Thus, the requirement $-0.047\ GeV^2/c^4 \leq P_o^2 \leq -0.002\ GeV^2/c^4$ was imposed on $K_{\mu 3}$ candidates. The background in the tails of the P_o^2 distribution is apparent in Figure 43. The effect of this cut was studied for all three decay modes using the Monte Carlo program. No further requirements were made on $K_{\mu 3}$ candidates.

The momentum of the K_L^o could not always be determined unambiguously because the momenta of only two of the three final state particles were measured. This can be seen as follows. We let the momentum vector of the K_L^o be $p_K \hat{n}$, where p_K is the magnitude and $\hat{n}$ is the unit vector pointing from the location of the target to the K_L^o decay point. The momenta of the three decay products are $\vec{p}_\mu$, $\vec{p}_\pi$, and $\vec{p}_\nu$. From momentum and energy conservation, we have

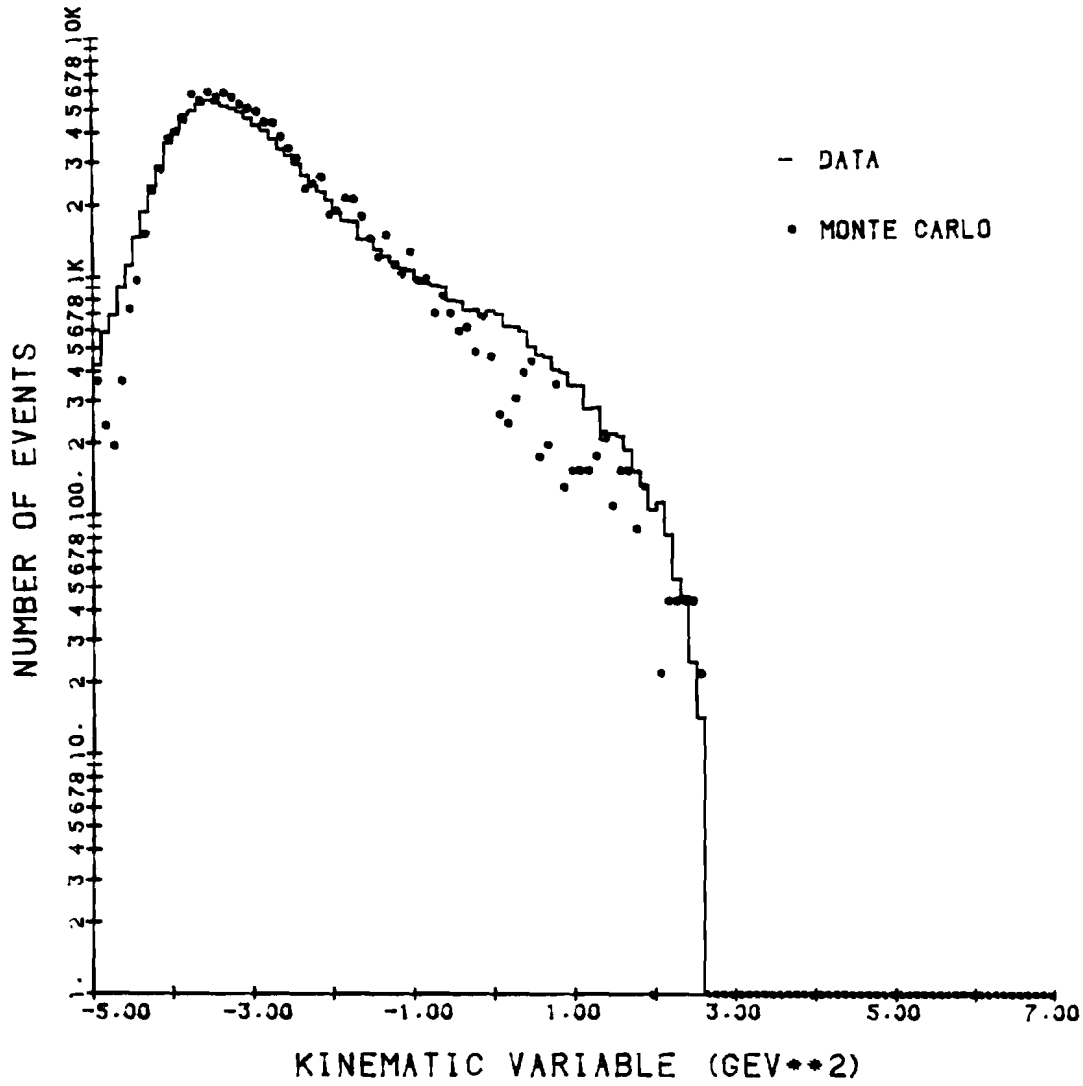

Figure 43. The kinematic variable P_o^2 defined in the text, for $K_{\mu 3}$ candidates, before cuts.

$$(\vec{p}_K - \vec{p}_\pi - \vec{p}_\mu)^2 = (\vec{p}_\nu)^2 = E_\nu^2$$

and

$$E_K = E_\pi + E_\mu + E_\nu \quad .$$

We eliminate E_ν and solve for p_K. The result is a quadratic equation with two solutions:

$$p_K = \left(1 \pm \sqrt{ARG}\right) \left(\frac{(\hat{n}\cdot\vec{p})\ X}{2(E^2 - (\hat{n}\cdot\vec{p})^2)}\right)$$

where

$$\vec{p} = \vec{p}_\pi + \vec{p}_\mu$$

$$E = E_\pi + E_\mu$$

$$X = m_K^2 - \vec{p}^2 + E^2$$

and

$$ARG = 1 - \frac{((\hat{n}\cdot\vec{p})^2 - E^2)(X^2 - 4E^2 m_K^2)}{(\hat{n}\cdot\vec{p})^2\ X^2} \quad .$$

When ARG is zero, the two solutions are the same and p_K is known, since $\hat{n}$, $\vec{p}_\mu$, and $\vec{p}_\pi$ have been determined already. In general, ARG is non-zero: the two solutions correspond to the two possible directions the neutrino can go, for fixed $\vec{p}_\pi$ and $\vec{p}_\mu$, when p_K is unknown. Accordingly, the average of the two solutions was used as the K_L^0 momentum. The variable ARG was useful in the analysis of the data, particularly in understanding the beam and the magnets (see Chapter 10). Histograms of ARG and p_K are presented in Figures 44 and 45 for the final $K_{\mu 3}$ sample.

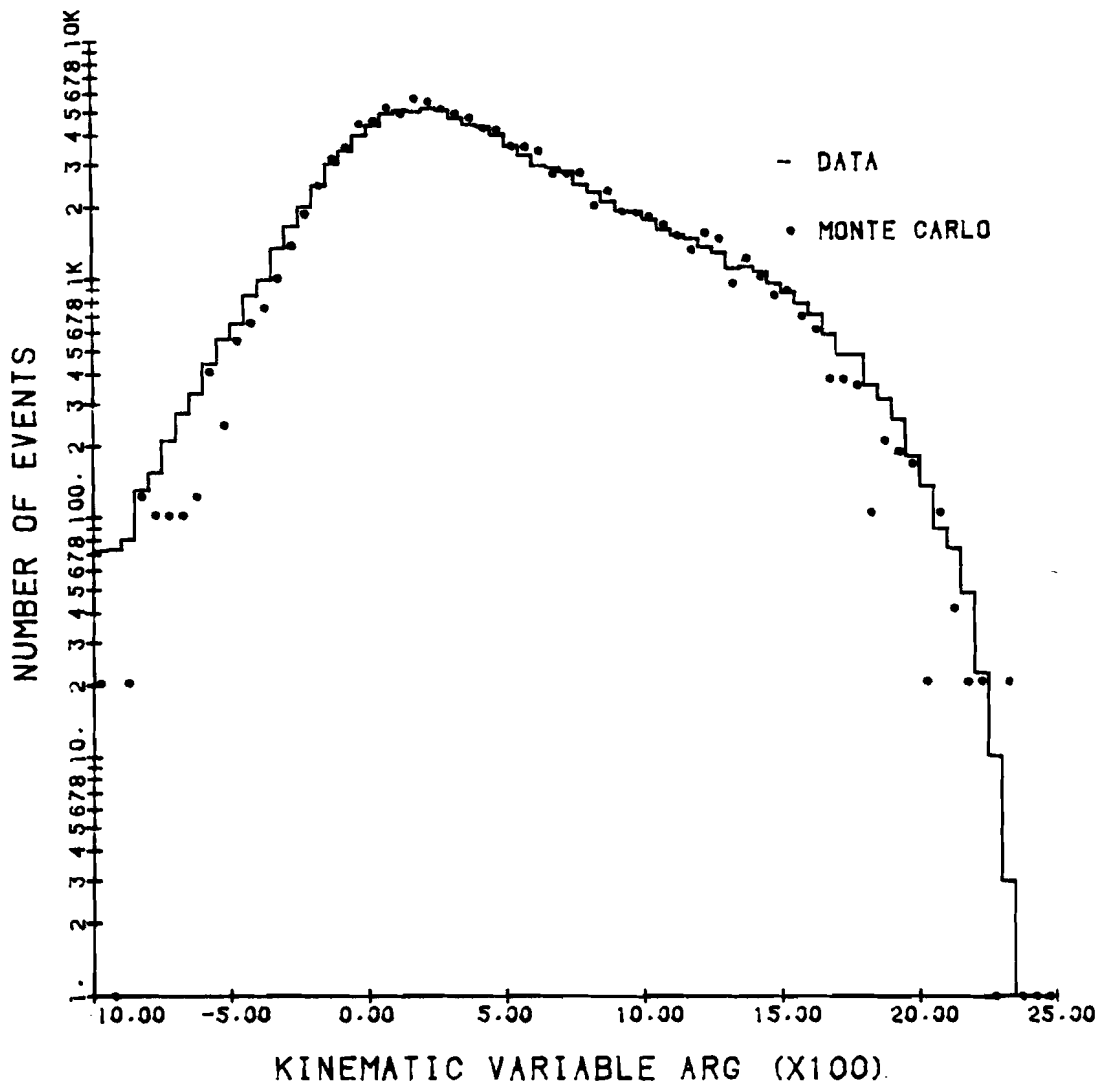

Figure 44. The variable ARG defined in the text, for the final sample of $K_{\mu 3}$ events, compared to Monte Carlo generated $K_{\mu 3}$ events.

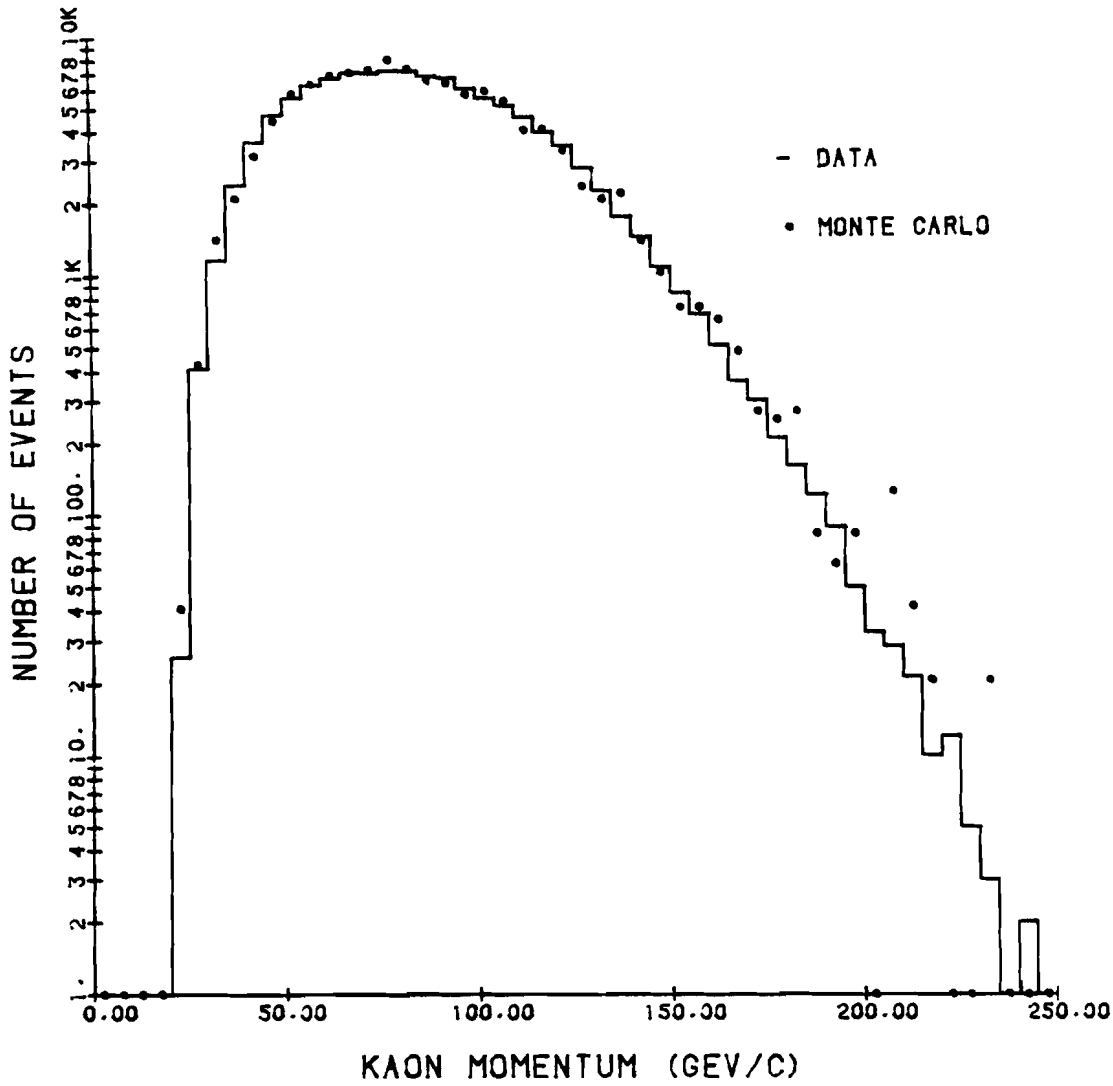

Figure 45. K_L^o momentum spectrum, for the final sample of $K_{\mu 3}$ events, compared to Monte Carlo generated $K_{\mu 3}$ events.

CHAPTER 10

CALIBRATIONS

10.1 DETERMINING THE GEOMETRY OF THE APPARATUS

The locations of the various components of the apparatus were ascertained initially from survey measurements made with respect to an established coordinate system within the Meson Laboratory. In that grid, the Meson Center target was at Z = -5 ft. These measurements were adequate for all the longitudinal (Z) positions.

The X and Y positions of the detector elements were determined more precisely from calibration data taken with the 100D40 magnet off and the beam stop in, which allowed only penetrating muons to traverse the spectrometer. The trigger required one or more hits in each of the six scintillation counter banks. Seven such data sets were accumulated during the course of the experiment. These data were used with a suitably modified analysis program to

align the MWPC's, and then the counters, taking as a starting point the survey measurements. By varying the X and Y coordinates for the centers of the MWPC's until the deviations of the hit wires from the computed muon trajectories (as determined by hit wires in other chambers) averaged to zero in each plane, the relative transverse positions of the wire planes were measured to ±40 microns.

The rotation of the second and fifth chambers relative to the others, and the departure of the pair of planes in each chamber from orthogonality, were measured by calculating deviations as a function of X and Y. These measurements of rotations agreed with the results of the surveying. The wires of adjacent planes in each MWPC were within 1 milliradian of a right angle. Although a small correction for non-orthogonality was included in the calculation of particle trajectories, no kinematic quantity was significantly affected.

Reconstructed single tracks were then used to fix the geometry of the counter banks. The distance between the projection of a particle trajectory at a counter that fired and that counter's assumed center was histogrammed, from which the centers were located to ±0.5 mm.

The locations of the decay pipe flanges at 211.7 m, 305.9 m, 321.1 m, and 400.2 m were measured relative to the beam using Polaroid film exposed to several beam pulses.

The relative separations of the beam center line and the pipe centers were measured to a precision of ±5 mm. The contour of the section of the pipe beneath the berm (211.7 m to 305.9 m) was surveyed by the Fermilab alignment group. The positions of the magnets, foil, and vacuum window were surveyed relative to the W counter bank to better than ±2 mm.

10.2 MAGNETIC FIELD CALIBRATIONS

Two sets of magnet calibration data were collected, one at the middle and the other at the end of the data taking period. During these, a 3/8 in. thick aluminum plate was placed in the path of the beam at 400.2 m. The beam was tightly collimated to produce a localized source of neutral lambdas and single charged particles from neutron interactions in the target.

The Λ^0 data were taken with a two-track trigger, and all the spectrometer magnets turned off except the 100D40, which was run at its usual current. Reconstructed two-track events which satisfied the following criteria were called $\Lambda^0 \rightarrow p\pi^-$ decays:

1. Two oppositely charged hadrons
2. A decay vertex between 395 m and 435 m in Z
3. A separation of the tracks at the vertex < 6 cm

4. $p_+/p_- > 3$, where p_+ is the momentum of the positively charged particle, and p_- is the momentum of the negatively charged particle.

The invariant mass of the pair was then calculated, assuming the positively charged particle was a proton, the other a pion. In order to center the observed invariant mass peak on the known Λ^0 mass, the overall field strength of the 100D40 was increased 1.2% over the value obtained by taking the ratio of the current at which the magnet was operated to the current at which the field had been mapped. A sample of about 4000 lambdas determined the field strength to 0.4%. This scale factor was also found to be the same for each of four regions of the magnet aperture.

The single charged particle calibration data were taken with the 100D40 at its customary current and the two pairs of vertically and horizontally bending magnets in the four combinations of on and off. A single-particle trigger requiring no hit muon counter was employed during these runs. Reconstructed single-track hadrons were selected with $p_t > 230$ MeV/c, so as to reduce the background from K_L^0 decays. From that portion of the data collected with only the 100D40 on, the extrapolation of the tracks to 400.2 m determined the center of the beam to ±0.2 mm in the X and Y directions. The two pairs of magnets about the foil were then calibrated against the 100D40, using the two sets of data in which one pair of magnets was off and the other run

at its standard field strength. The particles were tracked back trough the magnets using the previously determined field maps, weighted by an overall scale factor. By requiring that particles of both sign originate at the spot on the aluminum target, the overall field strengths of the vertically and horizontally bending magnets were found to better than 0.3%, and the deviations from the field maps were measured to be less than 0.9%.

10.3 DETERMINING THE GEOMETRY OF THE BEAM

The position of the beam at various Z locations was found initially by exposing Polaroid film placed in the beam to several pulses. Using these measurements, the downstream beam pipe sections and the detector were put into place, and the collimators aligned. The dimensions of the beam as a function of collimator settings were established from photographs taken at Z = 1756 ft.

Ultimately, the beam location was determined at three Z locations using a different technique at each, with consistent results. The measurement of the center of the beam at 400.2 m was described above (Section 10.2). Polaroid film placed in the beam directly beneath the D-shaped window (459.0 m) determined the center of the beam there to ±1.5 mm, using the measured location of the W

counters with respect to the window.

The variable ARG (see Section 9.5.2) provided a sensitive way to locate the production target. The fraction of Monte Carlo $K_{\mu 3}$ events whose two K_L^o momentum solutions differed from their average by less than 10%, i.e. which had $|ARG| < 0.01$, varied from about 5% to 19% as the position of the target used to calculate ARG varied vertically from 5 cm below to 5 cm above the target position used in the Monte Carlo generation of those events. $K_{\mu 3}$ events in the data behaved in precisely the same way as the target position was changed in the analysis program, so that the true position was determined once the data and Monte Carlo curves coincided. The horizontal position was established in the same manner, though only to a precision of ±5 cm, compared to ±1.5 cm vertically.

10.4 THE INPUT K_L^o MOMENTUM SPECTRUM

The Monte Carlo input K_L^o momentum spectrum at the target was based upon the measurements of Skubic, et al., (ref. 56) above 60 GeV/c, although the final spectrum was tuned using $K_{\mu 3}$ events in the data over the entire range of momenta (15 GeV/c to 200 GeV/c). This spectrum is shown in Figure 46. So-called "unambiguous" $K_{\mu 3}$ events with $|ARG| < 0.01$ were used to adjust the input spectrum. These events

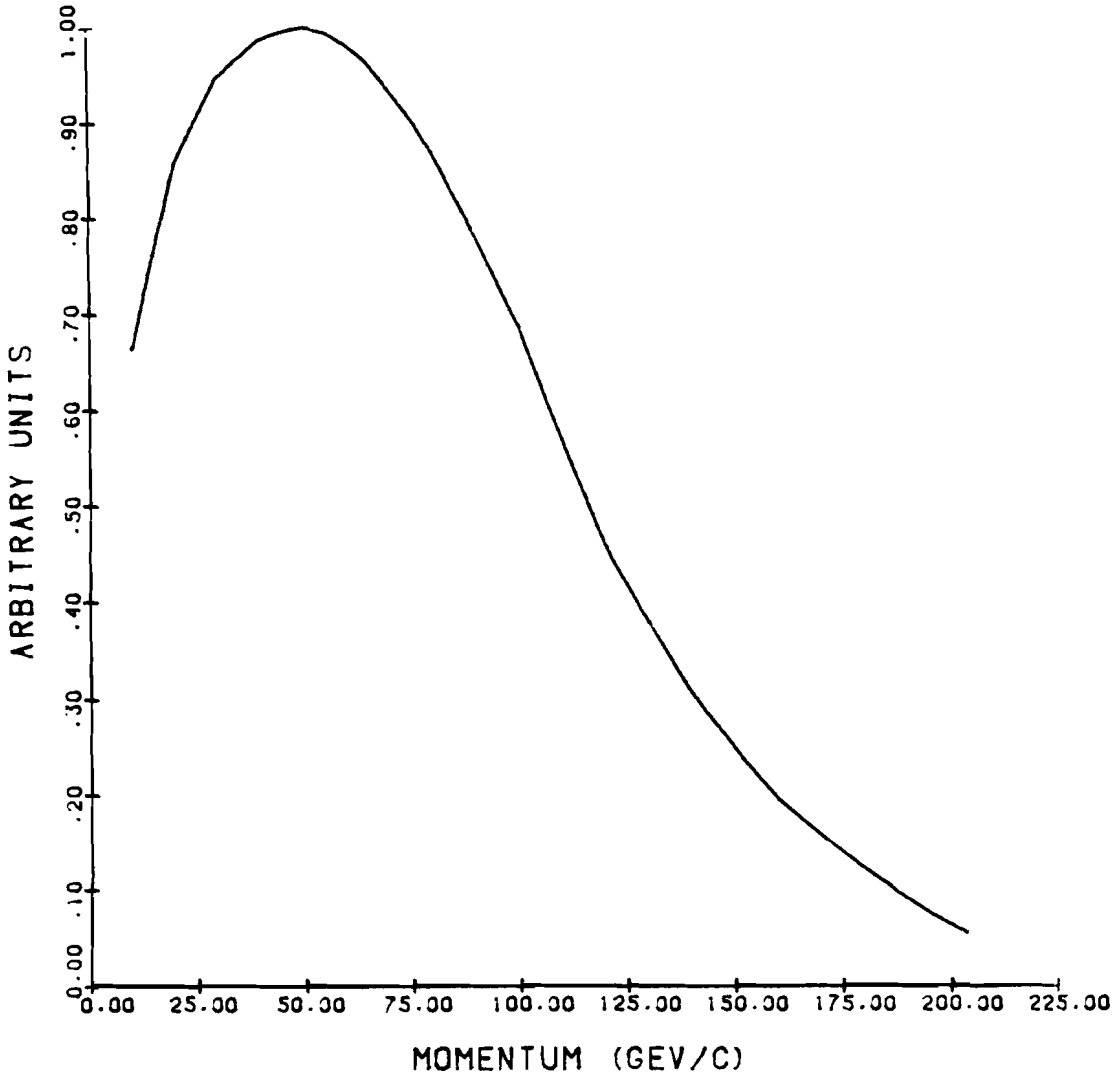

Figure 46. Momentum spectrum of forward neutral kaons emerging from the Meson target.

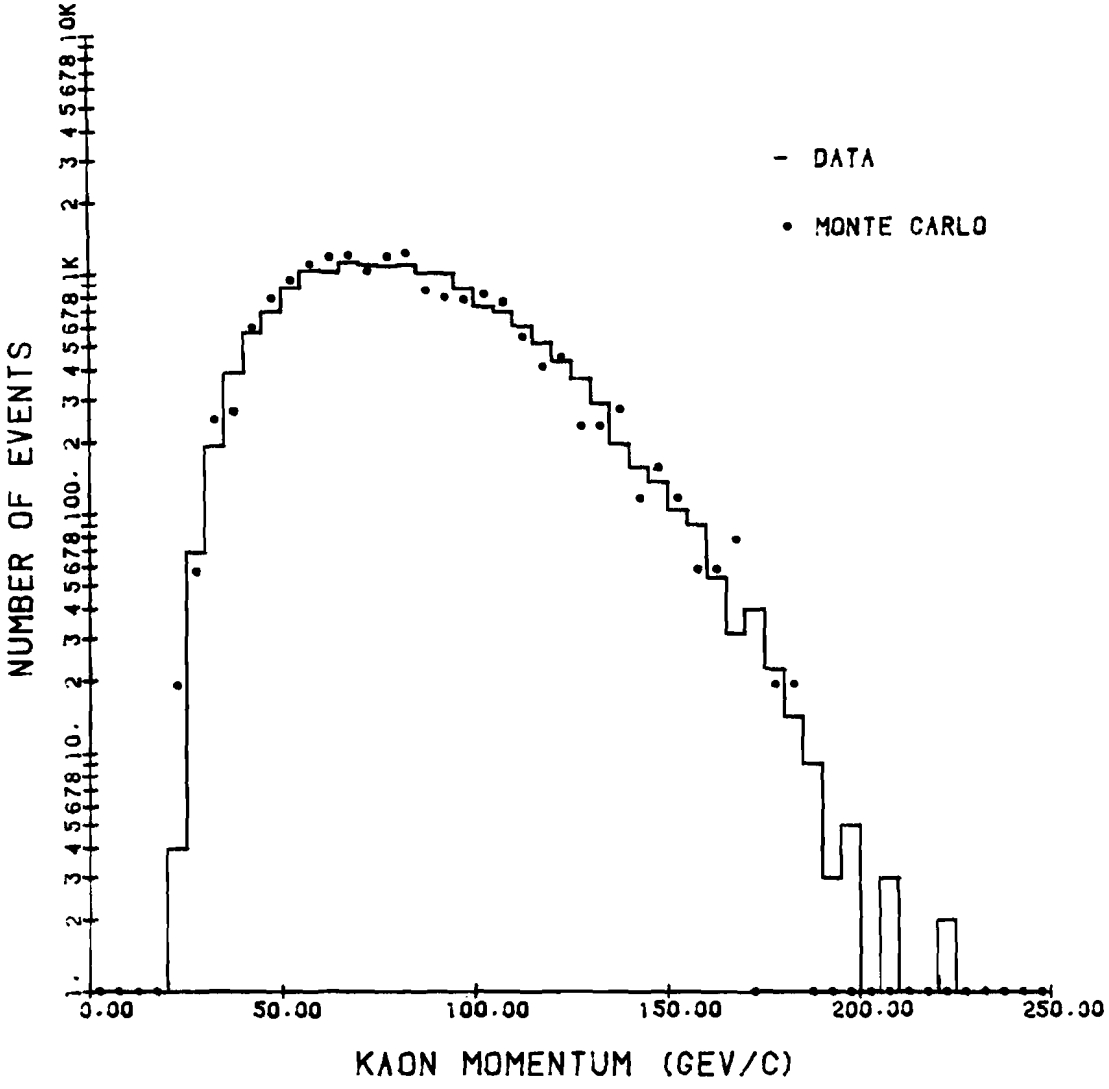

Figure 47. K_L^0 momentum spectrum cut on the variable ARG, for the final sample of $K_{\mu 3}$ events, compared to Monte Carlo generated $K_{\mu 3}$ events.

are compared with Monte Carlo $K_{\mu 3}$ events in Figure 47, and show good agreement.

10.5 MULTI-WIRE PROPORTIONAL CHAMBER EFFICIENCIES

The measurement of the efficiencies of the proportional wire chamber planes was performed using well identified $K_{\mu 3}$ and e^+e^- events, by not requiring the presence of a hit wire along a particle trajectory in the plane under study. The efficiencies increased from about 91% in the first two chambers, which were exposed to the highest charged particle fluxes (typically 5×10^6 per pulse), to about 98% in the last chamber. A conservative estimate of the error on the measurements was 3%.

Another MWPC characteristic measured was the average "spread" for each plane, i.e. the probability that the passage of a single charged particle would fire adjacent wires. Roughly 10% of the time, two adjacent wires registered the passage of the same particle. (The optimum position resolution is achieved when this occurs 50% of the time.) The spreads determined the width of the region midway between two adjacent wires through which a particle had to pass in order to fire both. The coordinates of the hits in the chambers for Monte Carlo events were translated into wire numbers, or pairs of wire numbers, on this basis.

10.6 SCINTILLATION COUNTER EFFICIENCIES

In order to measure the efficiencies of the counter banks, calibration data sets were collected with single- and two-track triggers, and each counter bank in turn removed from the trigger. Counter bank inefficiencies of two sorts were included in the Monte Carlo: those due to gaps between counters and those due to inefficiencies of the counters themselves. The gaps between counters were calculated from the measured breadth of the counter banks and the widths of the counters. The only subtlety of the measurement of the individual counter efficiencies was that counters in the horizontal hodoscopes (W and H) were typically hit by two particles at the same time for atom and e^+e^- triggers, but often by only one particle for $K_{\mu 3}$ triggers. The single- and two-particle inefficiencies were not simply related. Hence, in the Monte Carlo, care was taken to use the empirically determined efficiency appropriate to the number of particles striking a horizontal counter. The single-particle efficiencies for most of the counters were better than 98%. The effects of muon counter efficiencies were assumed to cancel in the ratio of the pi-mu atom and $K_{\mu 3}$ acceptances, hence the Monte Carlo simulations were run with 100% efficient muon counters. However, for the comparison of $K_{\mu 3}$ decays to $K_{\pi 3}$

decays, an overall efficiency for the muon bank of 0.97 ± 0.02 was used, which included losses due to interactions in the steel absorber.

10.7 EXTRA HITS IN THE W AND H COUNTERS

As indicated in Chapter 6, the only important difference between the atom and $K_{\mu 3}$ triggers was that the $K_{\mu 3}$ trigger allowed any number of horizontal counters to fire, whereas the atom (and e^+e^-) triggers demanded one hit in the W bank and one hit in the H bank. Thus it was necessary to measure the probability that an otherwise acceptable pi-mu atom or e^+e^- pair would be vetoed by extra hits in either bank. (The loss of pi-mu atoms and e^+e^- pairs due to multiple scattering was incorporated in the Monte Carlo, as previously described.)

Two sources of extra hits were studied: those due to delta rays produced by the particles in the pair, and those due to particles not associated with the event ("random" extra hits). The delta ray component was measured using single-track muon calibration data taken with the beam stops in the beam, since the likelihood of a beam-associated random track being in coincidence with a real event increased with counting rate (i.e. with the intensity of the beam). Events were selected which had one

reconstructed track in the MWPC's, and two hit counters in the bank. Since delta rays tended to strike counters nearer the trajectory of the primary particle, the desired probability

$P(i,j)$ = probability that counter j was hit by a delta ray if the reconstructed track hit counter i

was not uniform, but depended upon the separation between counters i and j (i.e. upon $k = i - j$). Moreover, since shorter counters were less likely to be hit, $P(i,j)$ depended upon the length $d(j)$ of counter j. (This was not the case for the H bank, which had counters of equal length.) Factoring out the dependence on length, we write

$$P(i,j) = P'(i-j)\, d(j) \quad .$$

$P'(k)$ was extracted from the histogram $H(k)$ of the separation k, using the following relations, where $N(i)$ was the number of times that a reconstructed track hit counter i:

$$H(k) = \sum_{\substack{i,j \\ i-j=k}} N(i)P(i,j)$$

$$= P'(k) \sum_{\substack{i,j \\ i-j=k}} N(i)d(j) \quad .$$

Since $N(i)$ and $H(k)$ were tallied and $d(j)$ was measured, $P'(k)$ and hence $P(i,j)$ was determined. Thus, the Monte Carlo simulation incorporated extra hits from delta rays for each event, using $P(i,j)$ for each bank. The method was

checked by comparing the histogram H(k) for Monte Carlo events with the data. The result was that 1.1% of pi-mu atom and e^+e^- events were lost due to delta rays in the W bank, and 2.5% in the H bank (ref. 57).

The probability that an extra W or H counter was hit by a random particle was found by studying $K_{\mu 3}$ events. In comparison with the $K_{\mu 3}$ Monte Carlo (with delta rays), the data exhibited an excess of events with extra counters hit. By assigning each Monte Carlo event a small probability that it was accompanied by a random track, the frequency distribution of hits in the counter banks could be made to agree with the data. Those probabilities were (1.8 ± 0.2)% and (4.6 ± 0.5)% in the H and W banks, respectively, yielding an average probability of (6.3 ± 1.0)%. Since these accidental coincidences were not correlated with the particular counters hit by reconstructed tracks, the random extra hit probability did not need to be included in the Monte Carlo on an event by event basis. Rather, an overall correction for this bias was made in the final calculation of branching ratios.

10.8 EXTRA HITS IN THE A, B, AND G COUNTERS

Each of the three triggers made the same requirements on the A, B, and G counter banks, so extra hits from delta rays and accidental coincidences introduced no trigger corrections for these banks.

As noted in Section 9.1, e^+e^- events were sometimes rejected in the B bank. Two calibration runs taken with the 234B requirement replaced by $\geq$2B facilitated a measurement of the probability, as a function of photon momentum, that an e^+e^- event was lost. Events were selected which showed no energy deposition in the shower counters aside from that due to the electron and positron, in order to eliminate events from $K_{\pi 3}$ decays which sent photons into the bank. (The Monte Carlo program performed only a crude simulation of the response of the shower counters to various kinds of incident particles.) The probability that an event was lost increased linearly with photon momentum, with a slope of 0.00225 ± 0.00013 GeV/c^{-1}. The net effect was a reduction of the acceptances for the decays $K_L^o \to \pi^o\pi^o\pi^o$, $K_L^o \to \pi^+\pi^-\pi^o$, $K_L^o \to \pi^o\pi^o$, and $K_L^o \to \gamma\gamma$ of (6.2 ± 0.3)%, (5.4 ± 0.3)%, (8.5 ± 0.5)%, and (11.1 ± 0.6)%, respectively. This trigger correction was included in the Monte Carlo generation of e^+e^- events.

CHAPTER 11

THE PROBABILITY OF FORMATION OF PI-MU ATOMS

11.1 PI-MU ATOM AND $K_{\mu 3}$ BACKGROUNDS

Pi-mu atoms were detected with a very small background, which was uniform across the histogram of the variable α (see Figure 32). Therefore, the number of background events was determined simply from the average number of events in each bin, excluding the regions defined by $0.09 < |\alpha| < 0.19$. Potential background events from $K_{\mu 3}$ decays in which one of the side view tracks was not reconstructed (due to MWPC inefficiencies) were eliminated primarily by the beam and p_t requirements, discussed in Chapter 9. Photons which converted to $\mu^+\mu^-$ pairs in the break-up foil accounted for most of the remaining background, according to estimates based upon the number of e^+e^- pairs detected and the relative cross-sections. However, attempts to reduce the pi-mu atom background were abandoned, because

the signal to noise ratio dropped with cuts made after the shower counter, beam, and p_t requirements.

There were two kinds of $K_{\mu 3}$ backgrounds. K_L^o decays such as $K_{\pi 3}$ and K_{e3}, in which the pion decayed before reaching the end of the apparatus, belonged to the first category. The requirements on p_t and P_o^2, specified in Chapter 9, lowered the magnitude of the $K_{\pi 3}$ contribution by 70% to (0.76 ± 0.10)% of the $K_{\mu 3}$ signal. Assuming 2.7% of the e-μ events were misidentified as π-μ events, the K_{e3} contribution was lowered by 28% to (0.07 ± 0.04)% of the $K_{\mu 3}$ signal (ref. 35).

$K_{\mu 3}$ background events in the second category, unlike the first, did not arise from single K_L^o decays. Included were events consisting of two random tracks from different K_L^o decays, and events from interactions of neutrons and kaons in the beam halo with the beam pipe wall. These backgrounds were studied in four different ways which gave consistent estimates for the magnitude of the contribution to the $K_{\mu 3}$ signal, which totaled (4.36 ± 0.73)%. The procedures are described in detail elsewhere (ref. 35). The total $K_{\mu 3}$ background from both categories was found to be (5.19 ± 0.75)%.

11.2 THE PI-MU ATOM BRANCHING RATIO

The number of detected pi-mu atoms was related to the total number of K_L^o decays which occurred in the decay volume while the experiment was "live" by the detection efficiency (acceptance) for pi-mu atoms and the probability that the K_L^o decays to a pi-mu atom and neutrino. The Monte Carlo simulation of 500,000 decays $K_L^o \rightarrow (\pi\mu)_{atom}\nu$ yielded 18797 events which survived the same requirements imposed on the data to define valid pi-mu atoms. As has been noted previously, scintillation counter and MWPC efficiencies, as well as extra hits in counters due to delta rays, were included in the simulation. The only correction which was not incorporated was the 6.3% loss of pi-mu atoms at the trigger level due to accidental coincidences causing extra counter hits (see Chapter 10). Thus if we make the following definitions

$N_{atom-MC}$ = total number of kaons which decayed in the decay volume in the Monte Carlo generation of pi-mu atoms

= 500,000

$T_{atom-MC}$ = total number of pi-mu atoms in the final Monte Carlo sample

$= 18797$

N_{data} = total number of kaons which decayed in the decay volume while experiment was "live"

$T_{atom-data}$ = total number of pi-mu atoms in the final data sample

$= 174.3$

B_{atom} = branching ratio $\Gamma(K_L^o \to (\pi\mu)_{atom}\nu)/\Gamma(K_L^o \to all)$

we may write

$$T_{atom-data} = N_{data} \cdot \frac{T_{atom-MC}}{N_{atom-MC}} \cdot (1 - 0.063) \cdot B_{atom} \quad .$$

For the measurement of the branching ratio

$$R \equiv \frac{\Gamma(K_L^o \to (\pi\mu)_{atom}\nu)}{\Gamma(K_L^o \to \pi\mu\nu)}$$

we used a sample of 182 pi-mu atoms, of which an estimated 7.7 were background. The pi-mu atoms were selected by requiring $0.09 \leq \alpha < 0.19$. The pi-mu atoms in the peak at $\alpha = -0.138$ were not used, since their inclusion would have doubled the background while increasing the signal by only 6%. These pi-mu atoms were found using the second event reconstruction routine referred to in Chapter 9.

The same data sample and event reconstruction program yielded 111,793 $K_{\mu 3}$ events, with an estimated background of 5.19%. Thus we identify

$$T_{K\mu 3\text{-data}} = 105991 \quad .$$

The detection efficiency for $K_{\mu 3}$ events can be inferred from the numbers

$$T_{K\mu 3\text{-MC}} = 5482$$

and

$$N_{K\mu 3\text{-MC}} = 20 \times 10^6 \quad .$$

These three figures were related by the expression

$$T_{K\mu 3\text{-data}} = N_{data} \cdot \frac{T_{K\mu 3\text{-MC}}}{N_{K\mu 3\text{-MC}}} \cdot B_{K\mu 3} \cdot 1/32$$

where $B_{K\mu 3}$ is the $K_{\mu 3}$ branching ratio relative to all K_L^o decays (0.270 ± 0.005). The factor 1/32 came from the fact that one in 32 $K_{\mu 3}$ triggers was recorded on tape.

Eliminating N_{data} in the two equations above gives the rate of formation of pi-mu atoms, relative to $K_{\mu 3}$ decays:

$$R \equiv \frac{B_{atom}}{B_{K\mu 3}} = \frac{T_{atom\text{-data}} \; (T_{K\mu 3\text{-MC}}/N_{K\mu 3\text{-MC}}) \cdot 1/32}{T_{K\mu 3\text{-data}} \; (T_{atom\text{-MC}}/N_{atom\text{-MC}}) \cdot 0.937}$$

$$= (4.00 \pm 0.31) \times 10^{-7} \quad .$$

The error quoted here is only statistical.

The systematic errors were determined by varying the input parameters of the Monte Carlo within their measured uncertainties, and noting the resultant effect on the branching ratio measurement. Table 4 lists sources of systematic errors and their magnitudes. The total systematic error was estimated to be 6.3% of the result, or 0.25×10^{-7}.

Table 4. Sources of Systematic Errors

Source of Error	Magnitude, as Fraction of Result
W and H bank trigger differences	0.010
Proportional chamber inefficiencies	0.006
Beam, spectrometer locations	0.022
Magnetic field strengths	0.028
K_L^o momentum spectrum	0.012
$K_{\mu 3}$ Dalitz plot parameterization	0.040
$K_{\mu 3}$ background subtraction	0.008
Track finding algorithm	0.026
$K_{\mu 3}$ vertex requirements	0.012
Total systematic error	0.063
Total statistical error	0.077
Total error	0.100

The data were subdivided to check for internal consistency. The results for the two foil thicknesses were:

R for data taken with 20 mil foil = $(4.31 \pm 0.43) \times 10^{-7}$

R for data taken with 35 mil foil = $(3.64 \pm 0.43) \times 10^{-7}$.

This verified that all of the pi-mu atoms were dissociated in the foil. The data were divided according to the Z location of the K_L^o decay, and found to be consistent. Also, groups of runs separated in time were in agreement, within statistics.

Our final result was

$$R \equiv \frac{\Gamma(K_L^o \to (\pi\mu)_{atom}\nu)}{\Gamma(K_L^o \to \pi\mu\nu)} = (4.00 \pm 0.31 \pm 0.25) \times 10^{-7},$$

where the first error was statistical, and the second systematic. This is to be compared with the theoretical prediction

$$R = (4.43 \pm 0.12) \times 10^{-7} \quad .$$

11.3 THE PI-MU ATOM LIFETIME

As noted in the Introduction, a discrepancy between the observed rate of formation of pi-mu atoms and the predicted rate could be due to an anomaly in the K_L^o decay rate to pi-mu atoms or in the lifetime of pi-mu atoms. Unfortunately, a sensitive measurement of the pi-mu atom

lifetime could not be made in this experiment, at least not with the small number of pi-mu atoms detected. This can be understood if the detector is regarded as a pin-hole aperture, located a distance h above the beam. In the pi-mu atom rest frame, its lifetime τ (from K_L^o decay to break-up at the foil) is

$$\tau = d/\beta c\gamma$$

where d is the distance of its flight to the foil, and βc is its velocity. Substituting $\beta\gamma = p/m$ and $p = p_t \cot\theta$, where p is the atom's momentum, m its mass, and θ the (small) angle it makes with respect to the beam, one finds

$$\tau \cong mh/p_t c \quad .$$

The p_t distribution, though, was sharply peaked, so that the detector saw pi-mu atoms that had a very narrow range of proper times. This is shown in Figure 48, where τ has been normalized to the mean pion lifetime. The Monte Carlo curve superposed corresponds to the assumption that the pi-mu atom lifetime is the lifetime of the pion. (The average of the Monte Carlo distribution is 0.078.) Figure 49 shows the same data, but with a Monte Carlo curve for one-third the pion lifetime. As can be plainly seen, there is little difference between the two Monte Carlo curves, and there are too few pi-mu atom events to favor one over the other. However, the expected number of pi-mu atoms for the shorter Monte Carlo lifetime was lower than the first

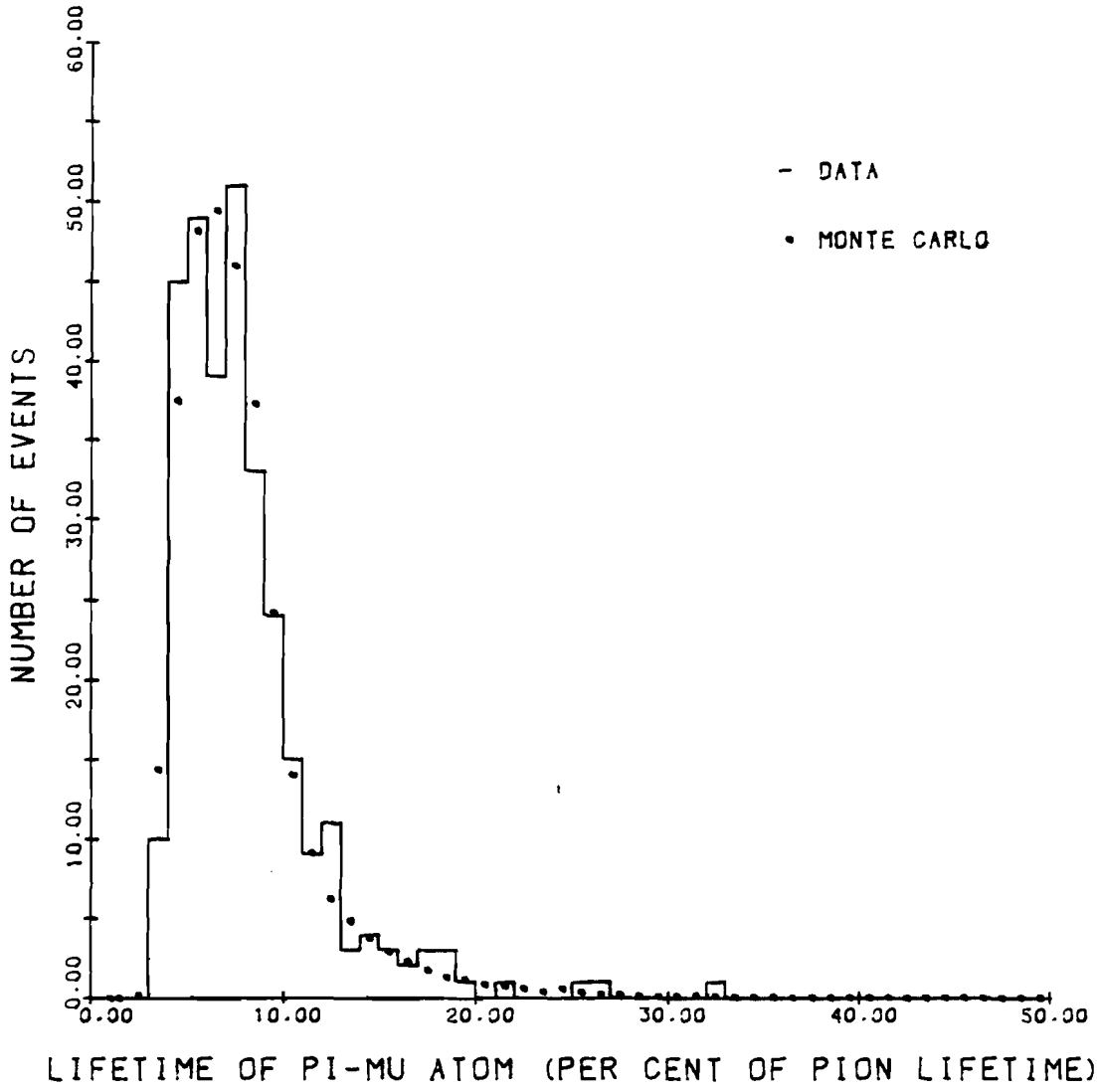

Figure 48. Lifetime of pi-mu atoms, compared to Monte Carlo pi-mu atoms generated with the lifetime of the pion (normalized to equal areas).

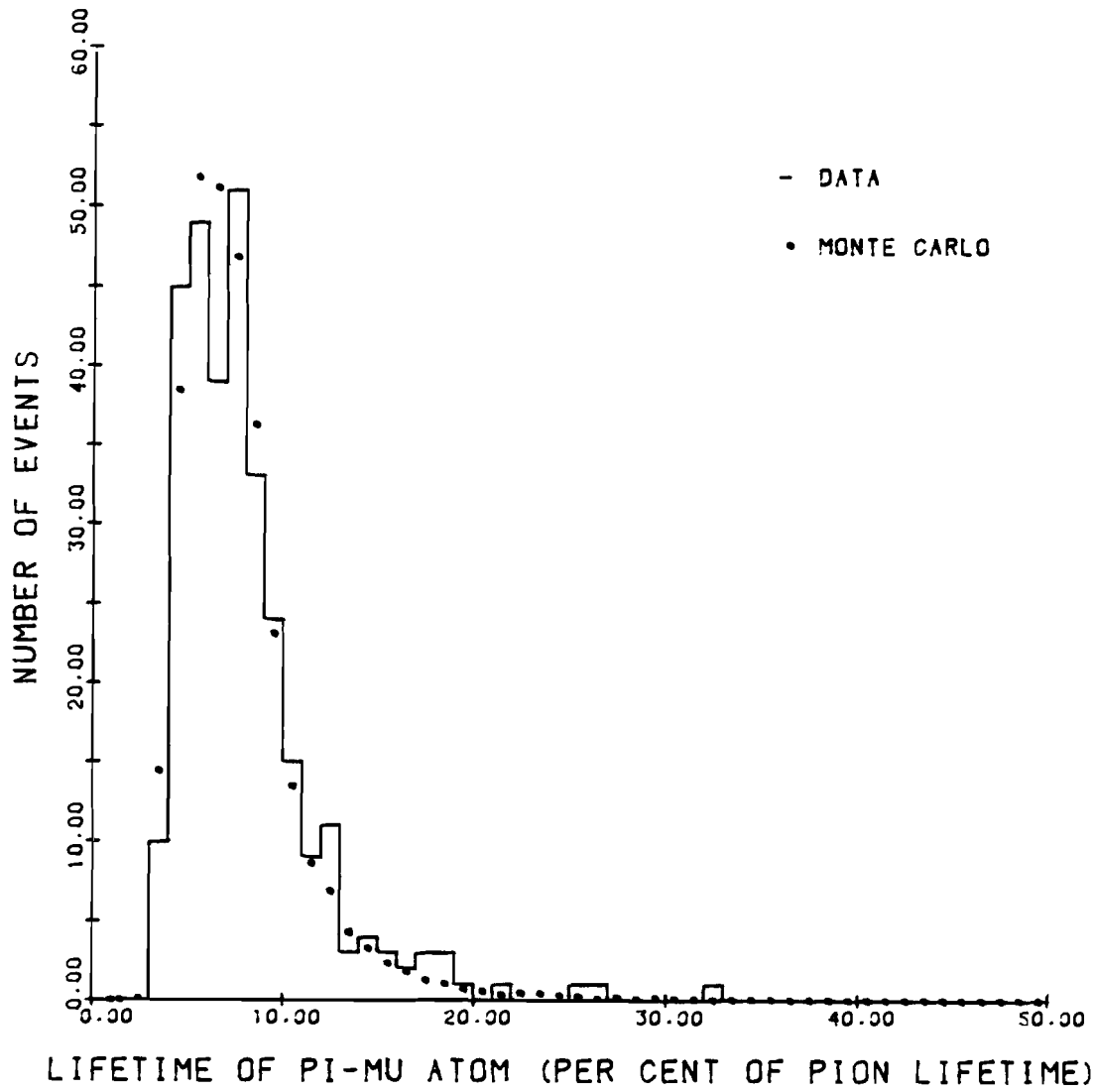

Figure 49. Lifetime of pi-mu atoms, compared to Monte Carlo pi-mu atoms generated with one third the lifetime of the pion (normalized to equal areas).

by 14%. Thus, to the extent that the measured branching ratio agreed with the theoretical prediction, there was no evidence for an anomalous pi-mu atom lifetime.

CHAPTER 12

THE SINGLE PHOTON TRANSVERSE MOMENTUM SPECTRUM

The object of the analysis of the single photon transverse momentum (p_t) spectrum was a measurement of branching ratios for the decays $K_L^o \to \pi^o \pi^o$ and $K_L^o \to \gamma\gamma$ in terms of the well-measured branching ratio for $K_L^o \to \pi^o \pi^o \pi^o$. The relative contributions to this spectrum from the many K_L^o decays yielding photons were determined by fitting the Monte Carlo p_t distributions of the individual decay modes to the data, subject to certain constraints. Two sources of background were also included in the fitting procedure: e^+e^- pairs from trident production in the foil, and photons from interactions of neutrons in the beam. Branching ratios were derived by combining the parameters of the fit with the acceptances for each decay, as determined by the Monte Carlo program and the EGS Code System.

12.1 THE COMPONENTS OF THE SPECTRUM, INCLUDING BACKGROUNDS

The photon p_t spectrum for those data which survived all cuts was displayed in Chapter 9. Figures 50 through 54 show the p_t spectra for Monte Carlo generated events subjected to the same cuts. The decay modes $K_L^o \to \pi^o\pi^o\pi^o$, $K_L^o \to \pi^+\pi^-\pi^o$, $K_L^o \to \pi e \nu \gamma$, $K_L^o \to \pi^o\pi^o$, and $K_L^o \to \gamma\gamma$ are represented in these figures. (The total number of events in each Monte Carlo histogram was scaled according to the fit to the data, described below.) The $K_{\pi 3}$ decays were confined to p_t less than 160 MeV/c, while the photons from $K_L^o \to \pi^o\pi^o$ extended from 15 MeV/c to 235 MeV/c. Notice that photons from radiative K_{e3} decays made a contribution to the spectrum just above the 3π fall-off, as well as below. The p_t spectrum of photons from $K_L^o \to \gamma\gamma$ illustrates the Jacobian shape discussed in Chapter 4. The $\gamma\gamma$ events reached 275 MeV/c and had no background from $K_L^o \to \pi^o\pi^o$ above 235 MeV/c.

The spectrum of photons expected from neutron interactions with the residual gas in the evacuated decay pipe was determined empirically, using data taken with a "spoiled vacuum", i.e. with the pressure in the decay pipe ranging from 900 to 2000 microns of mercury. The p_t spectrum for this data is shown in Figure 55. Superposed is a curve of the form $Ae^{-(Bp_t)}$ with a slope B = 6.53 $MeV^{-1}c$ (and amplitude A) determined from a fit for $p_t \geq 175$

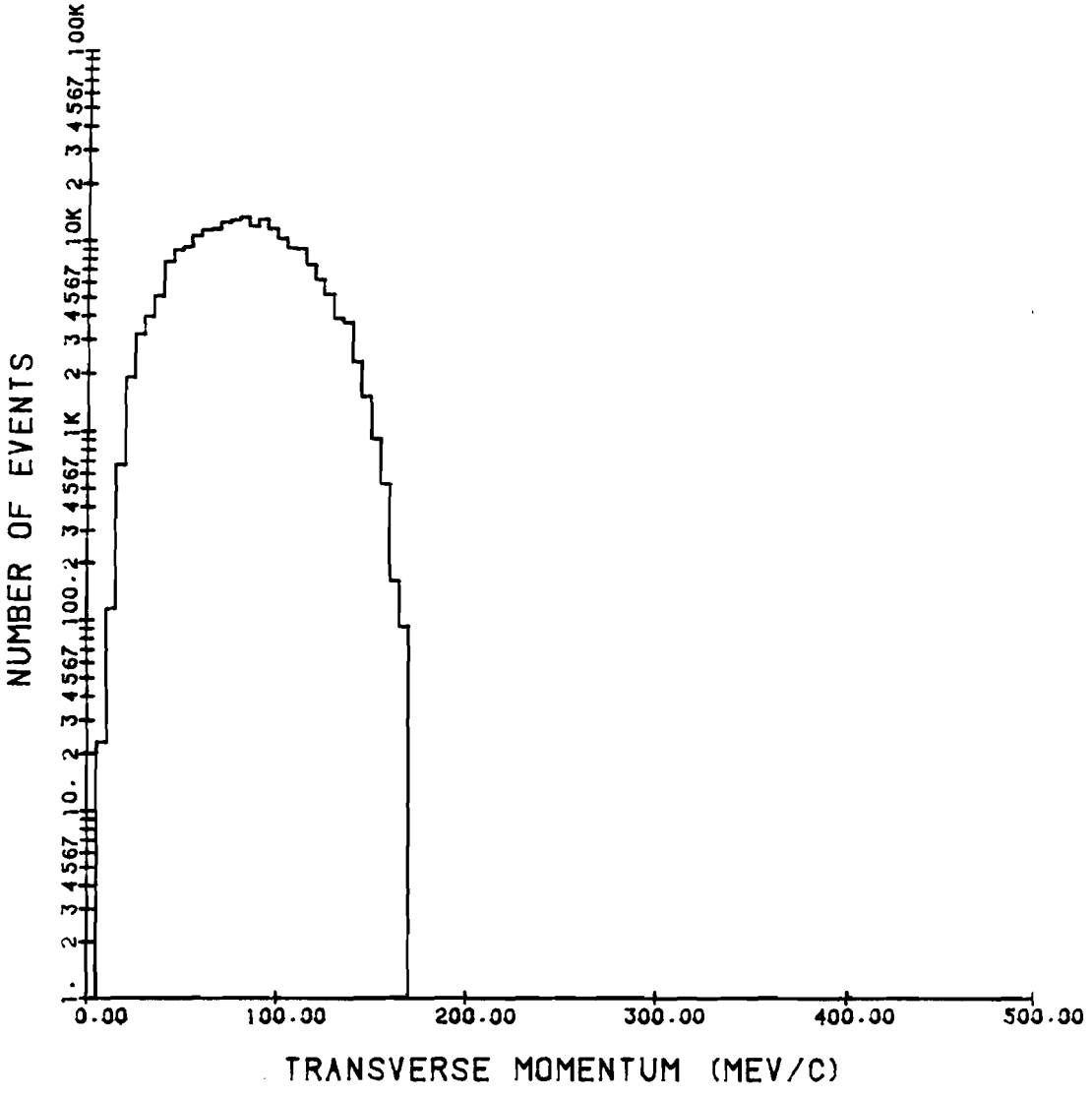

Figure 50. Monte Carlo simulation of the portion of the photon transverse momentum spectrum due to $K_L^0 \to \pi^0 \pi^0 \pi^0$.

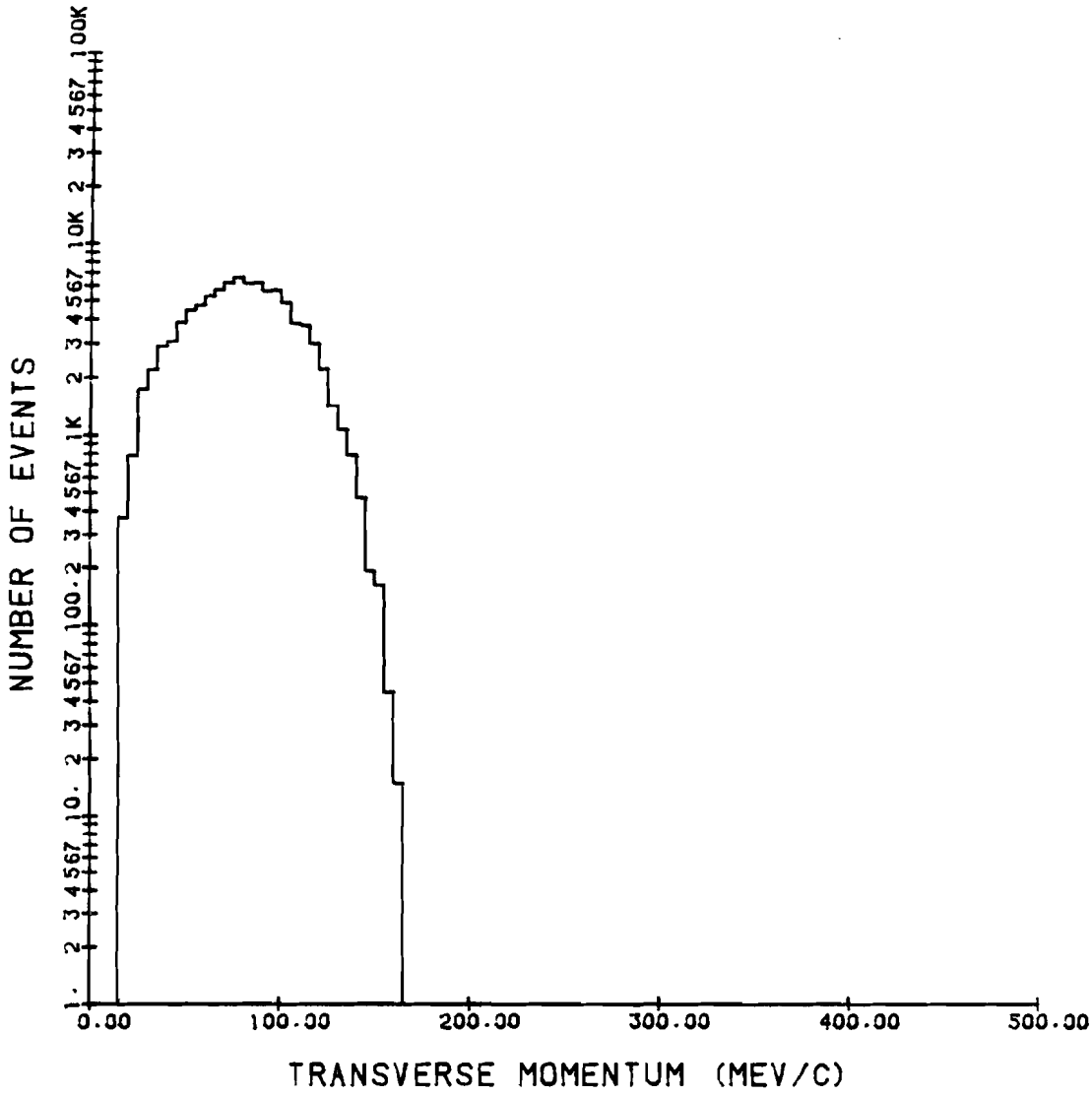

Figure 51. Monte Carlo simulation of the portion of the photon transverse momentum spectrum due to $K_L^0 \to \pi^+ \pi^- \pi^0$.

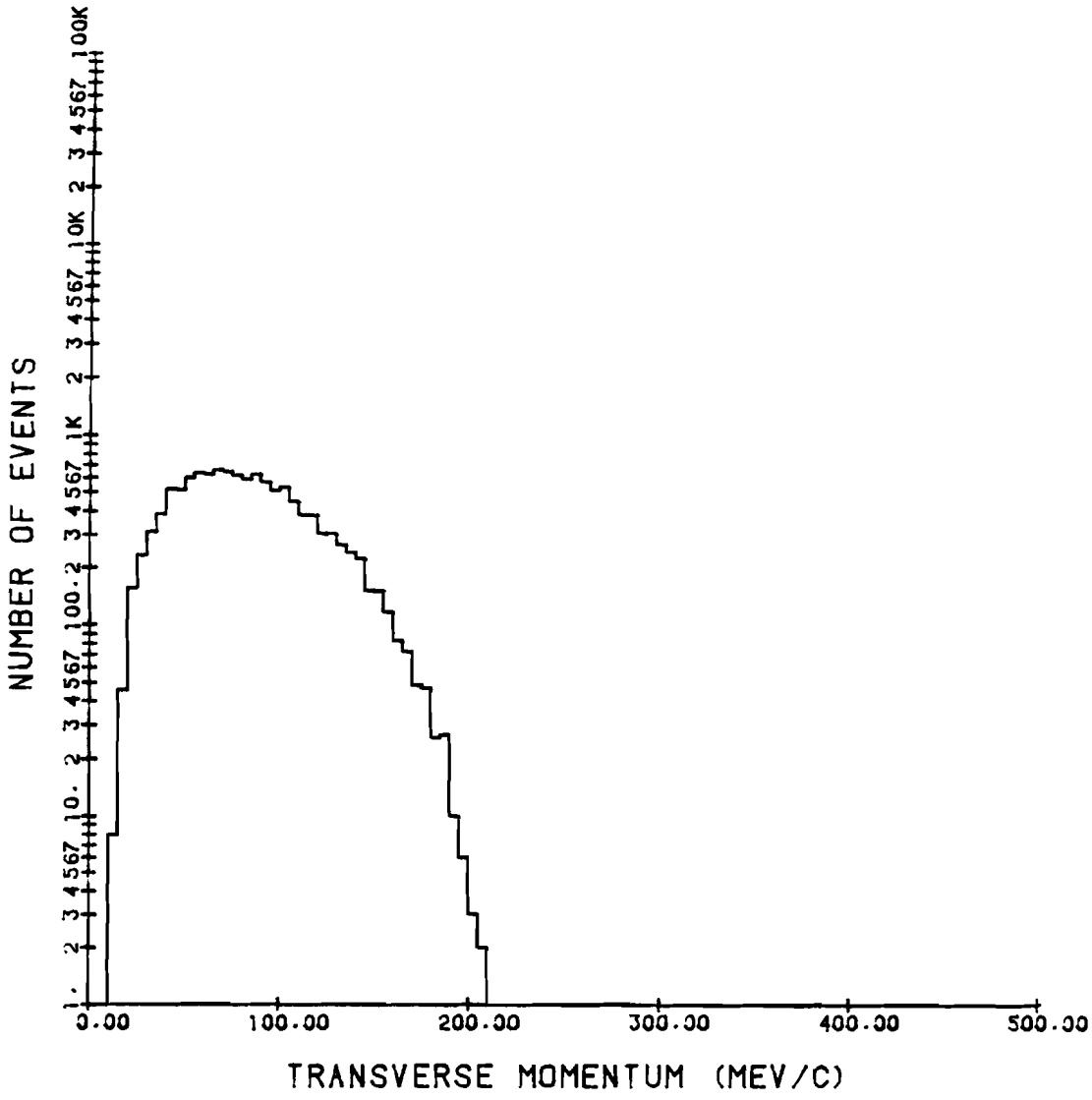

Figure 52. Monte Carlo simulation of the portion of the photon transverse momentum spectrum due to $K_L^o \rightarrow \pi e \nu \gamma$.

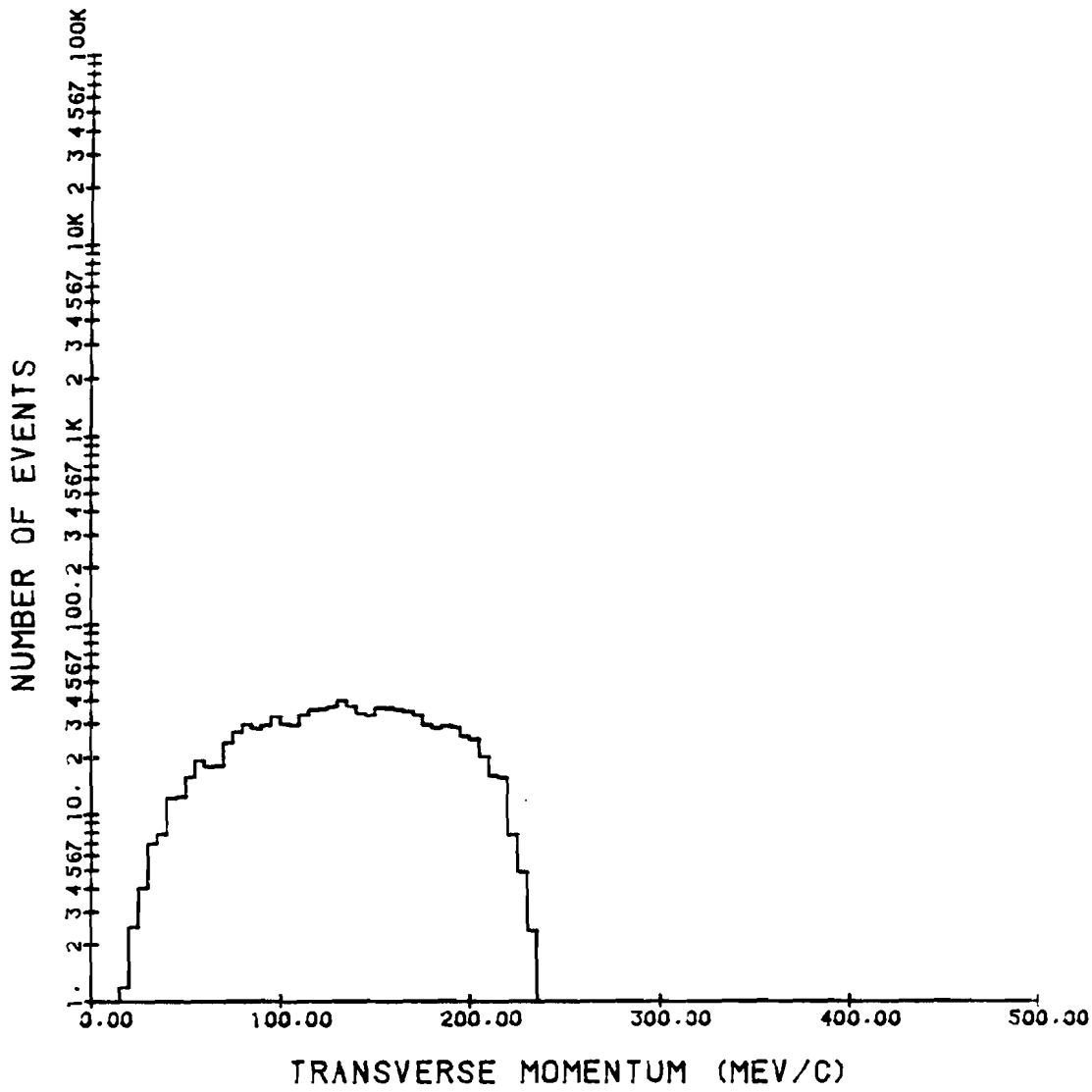

Figure 53. Monte Carlo simulation of the portion of the photon transverse momentum spectrum due to $K_L^o \rightarrow \pi^o \pi^o$.

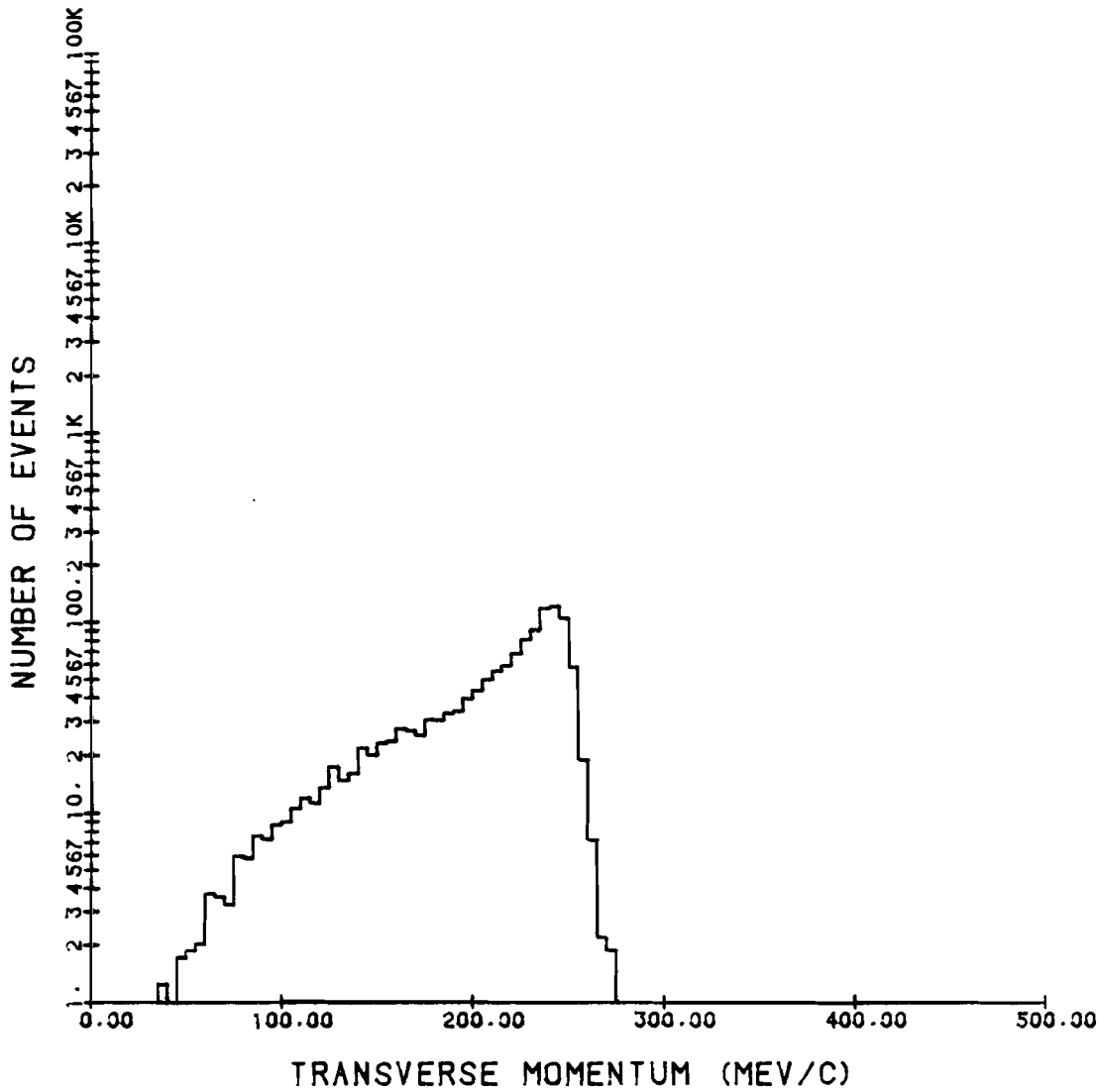

Figure 54. Monte Carlo simulation of the portion of the photon transverse momentum spectrum due to $K_L^o \rightarrow \gamma\gamma$.

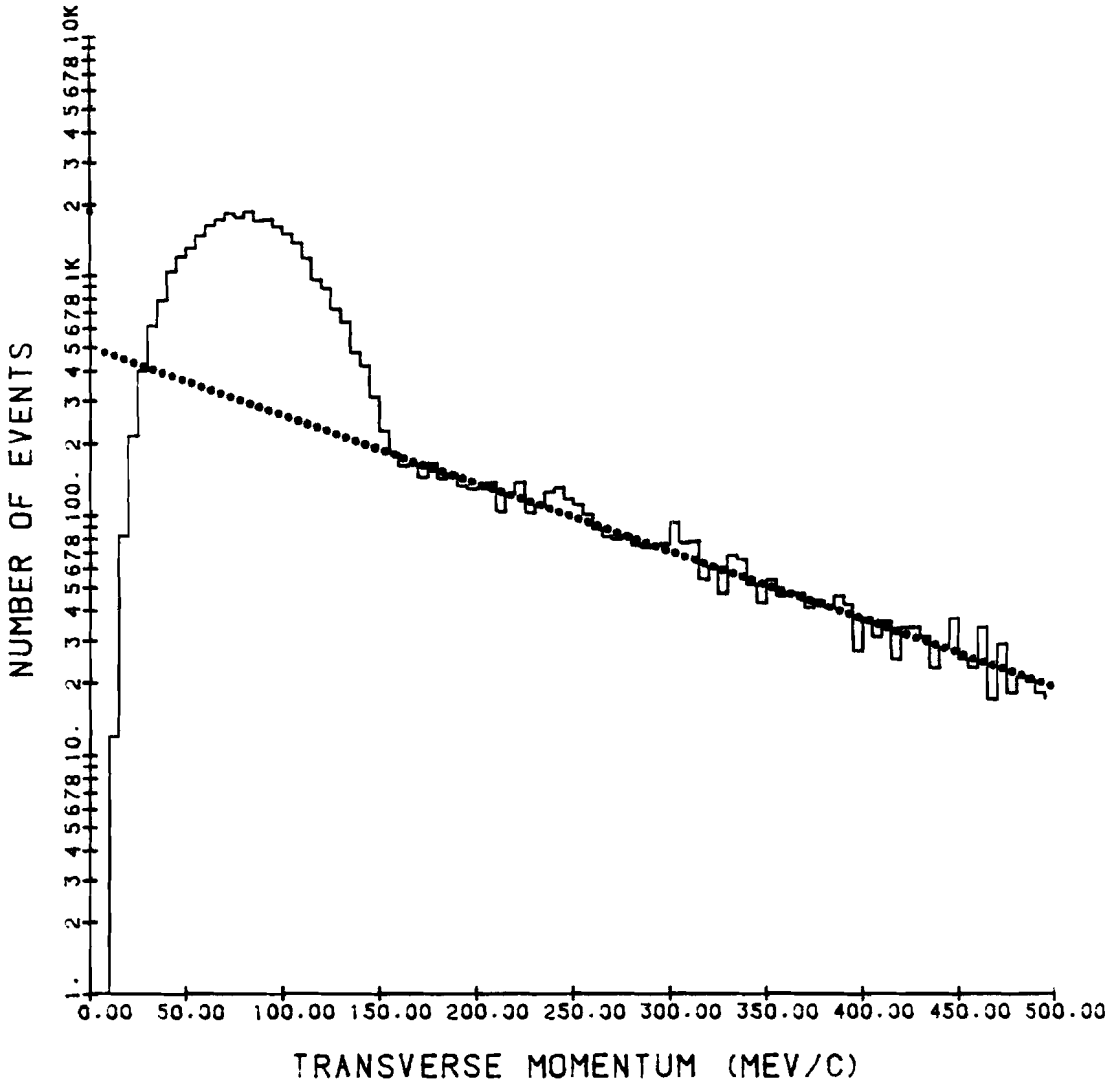

Figure 55. Transverse momentum of photons, from data taken with the vacuum spoiled.

MeV/c. (The fit gave B = 6.53 ± 0.17 $MeV^{-1}c$, with a χ^2 per degree of freedom 1.1.) This exponential spectrum was extrapolated to lower values of p_t, but forced to turn over where the acceptance of the detector vanished at very low p_t, using a multiplicative factor of

$$1 - e^{-(p_t-0.01)/5}$$

The precise form of this factor was not important, since it contributed a negligibly small background to the 3π peak, and preserved the shape of the exponential decay at high p_t. Thus the p_t spectrum for the beam background was characterized by

$$H_{neutron}(p_t) \sim [1 - e^{-(p_t-0.01)/5}][e^{-6.53p_t}]$$

This curve is drawn in Figure 56.

The simulation of the remaining contribution to the spectrum, a background from trident production in the foil, has been discussed at some length (see Chapter 7). The points relevant to the analysis may be summarized as follows. Electrons and positrons which produced an e^+e^- pair in the foil mimicked a photon conversion when the member of the pair with the same charge as the incident particle had so little momentum that it was either curled up in one of the magnets downstream, or swept out of the detector. (It could also happen that the primary particle gave up nearly all of its energy to the pair, but this was far less likely.) The observed pair of oppositely charged

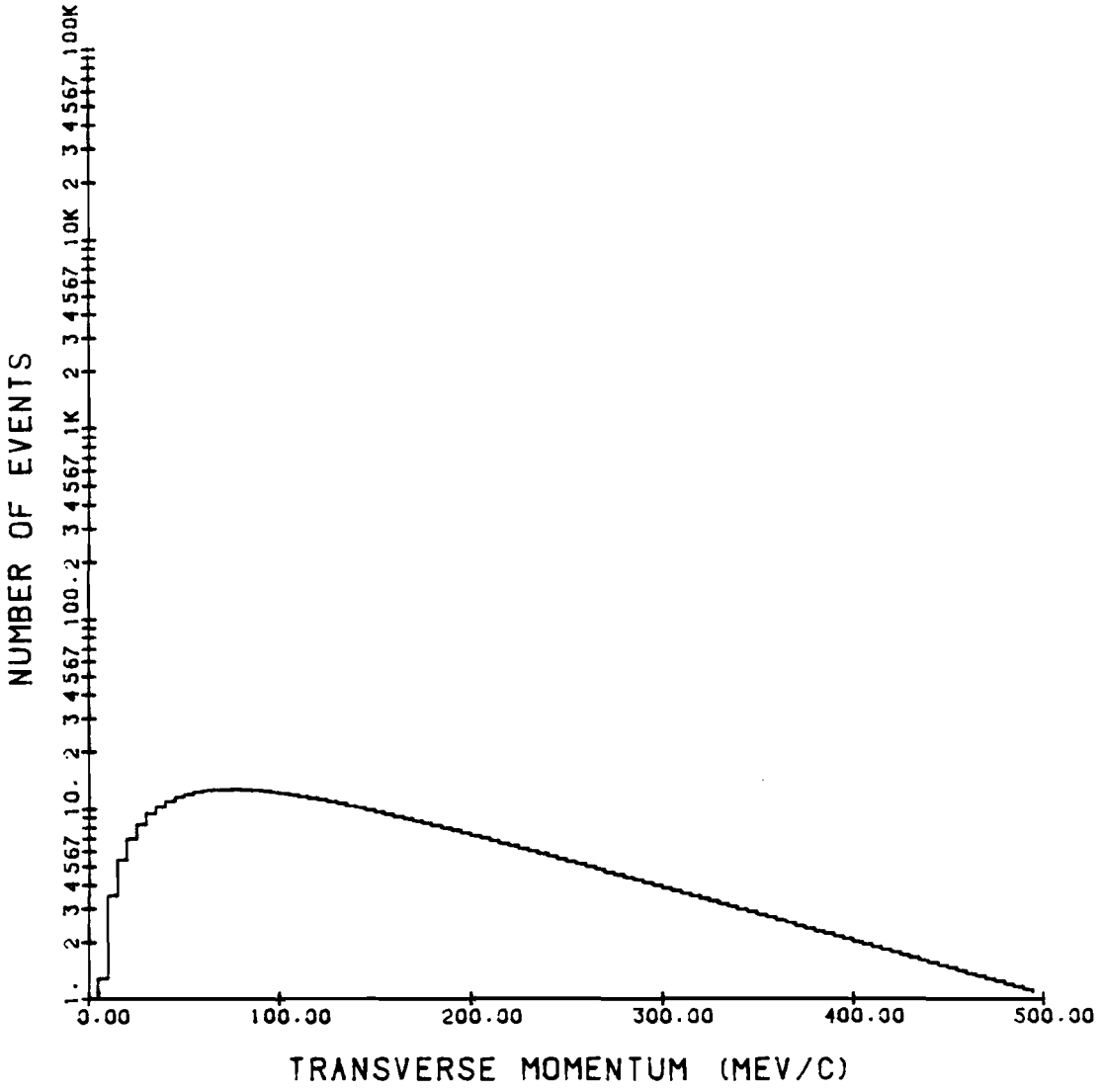

Figure 56. Transverse momentum of photons attributed to beam-gas interactions.

particles was mistaken for a pair produced by a photon. As a result, the apparent transverse momentum was actually the vector sum of the transverse momentum of the primary charged particle upstream of the vertically bending magnets and the transverse momentum impulse of those magnets, 83.9 MeV/c. Furthermore, because they deflected positively charged particles downward, the primary particles sent up into the foil were principally electrons, from K_{e3} decay. In any case, only those particles bent upward contributed a non-negligible background to the p_t spectrum above the 3π peak. Delta rays accompanied by an incident positron were therefore neglected. (Also, Monte Carlo studies of delta ray production in the foil revealed that the opening angle between the knock-on electron and the incident particle was in general larger than the opening angle of an e^+e^- pair produced by a photon, causing a significant number of such events to fail the geometric requirements imposed on the reconstructed tracks.)

That tridents were indeed a serious background beneath the high p_t "shoulder" was demonstrated by studying the fraction of the energy of the supposed photon that was carried off by the observed positively charged particle. In terms of the energy of the positron E_+, the pair production differential cross-section has a broad flat minimum around equipartition of the photon energy between

the electron and positron, and peaks at the maximum and minimum of E_+ (for a high energy photon). The distribution is also symmetric. Such a distribution would be expected from the detected photons as well, if the acceptance of the detector were uniform across the distribution. In fact, the acceptance was symmetric about equipartition of energy, but vanished toward the maximum and minimum of positron energy (since one of the two particles would be swept out of the apparatus). Figure 57 is a histogram of E_+/E_γ, where E_γ is the photon energy. The data and Monte Carlo events have been picked from the interesting region of transverse momenta 165 MeV/c $\leq p_t <$ 285 MeV/c. The Monte Carlo distribution does not include the trident (or the neutron) background. The data exhibit a clear excess of events on the low side of E_+/E_γ, above a symmetric Monte Carlo curve. These events had a stiff electron and a soft positron, characteristic of trident production by an electron, where the electron in the produced pair went undetected. Figure 58 displays the same sample of data, but the Monte Carlo distribution now includes e^+e^- pairs from trident production.

Although the agreement between the two E_+/E_γ curves is not perfect, this was not particularly troublesome, since the shape of the p_t distribution for tridents reflected mainly the p_t distribution of the electron from K_{e3} decay,

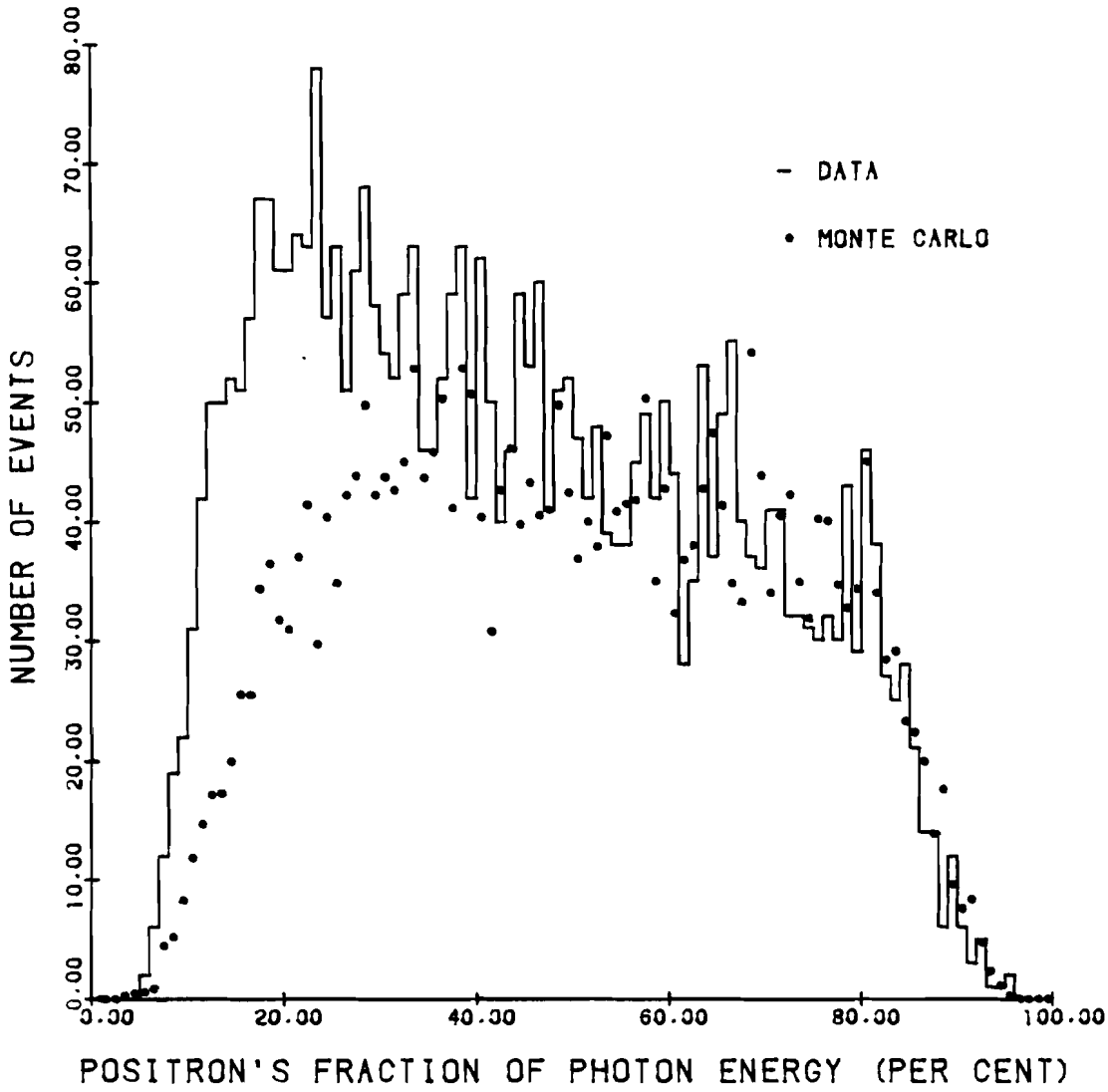

Figure 57. The ratio of the energies of the positron and photon, for the final sample of e^+e^- pairs, compared to Monte Carlo generated e^+e^- events, not including tridents.

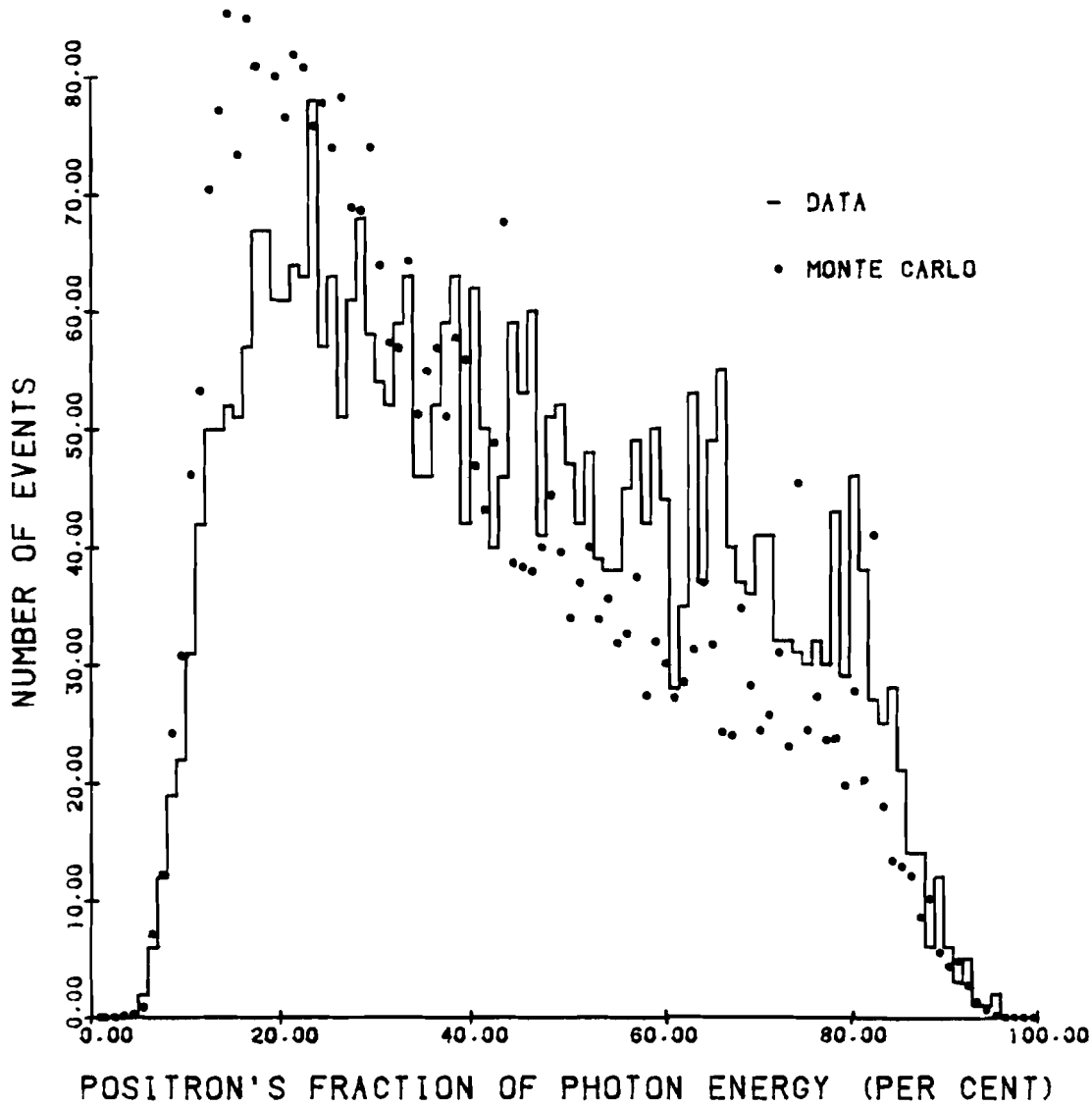

Figure 58. The ratio of the energies of the positron and photon, for the final sample of e^+e^- pairs, compared to Monte Carlo generated e^+e^- events, including tridents.

augmented by the momentum impulse provided by the magnetic field upstream of the foil. However, confidence that the Monte Carlo did correctly simulate the shape of this background came from the analysis of events with two particles of the same charge that originated at a point on the foil. Precisely the same cuts applied to e^+e^- pairs were applied to e^-e^- and e^+e^+ pairs, except, of course, that two particles of the same charge were required. Figure 59 shows the p_t spectrum for events of like charge. (Almost all of these were e^-e^- pairs.) The agreement between the Monte Carlo "like sign" tridents and the data is excellent. Finally, Figure 60 displays the Monte Carlo p_t distribution for "opposite sign" tridents, the background included in the present analysis.

12.2 THE LOSS OF EVENTS DUE TO ELECTROMAGNETIC SHOWERS

The EGS Code System parameter p has been discussed in Chapter 8 and Section 9.1. In this section a value for p is obtained, using the relative numbers of detected $K_{\mu 3}$ events and photons from $K_L^o \to 3\pi$. The EGS loss factors are then determined.

Proceeding in the same fashion as in Chapter 11, we make the following definitions:

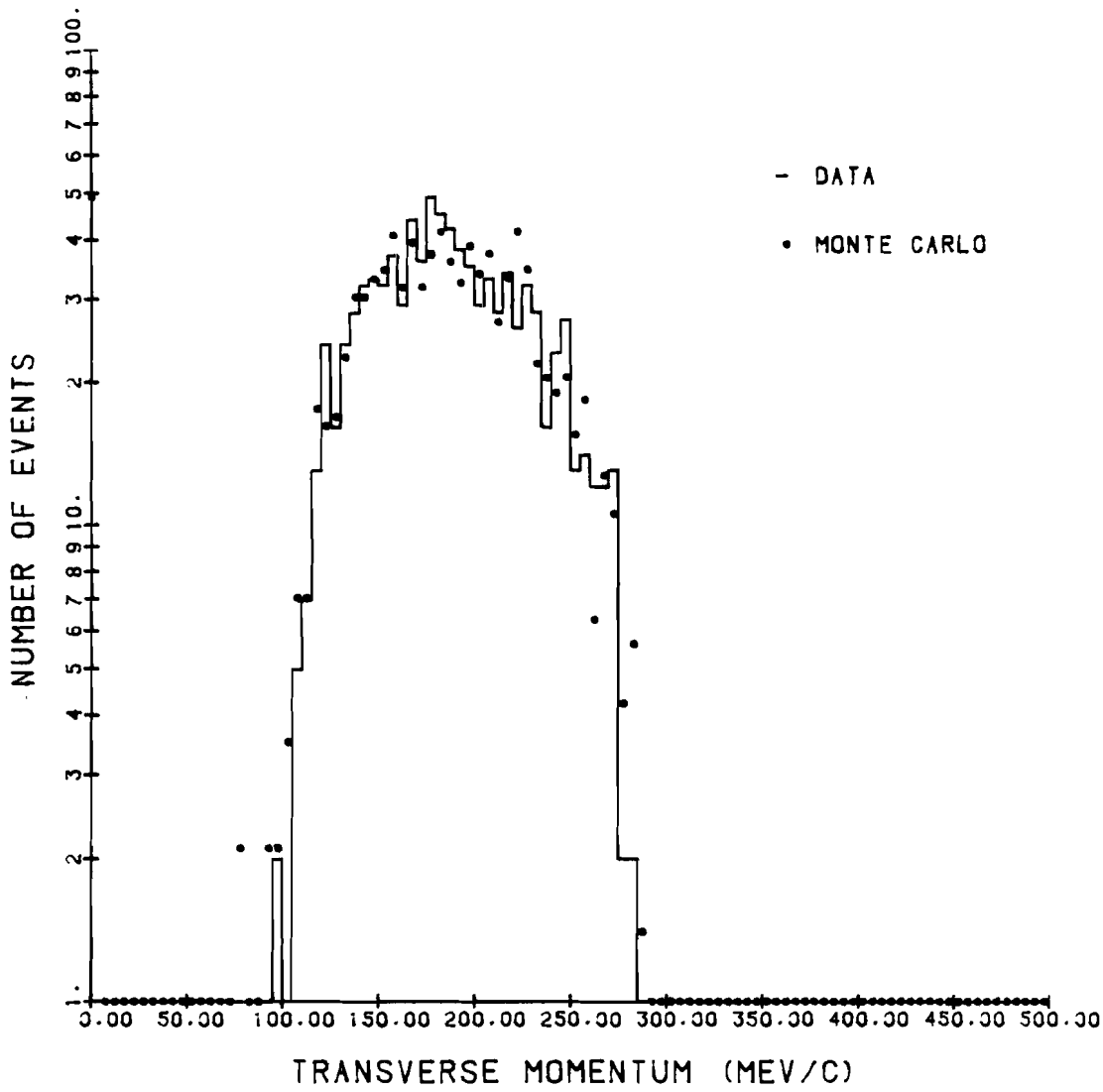

Figure 59. Transverse momentum spectrum of e^-e^- pairs passing all cuts for foil events, compared to Monte Carlo generated e^-e^- events from trident production.

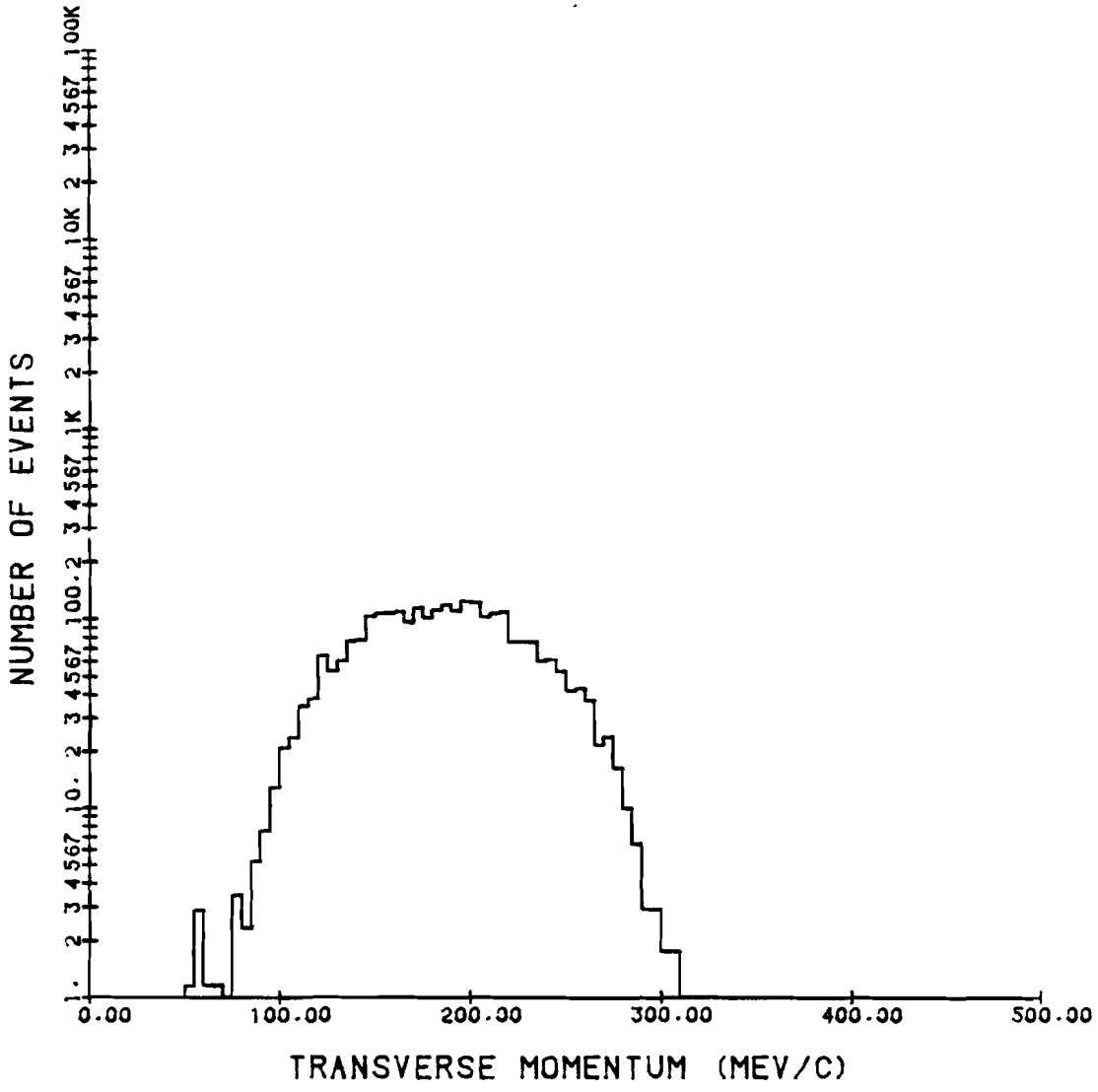

Figure 60. Monte Carlo simulation of the portion of the photon transverse momentum spectrum due to e^+e^- pairs from trident production.

$N_{K\mu3-MC}$ = total number of kaons which decayed in the decay volume in the Monte Carlo generation of $K_{\mu3}$ events

$T_{K\mu3-MC}$ = total number of $K_{\mu3}$ events in the final Monte Carlo sample

N_{data} = total number of kaons which decayed in the decay volume while experiment was "live"

$T_{K\mu3-data}$ = total number of $K_{\mu3}$ events in the final data sample, background subtracted

$B_{K\mu3}$ = branching ratio $\Gamma(K_L^o \to \pi\mu\nu)/\Gamma(K_L^o \to all)$.

They are related by

$$\frac{T_{K\mu3-data}}{N_{data}} = \frac{T_{K\mu3-MC}}{N_{K\mu3-MC}} \cdot B_{K\mu3} \cdot 1/32$$

where, again, the factor of (1/32) was in the $K_{\mu3}$ trigger. Analogous quantities may be defined for the decays $K_L^o \to \pi^o\pi^o\pi^o$ (shorthand $3\pi0$) and $K_L^o \to \pi^+\pi^-\pi^o$ (shorthand $3\pi c$, c for charged). In order to avoid cluttering the equations, acceptance corrections (discussed below) that were not included in the Monte Carlo simulation have been absorbed in $T_{3\pi0-MC}$ and $T_{3\pi c-MC}$, except for the loss of events due to electromagnetic showers. The EGS loss factors, as a function of p, are defined by

$E_{3\pi 0}(p)$ = fraction of $3\pi 0$ events remaining after EGS shower simulations .

Thus we have

$$\frac{T_{3\pi 0\text{-data}}}{N_{\text{data}}} = \frac{T_{3\pi 0\text{-MC}}}{N_{3\pi 0\text{-MC}}} \cdot B_{3\pi 0} \cdot E_{3\pi 0}(p)$$

and

$$\frac{T_{3\pi c\text{-data}}}{N_{\text{data}}} = \frac{T_{3\pi c\text{-MC}}}{N_{3\pi c\text{-MC}}} \cdot B_{3\pi c} \cdot E_{3\pi c}(p)$$

where the branching ratios are

$$B_{3\pi 0} = 0.215 \pm 0.007$$

$$B_{3\pi c} = 0.1239 \pm 0.0018 \quad .$$

Combining the above three equations and eliminating N_{data} gives

$$\frac{T_{3\pi 0\text{-data}} + T_{3\pi c\text{-data}}}{T_{K\mu 3\text{-data}}}$$

$$= \left(T_{3\pi 0\text{-MC}} \cdot B_{3\pi 0} \cdot E_{3\pi 0}(p)/N_{3\pi 0\text{-MC}} + T_{3\pi c\text{-MC}} \cdot B_{3\pi c} \cdot E_{3\pi c}(p)/N_{3\pi c\text{-MC}}\right) \cdot \left(T_{K\mu 3\text{-MC}} \cdot B_{K\mu 3}/N_{K\mu 3\text{-MC}}/32\right)^{-1} \quad .$$

This is the expression which determined the value of p, given the EGS curves displayed in Chapter 8.

The numerator on the left hand side of the equation was taken from the p_t spectrum of the data, for 0 MeV/c < p_t < 155 MeV/c. (The same event reconstruction routine used for

$K_{\mu 3}$ events was used here for the e^+e^- Monte Carlo and data.) The background contamination from the other sources of photons described in Section 12.1 was (2.0 ± 0.5)% in this region.

The acceptance corrections referred to above were of two kinds. One was related to the probability of photon conversion in the foil. Since the first photon (from a given K_L^o decay) that struck the foil was converted to an e^+e^- pair 100% of the time in the Monte Carlo simulation, in order to calculate the true acceptance, the number of events in the final sample had to be multiplied by the conversion probability for a photon traversing 20 or 35 mils of aluminum foil (see Chapter 5). However, for those events which had more than one photon hitting the foil, this procedure underestimated the detection efficiency. If the conversion probability for a single photon is P_{cnv}, then the probability that a photon converts when two strike the foil is $2P_{cnv} - P_{cnv}^2$. Similarly, when three strike the foil, the probability that a photon converts is $3P_{cnv} - 3P_{cnv}^2 + P_{cnv}^3$. Thus, if we denote by F_n the fraction of events in the final sample that had n photons hitting the foil, then the acceptance correction P'_{cnv} for the conversion probability was

$$P'_{cnv} = P_{cnv}\ (1 + F_2 + 2F_3 + \ldots)$$

(neglecting terms of order P^2_{cnv}). As might be expected, F_n was non-zero only for the $3\pi^o$ and $2\pi^o$ decay modes. These figures are summarized as follows:

$$3\pi^o:\quad P'_{cnv} = P_{cnv}\ (1 + 0.176 \pm 0.004)$$

$$2\pi^o:\quad P'_{cnv} = P_{cnv}\ (1 + 0.047 \pm 0.002)\quad .$$

(The errors are from the statistics of the Monte Carlo simulation.)

The other acceptance corrections were related to the trigger and particle identification efficiencies. Since the Monte Carlo did not attempt to reproduce the shower counter $FRAC_n$ distribution, or the inefficiencies of the muon identification (aside from that due to multiple scattering), the $K_{\mu 3}$ Monte Carlo acceptance was reduced by (4.0 ± 0.5)% to account for the loss of events that had large hadronic showers, and by (3.0 ± 2.0)% to account for the loss of events in the muon counter trigger requirement. The Monte Carlo acceptance for e^+e^- pairs was diminished by (0.9 ± 0.5)% to take care of the corresponding shower counter cut for electrons. (These acceptance corrections were necessary only in this part of the analysis, since the particles in the final state differed for the decay modes compared.) Also, just as for pi-mu atoms, a (6.3 ± 1.0)% loss of e^+e^- triggers was due to random coincidences in the W and H counters.

Numerically, the equations of constraint for p were

$$0.371 \pm 0.028 = E_{3\pi 0}(p) + (0.146 \pm 0.005)\ E_{3\pi c}(p)$$

and

$$0.363 \pm 0.027 = E_{3\pi 0}(p) + (0.146 \pm 0.005)\ E_{3\pi c}(p)$$

for the 20 mil and 35 mil data, respectively. The error for the coefficient of $E_{3\pi c}(p)$ came from the errors on the 3π branching ratios and the statistics on the numbers of events in the final Monte Carlo 3π samples. The error on the left hand side of each equation derived from the errors on the acceptance corrections noted above, the errors on the input branching ratios, and a 6.3% systematic error on the measurement of $K_{\mu 3}$ decays relative to foil events (see Table 4). These equations were satisfied by $p = 0.125 \pm 0.029$, where the error on p embraces the results for each data set, and reflects the errors in the equation of constraint. This value for p implied

$$E_{3\pi 0} = 0.25 \pm 0.03 \pm 0.02$$

$$E_{3\pi c} = 0.78 \pm 0.01 \pm 0.03$$

$$E_{2\pi 0} = 0.46 \pm 0.03 \pm 0.03$$

$$E_{\gamma\gamma} = 0.74 \pm 0.02 \pm 0.03 \quad .$$

The first error quoted came from the uncertainty in p, the second from the statistical errors on the EGS loss factors themselves. (Due to the shape of the EGS curves, the errors on p and on the EGS loss factors were not exactly

symmetric, but that fact was of little consequence.) The larger losses corresponded to the larger value of p.

12.3 THE FITTING PROCEDURE

The computer program MINUIT (ref. 58) was used to fit the p_t histogram of the data with a sum of Monte Carlo histograms. Let us define

$H_{data}(p_t)$ = p_t histogram for final data sample

$H_{3\pi 0}(p_t)$ = p_t histogram for Monte Carlo $3\pi 0$ sample

and so on for the other decay modes, and tridents. $H_{neutron}$ was defined above. The program MINUIT found, by iteration, the constants A_i which satisfied the following equation:

$$H_{data} = A_{3\pi}\left(H_{3\pi 0} + \frac{E_{3\pi c}\cdot B_{3\pi c}}{E_{3\pi 0}\cdot B_{3\pi 0}} H_{3\pi c}\right)$$

$$+ A_{2\pi 0}\cdot H_{2\pi 0} + A_{\gamma\gamma}\cdot H_{\gamma\gamma} + A_{\pi e\nu\gamma}\cdot H_{\pi e\nu\gamma}$$

$$+ A_{trident}\cdot H_{trident} + A_{neutron}\cdot H_{neutron}$$

$$\equiv H_{Monte\ Carlo} \quad .$$

The separate components of $H_{Monte\ Carlo}$ have been shown; their sum is shown in Figure 61. Figure 62 presents a superposition of $H_{Monte\ Carlo}$ on the data. The χ^2 of the fit was 188 for 94 degrees of freedom.

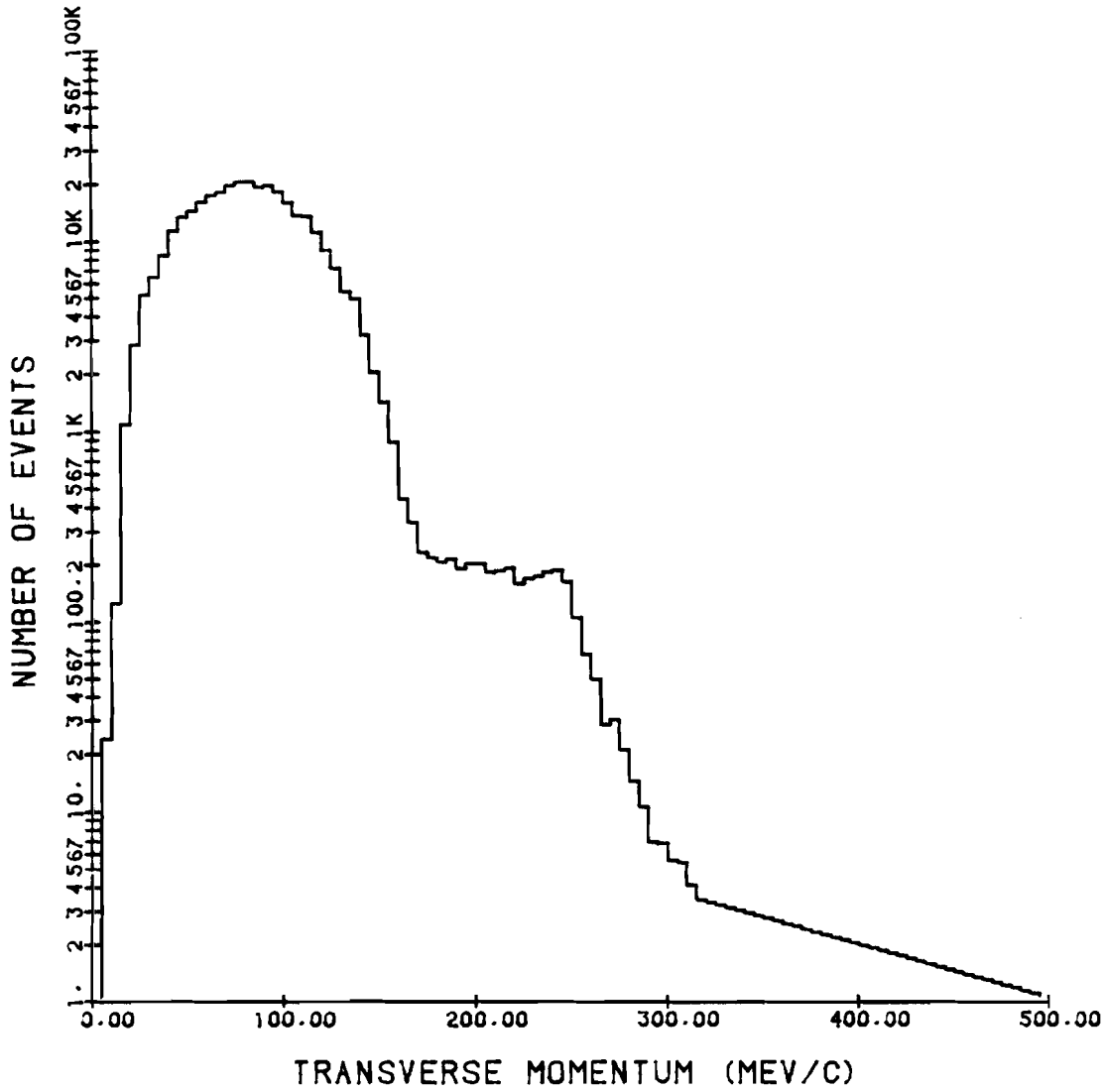

Figure 61. Complete Monte Carlo simulation of the transverse momentum spectrum of reconstructed photons, after the fit to the data described in the text.

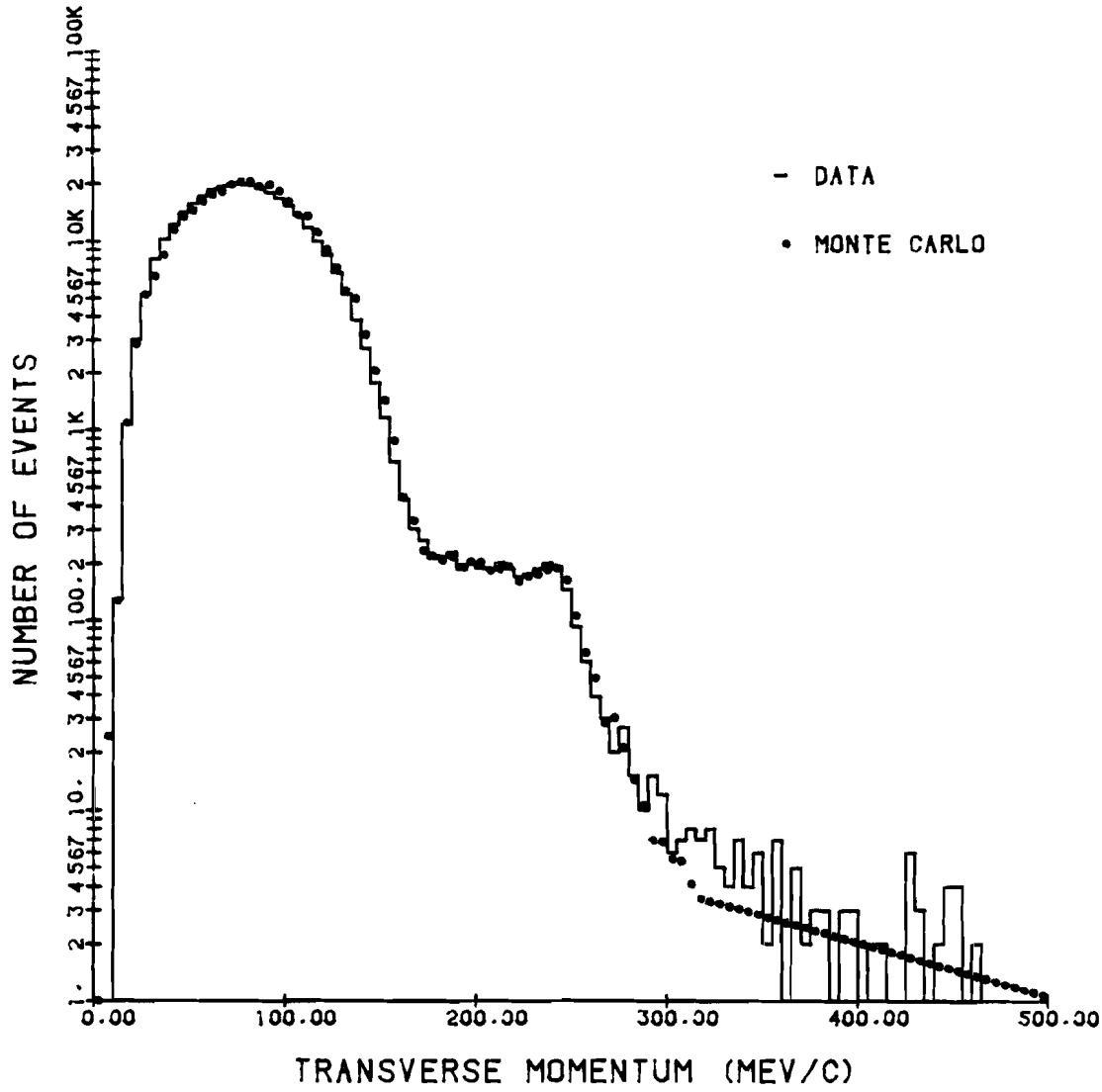

Figure 62. Transverse momentum of photons in the final sample, compared to the complete Monte Carlo simulation.

Of the acceptance corrections noted above, the only one which carried over to the fitting procedure was the conversion probability correction for the number of events with more than one photon passing through the foil. In other words, $H_{3\pi 0}$ and $H_{2\pi 0}$ were scaled by 1.176 and 1.047, respectively.

The relative contributions of the sources of photons were allowed to float freely, except for the decay $K_L^o \to \pi^+\pi^-\pi^o$, which was fixed relative to $K_L^o \to \pi^o\pi^o\pi^o$ because the p_t spectra for the two decay modes had essentially the same minima and maxima. Thus, the ratio of their EGS loss factors and the ratio of their decay rates were incorporated in the fit, as can be seen by inspection of the equation above. Each of the other sources of photons contributed, to a greater or lesser degree, to different regions of p_t above 165 MeV/c. In particular, the magnitude of the Monte Carlo trident background was partly governed by the few bins, 5 MeV/c wide, to the right of the $\gamma\gamma$ signal.

12.4 THE $2\pi^o$ and $\gamma\gamma$ BRANCHING RATIOS

The branching ratios for the rare decay modes were extracted as follows. Using the expressions in Section 12.2 for $T_{3\pi 0\text{-data}}$ and $T_{3\pi c\text{-data}}$, we have

$$T_{3\pi 0\text{-data}} + T_{3\pi c\text{-data}} = N_{data} \cdot T_{3\pi 0\text{-MC}} \cdot B_{3\pi 0} \cdot E_{3\pi 0} / N_{MC}$$

$$+ N_{data} \cdot T_{3\pi c\text{-MC}} \cdot B_{3\pi c} \cdot E_{3\pi c} / N_{MC}$$

where $T_{3\pi 0\text{-MC}}$, etc., have been renormalized so that $N_{3\pi 0\text{-MC}} = N_{3\pi c\text{-MC}} = N_{2\pi 0\text{-MC}} = N_{\gamma\gamma\text{-MC}} = N_{MC}$. From the fit, we infer

$$T_{3\pi 0\text{-data}} + T_{3\pi c\text{-data}} = \frac{A_{3\pi}}{E_{3\pi 0} \cdot B_{3\pi 0}} \left(T_{3\pi 0\text{-MC}} \cdot B_{3\pi 0} \cdot E_{3\pi 0} \right.$$

$$\left. + T_{3\pi c\text{-MC}} \cdot B_{3\pi c} \cdot E_{3\pi c} \right) .$$

Comparing the two equations, we find

$$\frac{A_{3\pi} \; N_{MC}}{E_{3\pi 0} B_{3\pi 0}} = N_{data}$$

$$\frac{A_{2\pi 0} N_{MC}}{E_{2\pi 0} B_{2\pi 0}} = N_{data} \quad .$$

Eliminating N_{data} gives expressions for the desired branching ratios in terms of the well-known $3\pi^{o}$ branching ratio, the parameters A_i of the fit, and ratios of EGS acceptance corrections:

$$B_{2\pi 0} = B_{3\pi 0} \frac{A_{2\pi 0} \; E_{3\pi 0}}{A_{3\pi} \; E_{2\pi 0}}$$

$$B_{\gamma\gamma} = B_{3\pi 0} \frac{A_{\gamma\gamma} \; E_{3\pi 0}}{A_{3\pi} \; E_{\gamma\gamma}} \quad .$$

Using the following figures

$$B_{3\pi 0} = 0.215 \pm 0.007$$

$$E_{3\pi 0} = 0.25 \pm 0.04$$

$$A_{3\pi} = 29.41 \pm 0.43$$

$$E_{2\pi 0} = 0.46 \pm 0.04$$

$$A_{2\pi 0} = 0.113 \pm 0.071$$

$$E_{\gamma\gamma} = 0.74 \pm 0.04$$

$$A_{\gamma\gamma} = 0.156 \pm 0.016$$

we found

$$\frac{\Gamma(K_L^o \to \pi^o \pi^o)}{\Gamma(K_L^o \to \text{all})} = B_{2\pi 0} = (4.6 \pm 2.9 \pm 0.4) \times 10^{-4}$$

and

$$\frac{\Gamma(K_L^o \to \gamma\gamma)}{\Gamma(K_L^o \to \text{all})} = B_{\gamma\gamma} = (3.9 \pm 0.4 \pm 0.4) \times 10^{-4}$$

for the entire e^+e^- pair data sample. These results are to be compared with the Particle Data Group world averages:

$$B_{2\pi 0} = (9.4 \pm 1.8) \times 10^{-4}$$

and

$$B_{\gamma\gamma} = (4.9 \pm 0.5) \times 10^{-4} \quad .$$

In each case, our results appear significantly lower. However, the $2\pi^o$ and $\gamma\gamma$ measurements were made to a precision of only 64% and 15%, respectively. As such, the error bars do overlap.

By similar means, we found that

$$\frac{\Gamma(K_L^o \to \pi e \nu \gamma,\ E_\gamma > 40\ \text{MeV})}{\Gamma(K_L^o \to \text{all})} = B_{\pi e \nu \gamma} = (11.1 \pm 3.7 \pm 0.6) \times 10^{-3} .$$

This compared favorably with the Particle Data Group value

$$\frac{\Gamma(K_L^o \to \pi e \nu \gamma,\ E_\gamma > 15\ \text{MeV})}{\Gamma(K_L^o \to \text{all})} = B_{\pi e \nu \gamma} = 0.013 \pm 0.008 .$$

However, this result was not taken too seriously because the Monte Carlo simulation did not include the other particles in the decay, and relied on a theoretical energy spectrum. Our intention was primarily to obtain a reasonable p_t spectrum for this decay to use in the fit to the data.

The first errors quoted above were calculated by the program MINUIT. The uncertainty in the magnitude of the trident background, among other things, accounted for these large errors. The second errors shown are systematic. The principal systematic error on these results came from the uncertainty in the EGS loss factors. (The MINUIT errors did not vary significantly with p.) Table 5 lists sources of systematic errors. The error associated with the K_L^o momentum spectrum represents the effect of varying the input spectrum by a weighting factor which depressed and raised the tails of the distribution by 30%. The systematic error is comparable to the MINUIT error for the $\gamma\gamma$ measurement, but is dwarfed by the MINUIT error for the $2\pi^o$ measurement.

Table 4. Sources of Systematic Errors

Source of Error	Magnitude, as Fraction of Result		
	$2\pi^0$	$\gamma\gamma$	$K_{e3\gamma}$
Slope of neutron background	0.027	0.0025	0.011
B counter trigger losses	0.005	0.006	
Kaon momentum spectrum	0.028	0.042	
EGS parameter p	0.035	0.056	0.055
Statistics on EGS factors	0.081	0.080	
Total systematic error	0.097	0.107	>0.056

The above branching ratios were calculated for subsamples of the data in order to check for consistency. In particular, results were obtained for 20 and 35 mil foils, for $E_{positron} > E_{electron}$ and $E_{positron} < E_{electron}$ (to check that the trident background was in hand), and for two different regions for the assumed K_L^o decay point. These checks were plagued by statistical fluctuations. Therefore, the larger data sample furnished by the first event reconstruction routine was analyzed in identical fashion, except that the EGS loss factors could not be calculated for these data, since that routine was not suited to the reconstruction of $K_{\mu 3}$ decays. The results obtained for p = 0.125 were

$$B_{2\pi 0} = (9.9 \pm 2.2) \times 10^{-4}$$

and

$$B_{\gamma\gamma} = (4.2 \pm 0.3) \times 10^{-4}$$

where only the MINUIT errors are given. Figure 63 displays the p_t spectrum for these data, with the Monte Carlo superposed. (The χ^2 of the fit was 159 for 94 degrees of freedom.) The agreement of the $\gamma\gamma$ results using the two event reconstruction routines gave us confidence that this procedure was not wholly unfounded. It suggested, further, that the $2\pi^o$ measurement was not so firm. The subsamples of the data were consistent with one another, when analyzed with the routine written expressly for foil event reconstruction.

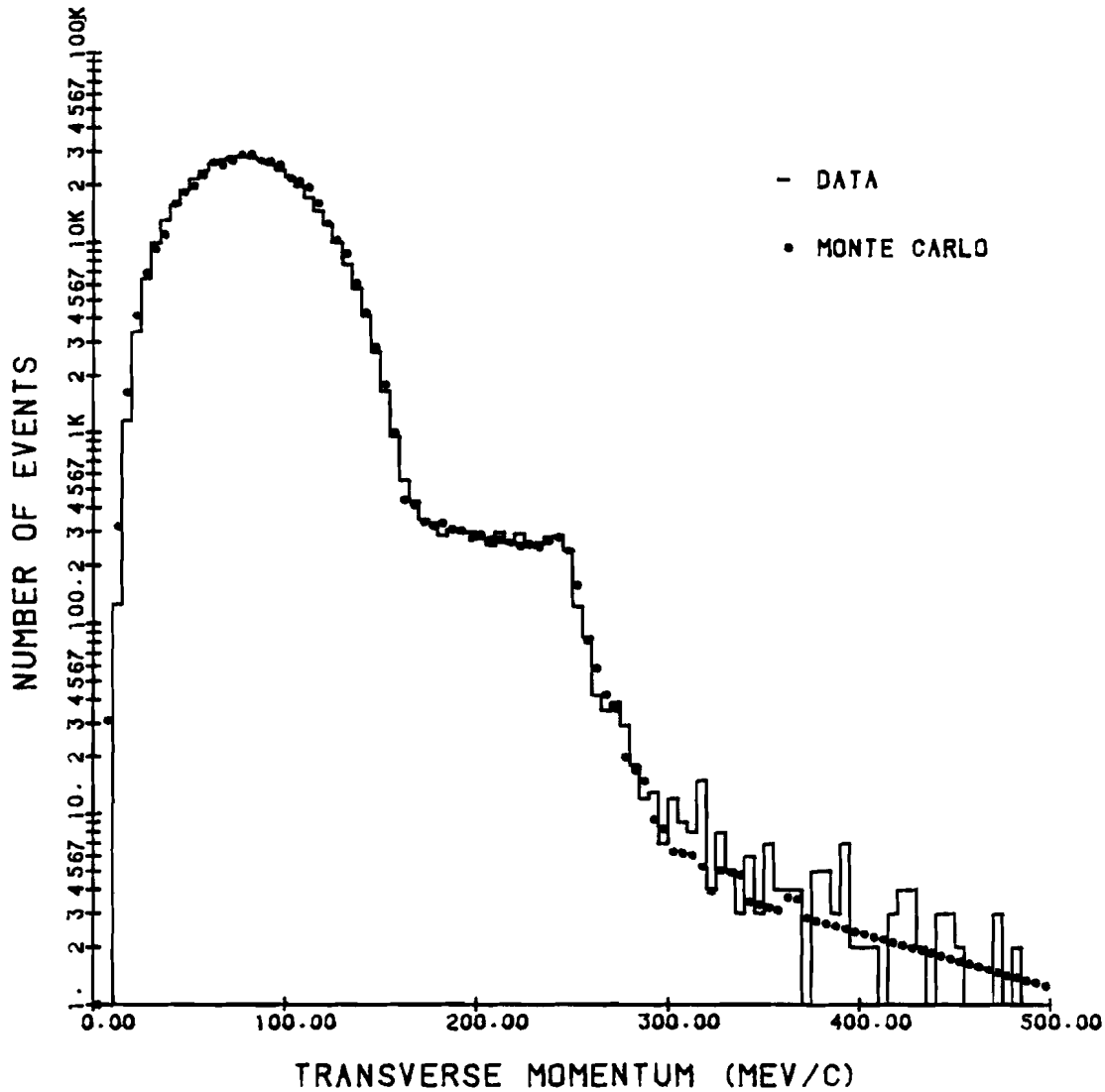

Figure 63. Transverse momentum of photons, compared to the complete Monte Carlo simulation, for the largest number of events available.

CHAPTER 13

CONCLUSIONS

In assessing the pi-mu atom branching ratio result presented in Chapter 11, one might bear in mind that measurements of extremely small branching ratios are difficult. This one was no exception. For instance, understanding the acceptance of the spectrometer over such a lengthy decay region required considerable effort, the success of which may be judged from the preceeding figures of the longitudinal position of the K_L^o decay point. The determination of the acceptances for the pi-mu atom and $K_{\mu 3}$ decay modes depended crucially upon a complicated Monte Carlo simulation of the experiment. Moreover, these acceptances were quite small (1.88×10^{-2} for pi-mu atoms, and 1.37×10^{-4} for $K_{\mu 3}$ decays). Nevertheless, systematic errors were estimated fairly.

Although the measured rate of formation of pi-mu atoms is lower than the theoretical prediction by 10%, the errors on the two figures overlap. The large discrepancy observed

in the first pi-mu atom experiment was not found in this one. Unfortunately, a measurement of the lifetime of the pi-mu atom, independent of the branching ratio result, could not be extracted from the data of this experiment. Theoretical prejudices based on experimental results notwithstanding (ref. 7), a pi-mu anomaly which manifests itself in the decay channels of a pi-mu atom remains a possibility, and calls for a new experiment.

The similarity of the means of detecting pi-mu atoms and photons in this experiment stimulated a study of the single photon transverse momentum spectrum. We have obtained new measurements of the branching ratios

$$\frac{\Gamma(K_L^o \to \pi^o \pi^o)}{\Gamma(K_L^o \to \text{all})}$$

and

$$\frac{\Gamma(K_L^o \to \gamma\gamma)}{\Gamma(K_L^o \to \text{all})} .$$

These results are lower than, but not inconsistent with, the Particle Data Group weighted averages of previous measurements.

The experimental hurdles involved in obtaining these results were also formidable. The principal uncertainty in the acceptance calculations for K_L^o decays with photons in the final state stemmed from the fact that only one photon was detected; the others had a high probability of

showering upstream of the detector. In addition, substantial backgrounds hampered efforts to reduce the errors on the measurements. (If only the vertically bending magnets had been run at a higher current!)

Precision measurements of the $2\pi^0$ decay mode have been sought for some time. The error on our result is far too large to shed new light on the theoretical issues.

REFERENCES

1. Anne L. Hall, The Detection of Pi-Mu Atoms, Ph.D. Thesis, Stanford University, 1977.

2. R. Coombes, R. Flexer, A. Hall, R. Kennelly, J. Kirkby, R. Piccioni, D. Porat, M. Schwartz, R. Spitzer, J. Toraskar, S. Wiesner, B. Budick, and J. W. Kast, "Detection of π-μ Coulomb Bound States", Physical Review Letters 37, 249 (1976).

3. Hall, op. cit., pp. 87, 97.

4. op. cit., p. 98.

5. op. cit., p. 100.

6. M. Schwartz, public communication.

7. Robin Staffin, Limits on a Pi-Mu Anomaly and The Low Lying Spectrum of Lattice QCD in Two Dimensions, Ph.D. Thesis, Stanford University, 1979;
   Robin Staffin, "Limits on a π-μ atom anomaly", Physical Review D 16, 726 (1977).

8. Uzi Bar-Gadda and C. F. Cho, "Pi-Muonium: A Determination of the Pion Charge Radius", Physics Letters, 46B, 95 (1973).

9. C. F. Cho, "The Energy Levels of Pi-Muonium", Il Nuovo Cimento 23A, 557 (1974).
   See also V. A. Rizov, I. T. Todorov, and B. L. Aneva, "Quasipotential Approach to the Coulomb Bound State Problem for Spin-0 and Spin-½ Particles", Nuclear Physics B98, 447 (1975);
   H. M. M. Mansour and K. Higgins, "On the Lifetime of the Excited States of the Exotic Atoms", Il Nuovo Cimento, 36A, 196 (1976).

10. L. L. Nemenov, "Atomic Decays of K_L^0 Mesons", Soviet Journal of Nuclear Physics 16, 67 (1973) (Yad. Fiz. 16, 125 (1972)).

11. Ching Cheng-rui, Ho Tso-hsiu, and Chang Chao-hsi, "On the (π-μ) Atoms Produced in K_L^o Decay", Preprint No. ASITP-80-006 (Fermilab Preprint No. 41,296), Institute of High Energy Physics, Academia Sinica, 1980.

12. This treatment is based on Anne Hall's, op. cit.

13. Particle Data Group, "Review of Particle Properties", Reviews of Modern Physics 52 (1980). See discussion Section VI.B.2. and Data Card Listings, p. S79 ff.
Particle properties (branching ratios, lifetimes, masses, etc.) quoted in the text all derive from this review, unless another reference is given.

14. G. Donaldson, et al., "Measurement of the form factors in the decay $K_L^o \to \pi\mu\nu$", Physical Review D 9, 2960 (1974).

15. H. W. Fearing, E. Fischbach, and J. Smith, "Current Algebra, $\bar{K}_{\ell 3}^o$ Form Factors, and Radiative $\bar{K}_{\ell 3}^o$ Decay", Physical Review D 2, 542 (1970). See in particular p. 560.

16. E. S. Ginsberg, "Radiative Corrections to $K_{\mu 3}$ Decays", Physical Review D 1, 229 (1970). See also Donaldson, et al., op. cit.

17. R. Staffin, private communication.

18. J. H. Christenson, J. W. Cronin, V. L. Fitch, and R. Turlay, "Evidence for the 2π Decay of the K_2^o Meson", Physical Review Letters 13, 138 (1964).

19. See, for example, T. D. Lee and C. S. Wu, "Decays of Neutral K Mesons", Annual Review of Nuclear Science 16, 511 (1966);
Eugene D. Commins, Weak Interactions (McGraw Hill, Inc., New York, 1973);
J. F. Greenhalgh, Junior Paper, Princeton University, Fall 1974 (unpublished).

20. L. Wolfenstein, "Violation of CP Invariance and the Possibility of Very Weak Interactions", Physical Review Letters, 13, 562 (1964).

21. See, for example, Commins, op. cit., pp. 251-254.

22. F. J. Gilman and M. B. Wise, "The $\Delta I=\frac{1}{2}$ Rule and Violation of CP in the Six-Quark Model", Physics Letters 83B, 83 (1979).

23. Experiment 617, Bruce Winstein, spokesperson: Fermilab Proposal P617.

24. A good starting point for a literature search is M. J. Shochet, P. Linsay, C. Grosso-Pilcher, H. J. Frisch, R. DeVoe, J. W. Cronin, and D. R. Moffett, "Measurement of the decay rate for the process $K_L^0 \to \mu^+\mu^-$", Physical Review D 19, 1965 (1979).

25. A. R. Clark, T. Elioff, R. C. Field, H. J. Frisch, R. P. Johnson, L. T. Kerth, and W. A. Wenzel, "Experimental Limits on the Decays $K_L^0 \to \mu^+\mu^-$, e^+e^-, and $\mu^\pm e^\mp$", Physical Review Letters 26, 1667 (1971).

26. Shochet, et al., op. cit., references 3,4,5,6,7 therein.

27. M. K. Gaillard and M. Nikolic, eds., Weak Interactions, Institut National de Physique Nucleaire et de Physique des Particules (Textbook on Elementary Particle Physics) pp. 124, 326.

28. M. K. Gaillard and B. W. Lee, Physical Review D 10, 897 (1974).

29. Hall, op. cit., pp. 13-20.

30. Frederic H. Middleton, Design Engineer, Physical Sciences Laboratory, University of Wisconsin-Madison.

31. Shochet, et al., op. cit.;
C. Grosso-Pilcher supplied the field maps.

32. R. Piccioni, et al., Pysical Review D 9, 2939 (1974);
Joseph Cobb, at SLAC, provided the field map.

33. Bruce Winstein, private communication.

34. Dan I. Porat and Dale A. Ouimette, "Track Correlator as a Fast Trigger in the Detection of π-μ Coulomb Bound States", IEEE Transactions on Nuclear Science NS-26, 209 (1979).

35. David Hedin, A Measurement of the Rate of Formation of Pi-Mu Atoms in K_L^o Decay, Ph.D. Thesis, University of Wisconsin-Madison, December 1980.

36. A. S. Carroll, I-H. Chiang, T. F. Kycia, K. K. Li, L. Littenberg, M. Marx, P. O. Mazur, J. P. de Brion, and W. C. Carithers, "Observation of the Dalitz Decay Modes of the K_L^o", Physical Review Letters, 44, 525 (1980).

37. Feinberg and Lederman, Annual Review of Nuclear Science 13, 431 (1963).

38. Fearing, et al., op. cit., figure 6.

39. Total cross-sections as a function of energy for electron and photon interactions in a lead absorber are plotted in Figures 3.1 and 3.3 in Messel and Crawford, Electron-Photon Shower Distribution Function Tables for Lead, Copper, and Air Absorbers (Pergamon Press, 1970).
The electromagnetic cascade shower development is approximately independent of absorber when the cross-sections are expressed in inverse radiation lengths.

40. Bruno Rossi, High Energy Particles (Prentice-Hall, Englewood Cliffs, N. J., 1952) p. 60.

41. J. W. Motz, H. A. Olsen, and H. W. Koch, "Pair Production by Photons", Reviews of Modern Physics 41, 581 (1969).

42. Motz, et al., op. cit.
We used Formula 3D-1009A, pp. 609-610, with a Coulomb correction function for aluminum.

43. A. Borsellino, "Momentum Transfer and Angle of Divergence of Pairs Produced by Photons", Physical Review 89, 1023 (1953);
Hart, et al., Physical Review 115, 678 (1959).
See footnote 15 for correction of misprints in Borsellino's paper.

44. Rossi, op. cit., p. 81.

45. Yung-Su Tsai, "Pair production and bremsstrahlung of charged leptons", Reviews of Modern Physics 46, 815 (1974).

Note erratum Reviews of Modern Physics 49, 421 (1977).

46. J. F. Carlson, W. H. Furry, Physical Review 44, 237 (1933).

47. A short review article, essentially an annotated bibliography, is A. G. Wright, "A critical evaluation of theories of direct electron pair production by muons", J. Phys. A: Proc. Phys. Soc., London, 6, 79 (1973).

48. S. R. Kel'ner, "Pair Production in Collisions Between a Fast Particle and a Nucleus", Soviet Journal of Nuclear Physics 5, 778 (1967).

49. S. R. Kel'ner and Yu. D. Kotov, "Muon Energy Loss to Pair Production", Soviet Journal of Nuclear Physics 7, 237 (1968).

50. R. P. Kokoulin and A. A. Petrukhin, "Analysis of the Cross-Section of Direct Pair Production by Fast Muons", Proceedings of the 11th International Conference on Cosmic Rays, Budapest 1969, Acta Physica Academiae Scientiarum Hungaricae 29, Suppl. 4, 277 (1970).

51. R. P. Kokoulin and A. A. Petrukhin, "Influence of the Nuclear Formfactor on the Cross-section of Electron Pair Production by High Energy Muons", Proceedings of the 12th International Conference on Cosmic Rays, Hobart 1970, vol. 6, (Hobart: University of Tasmania) p. 2436.

52. V. L. Highland, "Some Practical Remarks on Multiple Scattering", Nuclear Instruments and Methods 129, 497 (1975).
This paper suggests simple corrections to the Particle Data Group formula for multiple scattering.

53. J. B. Marion and B. A. Zimmerman, "Multiple Scattering of Charged Particles", Nuclear Instruments and Methods 51, 93 (1967).
See in particular Table 1 for B = 6.

54. Rossi, op. cit., p. 71, eqn. 6.

55. R. L. Ford and W. R. Nelson, "The EGS Code System:

Computer Programs for the Monte Carlo Simulation of Electromagnetic Cascade Showers (Version 3)", SLAC Report No. 210 (1978).

56. P. Skubic, et al., Physical Review D 18, 3115 (1978).

57. Robert D. Cousins, Jr., A Measurement of the Rate of Formation of Pi-Mu Atoms in K_L^0 Decay, Ph.D. Thesis, Stanford University, January 1981.

58. F. James and M. Roos, MINUIT, CERN Computer Program Library Long Writeups D-506,D-516 (1971). Documentation for use at Fermilab is Computer Note PM-020.